TWO-PHOTON PHOTOEMISSION INVESTIGATION OF ELECTRONIC AND DYNAMICAL PROPERTIES OF ALKALI ATOMS ADSORBED ON NOBLE METAL SURFACES

by

Vahit Sametoglu

B.S. in Physics, Bogazici University, Istanbul, 2000

M.S. in Physics, University of Pittsburgh, Pittsburgh, 2002

Submitted to the Graduate Faculty of

Arts and Sciences in partial fulfillment

of the requirements for the degree of

PhD in Physics

University of Pittsburgh

2009

UNIVERSITY OF PITTSBURGH

SCHOOL OF ARTS AND SCIENCES

This dissertation was presented

by

Vahit Sametoglu

It was defended on

March 2, 2009

and approved by

Hrvoje Petek, Professor, Department of Physics and Astronomy

David Snoke, Professor, Department of Physics and Astronomy

Hong Koo Kim, Professor, Departmental of Electrical Engineering

David Waldeck, Professor, Department of Chemistry

Gurudev Dutt, Assistant Professor, Department of Physics and Astronomy

Dissertation Advisor: Hrvoje Petek, Professor, Department of Physics and Astronomy

TWO-PHOTON PHOTOEMISSION INVESTIGATION OF ELECTRONIC AND DYNAMICAL PROPERTIES OF ALKALI ATOMS ADSORBED ON NOBLE METAL SURFACES

Vahit Sametoglu, PhD

University of Pittsburgh, 2009

We present a systematic time-resolved two-photon photoemission study of the electronic and dynamical properties of Li through Cs adsorbed on Cu(111) and Ag(111) surfaces. A fundamental problem in surface science is how to describe the electronic structure of a chemisorption interface based on the intrinsic properties of the interacting materials. Because of their simple s-electron structure, elements of the alkali atom group comprise paradigmatic adsorbates in many theories of chemisorption, whereas the complementary experimental studies are sparse and incomplete. Through a combination of spectroscopic and femtosecond time-resolved surface measurements, we are able to probe systematically the binding energies, symmetries, and electron and nuclear relaxation dynamics of the initially unoccupied alkali atom resonances. As a prelude, we study the two-photon photoemission process occurring at the bare Ag(111) surface. We develop a quantitative model for two-photon photoemission process, where

the nonresonant and **k**-dependent two-photon absorption between the lower and upper sp-bands is modeled by the optical Bloch equations, and the angle-dependent intensities are described by the Fresnel equations. Our two-photon photoemission spectra of Li through Cs chemisorbed Cu(111) and Ag(111) surfaces reveal two resonances with the $m = 0$ and $m = \pm 1$ symmetry ('m' is the projection of the orbital angular momentum '*l*' onto the surface plane). For the $m = 0$ resonance, which is derived from the hybridization of the *n*s and *n*p_z orbitals of alkali atoms, we find a binding energy of $1.84 - 1.99$ eV below the vacuum level, which is independent of the alkali atom period, and tunes with coverage in a universal manner. At $0.3 - 0.7$ eV higher energy, we discover and identify the $m = \pm 1$ resonance by its characteristic angular intensity distribution, which derives from the antisymmetry of the *n*p_x and *n*p_y orbitals. We implement a quantitative model for the alkali atom chemisorption based on the dominant Coulomb interactions invoked by Langmuir and Gurney. Moreover, the time-resolved photoemission measurements on Cs/Ag(111) surface reveal an unprecedented nonexponential electronic population decay, which is indicative of the $Ag - Cs$ bond rupture; we follow the femtochemistry, i.e., the dissociative wave packet motion, on nearly the picosecond time scale.

Contents

List of Tables

List of Figures

List of Abbreviations and Symbols

PES : photoemission/photoelectron spectroscopy

ARPES : angle-resolved photoemission spectroscopy

1PP : one-photon photoemission

2PP : two-photon photoemission

AR1PP : angle-resolved one-photon photoemission

AR2PP : angle-resolved two-photon photoemission

TR2PP : time-resolved two-photon photoemission

ITR2PP : interferometric time-resolved two-photon photoemission

I2PC : interferometric two-pulse correlation

XPS : X-ray photoelectron spectroscopy

UPS : ultraviolet photoelectron spectroscopy

IPES : inverse photoemission spectroscopy

ELS : energy loss spectroscopy

PEEM : photoemission electron microscope/microscopy

LEED : low energy electron diffraction

HOMO : highest occupied molecular orbital

LUMO : lowest unoccupied molecular orbital

EDC : energy distribution curve

SS : (Shockley) surface state

IPS : image-potential state

AR : antibonding resonance (i.e., $m = 0$ resonance)

WPP : wave-packet propagation

DFT : density functional theory

OBE : optical Bloch equations

RCT : resonant charge transfer

DOS : density of states

ML : monolayer

GVD : group velocity dispersion

BBO : beta-barium borate

SPM : self-phase modulation

FWHM : full-width half maximum

UHV : ultra-high vacuum

TSP : titanium sublimation pump

RGA : residual gas analyzer

QMS : quadrupole mass spectrometer

TE : transverse electric

TM : transverse magnetic

UV : ultraviolet

cps : counts per second

$f_{FD}(E)$: Fermi-Dirac distribution function

$f_{BE}(E)$: Bose-Einstein distribution function

D : detector (hemispherical electron energy analyzer)

E_p : pass energy

E_F : Fermi level

E_{vac} : vacuum level

E_{kin} : kinetic energy

E_i : initial state energy

E_m : intermediate state energy

E_{int} : intermediate state energy

E_f : final state energy

U_{sp} : upper sp-band

L_{sp} : lower sp-band

amu : atomic mass unit (= 1.66×10^{-27} kg)

fcc : face-centered cubic

bcc : body-centered cubic

eV : electron-volt

h : Planck's constant (= 6.626×10^{-34} J s)

$h\nu$: photon energy

m_e : mass of electron (= 9.11×10^{-31} kg)

k_B : Boltzmann constant (= 1.38×10^{-23} m^2 kg s^{-2} K^{-1})

R_{ads} : adsorption distance

H : Hamiltonian

H_0 : (unperturbed) Hamiltonian

H_{int} : interaction Hamiltonian

T_p : pulse width

L_{coh} : coherence length

Δk : phase-mismatch parameter

$\mathbf{A}$: vector potential

$\mathbf{p}$: momentum

$\boldsymbol{\nabla}$: momentum operator

m_{eff} : effective mass

m_e : mass of electron

V_{IP} : attractive image potential

V_{Δ} : repulsive ion core image-charge potential

$k_{\parallel}$: parallel momentum

$k_{\perp}$: perpendicular momentum

$|0\rangle$: initial state

$|1\rangle$: intermediate state

$|2\rangle$: final state

Θ_D : Debye temperature

Φ : work function

φ : potential energy

Δ : (energy) detuning

τ : pump–probe time delay

μ : dipole moment

ρ : radius in polar coordinates parallel to the surface; density operator

σ : adsorbate coverage; sigma-symmetry

π : pi-symmetry

Å : Ångström (= 10^{-10} m)

a_0 : atomic (length) unit, i.e., Bohr radius (= 52.9×10^{-12} m)

Publications

1. N. Pontius, V. Sametoglu, and H. Petek, *Simulation of two-photon photoemission from the bulk sp-bands of Ag(111)*, Physical Review B, **72**, 115105 (2005).

2. A. Winkelmann, V. Sametoglu, J. Zhao, A. Kubo, and H. Petek, *Angle-dependent study of a direct optical transition in the sp-bands of Ag(111) by one- and two-photon photoemission*, Physical Review B, **76**, 195428 (2007).

3. J. Zhao, N. Pontius, A. Winkelmann, V. Sametoglu, A. Kubo, A. G. Borisov, D. Sánchez-Portal, V. M. Silkin, E. V. Chulkov, P. M. Echenique, and H. Petek, *Electronic potential of a chemisorption interface*, Physical Review B, **78**, 085419 (2008).

4. A. G. Borisov, V. Sametoglu, A. Winkelmann, A. Kubo, N. Pontius, J. Zhao, V. M. Silkin, J. P. Gauyacq, E. V. Chulkov, P. M. Echenique, and H. Petek, *π-Resonance of chemisorbed alkali atoms on noble metals*, Physical Review Letters, **101**, 266801 (2008).

Acknowledgement

Many people have supported me during my PhD work, and this work could not have been completed successfully without their continuous help, relentless support and encouragement. I feel great appreciation and gratitude for this support and would like to acknowledge it herein. I am indebted to the support of my PhD advisor Dr. Hrvoje Petek for his guidance, close attention and dedication; and the guidance of my PhD committee members, Dr. D. Snoke, Dr. H.-K. Kim, Dr. D. Waldeck, and Dr. G. Dutt (and also the former members Dr. J. T. Yates Jr. and Dr. A. Heberle).

Without the financial, moral and spiritual support of my family, i.e., my beloved wife Gülden, my little angels Defne and Derya, my dear father Muttalip, my dear mother Mükerrem, my dear brothers Cemil and Abdullah, my dear grandparents (including my late grandparents, may their souls rest in peace), my uncles, aunts, cousins, and my in-laws, this long journey of doctoral degree would not have been finished with success.

I also appreciate all the support I received from the University of Pittsburgh community, including all the staff members in the Department of Physics & Astronomy, who always helped me under any circumstances. All the people that I befriended during my PhD including my lab

partners, office mates and collaborators (especially Dr. J. Zhao, Dr. N. Pontius, Dr. A. Winkelmann, Dr. K. Onda, Dr. M. Feng et al.) made my job easier and made this journey more bearable. Many of my friends were PhD students as well; their willingness to help at crucial instances without hesitation and their sense of humor enabled me to overcome many seen and unforeseen hurdles.

The last but not least, I would like to express my deepest gratitude to the God Almighty for giving me health, strength, time, opportunity, patience, endurance, and support in undertaking this challenging task and finishing it successfully.

To conclude this work, I must admit that any flaws and/or errors that may appear belong to me; and I do hope that this work will stimulate more fruitful studies in this field for more generations to come.

Vahit Sametoglu

Pittsburgh, 2009

Chapter-1

Introduction

The subject of this dissertation is a study of the electronic structure and dynamical properties of alkali atoms adsorbed on low index surfaces of noble metals by two-photon photoemission (2PP) spectroscopy. Combining alkali atoms with their simple electronic structures consisting of single s-orbital valence electron, with noble metal surfaces with their s- and p-orbital derived conduction bands, constitutes a particularly simple chemisorption system for elaborating how atoms and molecules interact with solid surfaces. Chemisorption of atoms and molecules controls many interfacial phenomena such as the charge transport, catalysis, and molecular electronics. The properties of such interfaces depend on the energy levels of the occupied and the unoccupied electronic states. Yet, even for this paradigmatic chemisorption system the interfacial electronic structure is poorly understood from the perspective of both experiment and theory. Two-photon photoemission spectroscopy provides the most direct means to study the occupied and unoccupied states of a chemisorption interface, but before it can be applied to definitive studies of the interfacial electronic structure and dynamics much needs to be done to understand how the coherent optical and electronic processes affect the experimental measurements. The goal of this study is to probe alkali/noble metal chemisorption interfaces by 2PP spectroscopy

and explain their electronic and dynamical properties in terms of unperturbed substrate surface and free adsorbate properties and their primary mode of interaction.

A bulk crystalline solid has three-dimensional translational symmetry and can be regarded as infinitely extended in all directions. This assumption simplifies the description of the physical properties of solids, because mathematical models rely on the translational invariance and invariance with respect various symmetry operations. Creating a solid surface, however, creates new boundary conditions, which change the properties of the solid on the length scales of screening of the boundary or externally applied fields. The particular properties of surfaces can be probed with particles and fields, which interact strongly with the solid and can penetrate only into its topmost few atomic layers. Photoemission spectroscopy (PES), which measures the energy and wave vector of emitted electrons in response to the excitation with energetic photons, is one of the most powerful techniques to study the electronic structure of solids, solid surfaces, and atoms and molecules adsorbed on surfaces [1]. It has numerous applications in surface science, materials science and engineering. Owing to the very limited escape depth of photoelectrons, the photoemission spectra carry information specific to the topmost few layers. Hence, the properties of surface atoms, being different from those of bulk atoms, gain significance.

Conventional photoemission spectroscopy, however, is limited to exploring the static electronic structure of the occupied states of solid surfaces. In order to probe the unoccupied electronic structure, one can resort to inverse photoemission, which probes the light generated by electron-hole recombination induced by an incident monoenergetic beam of electrons. Because inverse photoemission lacks the sensitivity and time resolution, and has poor spectral resolution, 2PP is

increasingly becoming the method of choice to study the electronic structure and dynamics of electronic interfaces. In 2PP, typically, a near-UV laser pulse excites an electron from an occupied state below the Fermi level (E_F), to an unoccupied state below the vacuum level (E_{vac}). Before this excitation can decay, absorption of another photon excites the electron above E_{vac}, where it is transmitted and detected in vacuum. If the light is delivered with femtosecond laser pulses, time-resolved two-photon photoemission (TR2PP), can even measure the electron and nuclear dynamics that affect the two-photon excitation process. We apply TR2PP to study the structure and dynamics of clean and alkali atom modified noble metal surfaces.

The purpose of this chapter is to present our motivation as to why we undertook this study and introduce fundamental concepts and methods that are used throughout this text. In the rest of this chapter, we introduce the following topics: section 1.1 - the noble metals and their fundamental properties; section 1.2 - the alkali atoms and their interaction with noble metal surfaces; section 1.3 - the theory of photoemission; section 1.4 - the specific photoemission techniques that we employed; and section 1.5 - the organization of the dissertation.

1.1 Characteristics of Noble Metals and Their Surfaces

Noble metals (copper, silver and gold) are monovalent elements with simple Fermi surfaces. Their band structures have been studied extensively by experiment and theory, and consequently are well-known [2]. All the noble metals have the face-centered cubic (fcc) crystal structures [3]. The Fermi surfaces of copper and silver, which are used in the present work, are completely enclosed within their first Brillouin zones. Their electronic configurations as isolated atoms are

$[Ar]3d^{10}4s^1$ for Cu and $[Kr]4d^{10}5s^1$ for Ag. Because the bulk does not have the full symmetry of the atomic orbitals, the outermost s-orbital electron hybridizes with the empty p-orbitals to attain a hybrid sp-character. Therefore, their electronic configurations in solid crystalline form become: $Cu:[Ar]3d^{10}4(sp)^1$ and $Ag:[Kr]4d^{10}5(sp)^1$.

Low index noble metal surfaces of fcc solids are designated as (111), (100) and (110); they have different atomic density and symmetry making each surface structurally, electronically, and chemically unique. Of the low index surfaces we employ the (111) surface, which is the most stable one, has a hexagonal close-packed arrangement of atoms with the highest in-plane atomic density making it the least corrugated one. Most importantly, the (111) surface has a projected band gap that extends between the occupied part of the lower to the unoccupied upper conduction bands. This band gap affects the electronic interactions with adsorbates such as alkali atoms. Fig. 1.1 displays top and side views of these three low index surfaces. The distance between atomic planes substantially affects the filling of electronic states along high symmetry axes, because it determines the location of the Brillouin zone boundary.

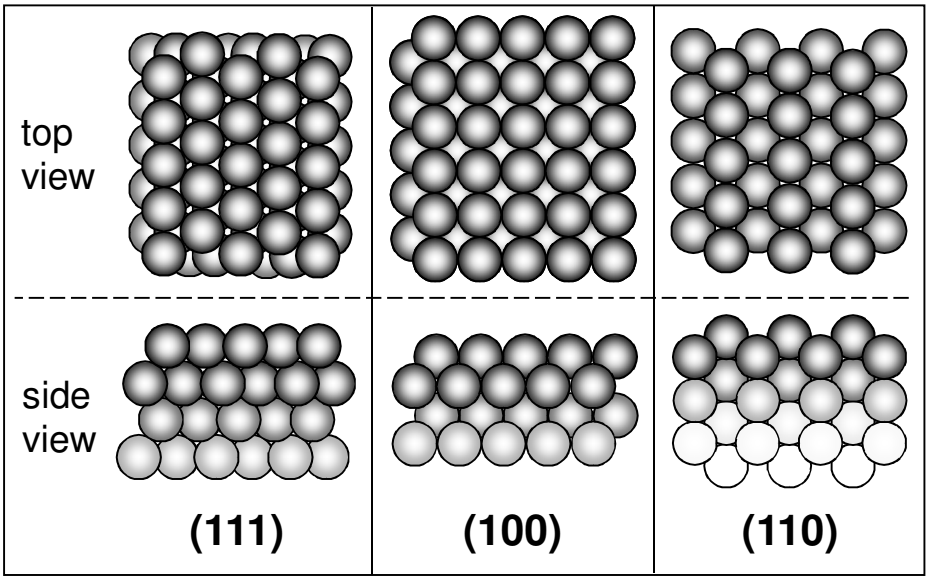

Figure 1.1 The atomic arrangements (top view and side view) of noble metal surfaces cut along the low index planes (111), (100), and (110), respectively [4].

Fig. 1.2(a) presents a typical fcc lattice structure with (111) planes. This representation enables us to calculate from the lattice constant 'a' (Ag: 4.090 Å; Cu: 3.610 Å) the interplanar distances (Ag: 2.361 Å; Cu: 2.084 Å) between the (111) planes [5]. Fig. 1.2(b) shows the 'reciprocal' (or 'momentum') space of a typical fcc lattice in the first Brillouin zone, which corresponds to a body-centered cubic (bcc) structure. The Brillouin zone spans the allowable range of crystal momenta that define the band structure of a solid. It is a polyhedron bounded by low-index planes normal to the reciprocal lattice vectors at their midpoints [6].

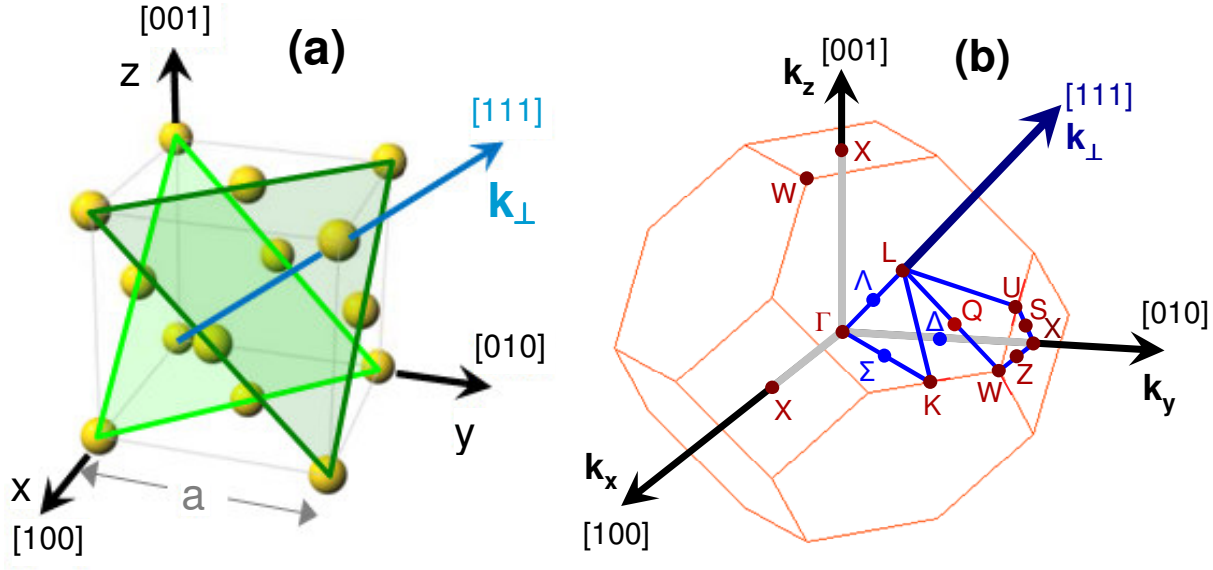

Figure 1.2 (a) The fcc lattice structure with (111) planes indicated by the light and dark green triangles. The space diagonal (blue arrow) of this lattice intersects three layers of successive (111) faces. **(b)** The first Brillouin zone of the fcc lattice structure. All major symmetry points (including the origin, the 'Γ' point), axes, directions, and zone faces are labeled.

All the energy bands of noble metals (including d-bands) are filled except the sp-derived conduction band. The closed-shell core levels of noble metals have the noble gas configuration ($\ldots n s^2\ n p^6$). Six additional valence bands accommodate eleven additional electrons ($\ldots m s^1\ n d^{10}$). In the reciprocal space description of the band structure of noble metals, one finds these six energy bands grouped into two sets: five fully occupied bands in the energy range of -5 to -2 eV for Cu(111) and -7 to -4 eV for Ag(111) (with respect to E_F) corresponding to the d-bands; and, a single partially occupied sp-band, which starts from -9 eV for Cu(111) and -7 eV for Ag(111) [3]. Because the d-bands of noble metals are located several electron-volts (eV) below E_F, they influence the optical and electronic properties, but not the density of states (DOS) at E_F. Fig. 1.3 presents the valence band electronic structures of copper and silver in the ΓL-direction. It is evident that sp-bands have nearly free electron dispersion with the wave vector **k**, except in the region of the d-bands where the sp-d hybridization is strong. By contrast, the d-bands (indicated within the 'orange' rectangle) have weak **k**-dispersion.

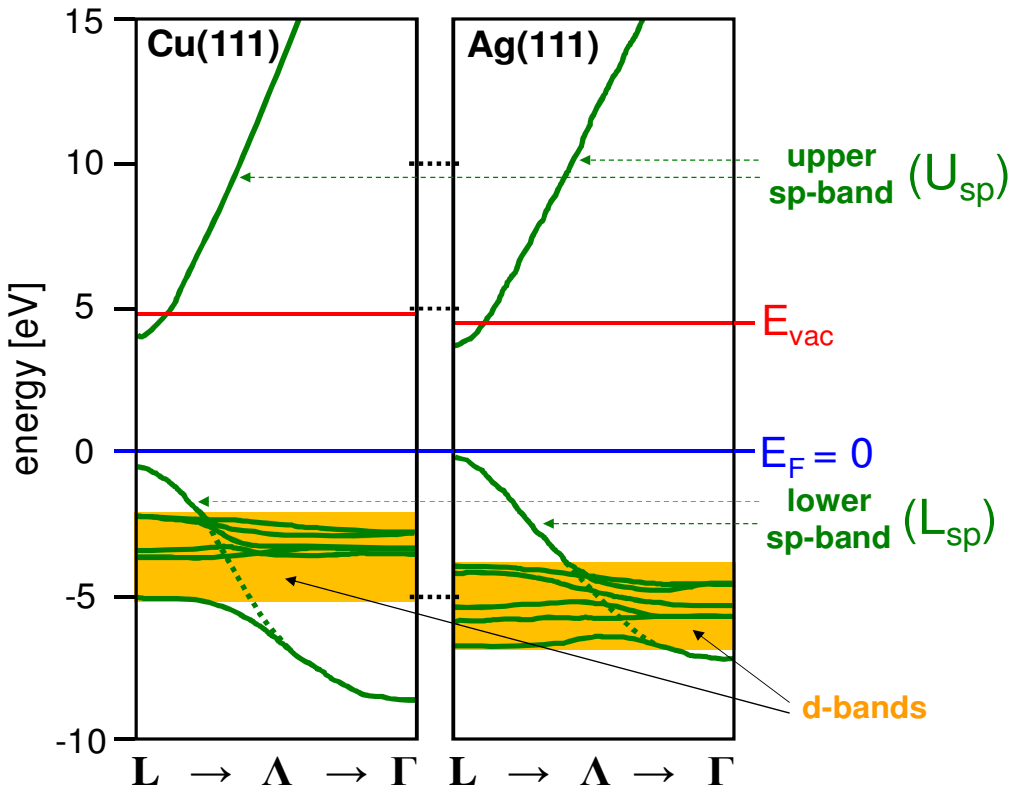

Figure 1.3 The band structures of copper and silver along the ΓL-direction [7,8,9,10]. The sp-band dispersion in the absence of hybridization with the d-bands is indicated by the dashed lines. The orange rectangles indicate the location of the d-bands.

1.2 Alkali Metals and Adsorption

1.2.1 Properties of Alkali Metal Atoms

Having a single valence s-orbital electron, the alkali atom group elements except hydrogen are the simplest metals. We employ all nonradioactive alkali metals (Li, Na, K, Rb, and Cs), which are located in the left-most column (Group-I) of the periodic table, as shown in Fig. 1.4. Li, Na, K, Rb, and Cs atoms have single valence orbital electron in their 2s, 3s, 4s, 5s, and 6s shells,

respectively. When condensed into a bcc lattice, their valence electrons form metallic conduction bands with nearly-free-electron dispersion and nearly spherical Fermi surface [3,6].

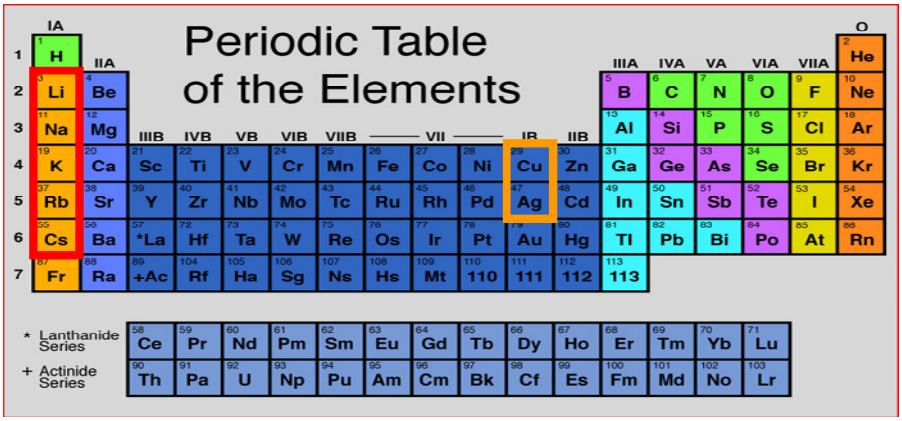

Figure 1.4 The periodic table of the elements where the alkali and noble metals that we study are marked by bold frames [11].

1.2.2 Alkali Metal Adsorption on Solid Surfaces

Because of their simple electronic structure, alkali atoms are prototypical systems for studying the interaction of atoms and molecules on solid surfaces. The interaction of alkali atoms with metal surfaces was studied already in 1920's by Langmuir and coworkers, because of the effect on the thermionic emission [12,13,14]. Alkali atom adsorbates lower the work function of their substrate surface thereby enhancing the thermionic emission, as well as play an important role as promoters or poisons of catalytic reactions.

The adsorption of atoms or molecules on solid surfaces involves the same fundamental forces that give rise to chemical bonding in molecules [15], but the bond formation takes place between vastly dissimilar partners [16]. Here, the atom or molecule, being the microscopic partner, comes

with discrete energy levels and a few occupied states. The two-dimensional surface of a semi-infinite solid, being the macroscopic partner, possesses many (about 10^{23} cm^{-3}) electrons. Adsorption is a consequence of surface energy. In a bulk, all the bonding requirements (ionic, covalent or metallic) of the constituent atoms of the material are satisfied. But atoms on bare surfaces experience a bond deficiency, because they have lower coordination number than the bulk atoms. Therefore, it can be energetically favorable for them to capture and form a bond with adsorbates that land on the surface. The exact nature of the bonding depends on the details of the species involved, and generally is classified as either physisorption or chemisorption.

'Physisorption' involves weak interaction between an adsorbate and a substrate that does not involve formation of a chemical bond. The adsorbate adhesion involves dispersion forces, such as 'Van der Waals' interaction between gas phase molecules. Physisorbed particles are typically located relatively far from the surface and are usually highly mobile in the plane parallel to the surface. The adsorption energy through the Van der Waals interaction is quite low, i.e., typically less than 0.3 eV per adsorbed particle [16].

In contrast, 'chemisorption' involves the formation of covalent or ionic bonds with short equilibrium distances ($0.1-0.3$ nm). The electronic structure of the interacting species is strongly perturbed and new hybrid orbitals can be formed. The chemisorption binding energies can be as large as a few eV. In the case the bonding has ionic character, there is charge transfer from one component to the other [15].

The study of alkali chemisorption has a long history; Langmuir and coworkers [12,13,14], in their pioneering work, found that the work function of a clean metal surface (tungsten: W) decreases by several eV upon adsorption of Cs at submonolayer to monolayer coverage (1 monolayer (ML) coverage contains typically $10^{14} - 10^{15}$ adsorbates/cm^2) [17,18]. They found that when a Cs covered surface at submonolayer coverage is heated, nearly all Cs atoms desorb as positive ions. Both these features laid the foundation for the surface science of alkali atoms on metal surfaces and led to numerous practical applications such as low work function cathodes and thermionic energy conversion [19]. To explain their work function and electron emission experiments, Langmuir and coworkers developed a simple model for the chemisorption of alkali atoms, which presumed complete donation of the alkali valence s-orbital electron to the substrate metal [20]. In 1932, Langmuir proposed that "In the case of cesium films we have very direct proof that the adatoms act as dipoles. Adsorption of alkali atoms occurs strongly only when the electron affinity of the absorbent metal exceeds the ionization potential of the underlying metal. The force holding the atom may thus be regarded as the attraction of the cesium ion and the negative charge induced in the metallic surface (image force)" [12]. This insight was based on the fact that alkali atoms K, Rb, and Cs have low ionization potentials that are significantly less than the work function of W, so if the metal and adatom electronic potentials are at the same E_{vac}, the transfer of valence electron of the alkali atom to the substrate is energetically favored.

In a more formal theoretical description of the alkali atom chemisorption, in 1935 Gurney proposed a quantum mechanical picture applicable to low adsorbate coverages [21] in order to explain experiments involving alkali earth atoms such as Ca, Sr, and Ba. These alkali earth atoms exhibit similar chemisorption properties to alkali atoms, although their ionization potentials are

higher than the work function of W. According to Gurney's interpretation, as an alkali or alkali earth atom approaches the substrate, its positive core is screened by the conduction band electrons in the substrate to create a negative image charge. The Coulomb repulsion between the negative image charge and the valence s-electron destabilizes the latter. If the s-orbital electron energy exceeds E_F of the substrate, it is broadened into a resonance because it can undergo partial transfer to the unoccupied states of the substrate. Therefore, the s-orbital electron resonance energy and width are determined, respectively, by the Coulomb repulsion and the tunneling rate. The degree of charge transfer is determined by the fraction of the resonance DOS above E_F [16,20]. The Langmuir and Gurney model is elaborated in Chapter-5.1.

In 1970's, Lang developed a model for chemisorption that treated the substrate with the 'jellium' model [22,23,24]. The jellium model describes the delocalized valence electrons in the bulk of a metal in which there is assumed to be a uniform positively charged background terminating at the physical interface between the metal and vacuum [22,25,26]. His calculations for the adsorbate-substrate interactions were based on pseudopotentials for the substrate and adsorbate atoms [22,27]. His model reproduced the general features of the Gurney model such as the position of the adsorbate valence level with respect to E_F of the substrate, as well as the characteristic work function decrease induced by alkali atoms [22,23,24]. Because the jellium model does not include details of the substrate band structure, the calculated widths of the resonances are much broader (~1 eV) than those for (111) surfaces of Cu and Ag, as presented in Chapter-5.1 [28].

To analyze the electronic structure of chemisorbed alkali atoms and the work function variation more quantitatively, Muscat and Newns constructed a new model in late 1970's, based on the

Anderson impurity model [29], in which they extended the surface dipole picture by considering the intraatomic polarization due to the electric field of the substrate [29,30,31,32,33]. The change in the work function is expressed in terms of adatom ion and intraatomic dipole moment. On account of intraatomic polarization, they predicted the hybridization of alkali atom s- and p-orbitals into a bonding and an antibonding pair forming two unoccupied resonances of differing widths [29]. The widths depend on whether the hybridized orbitals have maximum density between the substrate and adsorbate (wide), or on the vacuum side of adsorbate (narrow).

In late 1980's, Ishida performed density functional theory (DFT) calculations based on the local density approximation in which he extended the single atom chemisorption approach to finite coverages of alkali atoms on the semi-infinite jellium surface [34,35,36,37]. According to his work, the electron transfer from alkali atoms is small and the main effect of chemisorption is an internal polarization of the adatom transferring the charge density between the substrate and adsorbate. Thus, Ishida suggested that the ionic depiction of the alkali/metal bonding should be replaced by a covalent one. This model has been very controversial, and ultimately fails to predict the electronic structure of alkali atom covered surfaces.

In 1990's, Nordlander and Tully calculated the energy shifts and lifetime broadening of alkali atom valence states, under the influence of the surface potential [38]. Their computation method is close to our approach in Chapter-5.1; they, however, took nonlocal effects into account for a more accurate formulation. Their calculations, however, were more focused on the scattering processes that occur at bond distances that are much larger than the equilibrium chemisorption bond length obviating meaningful comparisons with static measurements of the interfacial

electronic structure. Their calculations indicated that intramolecular orbital hybridization influences the resonance energies and widths when the interaction strength becomes comparable with the energy splittings between the interacting levels. The lack of spectroscopic features in the occupied state spectra of chemisorbed alkali atoms [39] as well as the paucity of experimental techniques that probe the unoccupied electronic structure have hampered critical testing of these theoretical models with incisive experiments.

Until the emergence of 2PP, various structural and spectroscopic methods have been used in experimental studies of alkali atom chemisorption [20]. Low energy electron diffraction (LEED) has been utilized as a general tool to determine the structure of chemisorbed alkali atom overlayers on metal surfaces [40]. These studies have been performed at coverages of 0.07 ML and higher, where the coverage of 0.25 ML (with respect to the substrate atomic density) of a large alkali atom, e.g., Cs, corresponds to a full monolayer [20]. At low coverages, alkali atoms experience mutual repulsion, and therefore, form hexactic liquid structures [20,41]. At higher coverages that gave ordered structures, it has been possible to deduce that small alkali atoms (Li, Na) adsorb in three-fold hollow sites, while large alkali atoms (K, Rb, Cs) adsorb at on top sites [20,42]. This tendency has exceptions, such as Ag(111), for which large alkali atoms also adsorb in the three-fold hollow sites [43]. These tendencies are supported by DFT calculations. LEED was also used to determine the perpendicular substrate-overlayer spacing [42].

Because chemisorbed alkali atoms do not show evidence of occupied valence states, methods such as electron loss spectroscopy (ELS) and inverse photoemission spectroscopy (IPES) have been employed. Heskett and coworkers used ELS and IPES to study Na [44,45] and K [46]

chemisorption on Al(111) surface as a function of coverage. They found a strong correlation between the peak energy of ELS and the unoccupied alkali-induced state in IPES, which enabled them to interpret the ELS peak as an electronic transition at submonolayer alkali coverage. They attributed unoccupied state features at 0.6 eV and 2.7 eV for K at low coverage on Al(111) to s- and p-resonances. With the limited resolution of their methods, it was difficult to determine the true widths of the resonances. Bartynski and coworkers used angle-resolved IPES to observe alkali-induced states of Cs/Cu(100) and Cs/Cu(111). At low coverages these unoccupied states appeared at ~3 eV. From angle-resolved measurements, they concluded that the unoccupied resonances have predominantly d-character when resonant with the projected band gap, and sp-character when resonant with the propagating conduction band states [47].

The invention of 2PP as a surface science spectroscopic method by Steinmann and coworkers offered a higher sensitivity and resolution tool to probe the unoccupied electronic structure of clean and adsorbate modified metal surfaces [48]. In 1990's, Fischer and coworkers employed 2PP to study the unoccupied electronic structure of Na adsorbed Cu(111) surface [49,50]. They observed the alkali atom-induced unoccupied state and the image potential states. With increasing alkali atom coverage they could observe the downshift of all of the states as well as the expected change in work function, as shown in Fig. 1.5. They found that the alkali resonance emerges at low coverages at ~2.9 eV above E_F, and has a linewidth of 410 ± 30 meV. They measured how the resonance tunes to lower energy for coverages corresponding to the work function minimum ($\sim 0.40 - 0.45$ ML). They attributed the abrupt change in the occupancy of the alkali-induced resonance at this coverage to a transition from ionic to metallic bonding as the overlayer coalesces into close-packed islands [49].

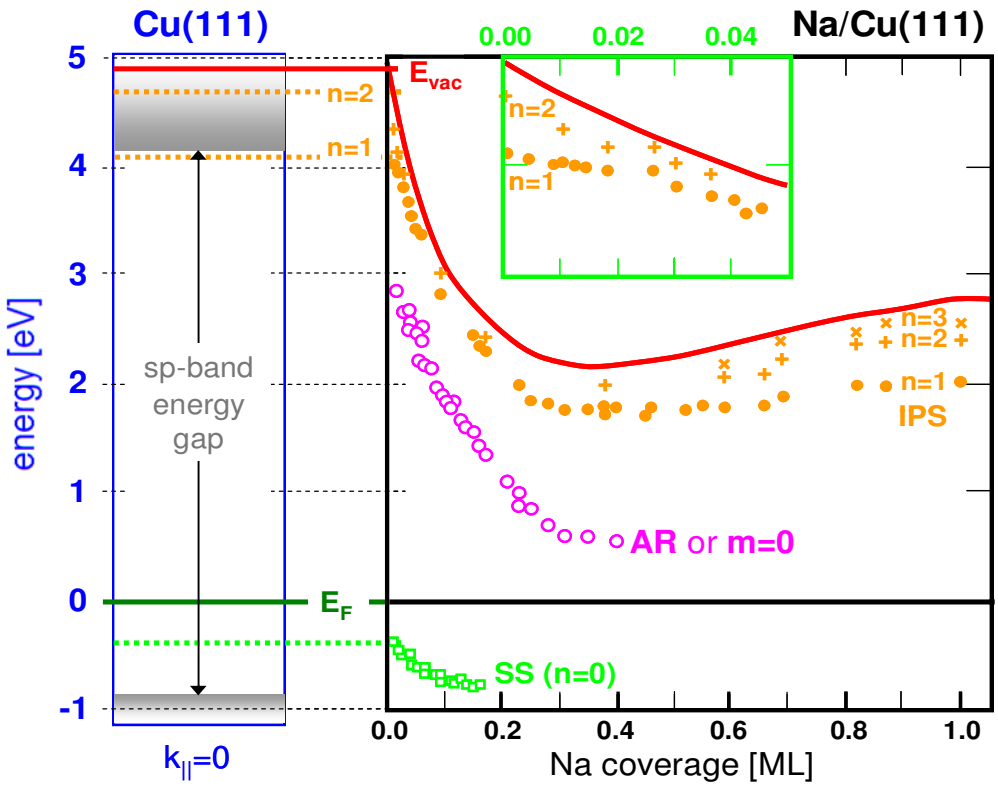

Figure 1.5 The electronic structure of a typical alkali/noble metal chemisorption system: Energy diagram of the bare Cu(111) surface at $k_{\parallel} = 0$ point (left) is compared with the electronic states of the Na/Cu(111) system as function of alkali coverage. The experimental data (right) are obtained from 2PP experiments [49,51]. The intrinsic Shockley surface state (SS) of Cu(111), the alkali-induced antibonding resonance ('AR' or '$m = 0$') state, and the $n = 1$, $n = 2$, and $n = 3$ image potential states (IPS) are shown. The work function, which starts from 4.91 eV above E_F, decreases nearly linearly on initial deposition (inset).

In late 1990's, Bauer and coworkers applied TR2PP to study energies and lifetimes of the unoccupied resonances of Cs covered Cu(111) and Cu(100) surfaces [52,53]. They found that the lifetime of the Cs resonance, which appears at ~3 eV in the low coverage limit, is 15 fs at 300 K. This was surprisingly long because the linewidths from theoretical models and observed in the

experiment of Fischer et al. for Na/Cu(111) suggested femtosecond to subfemtosecond lifetimes [49,50]. Moreover, Bauer et al. showed that the lifetimes depend on the crystal face, with Cu(111) supporting the longest lifetimes. Going one step further, at the turn of the millennium, Petek investigated the Cs/Cu(111) system by TR2PP at low (33 K) surface temperatures. They found that the resonance lifetime increases to ~50 fs, and the decay kinetics become nonexponential; this was interpreted as evidence for surface femtochemistry of desorption of Cs from Cu(111) surface [54,55,56].

Although TR2PP studies contributed much to our understanding of the unoccupied electronic structure of chemisorbed alkali atoms at low coverage, there have been no systematic studies that could test the many theories of alkali atom chemisorption. We have performed such study and report the results in Chapter-5. We also report on surface femtochemistry of alkali/Ag(111) chemisorption system by means of the same methodology in Chapter-6.

Because the chemisorption-induced changes in the work function is the defining aspect of how alkali atoms influence surface electronic structure, in the following section we address the concept of work function and its change owing to adsorption.

1.2.3 Variation in Work Function

Work function represents the minimum work required to extract an electron from a solid [57,58]. The work function (Φ) of a bare, unperturbed, infinitely large, homogeneous metal surface is the energy difference between the initial state where an electron is in the highest occupied level of

the neutral ground state, i.e., E_F, and the final state where the metal is singly ionized and the electron is at rest in vacuum at infinity, i.e., E_{vac} at 0 K [18, 59]. It can be formulated as $\Phi = E_{vac} - E_F$.

The work function of a metal can be separated into the bulk and surface components as in $\Phi = \Delta\varphi - \bar{\mu}$ [58]. The 'bulk' component is a negative contribution originating from the chemical potential $\bar{\mu}$ of the metal. It corresponds to the binding strength of electrons to the positive ions forming the solid [60]. The 'surface' component arises from the presence of the surface dipole layer, which is caused by excess negative charge spilling out of the physical interface into the vacuum and the complementary excess of positive charge inside the solid as in Fig. 1.6(a) [59]. A charged particle crossing the interface experiences a potential difference $\Delta\varphi$, which, as shown in Fig. 1.6(b), is the difference between the potential outside $\varphi(+\infty)$ and inside $\varphi(-\infty)$ of the metal [27,59]; the potential is proportional to the surface dipole as in

$$\Delta\varphi = \varphi(+\infty) - \varphi(-\infty) = 4\pi e \int_{-\infty}^{+\infty} z\left[n_-(z) - n_+(z)\right]dz \,. \qquad [1.1]$$

The thickness of the dipole layer, and therefore, the z-dependence of φ, are of the order of a few Å [59].

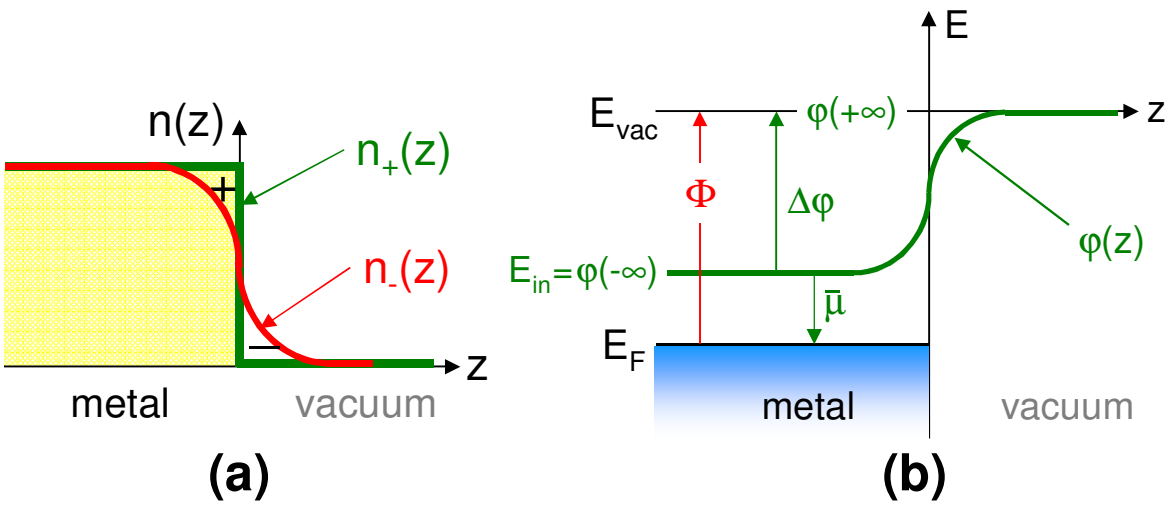

Figure 1.6 (a) Schematic charge density ($n_{\pm}(z)$) distribution of a jellium surface and the creation of surface dipole layer. **(b)** Potential energy diagram explaining the components of the work function (Φ), where $\bar{\mu}$ is the chemical potential (bulk component) and $\Delta\varphi$ is the surface dipole barrier (surface component).

For a semi-infinite jellium surface with the z-direction normal to the surface, the positive charge density can be expressed as a step function at $z = 0$, i.e.,

$$n_{+}(z) = \begin{cases} \bar{n}, & z \le 0 \\ 0, & z > 0 \end{cases}. \qquad [1.2]$$

The jellium model describes a metal as a medium composed of a uniform positively charged background terminating at the physical interface, which binds free valence electrons through the Coulomb interaction [22,25,26]. Fig 1.7(a) displays how the positive charge density ($n_{+}(z)$, the green solid line) declines discontinuously to zero at the geometric boundary of the surface, whereas the negative charge density ($n_{-}(z)$, the red line) spills out, creating an excess of negative charge immediately outside the surface and a corresponding depletion inside the bulk.

As an example, differences in the surface dipole layer make work function of a metal to be face-dependent (Table 1.1) [61]. The crystal face-dependent differences in surface termination shown in Fig. 1.1 are responsible for surface dipole layers of different strength. Table 1.1 presents experimentally determined work functions of low index noble metal surfaces, among which we employ the (111) surfaces.

	orientation		
Metal	**(111)**	**(100)**	**(110)**
Cu	4.91	4.63	4.48
Ag	4.56	4.42	4.35

Table 1.1 Experimentally determined values of the work function (in eV) for copper and silver [3, 18,62,63,64].

According to the discussion in section 1.2.2 and Fig. 1.7(b), an alkali atom approaching a metal surface is ionized, as its valence electron is destabilized with respect E_F of the substrate [12]. A charge near the metal surface, such as a positive alkali atom core in Fig.1.7(c), induces its image charge of the opposite sign within the metal. At low coverage, while the adsorbed species possess an ionic character, the two opposing charges give rise to an induced dipole moment of strength $\mu = 2R_{ads}$ (R_{ads}: adsorption distance), which adds to or opposes the original surface dipole moment to raise or lower the work function. At low alkali atom coverage the repulsive dipole-dipole interaction keeps the dipoles apart at maximum distance and the work function decreases linearly as a function of the coverage. As more ions are adsorbed on the surface, the interadsorbate distance decreases and the repulsive dipole-dipole interactions between adatoms increase. To lower the free energy, partial charge transfer occurs from the metal to adsorbed alkali atoms, thereby reducing the strength of the dipole moment and the repulsive interaction.

This noticeable weakening in the dipole moment strength is known as 'depolarization', (in Fig. 1.7(d)), which causes the work function to saturate at a minimum value. At even higher coverages (above 0.5 ML up to 1 ML), the adsorbate film attains metallic character because of the depolarization, as already discussed in the case of Na/Cu(111) [49,50]. Beyond 1 ML, the work function asymptotically converges to that of the corresponding alkali metal.

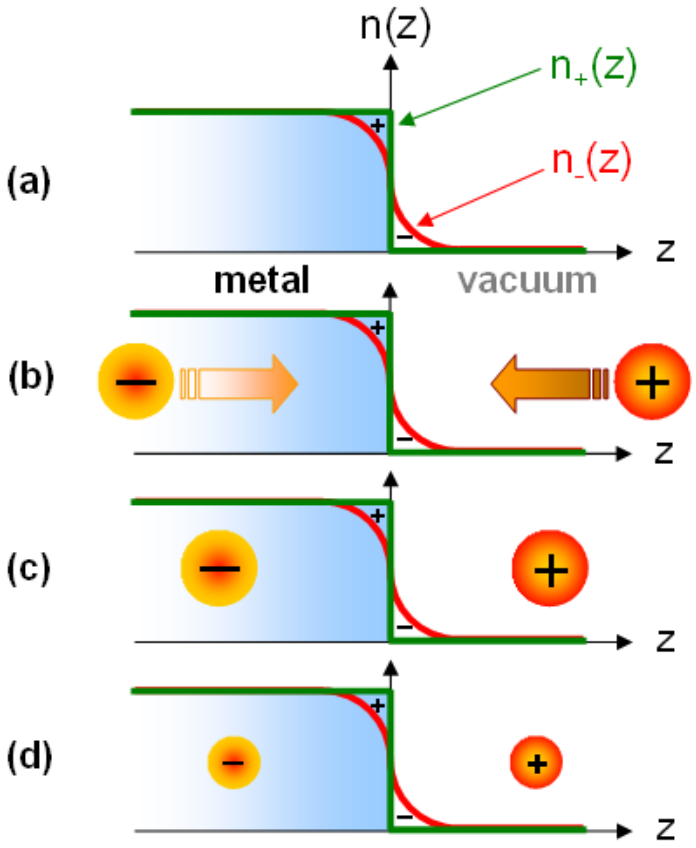

Figure 1.7 (a) Positive and negative charge densities in the vicinity of a bare unperturbed metal surface. **(b)** A positively charged ion is approaching the surface, and **(c)** induces its image charge on account of screening. The ion and its image charge form a dipole, which counteracts the original surface dipole. **(d)** When the surface is populated by large numbers of adsorbates, the interadsorbate interactions lead to depolarization, which lessens the induced dipole moment.

1.3 Basics of Photoemission

Photoemission is based on the 'photoelectric effect' in which light with energy larger than the work function of the solid can emit photoelectrons into vacuum [65,66,67]. The vast majority of surface science analysis methods (including photoemission spectroscopy) are based on energizing solid surfaces with photons (or electrons) and detecting emission of various combinations of particles such as electrons and photons. One can categorize these experiments into several subgroups: (1) Photon-in/photon-out as in X-ray diffraction or photoluminescence; (2) electron-in/electron-out as in electron diffraction or Auger electron spectroscopy; (3) electron-in/photon-out as in inverse photoemission; and (4) photon-in/electron-out as in photoemission spectroscopy [2,68]. Each method has it merits for probing the physical and/or chemical properties of solids and solid surfaces. Photoemission, in the form of 2PP, is employed in our experiments to study the band structure of the substrate, the DOS of alkali adsorbed noble metal surfaces, and the electron and nuclear dynamics of the unoccupied states.

Photoemission spectroscopy (also known as 'photoelectron spectroscopy') provides information on the density of initial states below E_F of a condensed matter system, from which electrons are photoemitted [69], provided that the final states above E_{vac} form a smooth continuum and the transition probability varies slowly with energy [62]. It employs monoenergetic photons to excite a surface and analysis of the energy and angle of emitted electrons [1,15,70]. It is usually performed with UV lamp or synchrotron radiation light sources. Synchrotron radiation makes it possible to cover the entire spectral range from near-UV to the hard X-rays, however, its brightness and temporal resolution can only be surpassed by coherent laser sources, such as used here [71].

Photoemission processes are often characterized with respect to the energy of the incident photons and classified into two main categories: (1) Ultraviolet Photoemission Spectroscopy (UPS) is done in the ultraviolet regime (3–100 eV) and it probes valence energy levels and chemical bonding of solids, especially the character of molecular orbitals; (2) X-ray Photoemission Spectroscopy (XPS) is done in the X-ray regime (100 eV – 10 keV) [18] and it probes the energy levels of atomic core electrons, primarily in solids [72]. Due to the photon energy range of our experiments (about $3-6$ eV), we use only UPS.

The principle of momentum-integrated photoemission spectroscopy is outlined in Fig. 1.8, which displays the relationship between an energy level diagram of a solid surface and the energy distribution of photoelectrons [1]. The electronic states of a solid can be classified as either the core levels or the valence bands. One needs photon energy of $h\nu > E_B + \Phi$ in order to photoemit electrons with a binding energy (E_B), which is measured with respect to E_F. The spectrum of the photoemitted electrons provides information on the DOS of the occupied bands of a solid. From the known photon energy, work function, and the binding energy, one can determine the measured electron kinetic energy (E_{kin}) by:

$$E_{kin} = h\nu - \Phi - |E_B|. \qquad [1.3]$$

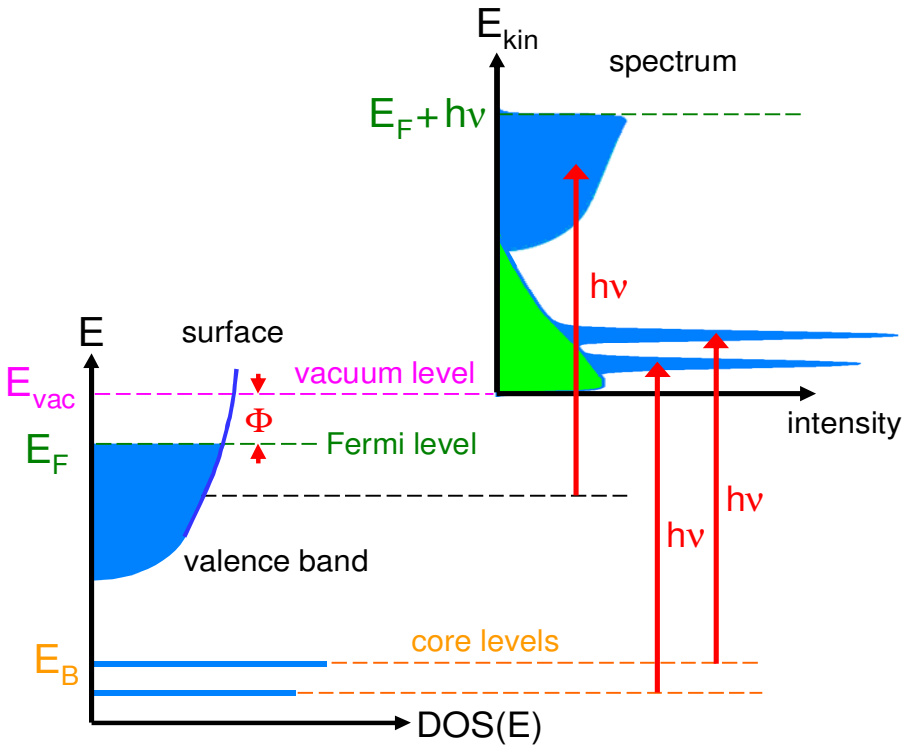

Figure 1.8 Schematic representation of a momentum- (i.e., angle-) integrated photoemission process in the single particle picture. The energy distribution of the photoelectrons represents the occupied DOS. The photoemission due to secondary electrons (green background) appears at the low energy edge of the spectrum.

Light of sufficient energy can eject electrons from the topmost layers of a solid [70]. Photoexcited electrons may escape from the solid without scattering or they may scatter with lattice ions (phonons) or other electrons. Electrons, which emerge without scattering, are called 'primary electrons' and retain information on the DOS. 'Secondary electrons' are generated by the scattering of the primary electrons; they appear as a featureless distribution that increases in intensity with decreasing kinetic energy. The scattering with phonons can cause large changes in momentum (**k**), but is quasielastic. By contrast, scattering with other electrons or collective excitations (plasmons) can cause photoelectrons to lose a significant amount of energy.

The optical penetration depth of photons in solids depends on the material and the photon energy; it is 100-150 Å within our energy range [73]. Even shorter than the penetration depth of photons is the escape length (i.e., mean free path) of photoelectrons, as shown by the 'universal curve' in Fig. 1.9. Because of the short escape length, photoemission is a truly surface-sensitive technique. We employ photoelectrons with about 6 eV final state energy (relative to E_F), which have escape depth of about 40-50 Å.

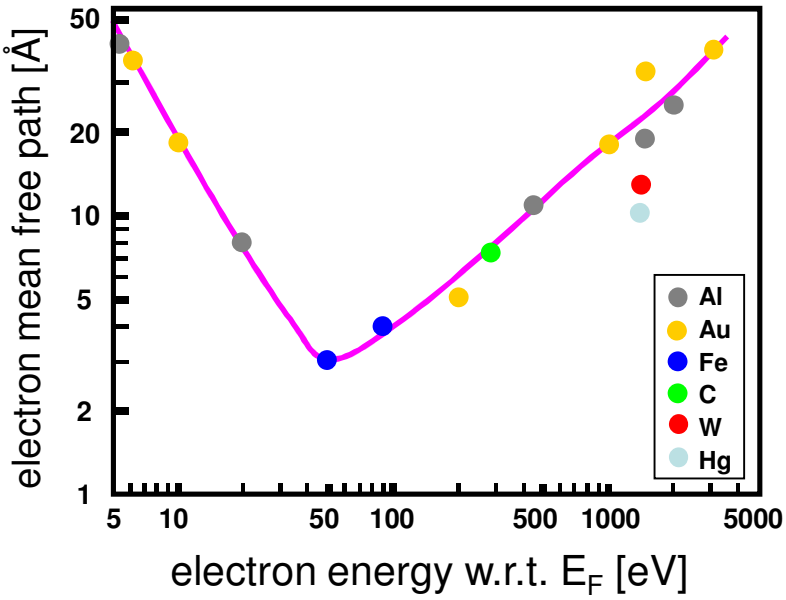

Figure 1.9 The 'universal curve' showing the mean free path of electrons for various metals (legend) versus their kinetic energy [74].

A photoemission experiment is initiated by incident light of energy 'hν' striking a solid surface at an angle 'ψ' with respect to the surface normal; photoelectrons with energy exceeding E_{vac} are ejected into the vacuum with polar and azimuthal angles 'θ' and 'φ', and the external momentum $\mathbf{k}^{ex}$, as illustrated in Fig. 1.10. The angle of incidence and the polarization vector with respect to

the optical plane of the incident electromagnetic wave determine the electric field direction and consequently the vector potential '**A**' with respect to the crystal lattice. The incident field can be represented as a superposition of two polarization modes, i.e., p-polarization (TM: transverse magnetic mode), where the electric field vector (and also the vector potential as in Fig.1.10) remains in the optical plane; and s-polarization (TE: transverse electric mode), where the electric field is perpendicular to the optical plane.

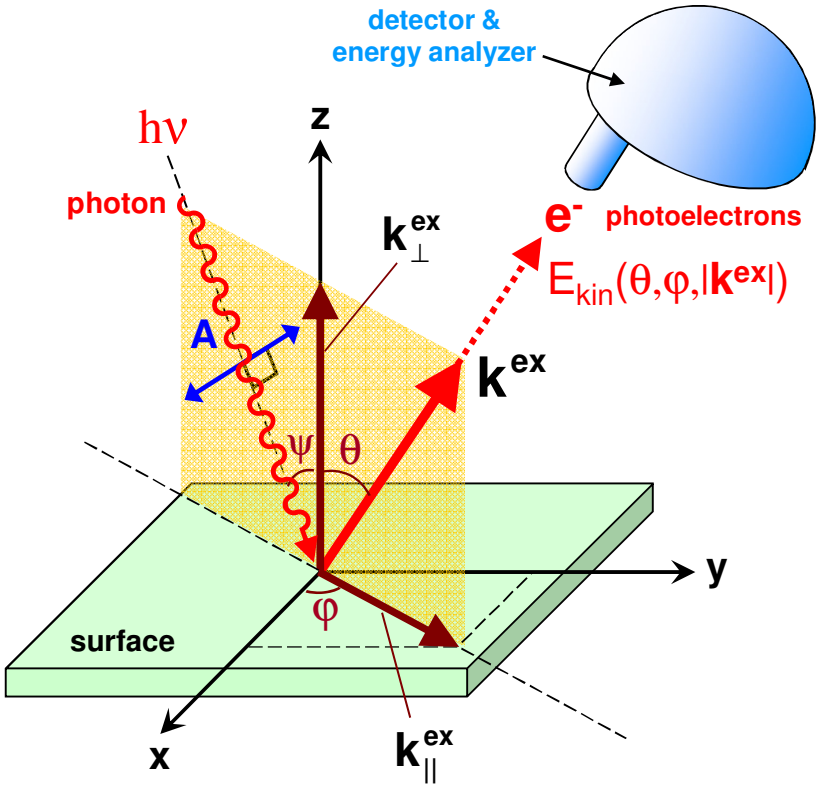

Figure 1.10 Three-dimensional illustration of a photoemission process at a solid-vacuum interface [15,70,75]: angles and wave vectors pertaining to the incident photon (of energy 'hν') and the photoelectron (e^-) are shown. Photoelectrons are detected and measured by an electron energy analyzer, and their energy distribution is displayed as a photoemission spectrum.

The outcome of a photoemission process depicted in Fig. 1.10 is a photoelectron ejected from the surface with a certain kinetic energy $E_{kin}(\psi,\theta,|\mathbf{k}^{ex}|)$, where the external wave vector '$\mathbf{k}^{ex}$' is related to the kinetic energy by

$$\left|\mathbf{k}^{ex}\right| = \frac{\sqrt{2m_e E_{kin}}}{\hbar}. \qquad [1.4]$$

The kinetic energy of photoelectrons is analyzed with an electron spectrometer providing the 'Energy Distribution Curve' (EDC), which depends on parameters such as emission angles θ and φ, photon energy and polarization [1,74].

Fig. 1.10 gives a vectorial representation of photoemission spectroscopy [2]. A physical description of the photoemission process entails a quantum mechanical treatment of the coherent light-matter interaction [15]. The most conventional theoretical formulation of the photoemission spectrum is based on the 'Fermi's golden rule' approximation [1], which gives the transition rate from an energy eigenstate of a quantum system into a continuum of energy eigenstates in response to an external perturbation. The interaction Hamiltonian between an electron and an electromagnetic field defined by a vector potential **A** can be written as

$$H_{int} = \frac{e}{mc}\mathbf{A}\cdot\mathbf{p}. \qquad [1.5]$$

H_{int} can be obtained by making the transformation $\mathbf{p} \rightarrow \mathbf{p} - \frac{e}{c}\mathbf{A}$ of the generalized momentum operator $\mathbf{p} = -i\hbar\nabla$ and substituting it for **p** in the unperturbed Hamiltonian $H_0 = p^2/2m + eV(\mathbf{r})$. The total Hamiltonian of the system is expressed as

$$
\begin{aligned}
H &= \frac{1}{2m}\left(\mathbf{p}-\frac{e}{c}\mathbf{A}\right)^2 + eV(\mathbf{r}) \\
&= \frac{p^2}{2m} + \frac{e}{2mc}(\mathbf{A}\cdot\mathbf{p}+\mathbf{p}\cdot\mathbf{A}) + \frac{e^2}{2mc^2}\mathbf{A}\cdot\mathbf{A} + eV(\mathbf{r}), \qquad [1.6] \\
&= H_0 + H_{int}
\end{aligned}
$$

and the perturbation operator is

$$
H_{int} = \frac{e}{2mc}(\mathbf{A}\cdot\mathbf{p}+\mathbf{p}\cdot\mathbf{A}) + \frac{e^2}{2mc^2}\mathbf{A}\cdot\mathbf{A}. \qquad [1.7]
$$

The quadratic term in **A** is usually disregarded, since it represents two-photon processes. Moreover, the perturbation Hamiltonian can be further simplified, if the photoemission due to surface (i.e., the '$\mathbf{p}\cdot\mathbf{A}$' term) is neglected:

$$
H_{int}^{bulk} \cong \frac{e}{mc}\mathbf{A}\cdot\mathbf{p}. \qquad [1.8]
$$

This approximation is valid in the bulk; however, the gradient of the vector potential changes significantly at the surface, since the dielectric function is discontinuous on going from the surface to the vacuum. The neglected terms due to two-photon processes and the surface discontinuity of the vector potential will be discussed for Ag(111) surface in Chapter-4.1. With the appropriate form of $H_{int}(t)$, the transition between the gound state 'ψ_i' and a final state 'ψ_f' can be calculated by an integral obtained from first-order time-dependent perturbation theory. Therefore, the transition probability 'w_{if}' per unit time between these states can be expressed within Fermi's golden rule approximation as

$$
w_{if} = \frac{2\pi}{\hbar}\left|\left\langle \psi_f(\mathbf{k})\middle|H_{int}(t)\middle|\psi_i(\mathbf{k})\right\rangle\right|^2 \delta(E_f(\mathbf{k}) - E_i(\mathbf{k}) - h\nu). \qquad [1.9]
$$

Thus, it can be approximated as

$$w_{if} = \frac{2\pi}{\hbar}\left|M_{if}\right|^2 \delta\left(E_{f^2} - E_i - h\nu\right), \qquad [1.10]$$

where 'M_{if}' is assumed to be a constant matrix element, and the Dirac-delta function describes energy conservation for the interband transition from $E_i(\mathbf{k})$ to $E_f(\mathbf{k})$.

The final state energy is given by adding the photon energy to the initial state energy E_i. Also, the kinetic energy of photoelectrons can be expressed in terms of the work function Φ, the binding energy $E_B\left(=-E_i\right)$, and the photon energy $h\nu$. These fundamental relationships are expressed by

$$h\nu = E_f - E_i = E_{kin} + \Phi + E_B, \qquad [1.11]$$

where all the energies are referenced to E_F.

An electron excited to the final state experiences a potential discontinuity on escaping from solid to vacuum. Because the discontinuity affects only the surface normal motion [15], the parallel component of electron momentum ($\mathbf{k}_{\|}$) is unaltered upon transmission through the surface into vacuum, whereas the normal component ($\mathbf{k}_{\perp}$) undergoes an explicit change. The internal and external momentum components are related by

$$\mathbf{k}_{\|}^{in} = \mathbf{k}_{\|}^{ex}$$
$$\frac{\sqrt{2m_e\left(E_f - E_0\right)}}{\hbar}\sin\left(\theta'\right) = \frac{\sqrt{2m_e E_{kin}}}{\hbar}\sin\theta, \qquad [1.12]$$

where θ' and θ are the angles of electron flux within the bulk and vacuum, respectively. This escape condition, which resembles the Snell's law for refraction of light, is depicted in Fig. 1.11, where E_0 stands for the bottom of the valence band.

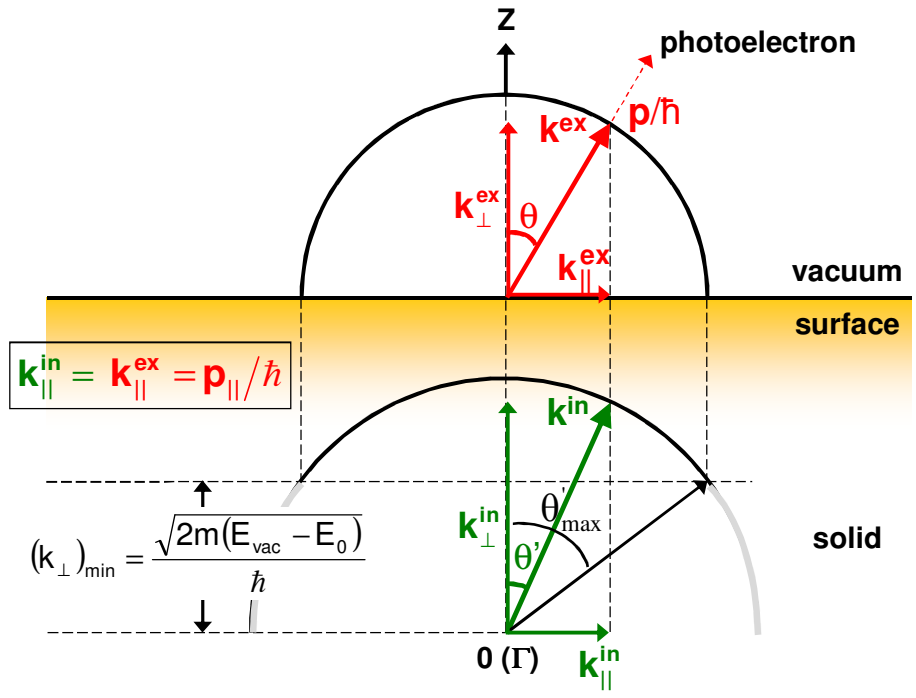

Figure 1.11 Escape condition for photoexcited electrons [15]. The thick 'black' solid curves signify the internal (bottom) and external (top) escape cones. Parallel component of the wave vector ($\mathbf{k}_{||}$) of photoelectrons is conserved upon transmission through the surface.

Equation [1.12] and Fig. 1.11 state that the escape direction of the photoelectrons is at a larger angle with respect to the surface normal (z-direction) upon transiting from solid to vacuum. Consequently, for every final state energy, there exists a maximum angle (θ'_{max}) inside the bulk beyond which the photoexcited electrons cannot escape. This total internal reflection condition is given by

$$\sin\theta'_{max} = \left(\frac{E_{kin}}{E_f - E_0}\right)^{1/2}. \qquad [1.13]$$

In other words, only electrons, which possess sufficient kinetic energy associated with the momentum normal to the surface to overcome the surface potential barrier

$$\frac{\hbar^2}{2m}\left(\mathbf{k}_{\perp}^{in}\right)^2 \geq E_{vac} - E_0 \qquad [1.14]$$

can escape into vacuum; whereas other electrons are totally reflected back into the bulk [3]. The kinetic energy of free photoelectrons can be expressed in terms of momentum components, or the final state energy E_f, and the work function Φ as

$$E_{kin} = \frac{\hbar^2}{2m}\left(\mathbf{k}^{ex}\right)^2 = \frac{\hbar^2}{2m}\left(\left(\mathbf{k}_{\perp}^{ex}\right)^2 + \left(\mathbf{k}_{\parallel}^{ex}\right)^2\right) = E_f\left(\mathbf{k}^{ex}\right) - \Phi . \qquad [1.15]$$

Fig. 1.11 and the equations pertaining to its discussion imply that measurement of the photoelecton kinetic energy and external momentum carries information on the momentum of the electrons in the occupied bands inside the solid. Hence, photoemission spectroscopy functions as an effective tool for mapping energy-momentum dispersion of the occupied bands in solids.

1.4 Two-Photon Photoemission Technique

A photoemission process that occurs through single photon absorption is referred to as 'one-photon photoemission' (1PP). Under intense laser excitation photoemission can occur by absorption of two or more photons. We refer to the two-photon process as 'two-photon photoemission' (2PP). In 2PP, the pump photon excites an electron located below E_F to a transiently populated, unoccupied intermediate state, E_{int}, which is usually located between E_F and E_{vac}. The intermediate state is usually 'virtual', because there is no energy and momentum conserving optical transitions between E_i and E_{int} that is available for the excitation light. Before it decays, electrons transiently occupying E_{int} can be excited further by absorbing another photon from the same or another time-delayed pulse (after a tunable time delay 'τ'). The second photon

excites the electron to its final state above E_{vac} and the electron is emitted [76]. Kinetic energy distribution of photoelectrons is recorded, and the corresponding EDC is known as a 2PP spectrum. Fig. 1.12 illustrates the excitation scheme for a typical 2PP process, assuming identical energy ($h\nu_1 = h\nu_2 = h\nu$) for the pump and probe pulses, and it contrasts it with a 1PP process.

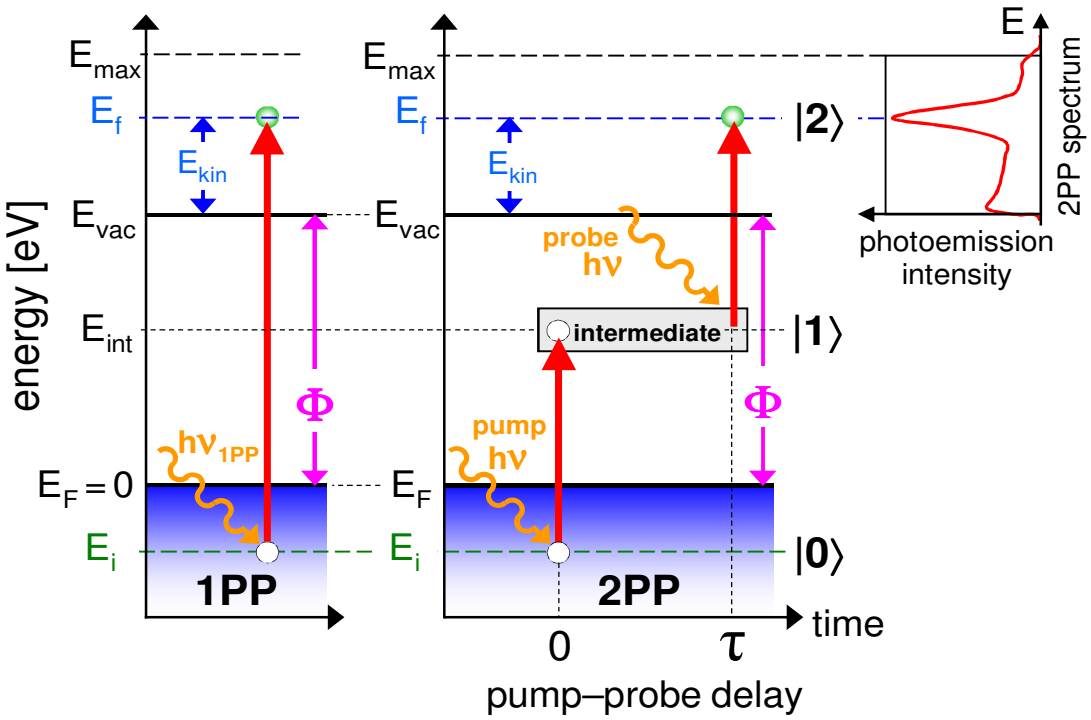

Figure 1.12 Photoexcitation scheme for a 2PP process (right) compared to a 1PP process (left). The first photon (pump) excites an electron from an occupied initial state $|0\rangle$ below E_F to an unoccupied intermediate state $|1\rangle$; then a second photon (probe) with a certain time delay τ excites the electron further to a final state $|2\rangle$ above E_{vac}, upon which the photoelectron is emitted, detected, and recorded.

2PP combines the complementary benefits of regular photoemission and inverse photoemission spectroscopy techniques, where the former probes the occupied states below E_F and the latter

probes the unoccupied states. Thus, it offers an effective method for exploring the electronic properties of unoccupied excited states between E_F and E_{vac} such as image potential states, transient hot-electron states, and adsorbate-induced states [62,76]. 2PP experiments can be performed in two different modes: (1) in energy-resolved 2PP, the kinetic energy of the photoelectrons is measured at fixed pump–probe delay; (2) in time-resolved 2PP, the time delay between pump and probe pulses is scanned at a fixed kinetic energy of observation [77]. In both modes we use fixed photon energy of $h\nu = 3.10$ eV.

By scanning the delay between identical pump and probe pulses, TR2PP spectroscopy enables us to measure the lifetimes of the fundamental electronic excitations with femtosecond time resolution. TR2PP can be performed with collinear or noncollinear pump-probe configuration; the 2PP signal in the collinear configuration depends on the incident electric field to the fourth power, while for the latter, the signal is quadratic in intensity. The collinear interferometric measurements, where the delay is scanned with suboptical cycle resolution provide information on both the phase and population dynamics of the coupled states, whereas the noncollinear configuration probes only the population dynamics. Our measurements are always performed in the interferometric mode.

Because 2PP is a nonlinear process, its intensity is usually weaker than 1PP, and therefore, excitation of 1PP must be avoided in order to prevent it from overwhelming the 2PP signal. This can be achieved by using photon energy smaller than the work function, i.e., $h\nu < \Phi$. This requirement often limits the energy range of accessible unoccupied states between E_F and E_{vac}.

1.5 Organization of the Dissertation

In the subsequent chapters we describe the following topics: Chapter-2 describes the apparatus for the experimental measurements; Chapter-3 discusses more advanced aspects of the 2PP technique, i.e., angle- and time-resolved 2PP techniques are elaborated; starting from Chapter-4, our experimental and computational studies are presented. First, we study the 2PP mechanism of the bare Ag(111) surface in an effort to develop a quantitative model for the 2PP process for normal emission and as a function of emission angle. In Chapter-5, we describe how alkali atom deposition modifies the electronic structure of Cu(111) and Ag(111) surfaces. We develop a simple model for the electronic structure of chemisorbed alkali atoms and describe the symmetry properties of a newly discovered unoccupied state. In Chapter-6, we employ TR2PP technique to characterize the lifetime of alkali-induced states of alkali/Ag(111) chemisorption systems. An unusual nonexponential decay feature found for Cs/Ag(111) is interpreted in terms of surface femtochemistry of Cs photodesorption. Chapter-7 presents the conclusive remarks pertaining to the aforementioned studies.

Chapter-2

Experimental Apparatus

The experimental measurements presented in this dissertation were obtained with a time-resolved photoemission apparatus. The apparatus consists of a laser system for excitation of 2PP, a second harmonic generation stage for doubling the frequency of the excitation light, a Mach-Zehnder interferometer for scanning the pump-probe delay, an ultrahigh vacuum (UHV) apparatus for preparing and containing the sample, electron optics for photoemission energy and momentum analysis, and electronics for data acquisition and instrument control. The key elements are depicted in Fig. 2.1. Each component serves different purpose and they are described in this chapter in the following order: section 2.1 describes the femtosecond Ti:Sapphire laser system and related optical instruments; section 2.2 illustrates the UHV system, its auxiliary components, and explains how they function; and section 2.3 presents the electronics for recording the experimental data.

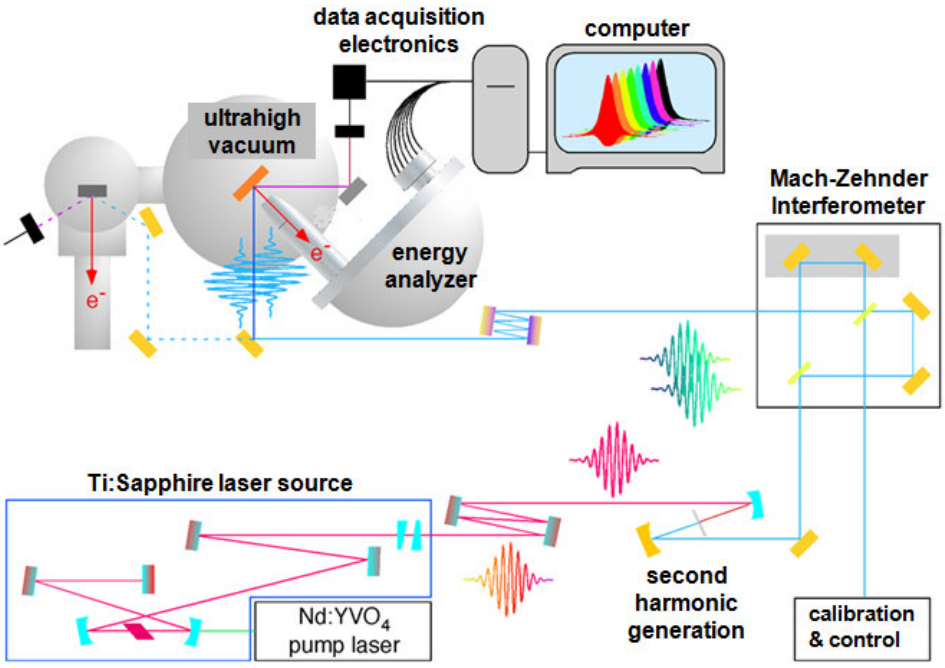

Figure 2.1 The key elements of our experimental apparatus: Ti:Sapphire laser system, second harmonic generation stage, Mach-Zehnder interferometer with calibration and control units, ultrahigh vacuum chamber, energy analyzer, and data acquisition electronics and computer.

2.1 Light Source and Optics

The schematics of the laser, optics and some of the related electronic instrumentation are shown in Fig. 2.2. A Ti:Sapphire laser oscillator was used as the source for the excitation light for the 2PP experiments described herein. The optical system can be divided into three groups as follows: (1) the Ti:Sapphire oscillator (laser source), (2) the second harmonic generation stage, and (3) the Mach-Zehnder Interferometer (MZI) for pump-probe delay scanning. Each component is custom made for the best attainable performance.

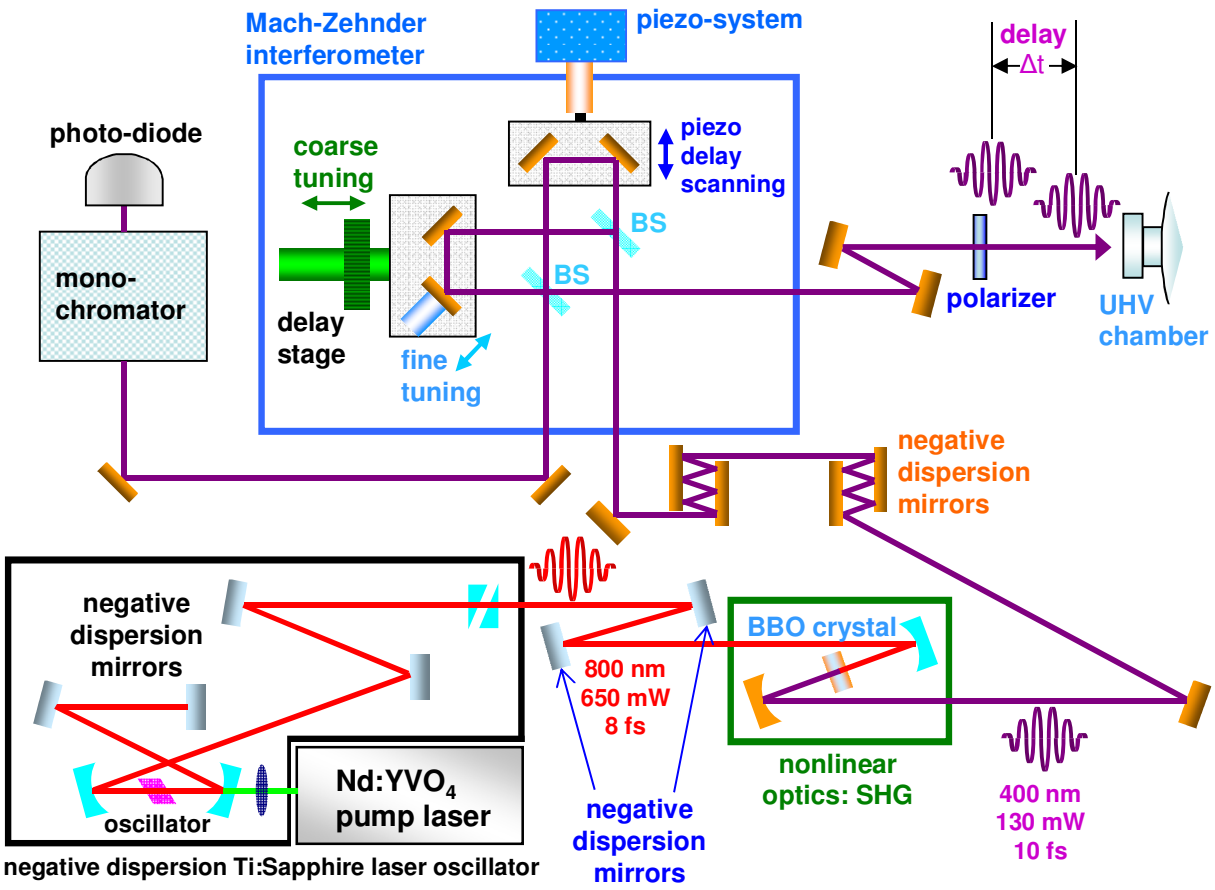

Figure 2.2 The optical part of the experimental apparatus for 2PP experiments. It consists of three major components: The black frame: Ti:Sapphire oscillator (laser source); the green frame: second harmonic generation stage; and the blue frame: Mach-Zehnder interferometer.

2.1.1 Ti:Sapphire Laser Source and Nonlinear Optics

The 'black frame' in Fig. 2.1 (left lower corner) shows the Ti:Sapphire laser oscillator system. A continuous wave (cw) 'neodymium-doped yttrium vanadate' ($Nd:YVO_4$) solid-state laser (Millennia Xs, from Spectra Physics) pumps the Ti:Sapphire crystal, which is the laser gain medium. About 5 W of output power of continuous green light (532 nm) from the pump laser is directed and focused (57–63 mm focal length lens) on the Ti:Sapphire crystal at the Brewster's

angle incidence [78]. The sapphire (Al_2O_3) crystal is doped with titanium ions (Ti^{3+}, with absorbance of 4.8 cm^{-1} and weight percentage of $0.250 \pm 0.045\%$). Ti:Sapphire lasers emit light in the near infra-red region and are tunable within the range of 650–1100 nm; their gain is the highest at 800 nm.

The bandwidth of laser output depends primarily on the properties of the gain medium, and secondarily on the optical elements comprising the laser cavity. The Ti:Sapphire gain medium is chosen for its broad bandwidth, high efficiency, and stability of operation. The laser cavity consists of mirrors, which form a standing wave pattern of the electromagnetic field trapped within the cavity. The constructive and destructive interference of the trapped field sets up oscillation at discrete frequencies, termed the 'longitudinal modes' of the cavity. In the absence of a frequency-selective optical element inside the cavity, the laser will oscillate in a multimode fashion, on randomly selected modes within the spectral gain profile [79]; while all other modes are suppressed by depletion of the gain. If several modes can be made to oscillate with a fixed phase instead of oscillating independently, the coupled modes interfere constructively in time to produce periodical and intense bursts (or pulses) of light. This is known as the 'mode-locked' operation. Therefore, mode-locking is achieved by establishing a coupling between the phases of the independently oscillating modes through a nonlinear process that favors phase-coherent oscillation. A coherent superposition of the mode amplitudes is obtained, resulting in the formation of laser pulses of extremely brief durations, as low as a few femtoseconds (10^{-15} s).

We employ the nonlinear 'optical Kerr effect' to mode-lock our laser. When an intense monochromatic electromagnetic wave passes through a 3rd order nonlinear medium of a centrosymmetric crystal, its dielectric response is expressed as

$$\varepsilon_t = \varepsilon + \varepsilon_2 \langle \mathbf{E} \cdot \mathbf{E} \rangle . \qquad [2.1]$$

The nonlinear dielectric response with this form requires the polarization of the form

$$\mathbf{P} \propto \varepsilon_0 \chi^{(1)} \mathbf{E} + \varepsilon_0 \chi^{(3)} \mathbf{EEE} \qquad [2.2]$$

where ε_0 is the permittivity of free space, $\varepsilon = 1 + \chi^{(1)}$, and $\varepsilon_2 = 1 + \chi^{(3)}$, and $\chi^{(n)}$ is the n^{th} order component of electric susceptibility [80]. The nonlinear index of refraction of a medium is defined as the square root of the 'effective' dielectric function (ε_{eff}):

$$\begin{aligned} n &= (\varepsilon_{eff})^{1/2} \\ &= (\varepsilon + \varepsilon_2 \mathbf{EE})^{1/2} , \end{aligned} \qquad [2.3]$$

where n_2 is the 2nd order nonlinear refractive index. Since $n_2 << n_0$, it can be approximated by a Taylor series expansion as [80]

$$\begin{aligned} n(\mathbf{E}) &\approx n_0 + \frac{1}{2} n_2 |\mathbf{EE}| \\ n(I) &\approx n_0 + \frac{1}{2} n_2 I \end{aligned} \quad , \qquad [2.4]$$

where the index of refraction varies linearly with the optical intensity ($I = |\mathbf{E}|^2$) on account of the 3rd order nonlinearity [81].

When an intense electric field is applied, it induces nonlinear polarization electrons with respect to ionic cores. The nonlinear polarization of the medium leads to an intensity-dependent change in the refractive index, as expressed in equation [2.4]. Because the laser beam intensity varies

transversely and peaks at the center of the beam profile, as illustrated in Fig. 2.3, the effective value of the index of refraction follows its radial gradient. Under these conditions, the quadratic index profile of the nonlinear medium acts as a focusing lens with an intensity-dependent focal distance [79]. In the case of our Ti:Sapphire laser, the laser crystal acts as the nonlinear Kerr medium for phase-locking the modes within the laser cavity.

The transverse gain profile of a Ti:Sapphire laser is defined by the focal length of the lens focusing 532 nm pump light into the Ti:Sapphire crystal. In the continuous mode of operation of a Ti:Sapphire crystal laser, the cw mode is larger than the pump laser-defined gain medium. Self-focusing of intense pulses oscillating within the cavity causes more optimal overlap of the mode-locked operation cavity mode with the gain medium. Because high intensity fluctuations attain better overlap with the gain medium, they are preferentially amplified to attain stable mode-locked operation.

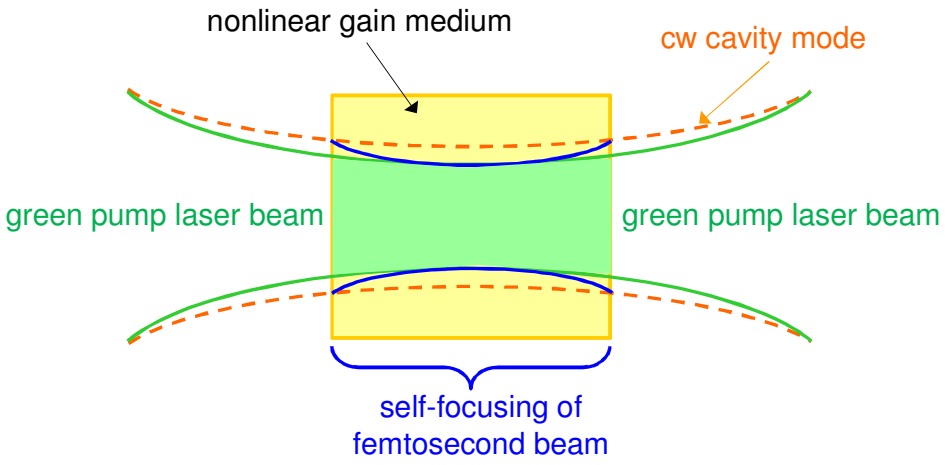

Figure 2.3 Kerr-lens mode-locking (KLM) in a 3rd order nonlinear gain medium acts as a lens whose focusing power depends linearly on the intensity of the incident laser beam.

In addition to the self-focusing, the instantaneous intensity-dependent change in the index of refraction induced a phase shift of the propagating field. The phase shift broadens the frequency spectrum of the field, thereby increasing the bandwidth, which allows the laser to sustain shorter pulses. The combined effects of this 'self-phase modulation' (SPM) and self-focusing lead to the generation of more intense, broader frequency pulses up to the limits imposed by the gain saturation, the bandwidth of the gain medium, and the bandwidth of the optical cavity elements. In our Ti:Sapphire oscillator this passive Kerr mode-locking mechanism can sustain ~8 fs pulses with 650 mW average output power and approximately 90 MHz repetition rate.

2.1.2 Second Harmonic Generation

Because the work functions of most metals lie within the range of $4.0-5.5$ eV, the photon energy of 1.55 eV corresponding to the 800 nm wavelength is insufficient to induce 2PP. The photon energy demands are even more severe for semiconductors, for which the gap from the highest occupied state to E_{vac} could be even larger. These considerations call for at least the second harmonic of Ti:Sapphire laser to be employed in one-color 2PP studies of metal and semiconductor surfaces.

Nonlinear optical conversion like second harmonic generation and sum frequency mixing can be accomplished in nonlinear optical crystals. When two incident waves of angular frequencies ω_1 and ω_2 pass through a nonlinear medium, they can mix and thereby induce a nonlinear polarization. The nonlinear polarization gives rise to new waves at frequencies $\omega = \omega_1 \pm \omega_2$, which traverse the nonlinear medium with a phase velocity $v_\varphi = \omega/k = c/n(\omega)$. If the wave

vectors of the incident and induced waves conserve momentum the sum and/or difference frequency waves can be produced with high efficiency. The 'phase-matching' condition described above is expressed by [79]

$$\mathbf{k}_3(\omega_1 \pm \omega_2) = \mathbf{k}_1(\omega_1) \pm \mathbf{k}_2(\omega_2) \qquad [2.5]$$

for the three interacting photons.

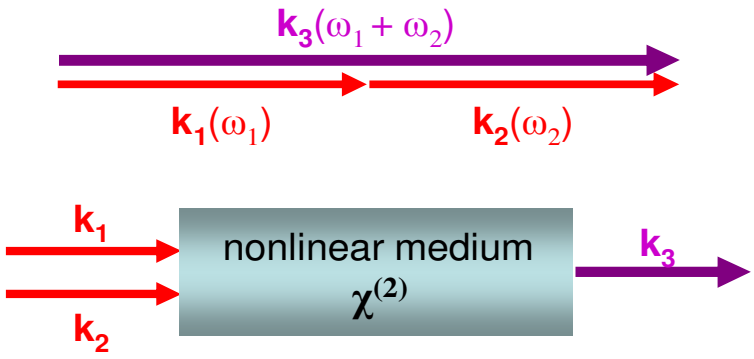

Figure 2.4 The 'phase-matching' condition for a typical second harmonic generation process where two incident waves ($\mathbf{k}_1$ and $\mathbf{k}_2$) and a resultant wave ($\mathbf{k}_3$) propagate collinearly.

As can be surmised from Fig 2.4, the maximum constructive interference between the propagating sum-frequency wave and the locally generated wave can be obtained, when both of the incident and resultant waves travel collinearly, i.e., $\mathbf{k}_1 \| \mathbf{k}_2 \| \mathbf{k}_3$, and with the same phase velocity, i.e., $|\mathbf{k}_3| = |\mathbf{k}_1| + |\mathbf{k}_2|$. Given that $c/n = \omega/k$ and $\omega_3 = \omega_1 \pm \omega_2$, the phase-matching condition can be rewritten in terms of indices of refraction and wave frequencies as

$$n_3\omega_3 = n_1\omega_1 \pm n_2\omega_2 \qquad [2.6]$$

where n_1, n_2, and n_3 are the frequency and crystal axis-dependent indices of refraction.

In a second harmonic generation process, two photons of the same angular frequency ω mix to produce a wave at 2ω. This process takes place within the 'green frame' shown in Fig 2.2. The intensity of the second harmonic light in terms of that of the fundamental light is given by [79]

$$I(2\omega) = \left(\frac{2\omega^2 \, | \chi_{eff}^{(2)} |^2 \, L^2}{n^3 c^3 \varepsilon_0} \right) I(\omega)^2 \left(\frac{\sin(\Delta k \cdot L)}{\Delta k \cdot L} \right)^2 \qquad [2.7]$$

where I(ω) is the intensity of the fundamental wave, $\chi_{eff}^{(2)}$ is the value of the effective nonlinear susceptibility tensor element, 'L' is the length (or thickness) of the nonlinear doubling crystal. The phase-mismatch parameter 'Δk' is defined as $\Delta k = k_2 - 2k_1$, and is zero at the phase matching condition. The effective second harmonic generation length is determined by the 'coherence length' of a doubling crystal, which is defined by the characteristic distance along which the second harmonic waves remain in phase, and it is expressed as

$$L_{coh} = \frac{\pi}{2\Delta k} = \frac{\lambda}{4(n_e^{2\omega} - n_o^{\omega})}. \qquad [2.8]$$

The efficiency of harmonic generation degrades when the fundamental and second harmonic waves have a phase difference $\Delta\varphi > \pi/2$, which happens if the thickness of the crystal exceeds the coherence length, i.e., $L > L_{coh}$. Then, the fundamental and second harmonic waves start to interfere destructively, resulting in a decrease in the amplitude of the second harmonic wave.

Phase-matching can be achieved by employing a negative birefringent uniaxial crystal, for which $n_e < n_o$, where n_e and n_o stand for the extraordinary and ordinary indices of refraction, respectively [82]. The condition that gives the angle of propagation of incident light with respect to the optic axis for which the extraordinary refractive index of the second harmonic light equals that of the ordinary index of the fundamental light is defined by [80]

$$\frac{1}{\left(n_e^{(2\omega)}(\theta)\right)^2} = \frac{\sin^2\theta}{\left(n_e^{(2\omega)}\right)^2} + \frac{\cos^2\theta}{\left(n_o^{(2\omega)}\right)^2} = \frac{1}{\left(n_o^{(\omega)}(\theta)\right)^2}, \qquad [2.9]$$

whereby one can calculate the phase-matching angle 'θ_p' with respect to the optic axis in such a crystal. The phase-matching condition can also be demonstrated graphically by the index of refraction ellipses in Fig. 2.5. At θ_p, the indices of refraction of the fundamental and second harmonic waves are equal, i.e., $n_e^{(2\omega)} = n_o^{(\omega)}$ and the phase-matching condition is fulfilled. When the incident light passes through the crystal at θ_p as an ordinary wave, the in-phase microscopic contributions $\mathbf{P}_i(2\omega\,\mathbf{r}_i)$ produce a macroscopic second harmonic wave of frequency 2ω as an extraordinary wave.

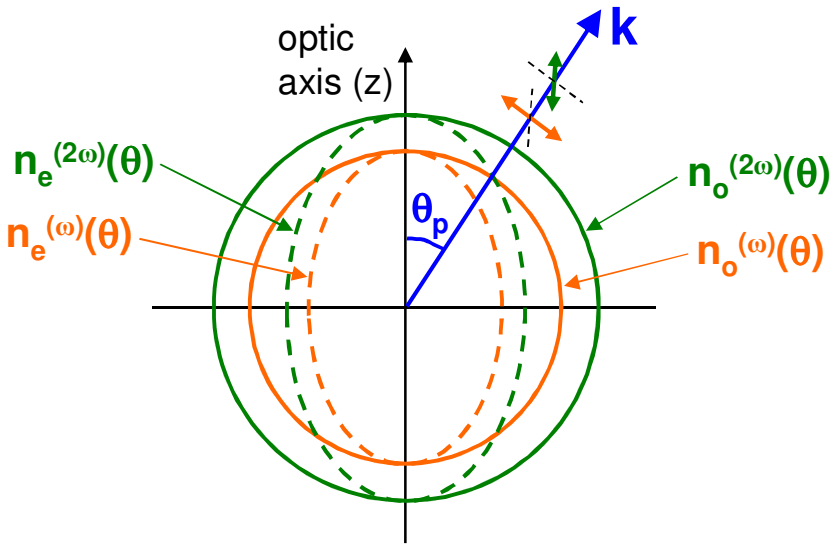

Figure 2.5 The phase-matching condition for second harmonic generation process where a negative birefringent uniaxial crystal is used. Type-I phase matching is employed where the interacting incident fundamental waves have parallel polarization and the resultant wave is orthogonal to the input waves. The phase-matching angle θ_p corresponds to the intersection of the ordinary and the extraordinary index curves. The eccentricities shown are exaggerated.

The optical arrangement of the second harmonic generation system is shown in Fig. 2.6. For frequency doubling or sum-frequency generation, various nonlinear media can be employed. We choose the BBO (β-BaB_2O_4) crystal, which has a large nonlinear coefficient, low temperature dependence, high damage threshold, high optical homogeneity, large angular acceptance, and a transparency range between 195 – 3500 nm [79]. A pair of spherical concave mirrors with 50 mm focal length is employed to focus the fundamental wave on the BBO crystal and to collimate the generated second harmonic light. The mirrors are mounted on translation stages to optimize focusing of 800 nm light onto the BBO crystal, and the generated second harmonic beam onto the sample in the photoemission chamber. The BBO crystal has 80 μm thickness; it produces a second harmonic wave with about 20% efficiency. The second harmonic light has ~200 meV spectral bandwidth centered at 400 nm and 10 fs pulse duration. The BBO crystal is mounted on a gimbal mount, which enables us to optimize the phase-matching condition. By changing the phase-matching angle θ_p, according to equation [2.9], we can tune the center output photon energy between 3.00 to 3.20 eV. This is possible, because the crystal cannot phase-match the full bandwidth of the fundamental pulse; changing the angle selects different frequencies for which the phase-matching condition is fulfilled.

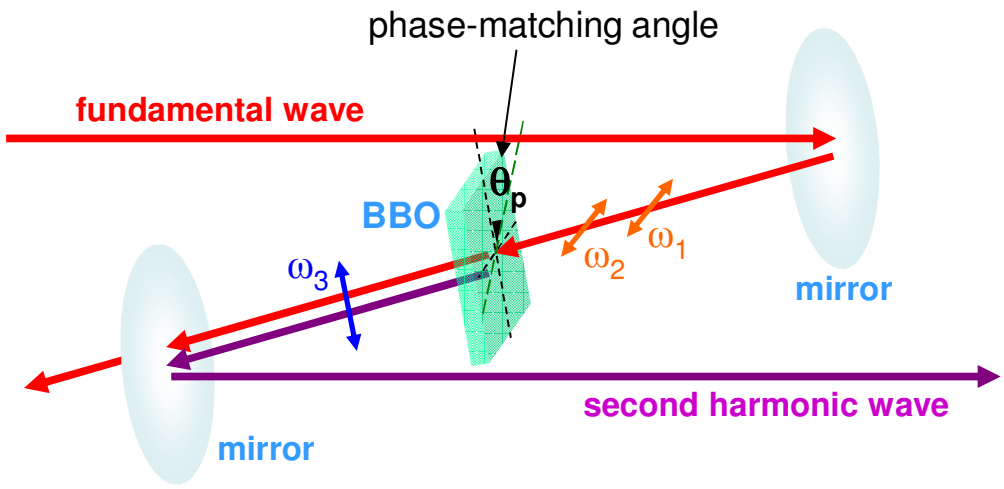

Figure 2.6 The optical arrangement inside the second harmonic generation stage: the fundamental wave is focused onto the BBO crystal at the phase-matching angle θ_p, giving rise to the second harmonic wave through type-I frequency doubling.

In Fig. 2.7, we juxtapose the spectra of the fundamental wave taken at the exit of the laser cavity and the second harmonic wave taken right after the second harmonic generation stage. The fundamental wave has a broad asymmetric spectrum, and the second harmonic wave exhibits a Gaussian shape spectrum centered at 400 nm.

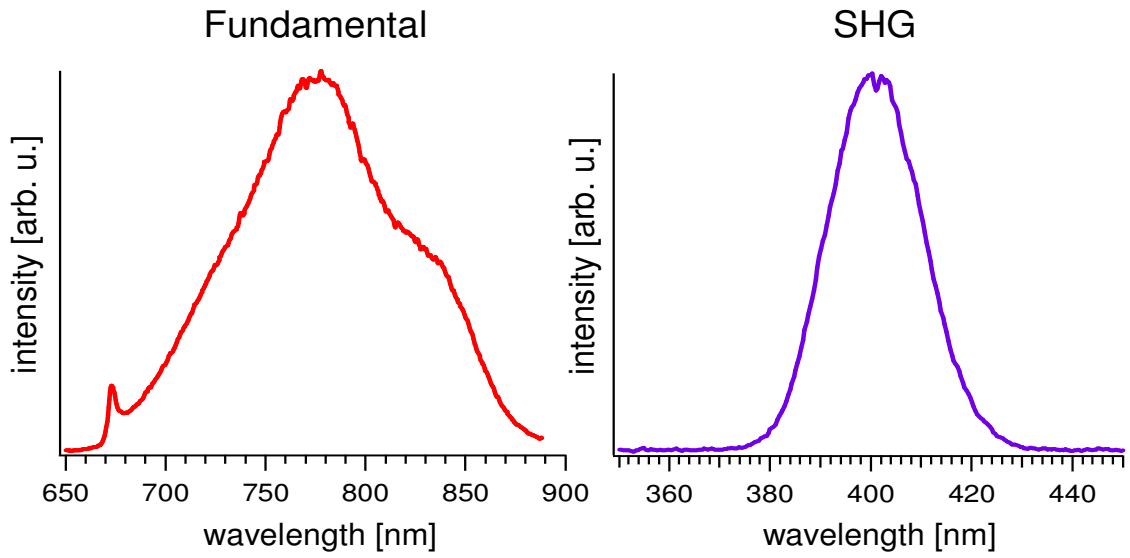

Figure 2.7 The fundamental (left) and second harmonic (right) spectra of the Ti:Sapphire laser.

According to Heisenberg's uncertainty principle for a Gaussian shape pulse, the time–bandwidth product is expressed as [80,83]

$$\Delta\nu \cdot \Delta\tau = \frac{2\ln 2}{\pi}. \qquad [2.10]$$

where the bandwidth can be calculated by differentiating frequency with respect to the wavelength in $\nu = c/\lambda$ as [79]

$$\Delta\nu = \frac{c \cdot \Delta\lambda}{\lambda^2}. \qquad [2.11]$$

The second harmonic laser pulse is centered at 400 nm and has a full-width half-maximum (FWHM) of about 23 nm. Therefore, the minimum pulse width can be estimated as

$$\Delta\tau = \frac{(2\ln 2/\pi)}{\Delta\nu} = \left(\frac{2\ln 2}{\pi}\right)\left(\frac{\lambda^2}{c \cdot \Delta\lambda}\right) = \left(\frac{2\ln 2}{\pi}\right)\left(\frac{(400\times10^{-9}\,\mathrm{m})^2}{(3\times10^{8}\,\mathrm{m/s})(23\times10^{-9}\,\mathrm{m})}\right) \approx 10 \quad \mathrm{fs}. \qquad [2.12]$$

The pulse duration can be confirmed by autocorrelation measurements at the sample surface.

2.1.3 Interferometric Pump and Probe Delay Scanning

We employ a 'Mach-Zehnder Interferometer', abbreviated as MZI (the 'blue frame' in Fig. 2.2), in order to create identical pump and probe pulses with a well-defined time delay [71,78]. In the MZI, the input beam is separated into two beams by a partially transmissive beamsplitter. After traversing two different optical paths, the two separated beams are recombined on a second beamsplitter. The difference between the optical paths gives the temporal or the phase delay between the two pulses. An MZI has two output beams, which differ by an additional π phase

shift corresponding to the difference in the number of reflections each beam suffers on passing through the interferometer. By translating one pair of retroreflecting mirrors back and forth with a piezo-driven flexure stage, the length of one of the arms is continuously scanned to produce a variable time delay between the pulse pair.

The MZI has two output beams, which serve different purposes. The output beam for which the dispersion is balanced is used for 2PP experiments, while the unbalanced one is used to monitor and control the scan delay. After exiting the MZI and right before entering the UHV chamber, the excitation laser beam passes through a λ/2-wave plate, by which one can select s- or p-polarized light. The beam goes through the viewport of the chamber, which is made of a plano-convex CaF_2 lens with a nominal focal distance of 200 mm. The lens focuses the beam on the sample as well as maintains the vacuum within the chamber. The diameter of the laser spot formed on the sample is approximately 70 μm [84].

2.1.4 Measurement of the Laser Pulse Duration

We employ ultrafast lasers to probe the electronic structure and electron dynamics at metal surfaces. Because many dynamical processes at surfaces occur on the time scale of the femtoseconds, it is essential to be able to characterize and accordingly optimize such pulses. The femtosecond regime is beyond the detection range of standard electronic instruments; therefore, we employ a pure optical method based on optical second-order autocorrelation technique to characterize directly not only the amplitude but also the phase of the laser pulse [80]. In MZI, the optical pulse from the laser is split into two identical pulses (‘pump’ and ‘probe’), which travel

different paths of nearly equal lengths before they are made collinear at the output of MZI [79]. The time delay between the two pulses is scanned and a second-order interferometric autocorrelation trace of a Ta sample plate is measured by TR2PP to check the quality of the laser pulse (see section 2.1.5 for further information). Optimization of the pulse is achieved by minimizing the overall dispersion in the optical path length through successive reflections of the laser light from negative dispersion mirrors; the dispersion compensation will be discussed in the following section [78].

The first-order interferometric autocorrelation in terms of pump and probe electric fields (i.e., electric field autocorrelation) and their delay τ is expressed as

$$I_1(\tau) = \int_{-\infty}^{+\infty} \left|\mathbf{E}(t-\tau) + \mathbf{E}(t)\right|^2 dt = \left|\mathbf{E}(t-\tau)\right|^2 + \left|\mathbf{E}(t)\right|^2 + G(\tau) + G^*(\tau) \qquad [2.13]$$

where $G(\tau)$ is the first order autocorrelation of a signal function with respect to a reference function, and $G^*(\tau)$ is its complex conjugate:

$$G(\tau) = \int_{-\infty}^{+\infty} F_{sig}(t) F_{ref}(t-\tau) dt \,. \qquad [2.14]$$

Here, both the signal and the reference functions are identical electric fields, except for the time delay τ. Therefore, $G(\tau)$ can be expressed as $G(\tau) \sim \mathbf{E}(t-\tau)\mathbf{E}(t)\exp(i\omega_1 t)$, indicating that it and its conjugate $G^*(\tau)$ oscillate with an average frequency ω_1. The Fourier transform of $G(\tau)$ is

$$\begin{aligned} G(\omega) &= \int_{-\infty}^{+\infty} G(\tau) \cdot \exp(-i\omega\tau) d\tau \\ &\propto E(\omega) \cdot E^*(\omega) \\ &\propto I(\omega) \end{aligned} \,. \qquad [2.15]$$

In other words, the Fourier transform of the first-order autocorrelation G(ω) is proportional to the spectral intensity of the laser pulse. Thus, the first-order field autocorrelation does not reveal information other than what can be gained from a spectrometer [83].

In order to gain more information on the shape and phase of the laser pulse, the nonlinear second-order interferometric autocorrelation technique should be used. It can be achieved by coherently superposing the two collinear partial beams, and scanning their delay with the interferometric (subwavelength) precision. It is expressed as

$$I_2(\tau) = \int_{-\infty}^{+\infty} \left| [\mathbf{E}(t-\tau) + \mathbf{E}(t)]^2 \right|^2 dt \ . \qquad [2.16]$$

If the pump and probe electric fields are described by $E(t)\exp[i(\omega t + \varphi(t))]$ and $E(t-\tau)\exp[i(\omega(t-\tau) + \varphi(t-\tau))]$ respectively, where E(t) is the slowly varying amplitude, their second-order interferometric autocorrelation is given by

$$I_2(\tau) = \int_{-\infty}^{+\infty} \left| \{[E(t-\tau)\exp[i(\omega_1(t-\tau) + \varphi(t-\tau))] + E(t)\exp[i(\omega_1 t + \varphi(t))]]\}^2 \right|^2 dt \ . \qquad [2.17]$$

After expanding equation [2.17], one obtains the following:

$$\begin{aligned} I_2(\tau) = \int_{-\infty}^{+\infty} \Big| & E^4(t) + E^4(t-\tau) + 4E^2(t)E^2(t-\tau) \\ & + 4E(t)E(t-\tau)\left(E^2(t) + E^2(t-\tau)\right)\cos[\omega_1\tau + \varphi(t) - \varphi(t-\tau)] \\ & + 2E^2(t)E^2(t-\tau)\cos[2(\omega_1\tau + \varphi(t) - \varphi(t-\tau))] \Big| dt \end{aligned} \ . \qquad [2.18]$$

The above expression is divided into three components: the first, second and third lines of the integral represent the phase averaged signal, and envelopes at ω and 2ω frequencies, respectively. Note that the phase averaged signal is independent of the phase, whereas the first and second

order envelopes oscillate at $1\omega_l$ and $2\omega_l$ frequencies respectively and contain explicit phase information, which can be used for diagnostic purposes for the determination of the laser pulse dispersion.

One can use equation [2.18] to calculate the relative intensities of second-order interferometric autocorrelations, when the pump-probe delay is zero (i.e., $\tau = 0$) as

$$I_2(\tau = 0) = 2^4 \int E^4(t)dt \,, \qquad [2.19]$$

and when the time delay is far from coherent superposition at very large delay (i.e., $\tau \to \pm\infty$) as

$$I_2(\tau \to \pm\infty) = 2 \int E^4(t)dt \,. \qquad [2.20]$$

Therefore, the corresponding contrast ratio is 8:1. We present the results of a simulation based on equation [2.18] for several chirp parameters and display a TR2PP measurement on a Ta sample plate in section 2.1.5. Their respective contrast ratios turn out to be 8:1 as computed here.

2.1.5 Characterization of the Laser Pulse and the Effects of Dispersion

In optics, dispersion is defined as the frequency (or wavelength) dependence of the phase velocity of a wave. When an ultrashort optical pulse propagates through a transparent medium, which may include optical elements (lens, beamsplitter, etc.) and even air, it suffers a phase distortion on account of its wide spectral width and the group velocity dispersion (GVD) of the medium through which it propagates. This phenomenon leads to change in pulse duration along the propagation path [80]. Each medium contributes to the total GVD, resulting in the pulse broadening. In femtosecond regime, this effect has substantial consequences and needs to be compensated. To do so, we reflect the laser pulse from pairs of mirrors that have dielectric stacks

with negative GVD. Dispersion compensation is achieved by adjusting the number of successive reflections from such mirror pairs.

To understand the effect of dispersion, we simulate how it affects interferometric autocorrelation scans. A typical Gaussian pulse of the form $E_0(t) \propto \exp\left[-\frac{1}{2}\left(t/T_p\right)^2\right]$ (of pulse width T_p) in the time domain can be represented by its Fourier transform:

$$E_0(\omega) = \mathfrak{F}[E_0(t)] = \exp\left[-\frac{1}{2}(\omega-\omega_1)^2 T_p^2\right]. \qquad [2.21]$$

When the pulse propagates in a transparent medium by a distance 'x', its spectrum takes the form

$$E(\omega, x) = E_0(\omega)\cdot \exp\left[-ik(\omega)x\right]. \qquad [2.22]$$

Here, dispersion basically dictates the relationship between the wave vector and frequency as [78]

$$k(\omega) = \frac{\omega}{c} n(\omega), \qquad [2.23]$$

where $n(\omega)$ is the frequency-dependent index of refraction. In order to analyze the propagation effects, the wave vector can be expanded by a Taylor series around the central frequency ω_l up to the second order as

$$k(\omega) = k(\omega_l) + k'(\omega-\omega_l) + \frac{1}{2!}k''(\omega-\omega_l)^2 + \dots, \qquad [2.24]$$

where

$$k' = \left.\frac{dk(\omega)}{d\omega}\right|_{\omega_l} \text{ and } k'' = \left.\frac{d^2k(\omega)}{d\omega^2}\right|_{\omega_l}. \qquad [2.25]$$

Let us consider the first and second order electric field expressions in the frequency domain and obtain their time domain representation by Fourier transform.

The first term, after a propagation distance L, can be written as

$$E^{(1)}(\omega) = E_0(\omega)\exp\left[i\left(\frac{n\omega}{c} - k(\omega)\right)L\right] = E_0(\omega)\exp\left[-i\left(\left(k_1 - \frac{n\omega}{c}\right) + k_1'(\omega - \omega_1)\right)L\right]. \qquad [2.26]$$

Its Fourier transform gives us the electric field in the time domain as

$$E^{(1)}(t) = E_0(t)\cdot\exp\left[i\omega_0\left(t - \left(\frac{k_1}{\omega_1} - \frac{n(\omega)}{c}\right)L\right)\right]\cdot\delta(t-\tau), \qquad [2.27]$$

where the time delay is expressed as

$$\tau = \left(\left.\frac{dk(\omega)}{d\omega}\right|_{\omega_1} - \frac{n(\omega)}{c}\right)L = \frac{L}{c}\left(\omega\cdot\left.\frac{dn(\omega)}{d\omega}\right|_{\omega_1}\right). \qquad [2.28]$$

Note that the first order dispersion term turns out to be simply a time delay and does not contain any phase information; therefore, it can be neglected.

The second term of the electric field in the frequency domain can be written as

$$\begin{aligned} E^{(2)}(\omega) &= E_0(\omega)\cdot\exp\left[-i\frac{1}{2}k_1''(\omega-\omega_1)^2 L\right] \\ &= \exp\left[-\frac{1}{2}(\omega-\omega_1)^2 T_p^2\left(1 + i\frac{k_1''}{T_p^2}L\right)\right] \quad . \quad [2.29] \\ &\approx \exp\left[-\frac{1}{2}(\omega-\omega_1)^2 T_p^2\left(1 + i\frac{k_1''}{2T_p^2}L\right)^2\right] \end{aligned}$$

The second order dispersion term turns out to be the GVD, and for a small value, the Fourier transform of the above expression becomes

$$E^{(2)}(t) = \exp\left[-\frac{1}{2}\left(\frac{t}{T_p}\right)^2\left(1 - i\frac{k_1''}{T_p^2}L\right)\right] = \exp\left[-\frac{1}{2}\left(\frac{t}{T_p}\right)^2(1+i\xi)\right]. \qquad [2.30]$$

It turns out that the GVD corresponds to the linear chirp defined for a Gaussian pulse as

$$\xi = -\frac{L}{T_p^2} k_1'' = -\frac{L}{T_p^2 c}\left(\omega_1 \cdot \left.\frac{d^2 n(\omega)}{d\omega^2}\right|_{\omega_1} + 2\left.\frac{dn(\omega)}{d\omega}\right|_{\omega_1} \right), \qquad [2.31]$$

where 'ξ' is the chirp parameter. If one combines the first and second order dispersion terms by convolution, the following quantitative expression is obtained:

$$E(t) = E^{(2)}(t) \otimes E^{(2)}(t) = \exp\left[-\frac{1}{2}\left(\frac{t-\tau}{T_p} \right)^2 (1 + i\xi) \right]. \qquad [2.32]$$

If a linearly chirped Gaussians laser pulse $E(t) = \exp\left[-\frac{1}{2}\left(\frac{t-\tau}{T_p} \right)^2 (1 + i\xi) \right]$ is substituted in the integrals in equation [2.18], the resulting interferometric second-order autocorrelation becomes

$$\begin{aligned} I_2(\tau) = 1 &+ 2\exp\left[-(\tau/T_p)^2 \right] \\ &+ 4\exp\left[-\left(\frac{3+\xi^2}{4} \right)(\tau/T_p)^2 \right] \cos\left[\frac{a}{2}(\tau/T_p)^2 \right] \cos(\omega_1 \tau). \\ &+ \exp\left[-(1+\xi^2)(\tau/T_p)^2 \right] \cos(2\omega_1 \tau) \end{aligned} \qquad [2.33]$$

As stated in section 2.1.4, the fundamental, first order and second order envelopes modulate the 0ω, 1ω and 2ω frequencies, respectively. In order to visualize the effect of chirp on the second-order interferometric autocorrelation signal, one needs to calculate and plot the corresponding signal as a function of the delay time for various values of ξ. In Fig. 2.8, we plot the second-order interferometric autocorrelation for different values of ξ for a pulse centered at 400 nm with the corresponding optical cycle of $T = 2\pi/\omega_1 = 1.33$ fs, and the pulse duration $T_p = 10$ fs. In our experiments, the chirp parameters ξ lies in the range of $0-3$.

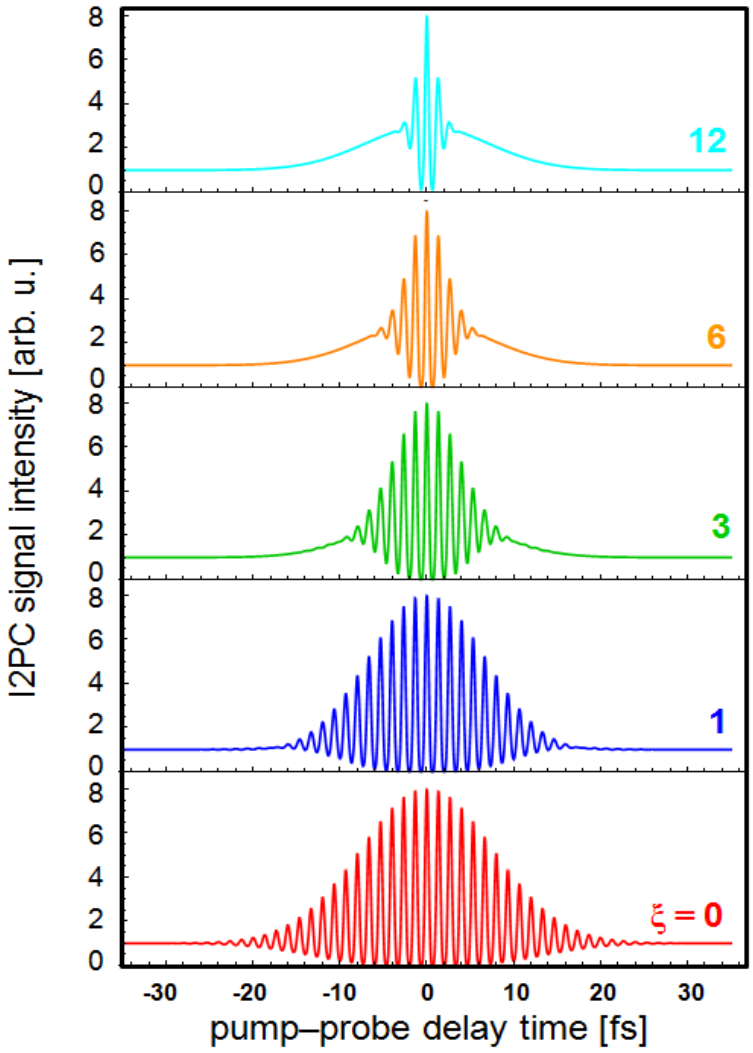

Figure 2.8 Second order interferometric autocorrelation (I2PC) for various chirp parameters ξ. The contrast ratio between the signal at $\tau = 0$ and $\tau \to \pm\infty$ is 8:1, as expected from the calculation.

The second-order interferometric autocorrelation of a laser pulse can be performed by means of the TR2PP technique. An interferometric two-pulse correlation (I2PC) measurement obtained by scanning the pump-probe delay interferometrically and recording the 2PP signal at a specific photoemission energy can converge to an interferometric autocorrelation measurement under the

assumption that the material responds instantaneously to the applied field. We perform such an I2PC measurement by exciting 2PP signal from a Ta sample plate within our UHV chamber. Because Ta has a high density of d-band states at E_F, its intermediate state lifetime is extremely short, and therefore, we assume that it causes minimal distortion of the autocorrelation scan. Fig. 2.9 compares a simulated interferometric autocorrelation by equation [2.18] for $\xi = 0$ (top) and a typical I2PC scan acquired by measuring TR2PP from the Ta sample plate (bottom). From the close correspondence between the simulation and I2PC measurement, one can conclude that the nonlinear interferometric autocorrelation signal from Ta plate is an effective tool for measuring the pulse characteristics and compensating the dispersion in order to minimize the laser pulse duration at the sample. As expected from equation [2.18], the experimental measurement approaches the theoretical ratio of 8:1.

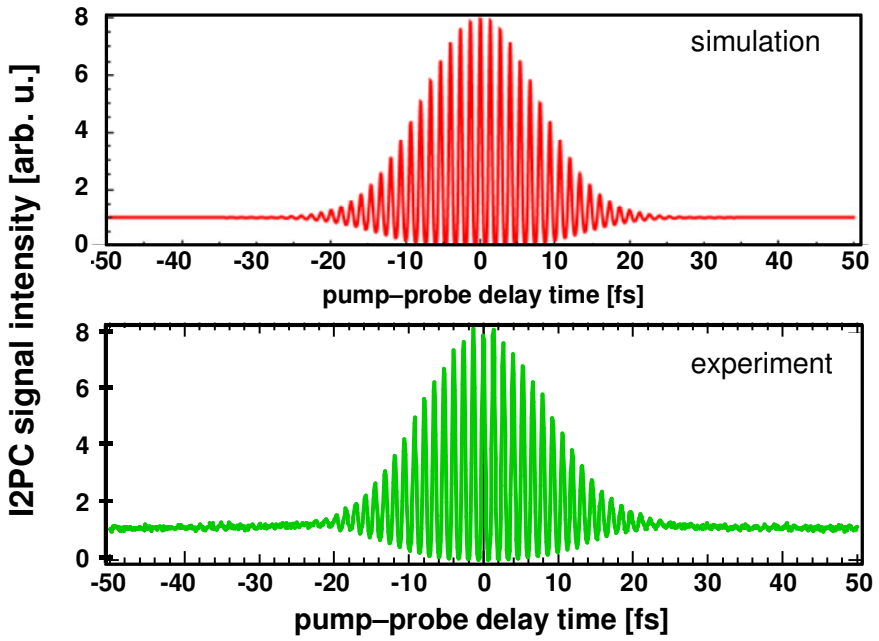

Figure 2.9 Interferometric autocorrelation signal obtained by simulating equation [2.18] with $\xi = 0$ (top) for a 10 fs Gaussian pulse, and an experimental I2PC scan obtained by recording 2PP signal from a Ta sample plate (bottom).

2.2 Ultrahigh Vacuum Chamber and Related Instruments

Atomic level characterization of solid surfaces requires that the composition of the surface stay constant during the experiment [18]. This implies that the flux of atoms or molecules impinging on the surface from the ambient environment must be minimized. This can be achieved if the experiment is performed under UHV conditions, which require pressures below ~5×10^{-10} mbar [15,18].

2.2.1 General Features of the Ultrahigh Vacuum Instrument

2PP measurements are performed in a UHV chamber (built by Omicron Vakuumphysik GmbH). The pressure within the chamber is maintained in the range of 1.0×10^{-10} to 2.0×10^{-11} mbar; as a result the surface can remain clean for several hours, which is typically 6-9 hours in our experiments. At this pressure level, the molecular density is 2×10^{6} per cm^3, and the molecular arrival rate is about 3×10^{10} molecules $cm^{-2}s^{-1}$, corresponding to a monolayer arrival time of the order of 10 hours [18]. In practice, many impurities, such as H_2, would not stick to and contaminate the surface.

Although the UHV chamber can be pumped down, there is always some amount of adsorbed gases on its interior walls, and their ensuing desorption limits the ultimate pressure. Therefore, the chamber needs to be baked over a period of 12–36 hours at some 140–150 °C temperature, after it has been exposed to air. The chamber is manufactured from μ-metal to screen external

magnetic fields, which would perturb low energy electrons. Exceeding this temperature limit may lead to trapping of magnetic fields, which would effectively make the chamber useless for electron spectroscopy. The duration and temperature of the bakeout process depend on the degree of contamination.

Pumping the chamber from 1 Atm to some 2×10^{-11} mbar level requires several pumping stages. In general, pumps can be divided into two main categories, (1) roughening pumps to evacuate the chamber down to $10^{-4}-10^{-6}$ mbar, and (2) the pumps for the UHV-regime [85]. In our UHV system, we employ a rotary vane pump, a turbo-molecular pump, an ion pump and an auxiliary titanium sublimation pump.

Rotary vane pumps are used in conjunction with turbo-molecular pumps and their function is to bring the pressure down to the 10^{-3} mbar level. According to Fig. 2.10(a), gas enters through the inlet and gets trapped in the volume between the rotor vanes and the stator; as the eccentrically mounted rotor turns, the gas is compressed and forced through the exhaust valve. Turbo-molecular pumps operate in the 10^{-4}–10^{-6} mbar pressure range. As shown in Fig. 2.10(b), a turbine rotor, which is composed of a stack of rotor blades with tilted leading edges, spins at very high speed (about 50,000–100,000 rpm) and shuffles gas molecules from the UHV side to the backing side, where they are pumped away by a rotary vane pump. Ion pumps are reliable, durable, and vibration-free; they operate in $10^{-3}-10^{-11}$ mbar range and are especially effective in maintaining the UHV conditions. As shown in Fig. 2.10(c), an ion pump consists of a collection of short, stainless steel anode tubes (a multicell array) situated between two titanium cathode plates, leaving a gap on both sides. A high potential (3000–7000 V) is applied between

anode and cathode, in the presence of a strong magnetic field. Electrons discharged from the cathode plates follow a helical trajectory to the anode plates. Because of their high energy, electrons ionize gas molecules. The ionized molecules are subsequently accelerated by the electric field and strike the cathode plates, which leads to sputtering of Ti atoms from the cathode. The sputtered Ti coats the interior walls of the cells, the cathode plates and the pump walls, where it chemically traps gas molecules that impinge [18,86]. Titanium sublimation pumps (TSP), as displayed in Fig. 2.10(d), are also used at low pressures in addition to ion pumps. Titanium is intermittently sublimated by passing a current through the Ti filaments. Reactive gas molecules such as nitrogen, oxygen, hydrogen, CO, CO_2 and water react with the exposed Ti film to form nonvolatile compounds; hence, low pressure is attained.

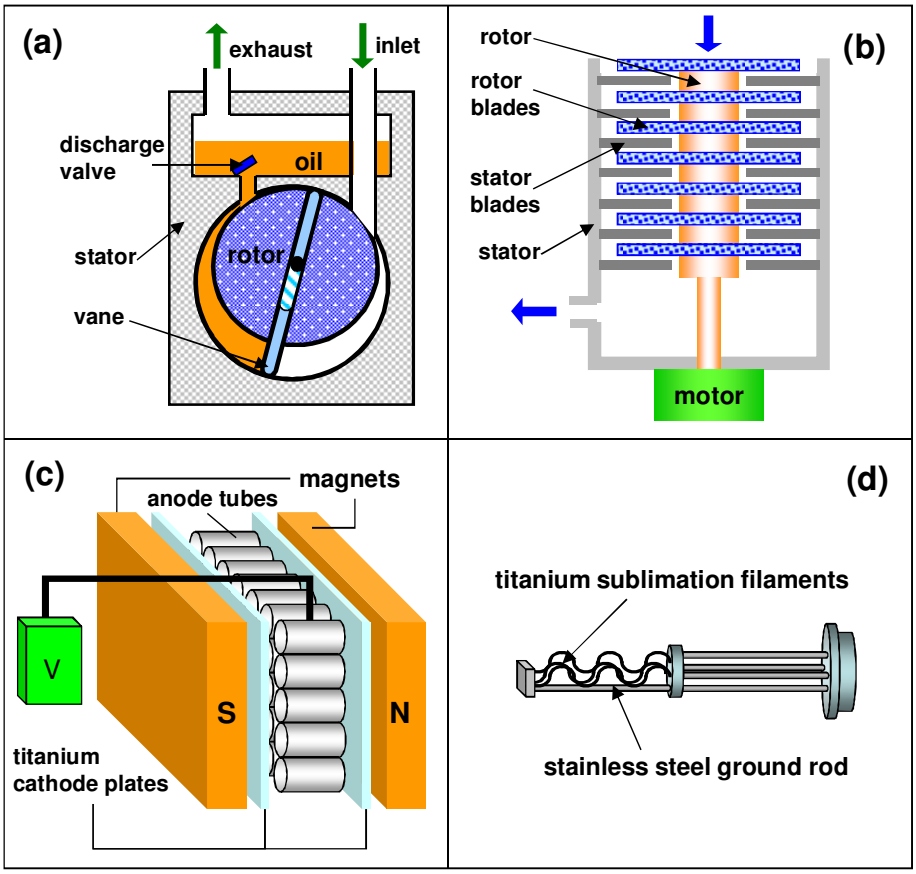

Figure 2.10 Schematic descriptions of **(a)** a rotary vane pump, **(b)** a turbo-molecular pump, **(c)** an ion pump (with its multicell structure), and **(d)** a titanium sublimation pump (TSP).

Having an apparatus to monitor the pressure of the UHV chamber is as important as having vacuum pumps to reach and maintain low pressure, especially during an experiment. There is no universal vacuum gauge for this purpose; different gauges function at different pressures for different experiments. Pressure under UHV conditions is usually measured by an ion gauge, which operates in the $10^{-4} - 10^{-11}$ mbar pressure range. As its name suggests, its operation is based on the ionization of the gas molecules. The ion current depends on the gas pressure, whereby the pressure can be determined.

One also needs to know about the gas composition in an UHV chamber, especially when an experiment is being conducted. This can be accomplished with a Residual Gas Analyzer (RGA), of which the most widely used type is the Quadrupole Mass Spectrometer (QMS). Mass spectroscopy of the gas in the chamber is needed (1) to monitor the exposure of surfaces to specific gases, (2) to monitor desorption from surfaces, and (3) to detect any malfunction of the UHV system. In general, a properly baked UHV system has residual background gases containing a mixture of H_2, CO, CO_2, and N_2.

Our UHV chamber, its components and auxiliary instruments are illustrated in Fig. 2.11. The UHV analysis chamber is where the actual experiments are conducted. The top view (Fig. 2.11(a)) shows the direction of the incident laser beam and that of photoemitted electrons that are captured by a hemispherical energy analyzer. The side view (Fig. 2.11(b)) shows how other

UHV components and related devices are located and connected to each other. There is a smaller 'load lock chamber' attached to the analysis chamber that is used to load, remove, exchange, and store samples in a revolving sample holder under UHV conditions.

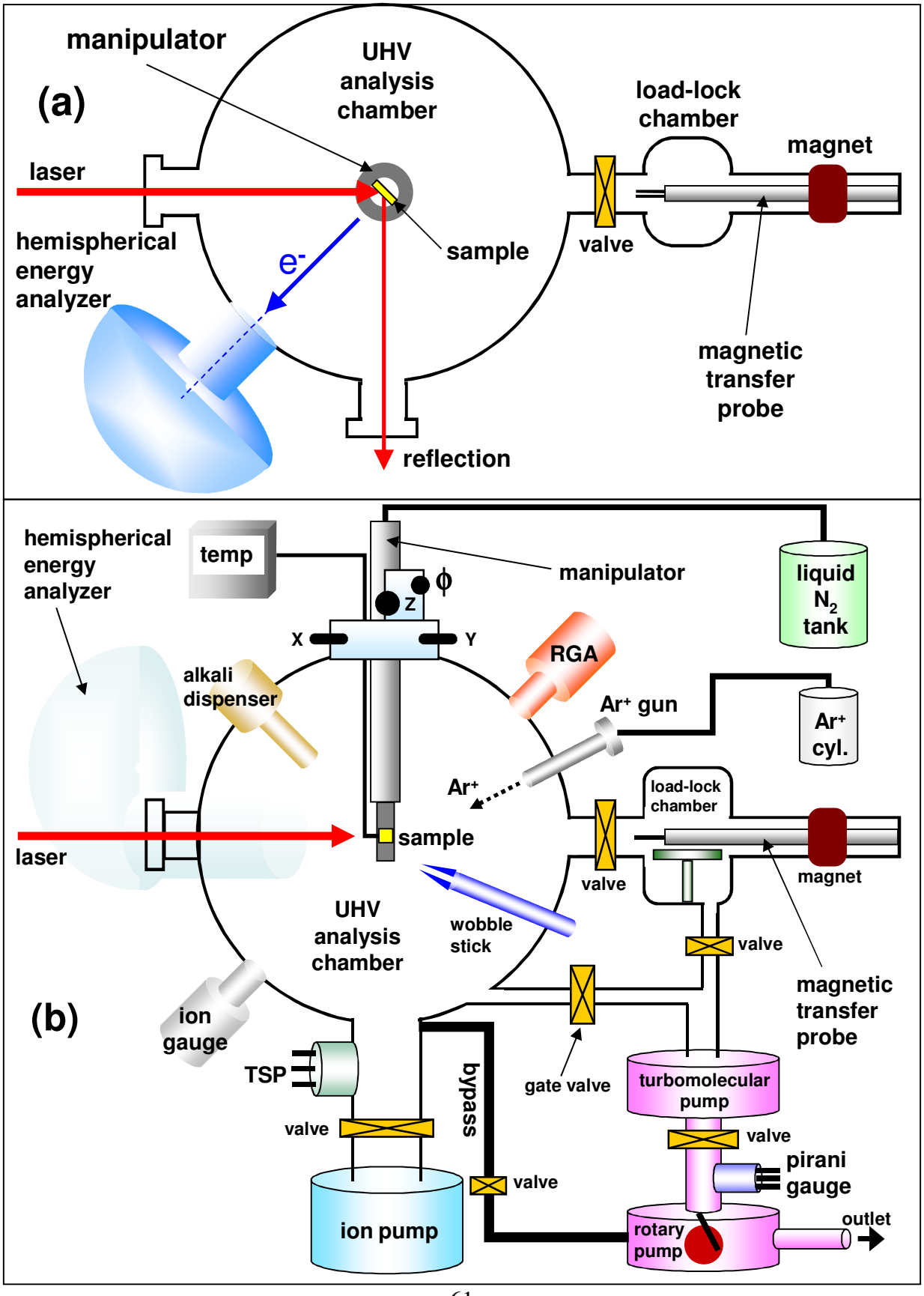
(a)
manipulator
UHV
analysis
chamber
load-lock
chamber
magnet
laser
hemispherical
energy
analyzer
e-
sample
valve
magnetic
transfer
probe
reflection
(b)
hemispherical
energy
analyzer
temp
manipulator
liquid
N2
tank
ϕ
z
x
y
RGA
alkali
dispenser
Ar+ gun
Ar+
cyl.
Ar+
load-lock
chamber
laser
sample
valve
magnet
UHV
analysis
chamber
wobble
stick
valve
magnetic
transfer
probe
ion
gauge
TSP
gate valve
turbomolecular
pump
valve
bypass
valve
pirani
gauge
ion pump
valve
rotary
pump
outlet

Figure 2.11 The **(a)** top view and **(b)** side view of our UHV system (TSP: titanium sublimation pump; RGA: residual gas analyzer; temp: temperature controller). The alkali metal dispensing unit is shown in more detail in Fig. 2.12.

There are several valves in the UHV system, each of which serves a different purpose. The function of the large gate valve is to cut off the analysis chamber from the turbo-molecular pump. It is actuated by high-pressure gas, and will close in the case of a power failure to protect the chamber from contamination with atmospheric gases. A manual valve is used between the analysis chamber and the load lock chamber, and another one between the latter and the turbo-molecular pump.

Our UHV system is also equipped with a 4-axis sample manipulator. It is used to move the sample in the x-, y- and z-directions, and to rotate it around the z-axis for angle-resolved measurements. The manipulator is designed such that the center of rotation can be made coincident with the incident laser beam where it hits the surface of the sample. Its center is a hollow cylinder, in which liquid nitrogen is introduced to cool down the sample. It is also possible to heat the sample by electron bombardment. By applying a high potential difference (about 1 kV) with respect to the sample, electrons emitted from a hot tungsten filament (carrying about 2 A current) are accelerated and hit the back of the sample plate. The energy provided by the electron current is the main mode of heating the sample. Temperature can be varied by adjusting the applied voltage and the electron emission current. Through cooling by liquid nitrogen and heating by electron bombardment we are able to control the sample temperature between 85–800 K. The upper part of the manipulator is a hollow tube made of stainless steel,

whereas the lower part is made of 'silver' (in a later version 'copper') and is braised to the stainless tube. The bottom of the manipulator is made of solid silver (copper) and is attached to the upper silver (copper) component. A thin sapphire plate is sandwiched between the two silver (copper) parts to provide high thermal conductivity and electric insulation. The bottom silver (copper) part holds a sample holder that accepts a Ta sample plate to which is attached a noble metal sample. The sample plate is fastened to the holder by flexible 'Mo' springs. Temperature is measured by means of an N-type (nicrosil-nisil) thermocouple, which is spot-welded onto one of the springs. All components in the vicinity of the sample, including the thermocouple and the screws, are made of nonmagnetic materials. Also, all insulating materials near the sample are shielded by metal foil. Both precautions are taken to prevent perturbation of low energy electrons by stray magnetic and electric fields.

According to Fig. 2.11, the hemispherical energy analyzer is at the ground potential as the rest of the UHV chamber [78]. The inner surface of the energy analyzer is coated with a layer of graphite to provide a homogeneous work function of 4.50 eV. The sample mounted on the manipulator is electrically insulated from the analysis chamber by a sapphire plate, which acts simultaneously as an electrical insulator and an effective thermal conductor. This allows us to apply a bias voltage of several volts between the sample and the analyzer, in order to improve the detection efficiency of low energy photoelectrons. The application of a bias voltage is necessary to minimize the residual influence of stray electric and magnetic fields within the chamber. The undesirable effect of the applied bias is to modify the angular distribution of photoemission, which has to be accounted for in angle-dependent measurements.

A home-made alkali metal dispensing unit (Fig. 2.12) is employed in the experiments involving alkali atom adsorption. This unit can accommodate three compact getter sources (SAES getters), each of which contains a mixture of an alkali metal chromate and a reducing agent. The reducing agent is a getter alloy called 'St101' (84% Zr and 16% Al). In addition to reducing the alkali ions back to their metallic state, St101 also removes chemically reactive gases from the environment, preventing them from contaminating the alkali metal vapor [87]. An electric current is applied through the getter source to emit alkali atoms through a slit. After applying a threshold current specific to each alkali atom species, the onset of adsorption of alkali atoms on the sample (Cu(111) or Ag(111)) can be seen through changes in the 2PP spectrum of the substrate. The deposition rate on the sample surface can be controlled by adjusting the current. This enables us to control the deposition rate and attain reproducible alkali atom coverage. The precise direction of the beam of alkali atoms must be aligned with respect to the position of the sample before taking actual data. To do so, the tilted flanges shown in Fig. 2.12 are rotated against each other, which enables directing the one of three separate getter sources toward the sample. Although the dispenser ejects alkali atoms effusively, only a narrow beam of alkali atoms passes through the rectangular exit aperture, which functions as a collimator. It is essential to direct the beam of the alkali atoms precisely onto the sample to achieve uniform alkali atom coverage throughout the sample surface. The coverage uniformity ensures uniform work function reduction; this minimizes lateral field gradients at the sample surface, which can interfere with detection of low energy electrons.

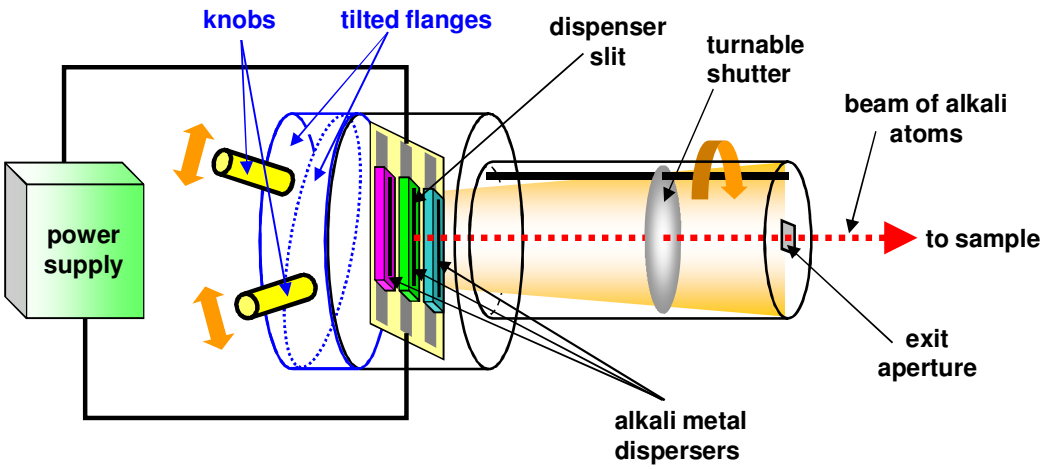

Figure 2.12 Alkali metal dispensing unit containing three alkali metal dispensers. The tilted flanges are moved against each other to align the exact direction of the beam of alkali atoms, while the shutter is used to start or halt alkali atom deposition.

2.2.2 Energy Analyzer

A typical experimental setup for photoemission spectroscopy consists of a combination of an electron lens system and an energy analyzer. Most analyzers use electrostatic forces for electron separation according to their kinetic energies and fall into two categories: (1) retarding field and (2) deflection analyzers.

We employ a deflection-type electrostatic electron energy analyzer of hemispherical shape (Omicron, EA-125), which is called a 'Spherical Deflection Analyzer' (SDA) [3] or a 'Concentric Hemispherical Analyzer' (CHA) [18]. Photoemitted electrons are analyzed with respect to their kinetic energy and momentum. A set of imaging and energy-dispersive electron optical elements are used as in a conventional spectrometer for photons. The notion of refraction (deflection)

defined by Snell's law in conventional optics can also be used to define the trajectories of photoelectrons by replacing refraction indices by the perpendicular components of electron velocity:

$$\frac{\sin\theta_{inc}}{\sin\theta_{ref}} = \frac{v_{ref}^{\perp}}{v_{inc}^{\perp}} \left(= \frac{n_{ref}}{n_{inc}} \right). \qquad [2.35]$$

The beam of photoelectrons is refracted toward or away from the normal to the equipotential lines depending on the potential gradient as illustrated for metallic apertures in Fig. 2.13 [15].

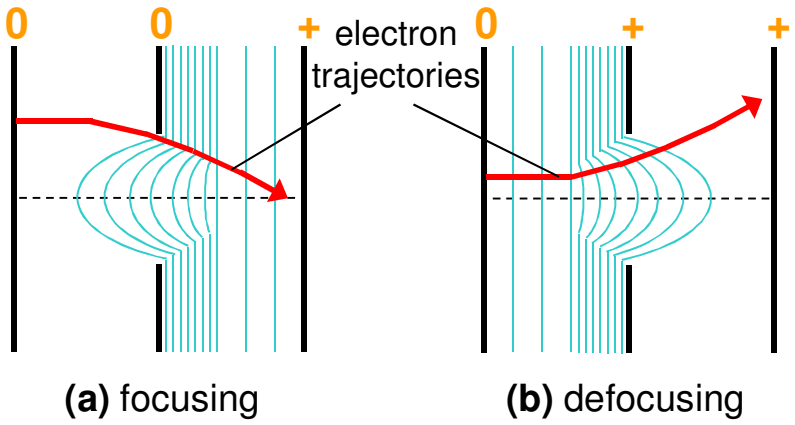

Figure 2.13 Electron lens formation by means of metallic apertures and the subsequent deflection of photoelectron trajectories in a **(a)** focusing and **(b)** defocusing setup.

When photoelectrons enter the energy analyzer, they pass through a multi-element electrostatic lens with 30 mm working distance. The lens system consists of two consecutive lenses, which collect electrons from the sample and focus them on the entrance aperture of the hemispherical energy analyzer [88]. The first 'Einzel' lens selects the analysis spot size and the electron acceptance angle; it has three magnification modes: high, medium and low. In the high (low) magnification mode, the focal plane is close to (far from) the sample and the lens accepts a wide (narrow) angle of incoming photoelectrons from a small (large) area. We use the 'low' mode,

since its angular resolution of ±1° offers the highest momentum resolution. The second 'focusing' lens accelerates or decelerates photoelectrons to adjust their kinetic energy to match the 'pass energy' (E_p) of the analyzer. The pass energy is the kinetic energy that photoelectrons must possess to have the appropriate trajectory from the entrance to the detector within the hemispherical energy analyzer. The second lens ensures that the focal point remains on the analyzer's entrance aperture.

The role of the analyzer is to resolve photoelectrons with respect to their energy [18]. The pass energy of transmitted electrons is controlled by the potential difference V_0 across the electrodes of the analyzer. Our energy analyzer has a mean radius (R_0) of 125 mm, and its structure and components are schematically presented in Fig. 2.14.

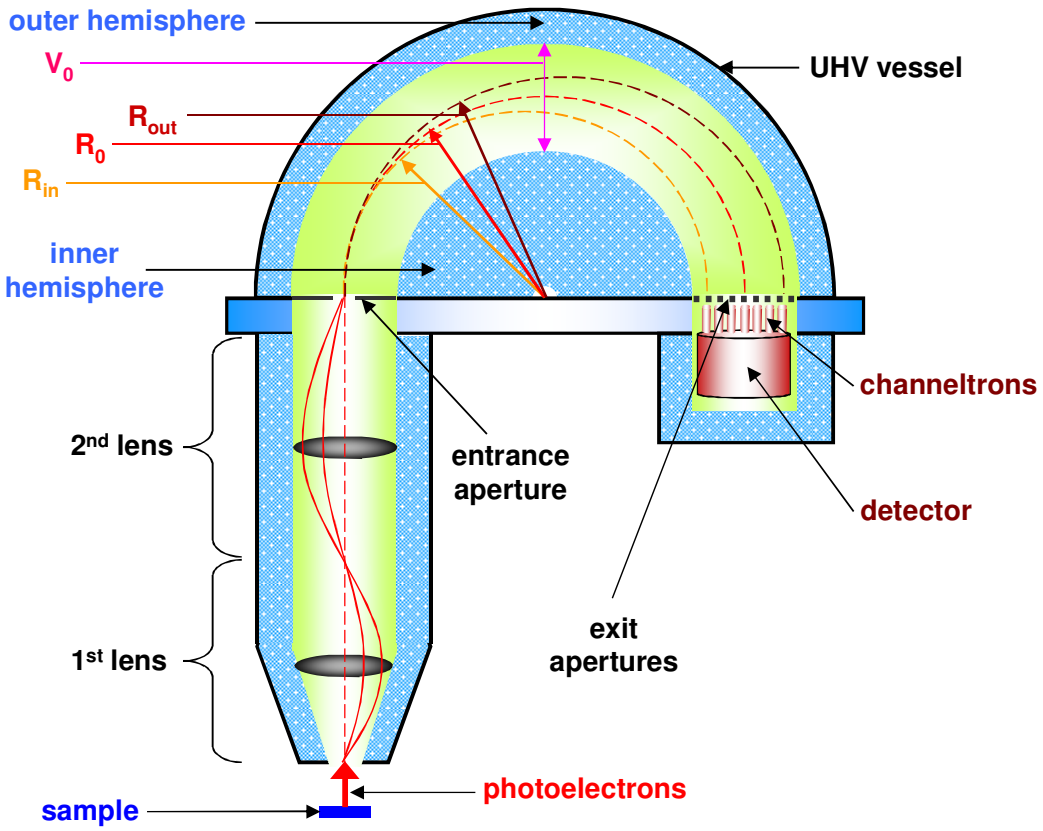

Figure 2.14 Schematic details of the hemispherical electron energy analyzer. Photoelectrons entering the instrument pass through two electron lenses and the entrance aperture. When they are in the hemispherical zone, they follow a circular path and arrive at the 7-channel channeltron array where they are detected. Each channel measures a slightly different trajectory from the others corresponding to a specific kinetic energy.

There is a set of variable slits at the entrance of the hemispherical analyzer, which adjust the transmission characteristics such as the number of photoelectrons and the energy resolution. The potential difference V_0 between the inner and the outer hemispheres of the analyzer is responsible for defining the radius of the circular photoelectron trajectories between the two hemispheres. Photoelectrons traveling between the hemispheres with an average energy 'eV_0' follow slightly different trajectories between the entrance and the exit apertures according to their kinetic energy dispersion. The 7-channel channeltron detector collects these arriving photoelectrons according to their energy. The size of the exit slit is also variable. Wide (narrow) slits provide coarse (fine) energy resolution with correspondingly high (low) photoemission signal intensity. The photoemission current within the energy window of a specific size slit is recorded as a function of energy with respect to E_F. The scanning of photoelectron energies to obtain photoemission spectra is accomplished by holding the pass energy fixed and varying the retarding voltage within the lens system to match the incoming electron kinetic energy to the pass energy. The matching occurs through a potential difference between the adjacent cylindrical electrodes within the lens system. Usually, we combine the spectra from the seven channels to obtain a combined photoemission spectrum, which describes the overall energy distribution of the photoelectrons.

The energy resolution of the analyzer can be estimated from [88]

$$\Delta E = E_p\left(\frac{d}{2R_0} + \alpha^2\right), \qquad [2.36]$$

where 'E_p' is typically 5 eV, 'd' is the width of the entrance slit (we usually use a circular aperture with 2 mm diameter), and 'α' is the half-acceptance angle for the incoming photoelectrons in radians (we generally use the 'Low Magnification' mode with $\alpha \approx 1^o = \pi/180$) [78]. Under these conditions, an energy resolution of less than or equal to 20 meV is attainable [89]. This is considerably smaller than the transform limited width of a ~10 fs duration excitation laser pulse. As equation [2.36] implies, our analyzer is operated in the 'Constant Analyzer Energy' (CAE) mode, which uses a fixed pass energy.

2.2.3 Detection of Photoelectrons

To obtain the highest sensitivity, it is necessary to count single electrons. Therefore, we use an array of seven channeltron detectors, with dedicated counting electronics for each channel. According to the sketch in Fig. 2.15, channeltron detectors multiply the electron current triggered by single electrons hitting their entrance (cathode) surface. The channeltrons consist of hollow, ceramic tubes that are curved. Because a bias of 2–3 kV is applied across the channeltron, the electrons are accelerated toward the anode. As electrons travel down the tube, they scatter many times along their trajectories to the anode. Each time they impinge on the ceramic surface, they generate multiple secondary electrons. Through this multiplication process one electron is able to produce a pulse of $10^7 - 10^8$ electrons, which are collected at the anode.

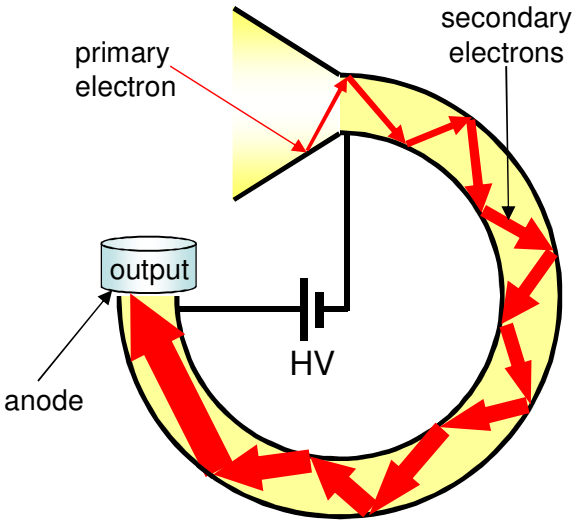

Figure 2.15 Amplification of a single photoelectron arriving at the entrance of a channeltron.

2.3 Acquiring and Recording the Photoemission Data

2.3.1 Energy-Resolved Photoemission Experiments

The photoelectron counts collected at the channeltron 'output' (Fig. 2.15) are sent to the data acquisition electronics depicted in Fig. 2.16. The electronics transform the analog electronic signals from the channeltrons into digital optical pulses, which serve as digital inputs to a digital acquisition card. The first component in the device ('input protection') employs a capacitor to isolate the high voltage (about 2-3 kV) applied across the channeltron and transmits to a 'wideband pulse amplifier' to be amplified. The signal exiting the amplifier has pulses of $0.3-1.3$ V amplitude and approximately 25 ns duration; and sent to a 'discriminator', a threshold control device, which is set to accept signals at or above a certain voltage (50 mV in our case) [90,91]. This voltage is set to reject low-intensity pulses generated as noise that do not

carry information on photoelectron counts. Next, the pulse signal is converted to a digital signal and sent to a 'high-speed comparator', which detects the pulses above the preset threshold. Then, the pulse passes through the 'dead time control unit', where its width is set to 35 ns and the dead time between pulses to 70 ns. This is regulated by external parameters. Afterwards, the pulses coming from the dead time control unit are transmitted to the 'pulse counter' where a digital acquisition card receives the signal via fiber-optic cables and counts the number of digital pulse events in a data acquisition cycle. When the next signal arrives, the computer clears the memory and starts a new cycle. This procedure continues during data acquisition and the computer compiles the data.

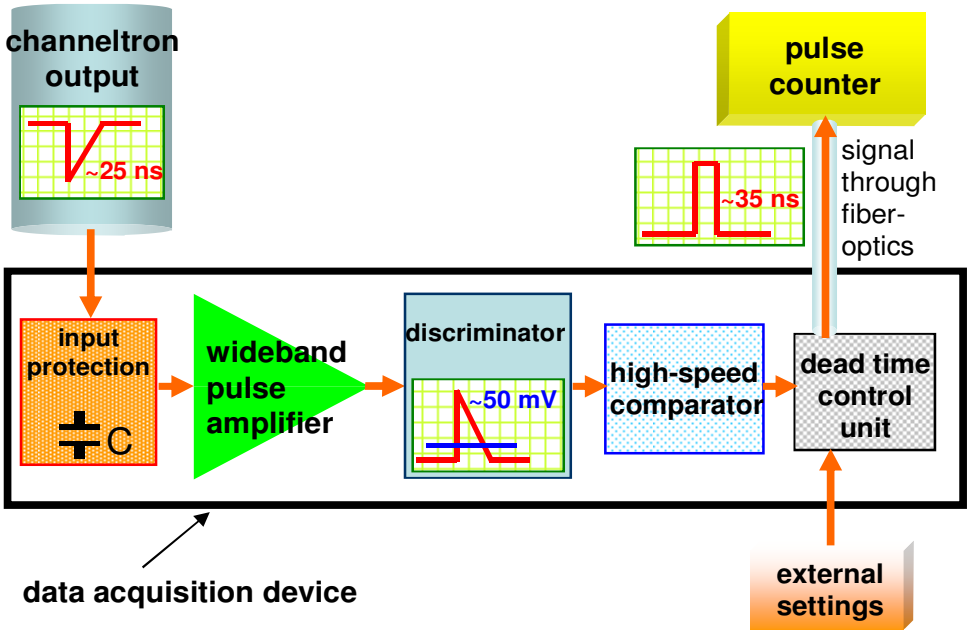

Figure 2.16 Electronics employed to acquire the photoemission counts.

The 7-channel channeltron introduced in the preceding section receives photoelectrons at slightly different kinetic energies (with intervals of 0.1 eV in our default mode). The signals coming from each channel are collected, counted and processed separately. One has the freedom to

display photoemission spectra of all seven channels separately or as a sum of component spectra. Photoemission spectra belonging to a Ag(111) surface are presented just the way they are recorded, when seven channels are separated (top) and combined (bottom) in Fig. 2.17.

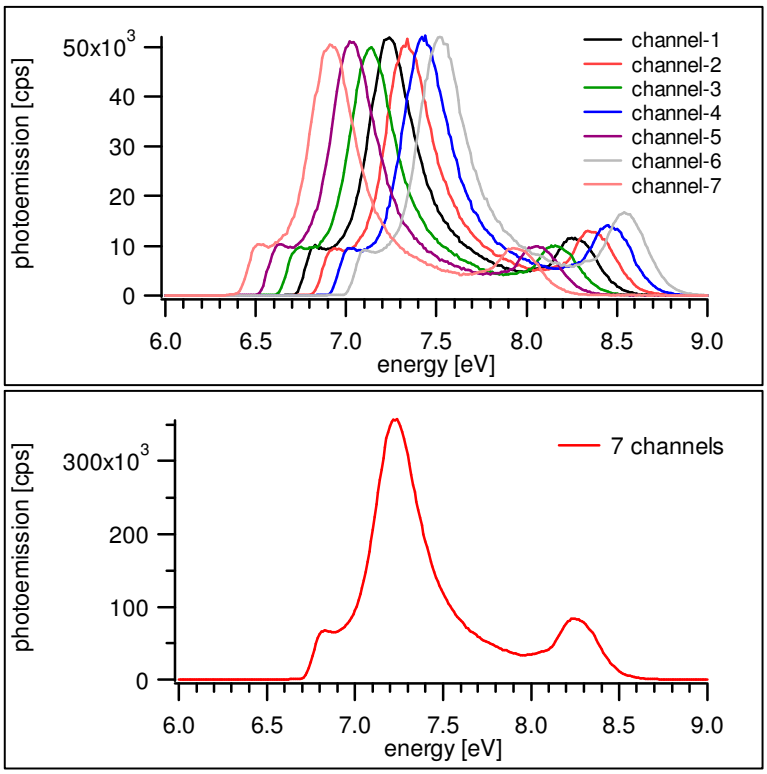

Figure 2.17 Photoemission spectra of a Ag(111) surface, when seven channeltron channels are recorded separately (top) and combined into a single spectrum (bottom). The energy axis is incremented by 2 V because of the applied bias voltage.

2.3.2 Time-Resolved Photoemission Experiments

In addition to energy-resolved 2PP experiments, we also carry out TR2PP measurements, where we measure the photoemission current at well-defined energies as a function of the time delay between identical pump and probe laser pulses.

To scan the time delay with MZI, the control computer for the scanning and data acquisition in this mode sends a signal via the GPIB board to the function generator to produce a 'sawtooth' output waveform, as seen in Fig. 2.18 [78]. The waveform is first processed with a band-pass filter to remove the high frequency components associated with the digital waveform generation, and then it is sent to the piezoelectric actuator control electronics to be amplified. The amplified signal causes the piezoelectric actuator to expand, and thereby scan the delay. The scan waveform is continuously monitored by an oscilloscope during the experiment. The oscillation of the mirror position within the MZI by ~60 μm scans the time delay by ~400 fs at a 1.33 Hz repetition frequency (see section 2.1.3 for how the MZI functions). The data acquisition is synchronized with the scanning of the mirror stage. The calibration and control of the MZI scanning was accomplished with interference fringes between the pump and probe pulses that were measured after transmission through the monochromator. As discussed before, the MZI has two output beams, one of which is directed into the UHV chamber to probe the sample, while the other one is sent to the monochromator. The monochromator selects the wavelength of light within the laser pulse (typically 400 nm), which is monitored with a photodiode.

The interference fringes created by the interference between the pump and probe pulses and received by the photodiode are transmitted to the control settings box #1, upon a command from the computer to the A/D-D/A boards. The analog fringe signal is digitized and saved for the subsequent linearization and calibration of the time axis. This is necessary because the driving waveform is nonlinear with time and the piezo-driven motion is nonlinear with respect to the applied voltage. The digitized fringes also provide a reference for the phase of the photoemission

signals. The A/D-D/A board reads the photoemission counts for each of the seven channels coherently with the scanning. We obtain I2PC measurements of 2PP signal, by adding a preset number of scans with each data point being acquired at a constant relative delay. Interference fringes of pump and probe pulses are utilized to measure the actual response of the piezo-driven motion from scan-to-scan. Slow drift in the scanning with respect to the data acquisition signal can be compensated by feeding a voltage to the fine tuning piezo in Fig. 2.2. Because we are able to synchronously monitor and control interference fringes by an oscilloscope and record the 2PP signal as a function of pump-probe delay, we can acquire accurate information on the polarization and population dynamics in the sub-10 fs regime. Since all seven channels can be synchronously employed during a measurement, it is possible to compare the photoexcitation dynamics of a surface under identical conditions but at different energies.

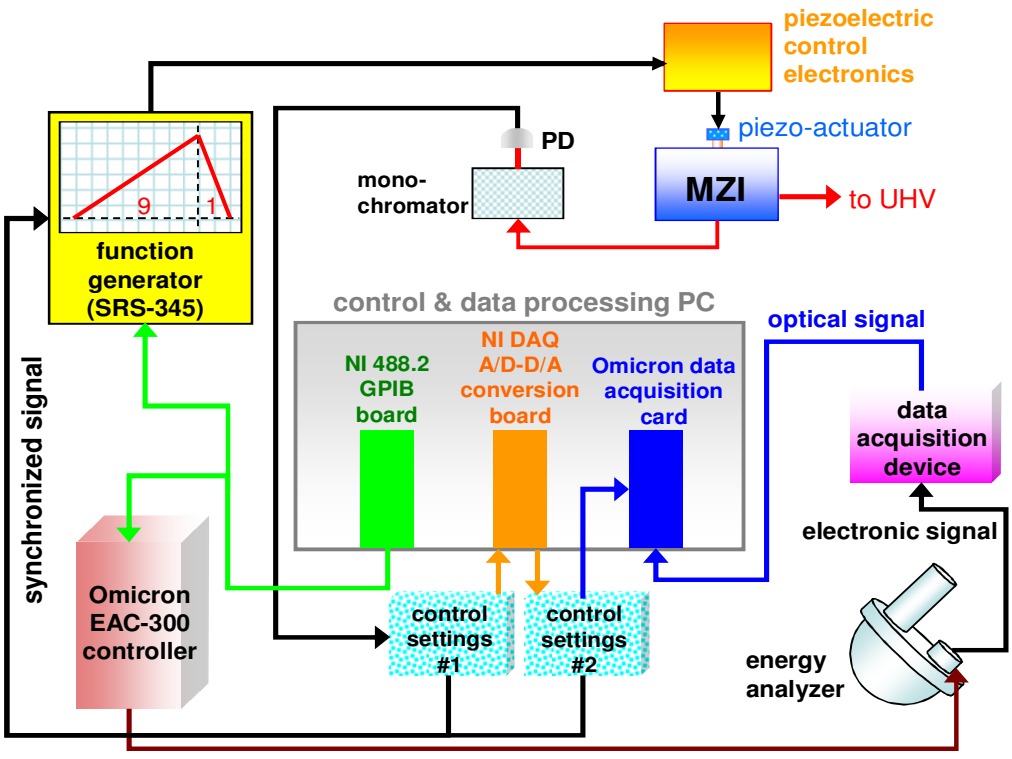

Figure 2.18 The experimental arrangement for the TR2PP measurements, including the MZI and various electronics to control the experiment, and acquire and process the data. The function and components of the 'data acquisition device' (pink box) are mentioned in section 2.3.1 and displayed in Fig. 2.16.

Chapter-3

Two-Photon Photoemission Techniques and Applications

As was introduced in Chapter-1, 2PP is a powerful and versatile technique that enables investigation of unoccupied electronic states between E_F and E_{vac} of a metal or a semiconductor. Photoelectrons ejected from solid surfaces can be detected and analyzed in terms of their energy, angular distribution, and pump-probe delay. The first section of this chapter introduces the angle-resolved 2PP technique, which is employed in Chapter-4.2 and 5.2; the second section is devoted to discussing time-resolved aspects of 2PP, which is the focus of Chapter-6.

3.1 Angle-Resolved Two-Photon Photoemission

Similar to photoemission processes involving one photon, angle-resolved photoemission spectroscopy (ARPES) probes the occupied and unoccupied states of solids and solid surfaces as a function of parallel momentum ($\mathbf{k}_{\|}$) of photoemitted electrons. ARPES is a direct experimental method to resolve the electronic distribution, or more precisely, the density of single particle electronic excitations in the momentum space of solids [92]. By measurement and analysis of band dispersions, it is possible to determine the effective carrier mass. ARPES is also used to map

Fermi surfaces of solids [93]. For localized states, which are nondispersive, ARPES can provide information on the symmetry of the electronic state from which the electron is excited [94]. As discussed in Chapter-1.4, 2PP can provide the same information on the unoccupied states of solid surfaces in addition to the initially occupied states.

In order to observe the dispersions of the occupied and unoccupied states of clean and alkali atom covered noble metal surfaces, we performed angle-resolved two-photon photoemission (AR2PP) [95]. We determine the electronic band dispersion (E_{kin} versus $k_{\parallel}$) by recording the kinetic energy as a function of the emission angle θ along a particular crystal symmetry direction. Then the angle-dependence can be converted to $k_{\parallel}$ by

$$k_{\parallel} = \frac{\sqrt{2m_e E_{kin}}}{\hbar} \sin\theta \,. \qquad [3.1]$$

In general, the band dispersion is a parabolic function between energy and momentum

$$E_{kin} = E_{min} + \frac{\hbar^2 k_{\parallel}^2}{m_{eff}}, \qquad [3.2]$$

where E_{min} is the energy at the band minimum ($k_{\parallel} = 0$) and m_{eff} is the effective mass of electron.

In this work, AR2PP is employed to study angle-dependent dispersion of the transition between lower and upper sp-bands of bare Ag(111) surface (Chapter-4.2), and the angular distribution of photoemission of nondispersive alkali-induced states of alkali/Cu(111) and alkali/Ag(111) chemisorptions systems (Chapter-5.2). The experimental set-up that we used is presented in Fig. 3.1, where the angle between the incident laser beam and detector is fixed at 45°. By rotating the

manipulator angle manually, we obtain angle-resolved photoemission spectra. The rotation of the sample simultaneously changes the incidence and photoemission angles.

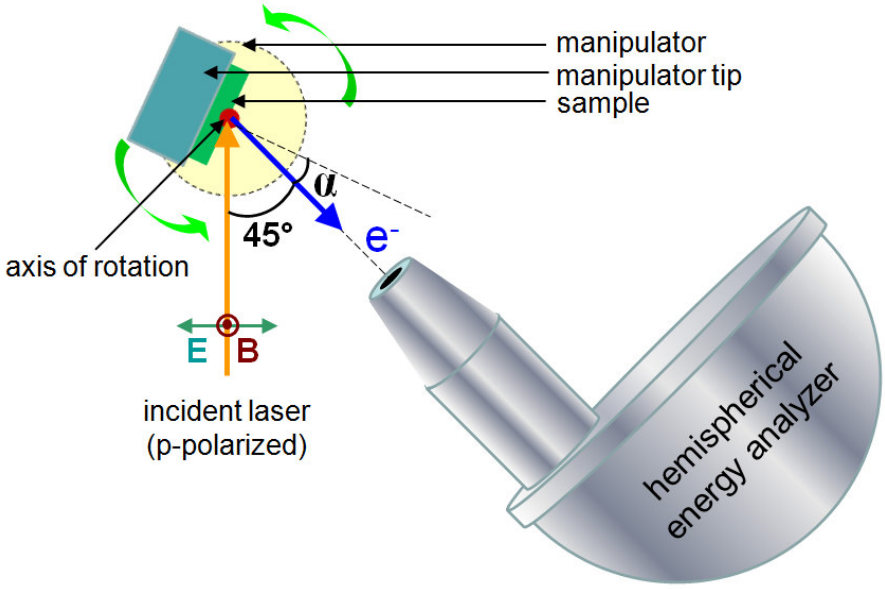

Figure 3.1 The top view of the experimental set-up for AR2PP. The angle between the incident laser beam and the hemispherical energy analyzer is fixed at 45°, whereas the manipulator is rotated manually about the axis of rotation (red dot). The angle 'α' is the variable in this measurement.

3.2 Time-Resolved Two-Photon Photoemission

In this section, fundamental physical processes occurring in TR2PP will be addressed. This technique has become the method of choice for investigating the energy- and momentum-resolved ultrafast charge carrier dynamics in solids and solid surfaces [62,96]. It enables us to study the time-resolved electron dynamics of alkali atom adsorbates on noble metal surfaces following the transient excitation of their otherwise unoccupied states. In short, TR2PP is the most suitable

technique to study the excited state electron dynamics, because it combines energy and momentum sensitivity with a time resolution that is limited only by the laser pulse duration.

3.2.1 Dynamics of Photoexcited States

In metals, conduction band electrons interact among themselves and with the ionic lattice [97]. Studying these electronic interactions with surface sensitivity elucidates of many fundamental condensed matter scattering processes and surface photochemistry. These processes may excite elementary excitations such as quantized lattice vibrations (phonons), collective electronic excitations (plasmons), and electron–hole pairs [98].

Photon absorption in metals results in creation of excited or 'hot' electrons above E_F, and 'hot' holes below E_F. Fig. 3.2 describes the electronic structure of both the occupied and unoccupied states for a typical metal surface. In a 2PP process, electrons are photoexcited to populate the originally unoccupied states, creating a hot electron population [78]. An intermediate state (E_{int}) can be populated from an initial state $E_i (= E_{int} - h\nu_1)$ by the pump pulse, and it can be successively excited to a final state $E_f (= E_{int} + h\nu_2)$ by the same pump pulse or a delayed probe pulse. If the final state electrons are excited above E_{vac}, they can be photoemitted, detected and analyzed with respect to their kinetic energy $E_{kin} (= E_f - E_{vac})$. A typical 2PP spectrum consists of a plot of the photoelectron current as a function of kinetic energy of the photoelectrons; it contains information on the joint density of states of the occupied and unoccupied states.

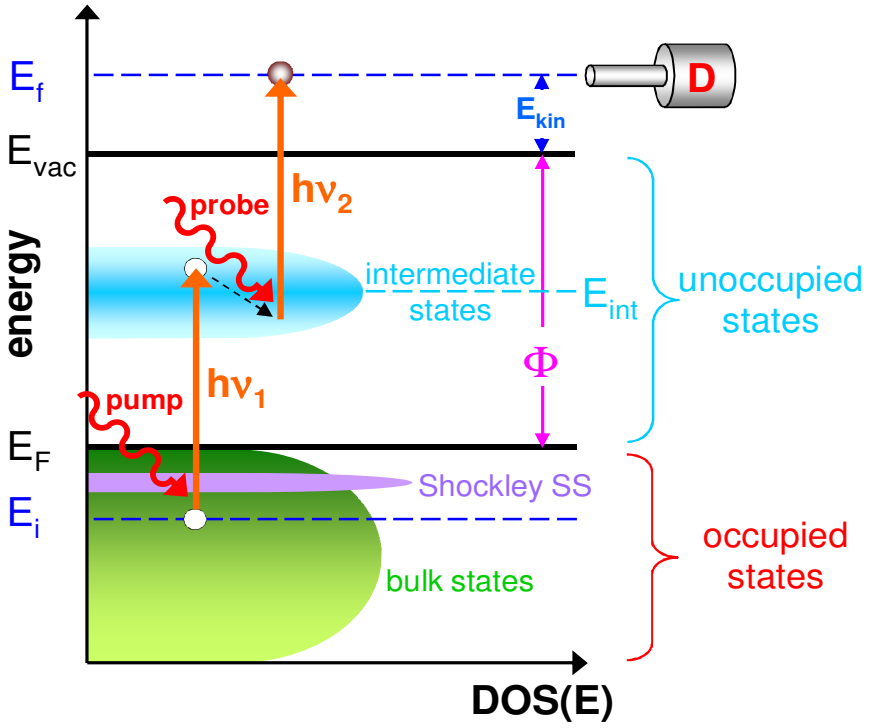

Figure 3.2 Photoexcitation scheme in a 2PP process from the occupied bulk and surface states below E_F to a final state above E_{vac} via initially unoccupied intermediate states. The horizontal axis describes the density of the occupied and unoccupied states as a function of energy.

When electrons are excited by a pump pulse to a level between E_F and E_{vac}, they tend to decay back to their initial energy levels, unless they are excited by a probe pulse which could lead to their photoemission. The lifetime of excited electrons is determined principally by electron-electron scattering, and to a lesser extent by electron-phonon scattering. The apparent lifetime can also be affected by electron transport from the surface to the bulk [77]. Theoretical calculations and experiments in most cases concur that the lifetime of excited electrons (τ_e) in an intermediate state is inversely proportional to the square of their energy relative to E_F:

$$\tau_e \propto \frac{1}{(E - E_F)^2}. \qquad [3.3]$$

Therefore, one can infer that the higher the excited electrons are above E_F, the shorter their lifetime will be [71].

3.2.2 Quantum Mechanical Description of the Excitation Dynamics

The goal of ultrafast laser spectroscopy of solid surfaces is to describe the light–matter interactions and characterize the dynamics of elementary excitations occurring as a consequence of photon absorption [80]. We employed a semi-classical treatment involving the 'density matrix' formalism to explain the coherences and population dynamics, where the electromagnetic field acts as a classical driving force, while the matter is expressed as a restricted quantized system composed of several energy levels and a macroscopic heat bath [83]. Only the quantum system is coupled to light, but its phase coherence in strongly affected by its own coupling to the heat bath. This rendition both leads to a simple explanation of the results in terms of measurable quantities and accounts for the quantum mechanical aspects of light–matter interaction.

When the excitation pulse width is shorter than or comparable to the phase relaxation time of the excited medium and the delay between pump and probe pulses is shorter or comparable to the dynamical change of photo-induced polarization, one needs a theoretical model to formulate the temporal response of the system, which includes the 'coherent interaction' between the electromagnetic field and the coherent oscillators composing the material. The quantum system is expressed in terms of its density operator 'ρ', which is assumed to obey the 'optical Bloch equations' (OBE). This formulation is developed directly from the Schrödinger equation with a phenomenological damping term accounting for the coupling with the heat bath:

$$i\hbar\frac{d}{dt}\rho = [H_0 + H_{int}, \rho] + i\hbar\frac{d}{dt}\rho\Big|_{relax} . \qquad [3.4]$$

Here, H_0 is the 'unperturbed Hamiltonian' of the electronic system and H_{int} is the Hamiltonian of the 'coherent dipolar interaction' with the electromagnetic field, which acts as a perturbation. The last term is responsible for the 'relaxation' of the excited medium via the coupling with the heat bath.

Fig. 3.3 shows the excitation scheme for a two-photon excitation in a metallic system. Although this three-level system is an oversimplification to describe a metal surface [99], under some circumstances where there are specific resonances, it is approximately valid. For instance, it can describe the momentum conserving transitions between the lower and upper sp-band of Ag(111) that will be discussed in Chapter-4.1 Here, the energy level $|0\rangle$ is an occupied state below E_F that acts as the initial state of the photoexcitation process; $|1\rangle$ is an unoccupied state located between E_F and E_{vac} that acts as the transient intermediate state; and $|2\rangle$ located above E_{vac} corresponds to a free photoelectron.

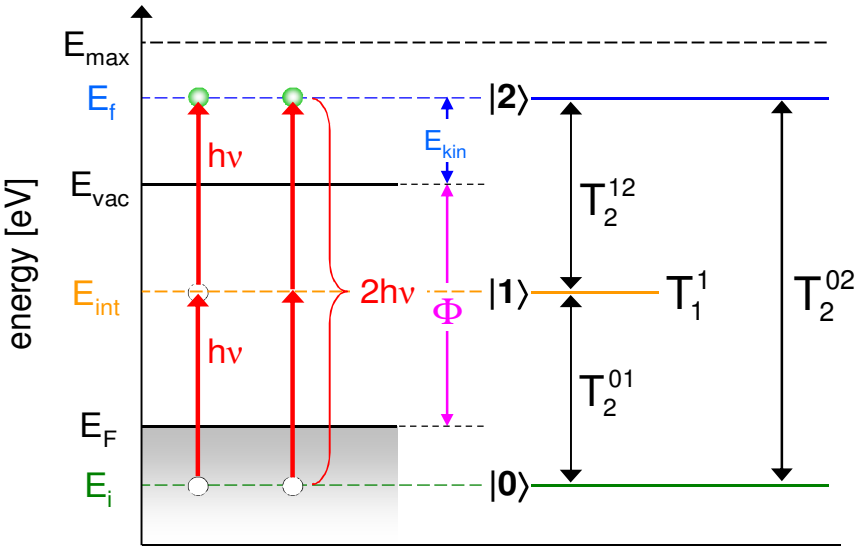

Figure 3.3 The photoexcitation scheme for a 2PP process involving three quantized states $|0\rangle$ (initial), $|1\rangle$ (intermediate), and $|2\rangle$ (final) [99]. The OBE are employed to describe the interstate couplings, population dynamics and polarization in a metal. T_1 and T_2 denote the phenomenological population and coherence times, respectively.

Consider the material as an ensemble of quantized electronic states defined by unperturbed Hamiltonian H_0 and normalized orthogonal basis vectors $|n\rangle$, such that

$$H_0|n\rangle = E_0|n\rangle = \hbar\omega_n|n\rangle . \qquad [3.5]$$

The femtosecond laser pulse introduces a time-dependent interaction that couples the eigenstates of the system:

$$H_{int}(t) = -\boldsymbol{\mu}\cdot\mathbf{E} = -e\cdot d\cdot E_{\omega_1}(t) = -e\cdot d\cdot E(t)\cos(\omega_1 t) . \qquad [3.6]$$

The new total time-dependent Hamiltonian will be $H(t) = H_0 + H_{int}(t)$, and the new wave function can be written in terms of the basis functions of the unperturbed system

$$|\psi(t)\rangle = \sum_n \exp(-in\omega_1 t)c_n(t)|n\rangle , \qquad [3.7]$$

where ω_l is the central laser frequency. After solving the time-dependent Schrödinger equation

$$H(t)|\psi(t)\rangle = i\hbar\frac{\partial}{\partial t}|\psi(t)\rangle , \qquad [3.8]$$

one obtains

$$\begin{aligned}&\sum_n\left[\left(c_n(t)(-in\omega_1)+\frac{\partial}{\partial t}c_n(t)\right)\exp(-in\omega_1 t)\right]|n\rangle \\ &= \frac{-i}{\hbar}\sum_n\left[\left(c_n(t)(H_0+H_{int}(t))\right)\exp(-in\omega_1 t)\right]|n\rangle\end{aligned} . \qquad [3.9]$$

If this is multiplied by the complex conjugate of the basis vector $|n\rangle$ and integrated over the spatial coordinates, one gets

$$\frac{\partial}{\partial t} c_m = -i(\omega_m - m\omega_1)c_m - \frac{i}{\hbar}\sum_n H_{int}^{mn} \exp[i(m-n)\omega_1 t]c_n \,, \qquad [3.10]$$

where the matrix element is $H_{int}^{mn} = \langle m^* | H_{int}(t) | n \rangle$.

The density operator 'ρ' is defined in terms of the occupation coefficients by $\rho_{mn} = c_m^* c_n$. According to this formulation, ρ_{mm} signifies the population of the level 'm', and the off-diagonal elements ρ_{mn} represent the coherences between states 'm' and 'n'. To describe the interdependence of the density matrix elements, one has to define the population decay times T_1^1 (the population decay at level $|1\rangle$) and T_1^2 (the population decay at level $|2\rangle$); and the first order decoherence times T_2^{01} (between states $|0\rangle$ and $|1\rangle$) and T_2^{12} (between states $|1\rangle$ and $|2\rangle$); and the second order decoherence time T_2^{02} (between states $|0\rangle$ and $|2\rangle$). Using the derivative of the product of the occupation coefficients, $\frac{\partial}{\partial t}\left(c_m(t)^* \cdot c_n(t)\right)$, and the aforementioned decay and decoherence times, one can construct the OBE to describe the temporal evolution of populations and polarizations in a three-level quantum system with a set of nine first-order coupled differential equations [69]. The corresponding density matrix can be written as

$$\rho(t) = \begin{bmatrix} \rho_{00} & \rho_{01} & \rho_{02} \\ \rho_{10} & \rho_{11} & \rho_{12} \\ \rho_{20} & \rho_{21} & \rho_{22} \end{bmatrix} = \begin{bmatrix} c_0^* c_0 & c_0^* c_1 & c_0^* c_2 \\ c_1^* c_0 & c_1^* c_1 & c_1^* c_2 \\ c_2^* c_0 & c_2^* c_1 & c_2^* c_2 \end{bmatrix}. \qquad [3.11]$$

Such a scheme will be employed in Chapter-4.1 to model an actual 2PP process on bare Ag(111) surface, and the OBE will be derived explicitly by means of the equations presented in this section.

We employ the TR2PP technique to measure the current of free photoelectrons in the final state at a specific energy. As mentioned above, we measure experimentally the density matrix element of the final state, $\rho_{22}(t,\tau)$, integrated over the pump–probe cycle. Because the laser pulse-to-pulse (T_{p-p}) time difference of 11 ns is much longer than the population and coherence times, one can express the 2PP signal by

$$I_{2PP}(\tau) = \int_0^{\infty} \rho_{22}(t,\tau)dt \cong \int_0^{T_{p\text{-}p}} \rho_{22}(t,\tau)dt \,. \qquad [3.12]$$

The integral in equation [3.12] is what is measured in a typical 2PP experiment.

3.2.3 Evaluation of Time-Resolved Measurements

I2PC measurements present the nontrivial task of extracting the phase and population decay time constants. If both are much shorter than the laser pulse, the I2PC measurement resembles an interferometric autocorrelation (IAC) measured for a medium with an instantaneous response, as discussed in Chapter-2.1.4 [100]. If the decay times are finite, I2PC measurements enable us to extract direct information on the excited electron population and polarization dynamics [71]. The pump laser pulse interacting with the sample surface creates both linear and nonlinear polarization components, which for resonant excitation oscillate at the excitation frequency ω and its higher harmonics [100]. The interference signal between the pump and probe excited

coherences in I2PC scans oscillates at ω and 2ω frequencies. In addition, the excitation process builds up an incoherent population in the intermediate state through various dephasing processes. The different contributions to the I2PC scan can be decomposed approximately by Fourier analysis into 1ω and 2ω components, and a phase averaged component (abbreviated as '0ω'), which evolves on a much longer time scale than the phase of the excitation pulse. The delay-dependent envelopes of these three components can be computed by Fourier transforming the experimental I2PC data over each optical cycle as given by

$$I_{0\omega}(\tau) = \frac{\lambda}{c}\int_{\tau-\lambda/2c}^{\tau+\lambda/2c} I_{I2PC}(t)dt\,, \qquad [3.13a]$$

$$I_{1\omega}(\tau) = \frac{2\lambda}{c}\left[\left(\int_{\tau-\lambda/2c}^{\tau+\lambda/2c} I_{I2PC}(t)\cos(\omega_1 t)dt\right)^2 + \left(\int_{\tau-\lambda/2c}^{\tau+\lambda/2c} I_{I2PC}(t)\sin(\omega_1 t)dt\right)^2\right]^{1/2}, \qquad [3.13b]$$

$$I_{2\omega}(\tau) = \frac{4\lambda}{c}\left[\left(\int_{\tau-\lambda/4c}^{\tau+\lambda/4c} I_{I2PC}(t)\cos(2\omega_1 t)dt\right)^2 + \left(\int_{\tau-\lambda/4c}^{\tau+\lambda/4c} I_{I2PC}(t)\sin(2\omega_1 t)dt\right)^2\right]^{1/2}. \qquad [3.13c]$$

Fig. 3.4 exhibits an experimental I2PC trace for K/Cu(111) and its decomposition into the 0ω (blue), 1ω (red), and 2ω (green) components: the measurement is for 2.1 eV intermediate state energy and at 17° off-normal emission direction.

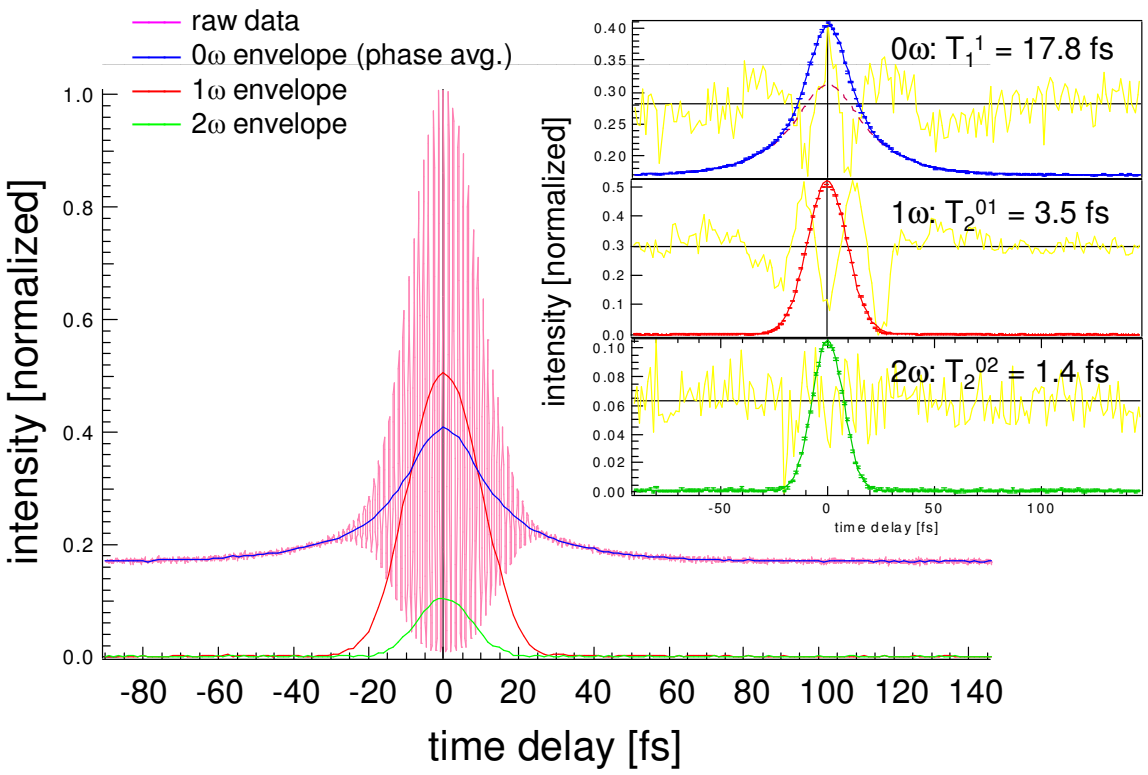

Figure 3.4 Raw experimental I2PC data for K adsorbed on Cu(111) surface (large image) together with 0ω, 1ω and 2ω component envelopes (inset). The yellow lines show residuals between the observed (markers) and simulated envelopes (lines). The program for this analysis was developed by Heberle and Nessler [101,100].

The phase and energy relaxation time constants of the charge carriers within the sample and the pulse width of the excitation laser pulse govern the temporal profiles of these components. Assuming that the material response were instantaneous, the electric field of the excitation pulse would have a Gaussian shape of FWHM of T_p, i.e., $E(t) \propto \exp\left(-4\ln 2\left(t/T_p\right)^2\right)$, then the I2PC signal could be decomposed to 0ω, 1ω and 2ω envelopes [71]:

$$I_{0\omega}(\tau) \propto \exp\left(-4\ln 2\left(\tau/T_p\right)^2\right), \qquad [3.14a]$$

$$I_{1\omega}(\tau) \propto \exp\left(-3\ln 2\left(\tau/T_p\right)^2\right), \qquad [3.14b]$$

$$I_{2\omega}(\tau) \propto \exp\left(-4\ln 2\left(\tau/T_p\right)^2\right). \qquad [3.14c]$$

Here, $I_{2\omega}(\tau)$ gives the coherent dephasing time T_2^{02} between states $|0\rangle$ and $|2\rangle$; $I_{1\omega}(\tau)$ gives the dephasing time T_2^{01} between states $|0\rangle$ and $|1\rangle$; and the phase averaged component $I_{0\omega}(\tau)$ gives both the coherent polarization and decay time T_2^{01} and the incoherent population decay T_1^1 of the intermediate state $|1\rangle$ [78].

Chapter-4

Simulation of Two-Photon Photoemission on Ag(111)

This chapter presents 2PP spectroscopic studies of bare Ag(111) surface. This surface is characterized by simple electronic structure, which makes 2PP spectra amenable to theoretical analysis. Furthermore, it is a substrate for chemisorption of alkali atoms, therefore, knowing the clean surface properties is a prerequisite for more advanced studies of adsorbate induced electronic states. Section 4.1 presents experimental 2PP spectra of Ag(111) surface excited with 3.1 eV light and its simulation based on the bulk band structure of Ag(111), and the optical Bloch equation simulation of the 2PP excitation process [84]. Section 4.2 presents angle-resolved 1PP and 2PP spectra of the same surface and the computation of the angle-dependent dispersion and 2PP intensities of the sp-band transition.

4.1 Simulation of Two-Photon Photoemission Spectra

The 2PP spectrum of Ag(111) is a good choice for theoretical modeling, because Miller et al. have developed a corresponding model for the 1PP spectrum that describes quantitatively one-photon transitions between the same initial and final states [102,103]. Their model was based on

calculating the optical transition matrix elements using the realistic bulk wave functions and the Fermi's golden rule approximation, and accounting for the interference between the bulk and surface photoemission channels. Because 2PP spectra have never been interpreted quantitatively based on the known electronic structure of metals, we simulate the 2PP spectra of Ag(111), by taking Miller's model [102,103] for 1PP as the starting point for the simulation.

4.1.1 Fundamental Considerations

Besides coupling of the initial and final states as in 1PP spectroscopy, 2PP spectroscopy involves passage through the resonant or virtual intermediate states. Not only does it provide information on the densities of the occupied initial and the unoccupied intermediate states, but 2PP spectra also reveal information on the population dynamics in the transient intermediate states and on different excitation pathways. The intermediate state dynamics are affected by decoherence of the direct transitions, excitation through indirect pathways, such as the Drude absorption, and relaxation phenomena involving electron-electron scattering [84]. These dynamical aspects influence the spectral linewidths and other aspects of photoelectron distributions. Because many dynamical aspects are difficult to evaluate, a quantitative simulation of 2PP spectra had not been reported prior to our simulation for Ag(111).

Earlier investigations on 2PP spectral distributions from metal surfaces mostly concentrated on photoemission involving surface states, such as image potential states [104] and adsorbate-induced states [55,105], which are localized in energy, because surface normal momentum is undefined or conserved in the photoemission process [106, 107]. Unlike surface states with localized energy,

photoemission from bulk states involves delocalized bands with surface normal dispersion that can be calculated or determined by experiment. The transitions are not localized in energy because perpendicular momentum is not conserved in photoemission.

The 2PP process within the bulk of Ag(111) with 3.1 eV photons takes place across the L-projected band gap from the (occupied) lower sp-band (L_{sp}) to the (unoccupied) upper sp-band (U_{sp}), i.e., $U_{sp} \leftarrow L_{sp}$, as shown in Fig. 4.1. The only unoccupied intermediate states of the correct symmetry to be coupled by p-polarized light and with the same parallel momentum as the initial states, which are available for photoexcitation in the two-step process, are those of the upper sp-band [84]. The minimum photon energy to excite across the band gap is 4.16 eV, while the minimum for photoemission through a vertical transition from the lower sp-band is 5.40 eV. Clearly, the 3.10 eV energy is insufficient for a resonant transition between the lower and upper sp-bands along the ΓL-direction, and for that matter, elsewhere in the **k**-space of silver; therefore, the coherent 2PP process must occur through the virtual excitation of the upper sp-band [108].

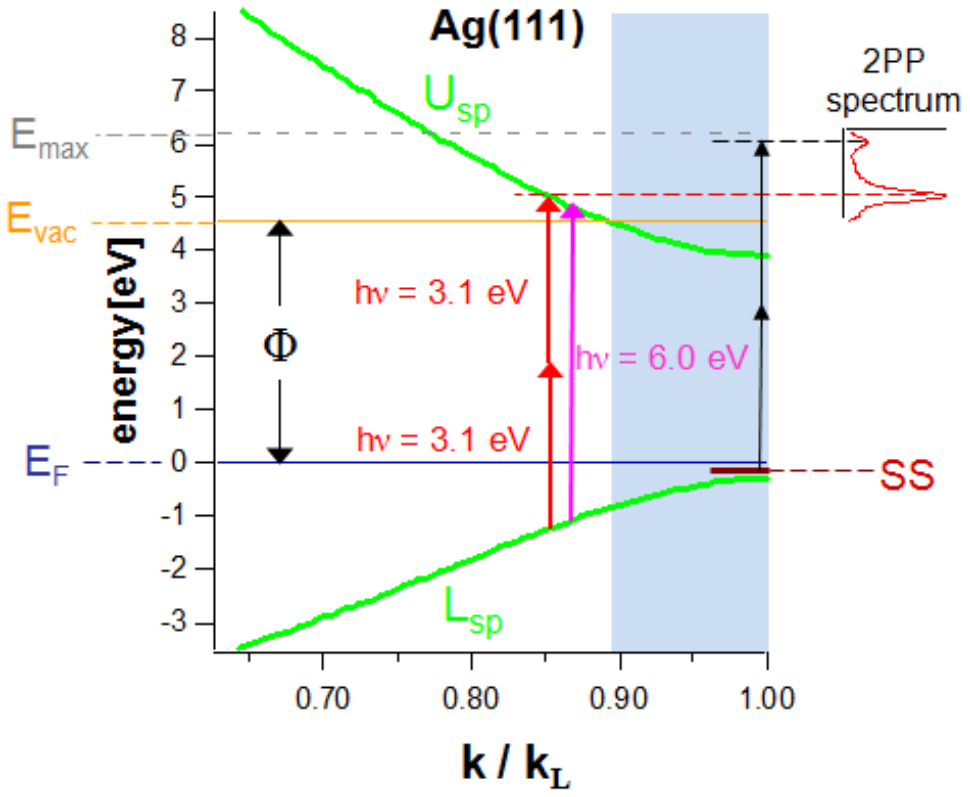

Figure 4.1 Dispersion of the lower (occupied) and upper sp-bands (unoccupied; abbreviated as U_{sp} and L_{sp}, respectively) of Ag along the surface normal (ΓL-direction) and possible resonant excitation paths for 1PP and 2PP processes with photon energies of 6.0 eV and 3.1 eV, respectively. The wave number on the horizontal axis is normalized so that the Brillouin zone boundary corresponds to $k/k_L = 1$, at which point the band gap is 4.16 eV. The Shockley surface state (SS) is located 63 meV below E_F [1,3], and does not disperse along the ΓL-direction. Electrons excited to the upper sp-band below E_{vac} ('blue' region) cannot escape into vacuum.

4.1.2 Experimental Aspects and Implementation

2PP measurements were performed on a single crystal Ag sample that was aligned better than 0.5° along the [111] crystallographic direction and polished to reduce roughness to less than 0.05

μm. Before measuring 2PP spectra, the crystal sample was cleaned by successive cycles of Ar^+ sputtering (at kinetic energy of 500–600 eV) and high-temperature annealing (at 700–750 K for 45 minutes) under strict UHV conditions (i.e., 10^{-10} mbar or lower) [84]. The number of cycles required for fresh samples was 30 or more. The overall surface quality of the sample was judged by two criteria: (1) at the appearance of the LEED pattern and (2) the appearance of the 2PP spectrum, i.e., minimum inelastic background, maximum work function, and sharp and intense Shockley surface state. The measurements were performed for sample temperatures between 100–500 K. The sample temperature was controlled by electron bombardment heating and liquid nitrogen cooling.

The photoemission experiments were performed with the femtosecond laser excitation source that was introduced in Chapter-2. The 3.1 eV excitation pulses had about 10 fs temporal and corresponding 200 meV spectral widths. The p-polarized light was incident on the sample at 45° angle. In addition, we performed 1PP experiments with the fourth harmonic of the Ti:Sapphire laser. To generate the fourth harmonic, the second harmonic was frequency doubled in another BBO crystal (of 100 μm thickness). The phase-matching of the BBO crystal permitted doubling of only the low energy portion of the second harmonic pulse; therefore, the fourth harmonic had a narrower spectral bandwidth centered around 6.0 eV photon energy.

4.1.3 Experimental Results

Typical, experimentally measured 1PP and 2PP spectra of bare Ag(111) surface with excitation photon energies of 6.0 eV and 3.1 eV are displayed in Fig. 4.2. The surface normal

photoemission spectra are recorded at ~100 K temperature. The spectra show two common features: (1) the occupied Shockley surface state (SS) [109], which is located within the L-projected band gap with a binding energy of 0.063 eV below E_F (see also Fig. 4.1); and (2) the direct interband photoexcitation from the lower sp-band to the upper sp-band corresponding to the peaks located at about $1.1-1.2$ eV binding energy.

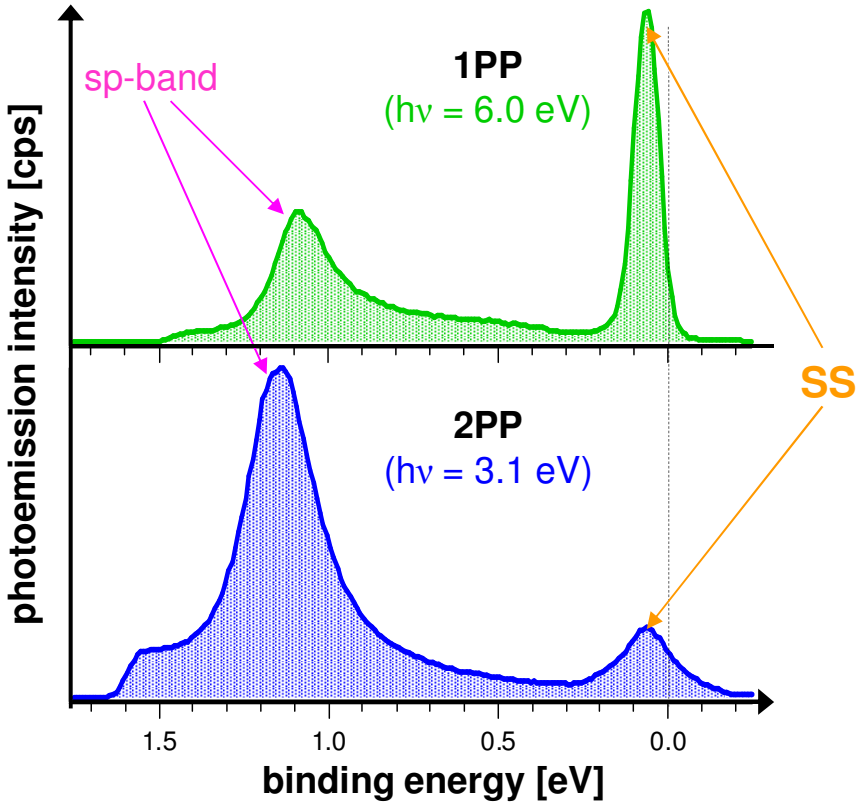

Figure 4.2 1PP (top; with $h\nu = 6.0$ eV) and 2PP (bottom; with $h\nu = 3.1$ eV) spectra of clean Ag(111) surface plotted with respect to the binding energy. The peaks at about $1.1-1.2$ eV are due to the direct, resonant photoexcitation $U_{sp} \leftarrow L_{sp}$, and the peaks corresponding to 0.063 eV originate from the Shockley surface state (SS).

As mentioned earlier, the spectra reflect the broader spectral bandwidth of the second harmonic light for the 2PP measurements as compared with the fourth harmonic for the 1PP measurements. Moreover, the exact position of the sp-band peaks differ, because the gross photon energies are 2×3.1 eV and 6.0 eV for 2PP and 1PP, respectively [84], which gives rise to resonant $U_{sp} \leftarrow L_{sp}$ excitation at different perpendicular momenta. The minimum observed binding energies differ by 0.2 eV for the same reason.

Another major difference is the strong asymmetry of sp-band peak in the 1PP spectrum compared with the 2PP spectrum; the asymmetry has been ascribed to a Fano interference between the bulk and surface contributions to the overall photoemission process [102,103]. The optical transition matrix element for a photoemission process consists of two terms, which are presented in Chapter-1.3 [103],

$$\left\langle \psi_f \left| \mathbf{A} \cdot \nabla + (\nabla \cdot \mathbf{A})/2 \right| \psi_i \right\rangle \equiv M_{bulk} + M_{surface} \qquad [4.1]$$

where **A** is the vector potential. The first term in equation [4.1], M_{bulk}, for an infinitely long electron mean free path, is proportional to the momentum matrix element. The second term in equation [4.1], $M_{surface}$, is assumed to be zero unless there is a pronounced surface component associated with the photoemission, and is generally overlooked. The gauge $\nabla \cdot \mathbf{A} = 0$ is used for light propagating through a translationally invariant medium such as bulk. A nonzero divergence of the vector potential suggests the presence of longitudinal electromagnetic waves or rapidly varying transverse fields [110]. It only contributes at the surface where there is a step-like abrupt change in the dielectric function leading to a significant vector potential gradient ($\partial A_z/\partial z$), as illustrated in Fig 4.3. It contributes over an extremely short range (d) of the order of the atomic layer thickness or the length scale for electrons to screen out an external perturbation. In other

words, the surface term is related to the difference between the substrate and vacuum dielectric functions, i.e., $(\varepsilon - 1)$. Because the translational symmetry is broken along the surface normal (i.e., z-direction) [110], the surface term generates a continuum of momenta. Consequently, perpendicular momentum in photoemission is not strictly conserved, and therefore, indirect transitions can occur, producing a continuous distribution of photoelectrons. This surface-induced indirect background remains phase-correlated with the bulk contribution given by '$\mathbf{A}\cdot\nabla$'; their interference is responsible for the asymmetric Fano line shape for the direct (inter sp-band) transition peak in 1PP spectra. One notices that the line shape of the bulk sp-band feature in the 2PP spectrum exhibits hardly any asymmetry, implying that the interference between the bulk and surface components is insignificant. The weaker surface contribution is consistent with the significantly weaker Shockley surface state peak in 2PP, as compared with 1PP.

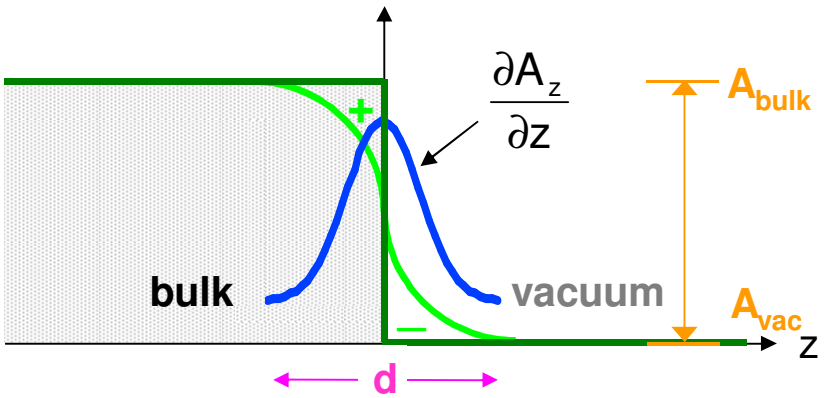

Figure 4.3 Bulk–vacuum interface: the discontinuity in the dielectric function at the surface suggests that its derivative ($\partial A_z/\partial z$) could be represented by a sharply-defined Gaussian function, when the range of the surface term 'd' is considered to be of the order of an atomic layer [103].

4.1.4 Model for Computing the Two-Photon Photoemission Spectrum of Ag(111)

4.1.4.1 Assumptions

Miller et al. modeled the 1PP spectrum of Ag(111) by employing Bloch wave functions for lower and upper sp-bands within the framework of one-dimensional 'nearly free electron model' [111]. The transition dipole matrix elements were calculated from electron wave functions consisting of the Bloch waves for a realistic surface contribution according to the one-step model of photoemission [3,15,112], where the bulk–vacuum interface was assumed to be a step potential corresponding to the work function of the Ag(111) crystal surface, as seen in Fig. 4.4. One may consider the sp-bands within the nearly free electron model, since they form delocalized states, and their crystal potential, i.e., the electrostatic potential of an ion within a periodic structured finite crystal [113,114], can be regarded as a weak perturbation. According to this model, the crystal potential varies sinusoidally along the z-direction. To simulate the 2PP spectrum, we took the same initial and final state wave functions, and we also had to formulate the intermediate state wave functions.

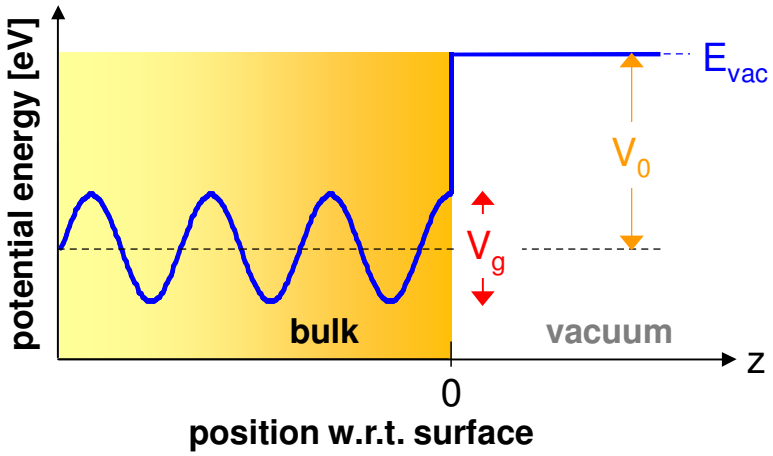

Figure 4.4 'The nearly free electron model' for a sinusoidal crystal potential (V_g) along the surface normal (z-direction). The surface ($z = 0$) is modeled as an abrupt potential step V_0 that extends from the center of V_g to E_{vac} [15].

In contrast to the 1PP simulation, the 2PP experiment employs a light source with extremely short duration (~10 fs) and the two-photon absorption process involves excitation and relaxation dynamics that also occur in the femtosecond regime; therefore, a rate equation approach is inadequate. For this reason, one needs to use the OBE (not to be confused with the Bloch wave functions for electrons in a periodic potential), which include the phase and energy relaxation terms missing in the rate equation approach [69,71,76,80,115].

4.1.4.2 Electron Wave Functions and Transition Matrix Elements

The wave function of the initial state (lower sp-band) in the bulk is composed of a Bloch wave propagating toward surface and its reflection from the surface propagating in the reverse direction with an additional reflection-induced phase shift. The phase shift is obtained quantitatively by matching the Bloch wave with the electron wave function on the vacuum side, which decays exponentially on account of an imaginary wave vector. The internal and external wave functions are matched at the 'image plane' to be continuous and differentiable at the matching point. The image plane is estimated at 2.20 a_0 (Bohr radius, $a_0 = 0.529$ Å [116]) in front of the physical interface or about half an interlayer spacing between consecutive (111)-planes; it is denoted by z_0 [117]. The wave function matching conditions are

$$\psi^{bulk}(z = z_0) = \psi^{vac}(z = z_0) \qquad [4.2]$$

$$\left.\frac{\partial}{\partial z}\psi^{bulk}(z)\right|_{z=z_0} = \left.\frac{\partial}{\partial z}\psi^{vac}(z)\right|_{z=z_0} . \qquad [4.3]$$

The initial state wave functions are given by

$$\psi_i^{bulk}(z) = \left\{Ae^{ik_i z} + Be^{i(k_i - g)z}\right\} + e^{iq}\left\{Ae^{-ik_i z} + Be^{-i(k_i - g)z}\right\}, \qquad [4.4]$$

$$\psi_i^{vac}(z) = Ce^{-k_i^{vac} z}, \qquad [4.5]$$

where $k_i^{vac} = \frac{\sqrt{2m(\Phi - E_i(k_i))}}{\hbar}$ for $\Phi - E_i(k_i) > 0$.

All of the wave functions involved in simulating the 2PP spectrum are illustrated in Fig. 4.5.

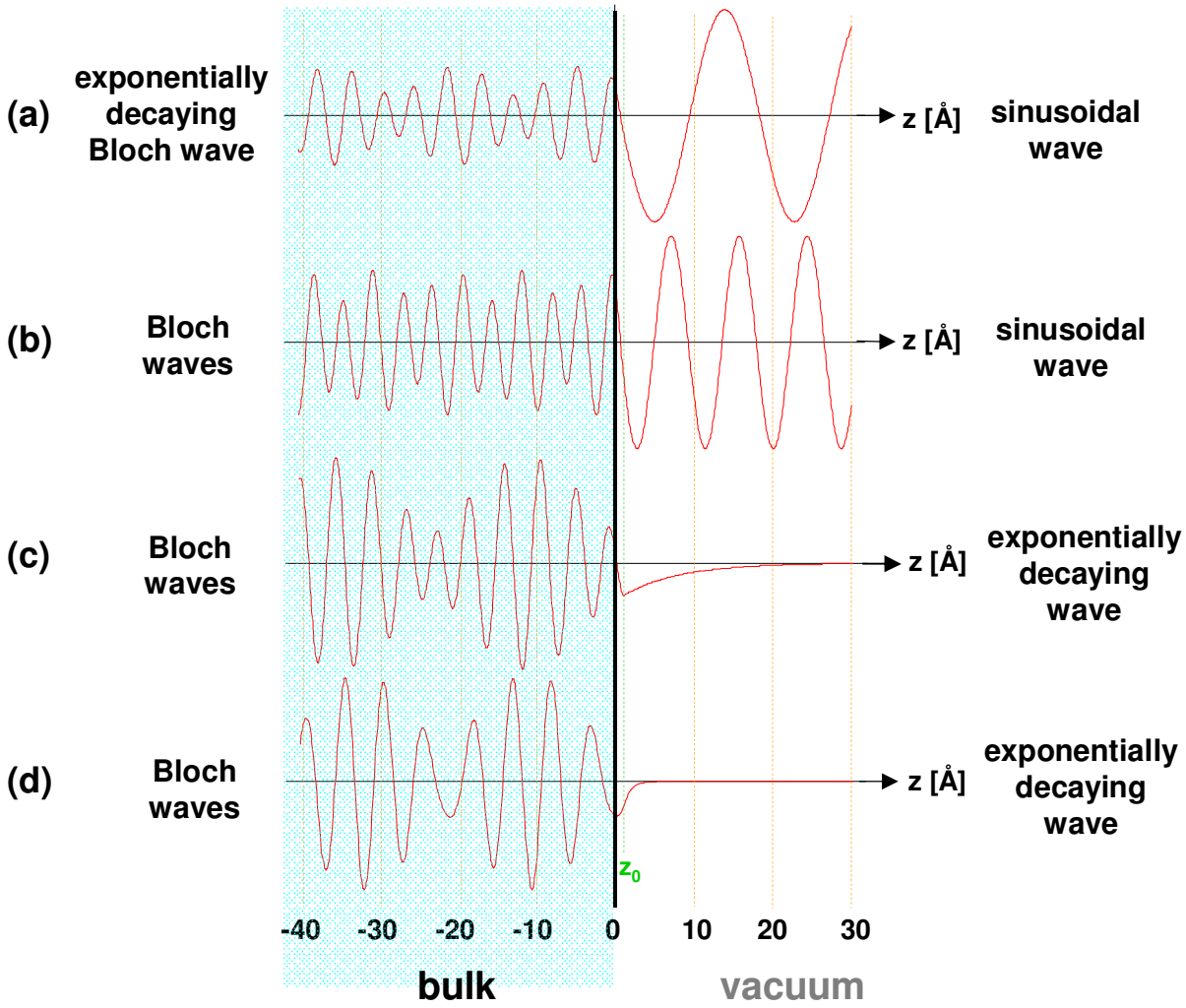

Figure 4.5 Electron wave functions for states involved in the computation of 2PP spectrum of Ag(111); wave functions for **(a)** the final state, **(b)** free (unbounded) electron intermediate state, **(c)** bounded electron intermediate state, and **(d)** initial state.

The final state electron wave function can be thought of as an 'inverse' LEED state [102,103,3]. To describe the inverse LEED state, one first needs to model a 'forward' LEED state by electrons incoming as a plane wave propagating from an electron source in the vacuum (the detector in the 'inverse' model) to the surface. At the surface, the incoming wave is partially transmitted and partially reflected according to the complex dielectric function of the surface. Transmitted electrons give rise to a Bloch wave of the upper sp-band propagating into the bulk, whereas the reflected part is a plane wave propagating back into vacuum. The transmitted wave is damped by the inelastic scattering processes, where complex damping wave vector is approximated by the universal curve [3,15] (Fig. 1.9 in Chapter-1.3). The electron wave functions from both sides are matched at the image plane as in equations [4.2] and [4.3], in order to obtain the complex transmission and reflection coefficients. The inverse LEED state wave function can be easily obtained by reversing the direction of propagation of the forward LEED state throughout. Hence, the wave function for the final state can be written as

$$\psi_f^{bulk}(z) = Te^{z/\xi}\left\{Ae^{-ik_f z} + Be^{-i(k_f - g)z}\right\}, \qquad [4.6]$$

$$\psi_f^{vac}(z) = e^{ik_f^{vac} z} + Re^{-ik_f^{vac} z}, \qquad [4.7]$$

where $k_f^{vac} = \frac{\sqrt{2m(E_f(k_f) - \Phi)}}{\hbar}$ for $E_f(k_f) - \Phi > 0$.

In the case of Ag(111), the only available intermediate states for two-photon excitation are the unoccupied upper sp-band states, which can only function as virtual states. Because the optical Bloch equations account for the excitation and relaxation of the intermediate states in an explicitly time-dependent manner, the intermediate sp-band wave functions do not include lifetime effects as do the final state wave functions, which undergo attenuation. Furthermore, virtual excitation of Bloch waves propagating in the reverse direction with respect to the detector is possible, and can contribute to the photoemission process. Thus, the intermediate state wave functions also include the counter-propagating Bloch waves as do the initial states [84]. Although the majority of the upper sp-band is located above E_{vac}, and therefore, is 'unbounded', a small portion of those states that are adjacent to the Brillouin zone edge are beneath E_{vac}, and therefore, is 'bounded'. Hence, the unbounded states are accounted for by matching the wave function from the bulk to a plane wave in vacuum:

$$\psi_m^{bulk}(z) = \left\{Ae^{-ik_m z} + Be^{-i(k_m - g)z}\right\} + D\left\{Ae^{ik_m z} + Be^{i(k_m - g)z}\right\}, \qquad [4.8]$$

$$\psi_m^{vac}(z) = Ee^{ik_m^{vac} z}, \qquad [4.9]$$

where $k_m^{vac} = \frac{\sqrt{2m(E_m(k_m) - \Phi)}}{\hbar}$ for $E_m(k_m) - \Phi > 0$.

By contrast, the bounded states are accounted for by matching them to an exponentially decaying (evanescent) wave function in vacuum:

$$\psi_m^{bulk}(z) = \left\{Ae^{-ik_m z} + Be^{-i(k_m - g)z}\right\} + e^{iq_m}\left\{Ae^{ik_m z} + Be^{i(k_m - g)z}\right\}, \qquad [4.10]$$

$$\psi_m^{vac}(z) = F\exp\left(-k_{m,bounded}^{vac} z\right), \qquad [4.11]$$

where $k_{m,bounded}^{vac} = \frac{\sqrt{2m(\Phi - E_m(k_m))}}{\hbar}$ for $\Phi - E_m(k_m) > 0$.

The aforementioned electron wave functions are employed to calculate the dipole matrix elements of the first and the second steps of optical transitions within first-order perturbation approximation as

$$M_{ij} \sim \left\langle \psi_j \left| \mathbf{A} \cdot \nabla \right| \psi_i \right\rangle = A \left\langle \psi_j(z) \left| \frac{\partial}{\partial z} \right| \psi_i(z) \right\rangle, \qquad [4.12]$$

where '**A**' is the vector potential and 'z' is the direction normal to the surface. Indices 'i' and 'j' denote the initial and intermediate states of the first excitation step, or the intermediate and final states of the second step, respectively. In terms of the appropriate wave functions for our three-level system, the optical transition matrix elements are

$$d_{01} = \left\langle \psi_m^*(k_m, z) \left| \mathbf{A} \cdot \nabla \right| \psi_i(k_i, z) \right\rangle = \int_{-\infty}^{z_0} \psi_m^*(k_m, z) \frac{\partial}{\partial z} \psi_i(k_i, z) dz, \qquad [4.13]$$

$$d_{12} = \left\langle \psi_f^*(k_f, z) \left| \mathbf{A} \cdot \nabla \right| \psi_m(k_m, z) \right\rangle = \int_{-\infty}^{z_0} \psi_f^*(k_f, z) \frac{\partial}{\partial z} \psi_m(k_m, z) dz \qquad [4.14]$$

for the 'unbounded' intermediate states; and

$$d_{01}^{\text{bounded}} = \left\langle \psi_{m,\text{bounded}}^*(k_m, z) \left| \mathbf{A} \cdot \nabla \right| \psi_i(k_i, z) \right\rangle = \int_{-\infty}^{z_0} \psi_{m,\text{bounded}}^*(k_m, z) \frac{\partial}{\partial z} \psi_i(k_i, z) dz, \qquad [4.15]$$

$$d_{12}^{\text{bounded}} = \left\langle \psi_f^*(k_f, z) \left| \mathbf{A} \cdot \nabla \right| \psi_{m,\text{bounded}}(k_m, z) \right\rangle = \int_{-\infty}^{z_0} \psi_f^*(k_f, z) \frac{\partial}{\partial z} \psi_{m,\text{bounded}}(k_m, z) dz \qquad [4.16]$$

for the 'bounded' intermediate states. The subscripts '01' and '12' denote the first and second transition steps in 2PP, respectively.

4.1.4.3 Coherence Effects in Two-Photon Photoemission Processes

The complete picture of the photoexcitation processes and the significance of various computational parameters used in the 2PP simulation are plotted with their energy versus perpendicular momentum ($\mathbf{k}_\perp$) in Fig. 4.6. In the first step, an electron is excited from the initial state, $E_i(k_i)$, on the lower sp-band, to the upper sp-band with the same $k_\perp$ serves as a virtual intermediate state, because the transition dipole matrix elements obtained from semi-infinite wave functions of the initial and intermediate states vanish for any $k_i \neq k_m$. In the second excitation step, violation of conservation of momentum is permitted because $k_\perp$ is not conserved in the photoemission process. The energy of the final state, $E_f(k_f)$, is what is recorded by the energy analyzer.

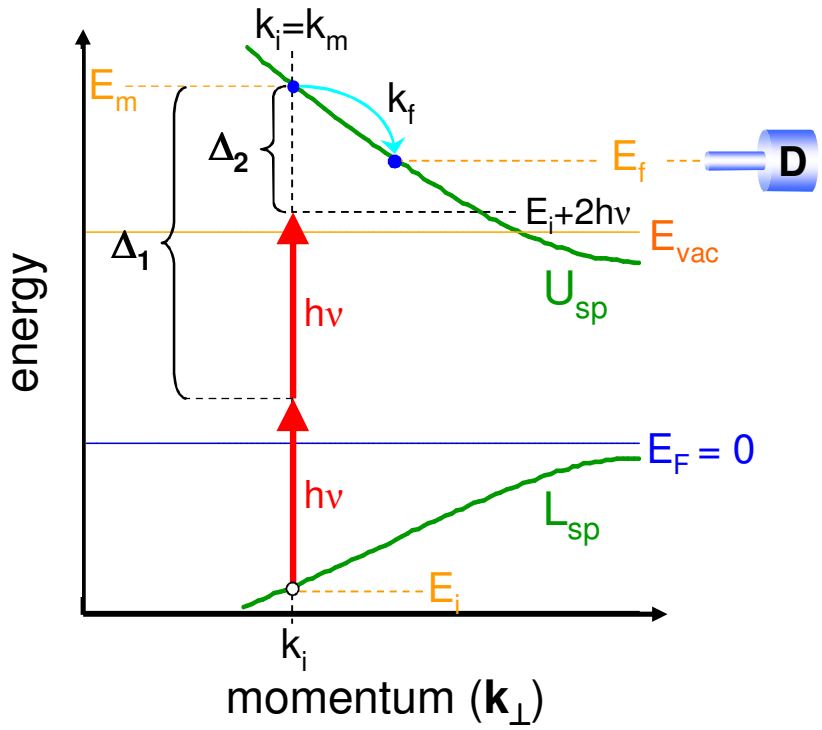

Figure 4.6 Energy–momentum ($\mathbf{k}_\perp$) photoexcitation diagram used for calculating the 2PP spectrum from Ag(111) including the coherence effects [84]. The first step, where the momentum is conserved, is displayed as a nonresonant excitation from the initial state $E_i(k_i)$ to the intermediate state $E_m(k_m)$ on U_{sp} with energy detuning of Δ_1; the second step, where the absorption of the second photon gives rise to transition to the final state $E_f(k_f)$ above E_{vac}, is detuned by Δ_2. The number of photoelectrons with respect to their kinetic energy is obtained by solving the OBE tailored for the energy levels $E_i(k_i)$, $E_m(k_m = k_i)$, and $E_f(k_f)$; the spectrum is obtained by integrating $E_f(k_f)$ over L_{sp}.

The photoexcitation scheme outlined in Fig. 4.6 consists of three electronic levels denoted by $E_i(k_i)$, $E_m(k_m = k_i)$, and $E_f(k_f)$. Following the scheme presented in Fig. 4.6, one can write the Hamiltonian of the unperturbed three-level system explicitly as

$$H_0 = \begin{bmatrix} E_0 & 0 & 0 \\ 0 & E_1 & 0 \\ 0 & 0 & E_2 \end{bmatrix}, \qquad [4.17]$$

where

$$E_0 = \hbar\omega_0,\ E_1 = \hbar\omega_1, \text{ and } E_2 = \hbar\omega_2. \qquad [4.18]$$

The time-dependent perturbation term (according to equation [3.6]) due to interaction is expressed explicitly as

$$H_{int} = E_{\omega_1}(t) = E(t)\cos(\omega_1 t) = \begin{bmatrix} 0 & -d_{10}eE_{\omega_1}(t) & 0 \\ -d_{01}eE_{\omega_1}(t) & 0 & -d_{21}eE_{\omega_1}(t) \\ 0 & -d_{12}eE_{\omega_1}(t) & 0 \end{bmatrix}, \qquad [4.19],$$

where the total Hamiltonian, $H = H_0 + H_{int}$, is written as

$$H\left|\psi(t)\right\rangle = \begin{bmatrix} E_0 & -d_{10}eE_{\omega_1}(t) & 0 \\ -d_{01}eE_{\omega_1}(t) & E_1 & -d_{21}eE_{\omega_1}(t) \\ 0 & -d_{12}eE_{\omega_1}(t) & E_2 \end{bmatrix} \begin{bmatrix} a_0(t) \\ a_1(t) \\ a_2(t) \end{bmatrix} = i\hbar \frac{\partial}{\partial t} \begin{bmatrix} a_0 \\ a_1 \\ a_2 \end{bmatrix}. \qquad [4.20].$$

When this matrix equation is solved by means of equations [3.10] and [4.18], one obtains a set of differential equations for the occupation coefficients given by

$$\frac{\partial}{\partial t} c_0(t) = -i\omega_0 c_0(t) + \frac{i}{\hbar} c_1(t) d_{10} eE_{\omega_1}(t) \exp(-i\omega_1 t), \qquad [4.21a]$$

$$\frac{\partial}{\partial t} c_1(t) = -i(\omega_1 - \omega_1) c_1(t) + \frac{i}{\hbar} c_0(t) d_{01} eE_{\omega_1}(t) \exp(i\omega_1 t) + \frac{i}{\hbar} c_2(t) d_{21} eE_{\omega_1}(t) \exp(-i\omega_1 t), \qquad [4.21b]$$

$$\frac{\partial}{\partial t} c_2(t) = -i(\omega_2 - 2\omega_1) c_2(t) + \frac{i}{\hbar} c_1(t) d_{12} eE_{\omega_1}(t) \exp(i\omega_1 t). \qquad [4.21c]$$

The time-dependent excitation and relaxation of these states in response to an ultrashort pulse laser is calculated by means of OBE, which generate 9 coupled differential equations as discussed in Chapter-3.2.2 [118]. Because the off-diagonal elements of the matrix in equation [3.11] are complex conjugates of each other, however, by symmetry they reduce to 6 equations: (given as equations [4.22a] through [4.22f])

$$\frac{\partial \rho_{11}}{\partial t} = \frac{i}{2\hbar}|d_{01}|\left\{E^*(t)\rho_{10}^*(t) - E(t)\rho_{10}(t)\right\} + \frac{i}{2\hbar}|d_{12}|\left\{E(t)\rho_{21}(t) - E^*(t)\rho_{21}^*(t)\right\} - \frac{\rho_{11}(t)}{T_1^1}$$

$$\frac{\partial \rho_{22}}{\partial t} = \frac{i}{2\hbar}|d_{12}|\left\{E^*(t)\rho_{21}^*(t) - E(t)\rho_{21}(t)\right\} - \frac{\rho_{22}(t)}{T_1^2}$$

$$\frac{\partial \rho_{00}}{\partial t} = -\frac{\partial \rho_{11}}{\partial t} - \frac{\partial \rho_{22}}{\partial t}$$

$$\frac{\partial \rho_{10}}{\partial t} = \frac{i}{2\hbar}|d_{01}|E^*(t)\{\rho_{00}(t) - \rho_{11}(t)\} + \frac{i}{2\hbar}|d_{12}|E(t)\rho_{20}(t) - \left\{i\Delta_1 + \frac{1}{2T_1^1} + \frac{1}{T_2^{01}}\right\}\rho_{10}(t)$$

$$\frac{\partial \rho_{21}}{\partial t} = \frac{i}{2\hbar}|d_{12}|E^*(t)\{\rho_{11}(t) - \rho_{22}(t)\} - \frac{i}{2\hbar}|d_{01}|E(t)\rho_{20}(t) - \left\{i(\Delta_2 - \Delta_1) + \frac{1}{2T_1^1} + \frac{1}{2T_1^2} + \frac{1}{T_2^{12}}\right\}\rho_{21}(t)$$

$$\frac{\partial \rho_{20}}{\partial t} = \frac{i}{2\hbar}E^*(t)\left\{|d_{12}|\rho_{10}(t) - |d_{01}|\rho_{21}(t)\right\} - \left\{i\Delta_2 + \frac{1}{2T_1^2} + \frac{1}{T_2^{02}}\right\}\rho_{20}(t)$$

The photoelectron population of the final state, which is detected by the energy analyzer, is computed by integrating the OBE within a time frame sufficiently longer than the pulse width of the laser, where the lifetime of the final state is assumed to be infinite. Then, the population of the final state is multiplied by the density of the initial ($DOS_i(E)$), intermediate ($DOS_m(E)$) and final states ($DOS_f(E)$) given by [119]

$$DOS_i(E) \propto \left(\left|\frac{\partial}{\partial k_\perp}E(k)\right|_{L_{sp}}\right)^{-1} = \left|\frac{\partial}{\partial E}k_\perp(E)\right|_{L_{sp}}, \qquad [4.23a]$$

$$DOS_m(E) = DOS_f(E) \propto \left(\left|\frac{\partial}{\partial k_\perp}E(k)\right|_{U_{sp}}\right)^{-1} = \left|\frac{\partial}{\partial E}k_\perp(E)\right|_{U_{sp}}, \qquad [4.23b]$$

which were obtained from the energy band dispersions [120,121].

For any given fixed initial state, the detector energy (i.e., E_f) is scanned over the pertinent final energy range to obtain $N_i(E_f, E_i)$. The total calculated 2PP spectrum is obtained integrating the contribution from each initial state over all the contributing initial states [84]:

$$N_{tot}(E_f) = \int_{L_{sp}} N_i(E_f, E_i) dE_i \qquad [4.24].$$

The integral is approximated by a summation over states separated by a sufficiently narrow energy gap ($\Delta E \approx 20$ meV).

To test the validity of our OBE approach, we input realistic decay times into equations [4.22], and calculated the time dependent populations. Fig. 4.7 displays the change in the electron populations in all three states with respect to time. Note that the total number of electrons in the system remains fixed at all times; the initial state is depopulated rapidly at the time of photoexcitation, reaching a minimum, and gradually recovering to a depleted value. The final state population increases rapidly and saturates after the interaction has ceased, because the lifetime of photoelectrons is assumed to be infinite. The intermediate state population rises and decays according to the excitation and relaxation mechanisms. The conservation of population in the three states confirms the validity of our model for describing the excitation and relaxation dynamics of the three-level system in Fig. 4.6.

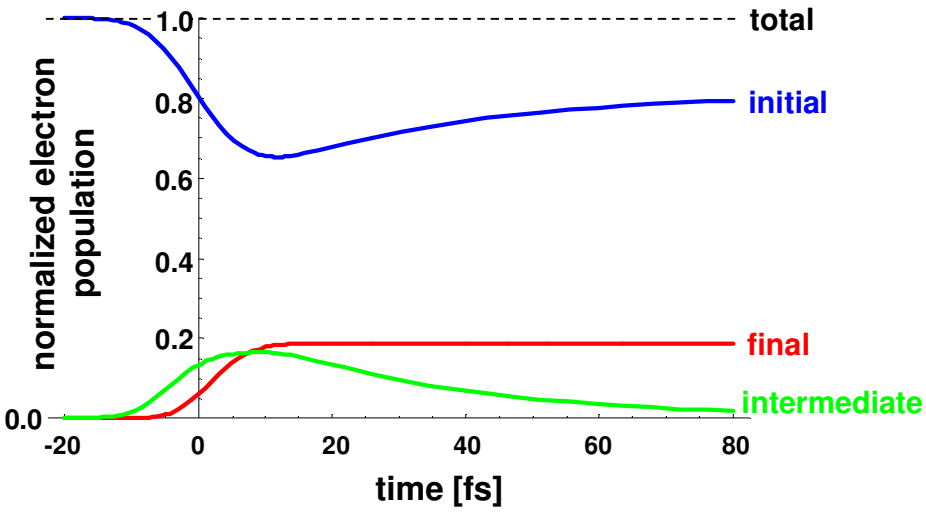

Figure 4.7 The time evolution of the normalized electron populations in 2PP excitation obtained by solving the OBE.

4.1.4.4 Temperature-Dependent Background Spectrum

At finite temperatures, electron–phonon interaction gives rise to a continuous contribution of photoelectrons underlying the $k_{\|}$-conserving 2PP spectral features. Therefore, a complete description of the experimental 2PP spectra must include both the elastic and inelastic components. Momentum scattering by phonons can contribute to the $k_{\|} = 0$ component of photoemission through two distinct processes: (1) coherent two-photon absorption accompanied by phonon absorption or emission; and/or (2) sequential absorption of single photons mediated by phonon scattering at each step. The sequential process necessarily involves two independent phonon scattering processes, because there are no resonant transitions from the lower sp-band that can be excited by 3.1 eV light, as well as no intermediate states at $k_{\|} = 0$ for direct $k_{\|}$-conserving transition to final states above E_{vac}. The latter process is depicted in Fig. 4.8. Because these higher order indirect processes take place by absorbing or emitting phonons, the inelastic photoelectron signal should manifest temperature dependence. In agreement with this expectation, 2PP spectra shown in Fig. 4.8 for temperatures ranging from 100 to 500 K show a continuous background that increases with temperature, and a shift and broadening of the sp-band.

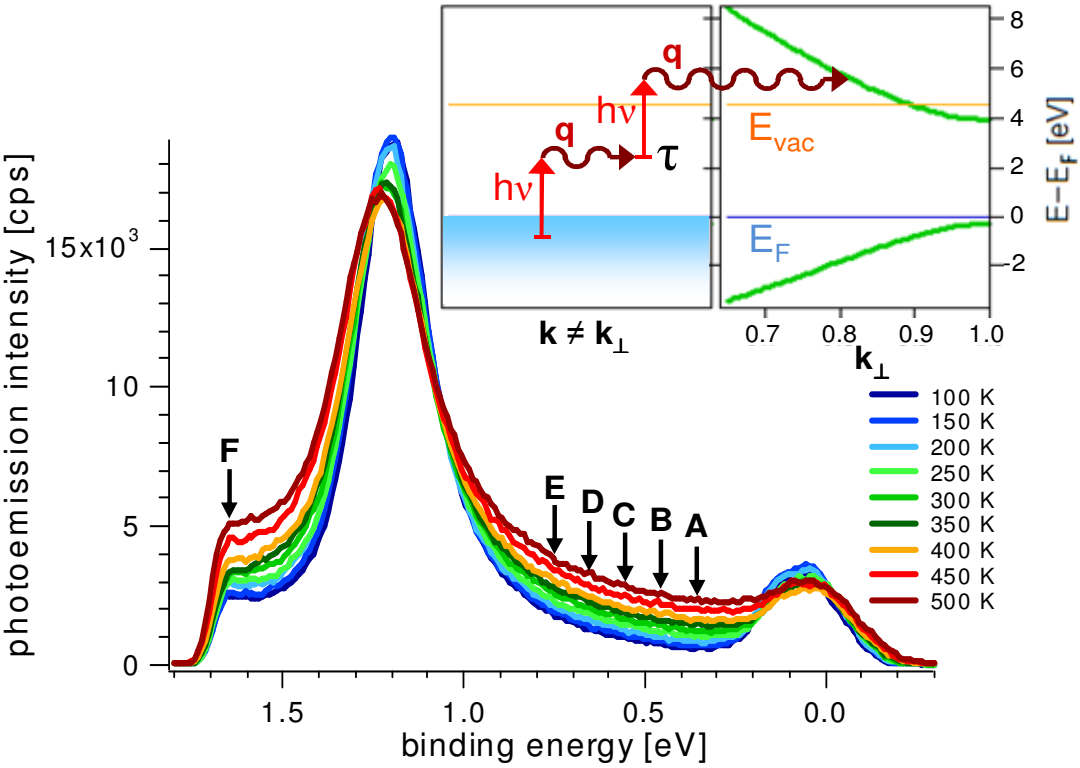

Figure 4.8 Temperature-dependent 2PP spectra on Ag(111) measured from 100 to 500 K. For increasing sample temperature, the inelastic electron–phonon interaction increasingly contributes a continuous background to the 2PP spectra. The temperature-dependent background is evaluated at energies marked by letters 'A' through 'F'.

If there is substantial quasielastic contribution to 2PP spectra via the second mechanism involving real population in the intermediate state and the intermediate state lifetimes are shorter than the laser pulse, the probability of this process should be energy-dependent because of the $(E-E_F)^{-2}$ dependence of electron-electron scattering [122,123,124,125,126]. For a decreasing lifetime-to-pulsewidth ratio, the photoexcited electrons in the intermediate state are less likely to be excited further owing to competing population decay.

When the optical Bloch equations for this three-level system are solved for the final state population via phonon-assisted processes by considering the energy dependence of the intermediate state lifetime in response to 10 fs laser pulse excitation, one obtains a nearly linearly decreasing photoelectron background as in Fig. 4.9, where the intermediate state lifetime causes variation in intensity. According to our model, the pulse duration of the excitation laser is a key factor in determining the amplitude as well as the characteristics of the background. When the pulse duration is longer than the intermediate state lifetime, the energy dependence of the phonon-assisted contribution obeys the Fermi liquid theory ($\propto (E - E_F)^{-2}$). When the pulse duration is noticeably shorter than the hot electron lifetimes, the photoexcitation probability does not depend on energy and the phonon-assisted contribution attains a nearly energy independent value. The lack of energy dependence could also be explained by the phonon-assisted two-photon nonresonant absorption mechanism, which does not require consideration of the intermediate state lifetime. Because the momentum-integrated density of initial, intermediate and final states vary slowly with energy [127], the DOS effects are excluded in estimating the phonon-assisted signal.

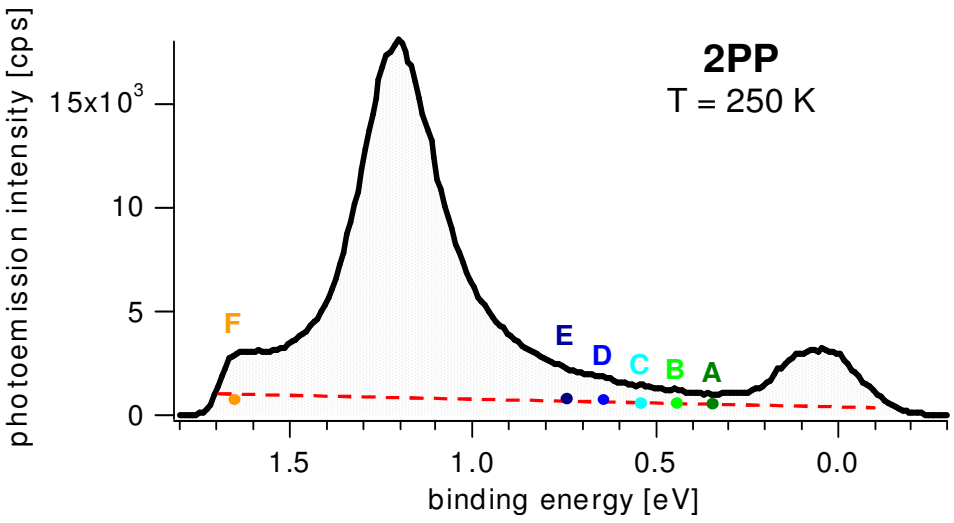

Figure 4.9 Experimental 2PP spectrum of Ag(111) at 250 K. The phonon-assisted contribution extracted from the data in Fig. 4.8 is indicated by the red dashed line. The analysis of the temperature-dependent phonon-assisted background is shown in Fig. 4.10.

The temperature-dependent background requires interaction of electrons with phonons. The electron–phonon scattering rate for electrons of energy E and temperature T within the Debye model is expressed by [3,128,129,130,131]

$$\Gamma(E,T) = 2\pi\lambda \int_0^{E_D} \left(\frac{E'}{E_D}\right)^2 \left(1 - f_{FD}(E - E') + 2f_{BE}(E') + f_{FD}(E + E')\right) dE' \qquad [4.25]$$

where f_{FD} and f_{BE} are the Fermi-Dirac and the Bose-Einstein distribution functions; E_D is the Debye energy (~19.4 meV for silver [128]), and λ is the electron-phonon mass enhancement parameter. In the energy range above E_D, this function is nearly independent of the electron energy E. The Debye energy is defined as $E_D = k_B\Theta_D = \hbar\omega_D$, which corresponds to the crystal's highest normal mode of vibration (Θ_D: Debye temperature; k_B: Boltzmann constant; ω_D: Debye frequency) [132]. For temperatures above Θ_D, the equation [4.25] can be approximated with a line of slope of $2\pi\lambda k_B$. For temperatures below Θ_D, its slope tends to zero and attains a constant value equal to $(2/3)\pi\lambda k_B\Theta_D$. This intercept for $T = 0$ K corresponds to the scattering rate associated with phonon emission [128]. The electron–phonon scattering through phonon emission is independent of temperature and subsists at all temperatures.

To determine the contribution of Drude absorption, photoelectron intensity for 6 different energies (indicated by letters 'A' through 'F' and shown in Figs. 4.8 and 4.9) is calculated and plotted as a function of temperature in Fig. 4.10. The measurement energies were chosen because

of the minimum contribution from the direct two-photon transition, which shows a different temperature effect. Extrapolation of the experimental data to 0 K (solid lines) is carried out by fitting the 2PP intensities to equation [4.25] with an offset at the ordinate as a fitting parameter to account for the contributions from the coherent 2PP signal. This procedure gives $\lambda = 0.26$, as compared with $\lambda = 0.29$ from literature [128,133]. The ordinate intercept of the dashed line obtained by fitting the linear portion of equation [4.25] corresponds to the pure direct 2PP signal, while the difference between the full and dashed lines represents the contribution from phonon emission. The phonon-assisted Drude absorption contribution at a given observation energy and temperature can be estimated by Fig. 4.10 by the difference between the photoemission counts at a given temperature and the value corresponding to the intercept of the corresponding dashed line. In this way, we can determine the phonon-induced background in a 2PP process, as it is displayed for 250 K in Fig. 4.9.

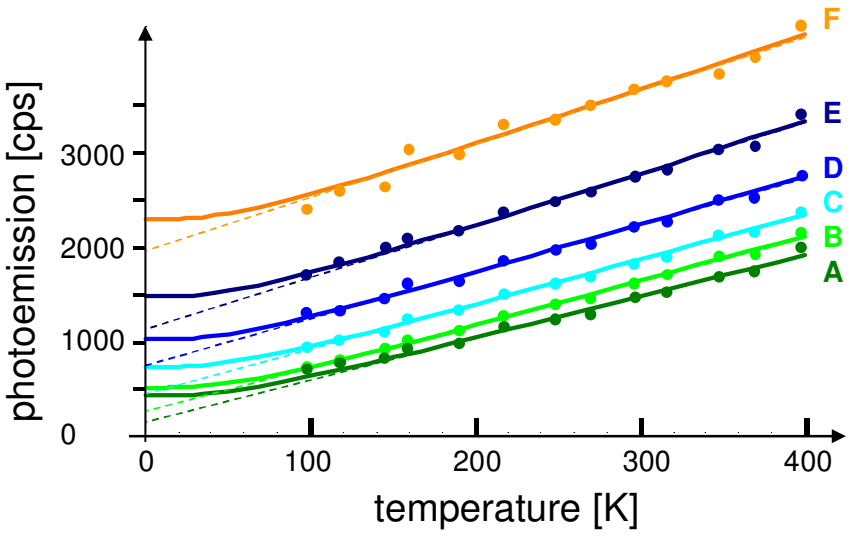

Figure 4.10 Temperature-dependent 2PP intensity due to phonon-assisted Drude absorption on Ag(111) surface at various binding energies and their extrapolation to $T = 0$ K. The dots (experimental data) around the solid lines (fit) are fitted to the Debye model; the dashed lines

show extrapolation of the linear portions for $T \geq \Theta_D$ to the ordinate. Points 'A' through 'F' are indicated in Figs. 4.8 and 4.9.

4.1.4.5 Inelastically Scattered Photoelectrons

Inelastically scattered final state electrons with momentum along the surface normal also contribute to the background of 2PP spectra. Their contribution is included using the conventional 'Shirley function' [134], in which the inelastic component is given by the integral of the elastic photoelectrons along the energy axis from the Fermi edge to lower binding energy. The amplitude of the integral is used as a free parameter to optimize the fit of the experimental spectrum (see Fig. 4.11(c), the 'green' line). The inelastic background augments the overall intensity particularly in the interval between the sp-band peak and the vacuum edge.

As evidenced in Fig. 4.2, both 1PP and 2PP should have comparable contributions from the inelastically scattered photoelectrons (Shirley background), which depend on the final state energy distribution rather than the excitation process [134]. Assuming that the background signal at the vacuum edge in both cases is composed of inelastically scattered photoelectrons, one can compare their intensity and check for consistency. This test shows that the 2PP background is about 1.8 times larger than that of 1PP. The elevated background for 2PP suggests that there could be an additional contribution to the 2PP signal near the vacuum edge. Studies of 2PP on rough Ag films demonstrated that there exists an additional 2PP excitation pathway linked to the excitation of local surface plasmons at roughness features [108]. Another experiment conducted on the same Ag(111) surface by a photoemission electron microscope (PEEM) reveals that such

roughness features exist and give rise to intense photoemission signals ('hot spots') mediated by surface plasmons [135]. Nonetheless, the photoemission contribution from these surface plasmons makes a minor contribution to the overall photoemission yield.

4.1.4.6 Total Two-Photon Photoemission Spectral Distribution

Fig 4.11 presents all of the contributions to the 2PP signal obtained in the computations of section 4.1 and comparison of their sum with the experimental 2PP spectra. The three major elements contributing to the 2PP spectrum in the order of significance are the coherent 2PP (Fig. 4.11(d)), incoherent Drude absorption (Fig. 4.11(b)), and inelastic electron background (Fig. 4.11(c)). The Shockley surface state (shown in Fig. 4.11(a)) is assumed to be a Gaussian function centered at 0.063 eV binding energy. It is added by hand, since the relative surface and bulk 2PP contributions are not known. The direct coherent 2PP signal has a peak at about 1.2 eV initial state binding energy corresponding to the energy conserving resonant two-photon excitation between the lower sp-band to the upper sp-band by 400 nm wavelength laser pulse (Fig. 4.11(d)). This peak displays a slight asymmetry, which we attribute to decreasing surface transmittance probability of the low kinetic energy photoelectrons [108,136]. The surface transmittance, which is also known as the 'escape function', modulates the pure photoexcitation probability of bulk electrons. In this study, it is obtained from the surface transmission coefficient of the final state electron wave function and by matching the vacuum and bulk sides of the wave function at the image plane. A substantial change in the surface transmittance of an intrinsically symmetric spectral distribution gives rise to discernible asymmetry (and minor consequent augmentation in intensity) for the transmitted electrons on the lower binding energy side.

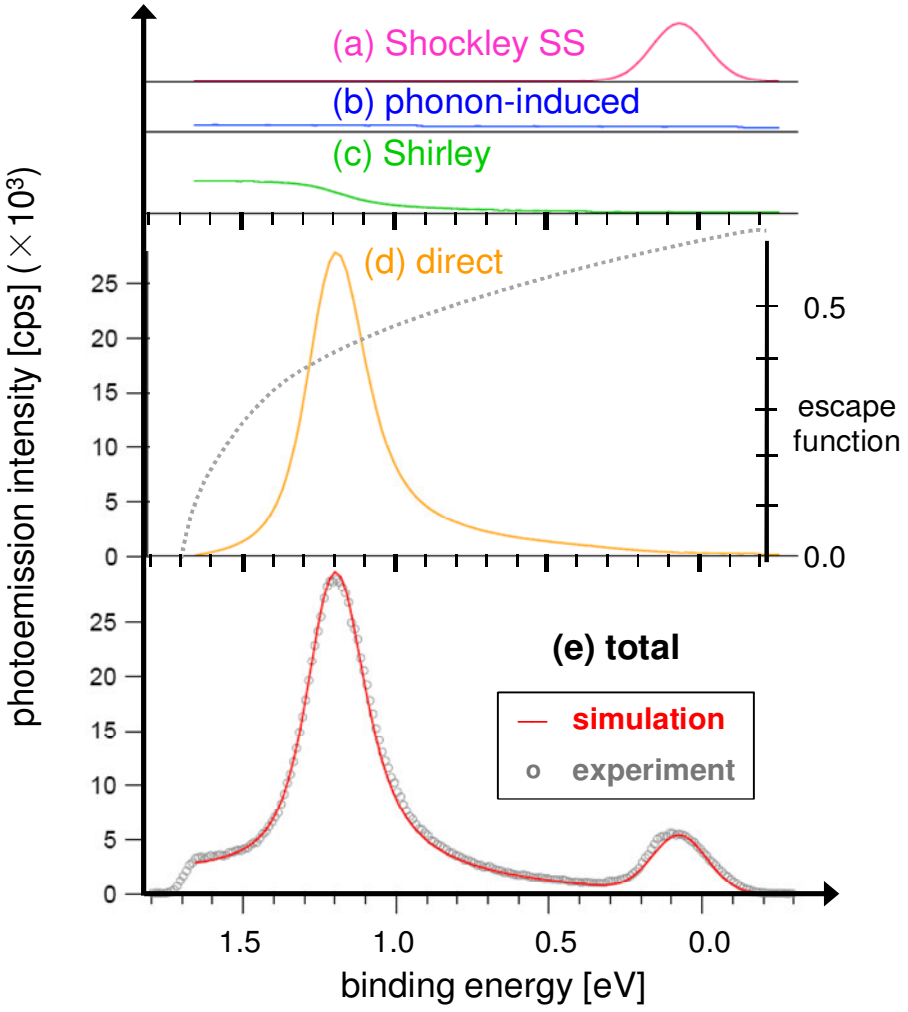

Figure 4.11 Contributions to 2PP spectrum from Ag(111) surface at 100 K, and the comparison of the experimental data with the aggregate simulated contributions. **(a)** Shockley SS is assumed to possess a Gaussian shape. **(b)** Phonon-induced background depends on temperature and exhibits a nearly linear behavior decreasing toward lower binding energy. **(c)** Shirley background is approximated as an integral of elastic electrons from the Fermi edge to lower binding energy. **(d)** The direct coherent 2PP signal shows slight asymmetry caused by the escape function (dotted line). **(e)** Aggregate of all components (red line) and comparison with the experimental data (gray circles).

In the absence of an actual intermediate state in the sp-band gap of Ag(111), the continuum of the upper sp-band serves as the virtual intermediate states, while the energetically more favorable image potential states (n = 1, 2, 3, etc.), which are located about 0.77 eV below E_{vac} [62,137], appear not to be involved in the 2PP mechanism of the bulk states. If the image potential states were to engage, they would introduce a surface-mediated excitation channel that could interfere with the bulk excitation channel. As mentioned earlier, the considerably smaller asymmetry of the bulk bands in 2PP, as compared with the 1PP spectra, argues against the surface channel having a significant contribution. The Shockley surface state intensity difference between the 2PP and 1PP spectra confirms that the surface excitation channel is less prominent in the 2PP process. Because the initial and final states are in principle the same for the 2PP and 1PP processes, the difference between the surface versus bulk photoemission in the linear and nonlinear excitation must arise from different surface and bulk transition moments involving the intermediate states.

According to the band structure of Ag(111), it is clear that the upper sp-band states above E_{vac} are available as final states only for $k_{\perp} \leq 0.89 k_{\Gamma L}$ (the 'white' zone in Fig. 4.1), which is far from the Brillouin zone edge. Not even does the penetration of the image potential states due to imaginary momentum within the band gap enable them to be effective virtual intermediate states. Nevertheless, one can expect them to be effective virtual intermediate states for 2PP from the Shockley surface state, which was studied for Cu(111) [104].

Although the entire 2PP process on Ag(111) surface involves continuous energy bands, the OBE model is implemented by considering discrete states of a three-level system with a single intermediate state, which corresponds to the upper sp-band at the same $\mathbf{k}_{\perp}$ as the initial state. The

simulation of 2PP spectra of Ag(111) shows that in the case that band-to-band transitions are localized in **k**-space, it is possible to reproduce the spectra based on relatively simple models that are grounded in conventional theory of 1PP. For 2PP the dynamical processes in metals in addition to the coherence properties of the excitation source play an enhanced role. Ag(111) is an ideal case for simulation because there is substantive theoretical ground work from previous 1PP studies, and the lack of real intermediate states diminishes the role of electron scattering effects. Although Cu(111) has a similar band structure, its spectra with the same photon energy are almost featureless obviating description by models such as presented here. The difference may arise from the proximity of the d-bands to E_F, which provides additional indirect channels for hot electron excitation [138,139].

4.2 Angle-Resolved Two-Photon Photoemission from the sp-Bands of Ag(111)

4.2.1 Introduction

Using the ARPES technique, one can obtain information about the electronic band structure by analyzing the observed dispersion of peak positions in photoemission spectra. As a model system for quantitative analysis of the photoemission mechanism and spectra, the bulk band structure of silver has been widely investigated by ARPES [84,140,141,142]. In terms of analyzing the relative intensity information of angle-resolved photoemission studies, the role of the polarization of the incident light was studied experimentally and theoretically [143,144,145], and the relationship between the momentum matrix elements and the measured intensities of energy-dependent transitions was also described [146]. In the photon energy range relevant to our study, considerable interference

between the surface and bulk photoemission has been observed in the surface normal 1PP spectra of Ag(111) surfaces [102,103].

We have performed both angle-resolved one-photon photoemission (AR1PP) and two-photon photoemission (AR2PP) experiments on bare Ag(111) surface. The two-photon transition between the lower and upper sp-band described and analyzed in the previous section provides an opportunity to examine whether theory can also account for the differences in the angle-dependent intensities between the AR1PP and AR2PP spectra of Ag(111), to be described in this section. We explain the angle-dependent intensity variation observed in AR2PP experiments within the framework of Fresnel equations, in the case where additional effects such as surface photoemission are negligible. We also examine how refraction suffered by low-energy photoelectrons at the metal–vacuum interface affects quantitative band structure mapping. We find that low energy photoelectrons of a well-defined direct optical interband transition can provide accurate information on the inner potential [147]. After accounting for the refraction effects, the observed dispersion of the sp-band transition of Ag(111) can be simulated by a nearly free electron model for the initial and final states. The measured sp-band dispersion agrees with the known band structure.

4.2.2 Experimental Details

The angle-resolved measurements were performed by rotating the angle of the sample with respect to the laser incidence and photoelectron analyzer axes, which were fixed with respect to each other at an angle of 45°. Fig. 4.12 defines the relevant angles for the angle-resolved

photoemission measurements. The experiment was started with the incident laser beam with p-polarization at 45° angle with respect to the sample normal. After the acquisition of repetitive spectra was started, after each scan the sample was turned back and forth in 1° increments by rotating the sample manipulator about the perpendicular axis to the optical plane.

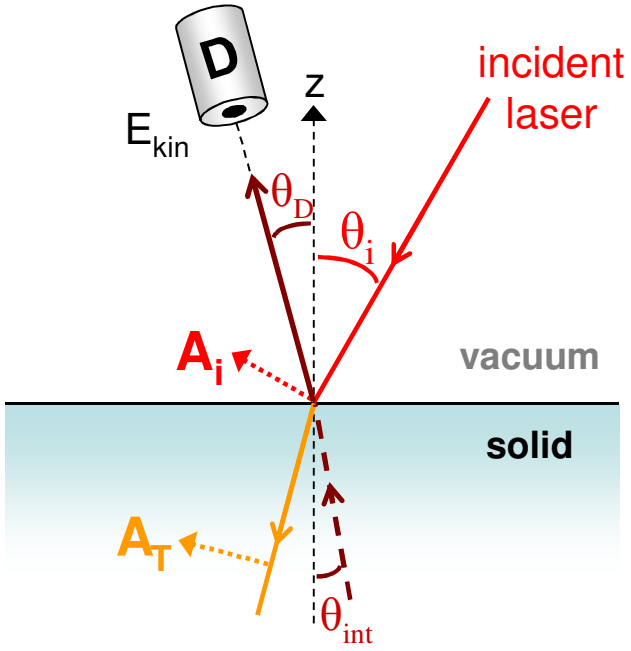

Figure 4.12 The geometry used in angle-resolved photoemission experiments. The angle between the incident light (laser beam) and the detected electrons (energy analyzer) is fixed to $\theta_i + \theta_D = 45°$. $\mathbf{A_i}$ and $\mathbf{A_T}$ stand for vector potentials for 'incident' and 'transmitted' light. The photoelectrons leaving the surface with θ_D propagate inside the solid with an angle θ_{int}.

4.2.3 Experimental Results

Angle-dependent 1PP and 2PP experiments in Fig. 4.13 were carried out on a cleaned and annealed Ag(111) surface with p-polarized incident light. Dispersing spectral features due to the bulk sp-band transition and the Shockley surface state are evident. The surface state disperses

above E_F within several degrees from the surface normal (red dashed line), where it can no longer be observed. The dispersions of the sp-band transition in both 1PP and 2PP measurements, however, are observable over an extended range of angles before the lower sp-band disperses above E_F. The intensity distribution of the bulk transition in the AR2PP spectra is conspicuously asymmetric, whereas the AR1PP appears symmetric with respect to the surface normal. As in Fig. 4.2, the Shockley surface state has higher (lower) photoemission intensity relative to the sp-band peak because of different surface and bulk contributions, and has a narrower (broader) spectral width in AR1PP (AR2PP) because of the phase matching limitations of the BBO crystal.

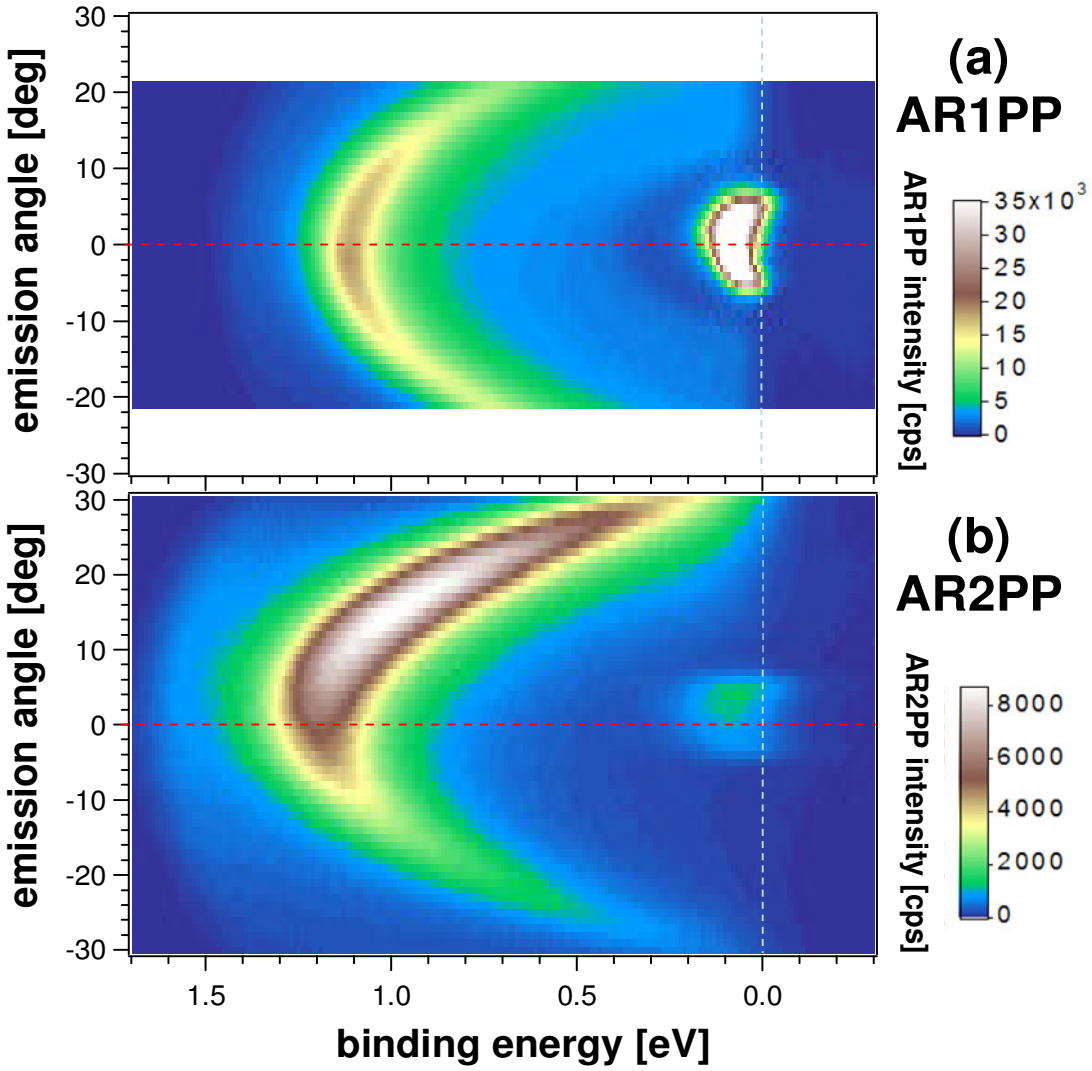

Figure 4.13 Experimental **(a)** AR1PP ($h\nu = 6.0$ eV) and **(b)** AR2PP ($h\nu = 3.1$ eV) measurements. The dashed horizontal lines indicate the surface normal emission angle. The AR2PP intensity angular distribution is conspicuously asymmetric with respect to the surface normal, whereas the AR1PP intensity distribution appears nearly symmetric.

4.2.4 Theoretical Modeling

4.2.4.1 Dispersion of the sp-Band Transition Peaks

In order to account for the differences between the AR1PP and AR2PP spectra, in Fig. 4.14 we present a three dimensional **k**-space representation of the lower and upper sp-bands and illustrate the possible photoexcitation pathways. The sp-band gap width at the L-point is 4.16 eV [84], whereas the lower sp-band maximum at $k_{\parallel} = 0$ occurs at -0.30 eV [147].

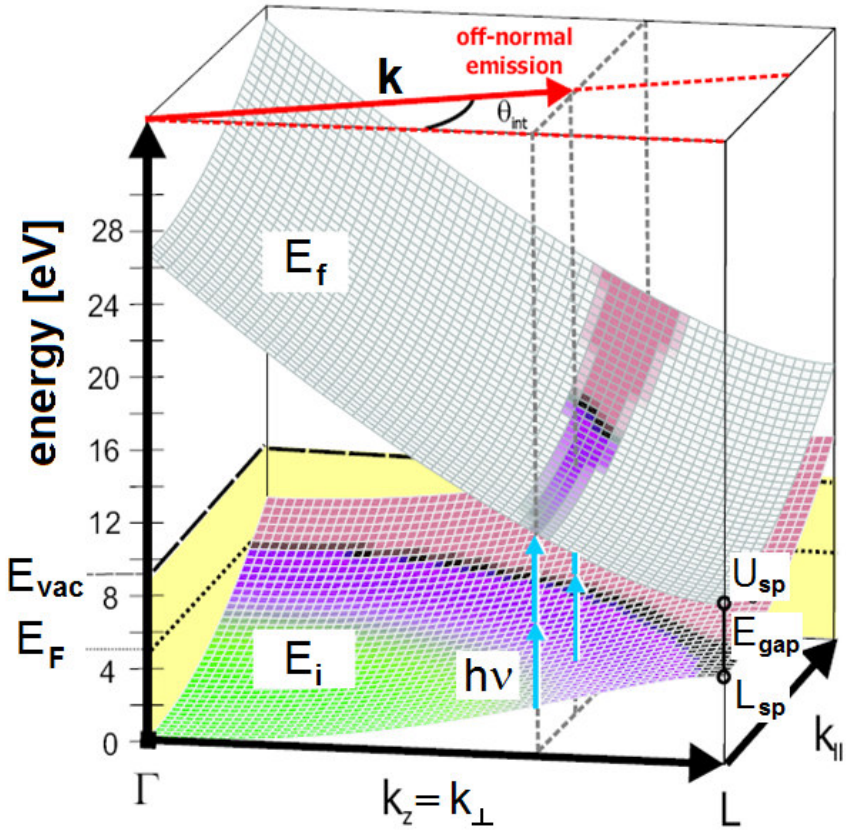

Figure 4.14 Three-dimensional illustration of the nearly free electron band structure for the lower and upper sp-bands involved in the direct two-photon transition for Ag(111). The zero of the energy scale is set at the bottom of the lower sp-band. The lower sp-band is filled up to E_F, as indicated by the black shading. The internal emission angle of electrons is denoted by θ_{int}.

Direct photoexcitation occurs in the momentum space where the difference between the initial and final state energies equals the 1PP photon energy or twice the 2PP photon energy. The resonance condition determines the perpendicular and parallel components of **k** participating in the excitation and consequently the internal angle inside the solid (θ_{int}) prior to emission.

As described in Fig. 1.11, for an electron to be emitted, it must overcome a surface potential barrier ($V_R = E_{vac} - E_0 > 0$), which corresponds to the energy difference between E_{vac} and the band origin (E_0) given by the nearly free electron model. Since the kinetic energy of photoelectrons is measured relative to E_{vac}, the electrons inside the solid have energy of $E_{kin} + V_R$. The potential step at the interface corresponding to V_R causes refraction of electrons such that energetic electrons inside the solid with an angle 'θ_{int}' emerge into vacuum at an angle 'θ_D'; the internal and external angles are related by [3]

$$\frac{\sin\theta_D}{\sin\theta_{int}} = \left(\frac{E_{kin} + V_R}{E_{kin}} \right)^{1/2}, \qquad [4.26]$$

as well as implicitly by equation [1.12]. According to this simple model, the dispersion of the sp-band transition is governed by several parameters: the minimum of the upper sp-band and the maximum of the lower sp-band at $k_{\parallel} = 0$, E_{vac}, and E_F. Obviously, we expect this model to remain valid within a limited range of $k_{\parallel}$, because of deviations of the actual band structure from the nearly free electron model.

4.2.4.2 The Angular Photoemission Intensity Distribution

As introduced in Chapter-1.3, 1PP process can be described by first-order perturbation theory through a Fermi's golden rule approximation to describe how an electromagnetic field interacts with atoms of a solid. The corresponding photocurrent in 1PP process can be expressed by equation [1.9] as

$$\begin{aligned} I(E_f)^{1PP} &\propto \left| \langle \psi_f | H_{int} | \psi_i \rangle \right|^2 \delta(E_f - E_i - h\nu) \\ &= |M_{if}|^2 \delta(E_f - E_i - h\nu) \end{aligned} . \qquad [4.27]$$

After evaluating the integral within the absolute value sign, the matrix element between the initial and final states can be expressed as

$$M_{if} = \frac{ie\hbar}{2mc}\langle \psi_f | \mathbf{A}(\mathbf{r}) \cdot \nabla | \psi_i \rangle = \mathbf{A} \cdot \mathbf{P_{if}}, \qquad [4.28]$$

where $\mathbf{P_{if}}$ is the momentum matrix element and the photocurrent of 1PP can be simplified as

$$I(E_f)^{1PP} \propto |\mathbf{A} \cdot \mathbf{P_{if}}|^2 \propto \cos^2 \Theta, \qquad [4.29]$$

which shows a proportionality between the 1PP intensity and the square of the matrix element.

The 2PP intensity can be expressed through second-order time-dependent perturbation theory as a sum over all possible intermediate states 'm':

$$I(E_f)^{2PP} \propto \left| \sum_m \frac{\langle \psi_f | H_{int} | \psi_m \rangle \langle \psi_m | H_{int} | \psi_i \rangle}{E_m - E_i - h\nu} \right|^2 \delta(E_f - E_i - 2h\nu). \qquad [4.30]$$

For the observed transition in Ag(111), there are no resonant intermediate states, as explained in section 4.1 for the normal emission. In the case of nonresonant excitation between bands of the nearly free electron two-band model, the square of the product of the matrix elements in equation [4.30] can be expressed as

$$\left| M_{im}^* M_{mf} \right|^2 \propto \cos^4 \Theta, \qquad [4.31]$$

where Θ is the angle between $\mathbf{A}$ and $\mathbf{P_{eff}}$, the effective momentum matrix element of the 2PP process (only the angle is important). The 2PP photocurrent is then proportional to

$$I(E_f)^{2PP} \propto |\mathbf{A} \cdot \mathbf{P_{eff}}|^4 \propto \cos^4 \Theta. \qquad [4.32]$$

The momentum matrix elements $\mathbf{P_{if}}$ (for 1PP) and $\mathbf{P_{eff}}$ (for 2PP) are in general complex vectors with amplitudes that need not be explicitly calculated to determine that angle dependence of 1PP and 2PP [148].

From the above formulation, the measured angle-dependent intensities originate from two main factors. First, the electric field vector changes in the solid with the angle of incident laser beam. This phenomenon is described by the Fresnel equations in classical optics, as it quantitatively describes the direction, magnitude, and relative phase of the vector potential, and consequently, the transmission and reflection coefficients at the solid–vacuum interface [149,150]. Second, the coupling of the vector potential **A** of the incident light to the electronic system leads to an angle-dependent probability of photoelectron detection in the direction of the electron analyzer, as expressed in equations [4.29], [4.31], and [4.32].

The photoelectron yield in photoemission, regardless of the direction of electron emission, is proportional to the total energy deposited on the sample surface. The deposited energy is proportional to $(1-R)^n$, where 'R' is the reflectivity of the sample in response to the s- or p-polarized light and 'n' denotes the order of the photoemission process. For p-polarized light, the photoemission intensity increases near the pseudo-Brewster's angle, where the reflectivity is minimum and the transmission is maximum.

In angle-resolved photoemission, the transition matrix element is largely controlled by the relative orientation of the vector potential $\mathbf{A_T}$ and the photoelectron momentum $\mathbf{P_{if}}$, as indicated in equation [4.32]. These effects are separately described in equation [4.28] by the vector

potential **A** and the momentum matrix element $\mathbf{P_{if}}$, which depends on the angle of the emitted final state photoelectron. This angle is fixed with respect to the incident beam in our experiment. The variation in the z-component of $\mathbf{A_T}$ is the dominant contribution to the photoemission intensity for p-polarized incident light. The term '$\nabla \cdot \mathbf{A}$' in equation [1.7] is nonvanishing at the surface due to the dielectric discontinuity. This surface contribution to the transition matrix element for photoemission can be approximated by [103,151]

$$M_{if} \propto M_{bulk} + M_{surface} \equiv \mathbf{A_T} \cdot \mathbf{P_{if}} + \Delta A_z \left(\frac{C}{2d} \right), \qquad [4.33]$$

where 'C' is a complex fitting parameter. The change in the z-component of A (ΔA_z) in transition from vacuum into the solid through an effective depth 'd', which is of the order of interatomic distance is given by [147,151,152]

$$\Delta A_z = |\mathbf{A_i}| \left(\frac{2\cos\theta_i \sin\theta_i}{\varepsilon \cos\theta_i + \sqrt{\varepsilon - \sin^2\theta_i}} - \sin\theta_i \right), \qquad [4.34]$$

which can be calculated by the Fresnel equations. Apart from the surface photoemission, several other processes could also impact the angle-resolved photoemission intensity. Photoexcited electrons traveling from a certain depth within the solid toward the solid-vacuum interface with larger angles relative to the surface normal are more likely to undergo inelastic scattering, because they propagate over longer distance within the solid [147]. Moreover, the photoemission peak shapes will depend on the varying **k**-space resolution with the exit angle, which is caused by refraction. These factors can be seen at exit angles of 30° or more and are symmetric with respect to the surface normal [147].

Our model employs the Fresnel equations to deduce the refracted vector potential $\mathbf{A_T}$ as a function of the incident vector potential $\mathbf{A_i}$ for the known dielectric function $\varepsilon(\omega)$ of Ag [153,154]:

$$\mathbf{A_T} = \mathbf{A_T}\left(\mathbf{A_i}(\theta_i), \varepsilon(\omega)\right). \qquad [4.35]$$

If the dipole matrix element for the observed transition is directed along the surface normal, the photoemission intensity is determined by the z-component of the vector potential outside the metal and given by [153,154]

$$\frac{A_z}{|\mathbf{A_i}|} = \frac{2\cos\theta_i \sin\theta_i}{\varepsilon\cos\theta_i + \sqrt{\varepsilon - \sin^2\theta_i}}. \qquad [4.36]$$

The variation of A_z as a function of angle of incidence is nearly independent of the photon energy (within or around the energy range that we use) and whether we look at silver or copper [147]. Therefore, our results can be generalized to a wide variety of materials and at the aforementioned photon energies.

The momentum matrix element $\mathbf{P_{if}}$, is a complex vector that depends on the initial and final states in the photoemission process. In general, it is also a function of the wave vector of the emerging photoelectrons. Studying the momentum matrix element can potentially reveal information on the wave functions of the states involved and their symmetry [155]. Our model assumes that the momentum matrix element points in the direction of the surface normal and the z-component of the vector potential inside the solid is a critical factor for the overall angle-dependence of the photoemission intensity for p-polarized incident light.

Combining these effects by the results shown in equations [4.29] and [4.32], the general behavior for the angle-dependent intensity of sp-band transition spectra can be formulated as

$$I(E_f)^{nPP} \propto \left|A_z(\theta_i, \varepsilon(\omega)) \cdot P_z\right|^{2n}, \qquad [4.37]$$

where 'n' denotes the order of the photoemission process [147]. Fig. 4.15 shows the angle-resolved intensity variation computed with the above formula as a function of the angle of incident light for 1PP and 2PP, where they designate the square and the fourth power of A_z, respectively.

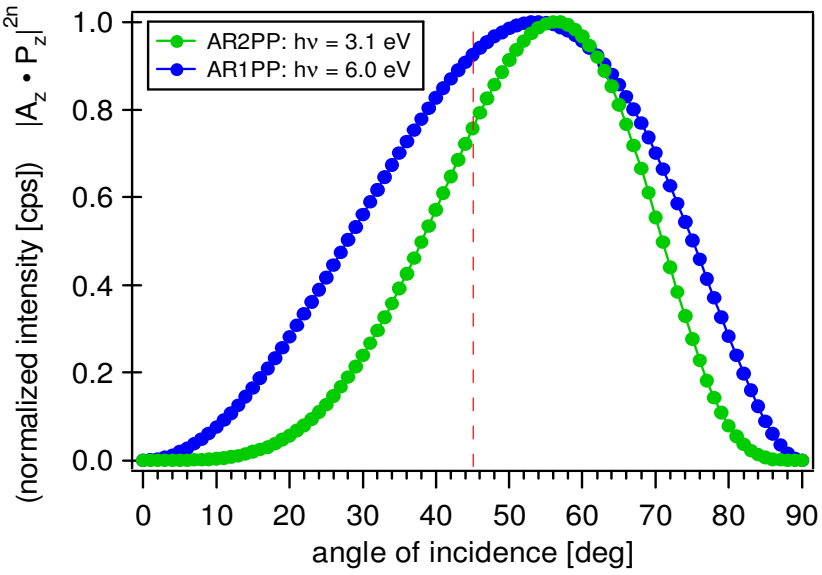

Figure 4.15 Angle-resolved photoemission intensity variation computed by $\left|A_z \cdot P_z\right|^{2n}$ for the $n = 1$ (1PP) and $n = 2$ (2PP) cases. The 45° angle of incidence (red dashed line) signifies the 0° (normal) emission angle for photoelectrons.

Because we applied 2 V of bias voltage to our sample, some deflection occurs on the photoelectron trajectories for off-normal directions. The deflection increases at larger exit angles. To quantify this effect, we calculated the apparent effective mass (m_{eff}) of photoelectrons for the Shockley surface state of Cu(111), which produced $m_{eff}/m_e = 0.30$; this is less than what has been reported in the literature, i.e., $m_{eff}/m_e = 0.40 - 0.45$ [156,157,3]. This means that the applied bias voltage enhances the effective dispersion and restricts the accessible **k**-space.

The $k_{\parallel}$-dispersion of the transition energy between the initial and final states for the direct photoexcitation is amplified by refraction at the solid-vacuum interface. The best agreement between experiments and our simulation is found for an inner potential $V_0 = V_R - \Phi = 5$ eV after correcting for the bias voltage-induced deflection by the effective mass of the Shockley surface state. Inner potentials of 4.0 eV [158], 5.0 eV [159], and 6.7 eV [160] reported elsewhere are very close to our findings. The reason for the ambiguity of the inner potentials stems from the intermixing of the lower sp-band and the d-bands of Ag(111) as well as using different models to calculate them. Considering these factors, one can conclude that there exists sizable uncertainty in the exact value of the potential step that leads to refraction, especially at very low energies as in 2PP measurements. This uncertainty could be of minor significance for band mapping in ARPES experiments with high photon energy; the error in the exit angles at low electron energies that is caused by the uncertainty in the inner potential, however, will overwhelm the effects caused by the band structure. If we reverse this assumption and suppose that the sp-band structure is sufficiently well-known from high energy ARPES experiments, we have a sensitive probe for the inner potential in the form of the refraction of very low-energy photoelectrons [147]. Thus, the measurement of the inner potential could be calibrated against sp-band photoexcitation that is well-defined in **k**-space. The information imparted by the inner potential is of paramount importance for the analysis of spectroscopic and imaging methods where low energy photoelectrons are employed such as LEED and PEEM [161].

Fig. 4.16 presents simple simulations of the refraction through the solid-vacuum interface for different kinetic energies (E_{kin}) and potential barriers (V_R). One can see that nearly all

photoelectrons originate from a cone of half opening angle of about 10° within the sample for the kinetic energy range in our experiments. This effect indicates that the detected region within the **k**-space is narrow. It, nevertheless, does not preclude band mapping of bulk bands of solids by AR2PP. With photon energies available for 2PP experiments (up to $E_{kin} \approx 4$ eV) and wide detection angles (up to $\theta_D \approx 70^o$), it is still possible to acquire substantial information (up to $\theta_{int} \approx 30^o$) on the dispersion of the parallel wave vector components [147].

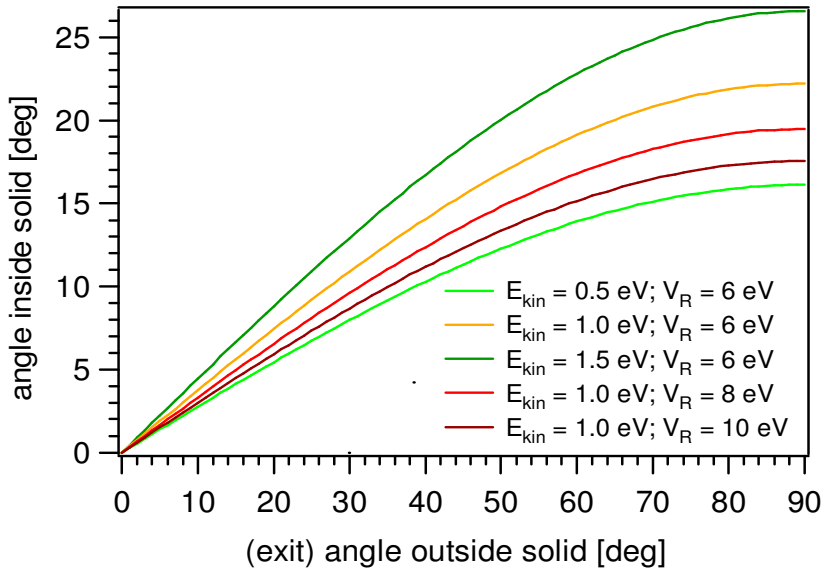

Figure 4.16 Refraction of photoelectrons through the solid-vacuum interface reduces the range of angles of electrons that can emerge from the solid.

According to our model formulated in equation [4.37] and shown in Fig. 4.15, angle-dependent distributions of photoelectrons from both 1PP and 2PP should be asymmetric with respect to the surface normal, and because of its higher order in light intensity the AR2PP distribution should be narrower than the AR1PP distribution. Once the data presented in Fig. 4.13 are translated into normalized photoemission intensity as a function of emission (detection) angle, as demonstrated

in Fig. 4.17, one notices that the model for AR2PP agrees very well with the data, whereas the data from AR1PP do not fit the simple Fresnel model. The relative deviation of the AR2PP data from the model at large negative exit angles (Fig. 4.17) can be ascribed to the unavoidable uncertainty in extracting the intensity sp-band transition peaks from a large background. This can also be seen at very low photoemission intensity at very large negative angles as shown in Fig. 4.13(b). To validate the model for both the 1PP and 2PP cases, Winkelmann [147] also compared the angle-dependence of the intensity of electrons excited from near the Fermi edge of Cu(001) in AR1PP and AR2PP spectra excited with comparable photon energies as for Ag(111). The Cu(001) intensities in both linear and nonlinear spectra agreed with our model based on Fresnel equations for the angle-dependent intensities. The ability of our model to predict the angle-dependent intensity distributions of AR2PP spectra from Ag(111) and AR1PP and AR2PP spectra of Cu(001) indicates that it can be generalized to other substrates. The AR1PP angular distributions for Ag(111) remain the exception.

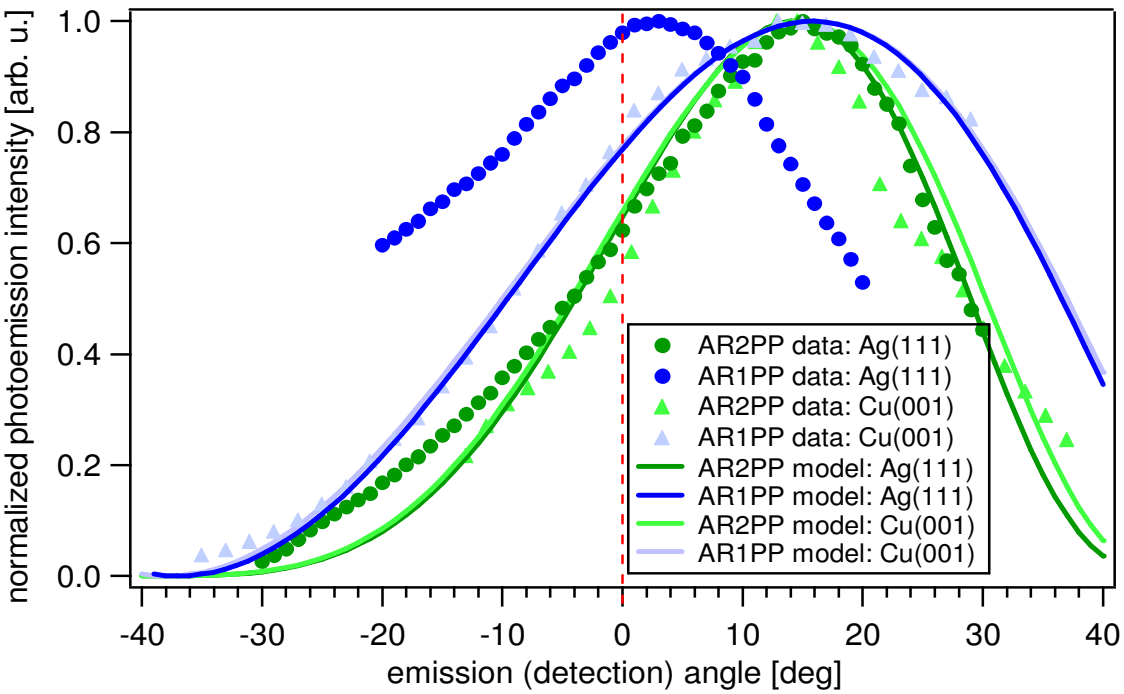

Figure 4.17 Normalized intensities of AR1PP (with $h\nu = 6.0$ eV) and AR2PP (with $h\nu = 3.1$ eV) experimental data taken for Ag(111) and Cu(001) surfaces and their comparison with our model based on the Fresnel equations. The calculations reproduce the experiments well except for the AR1PP of Ag(111). We attribute the discrepancy to interference with the surface photoemission, which is not accounted for in our model.

To scrutinize the origin of the anomalous AR1PP intensities for Ag(111), in Fig. 4.18 we compared the 2PP and 1PP spectra recorded at +20° and -20° from the surface normal. The sp-band transition peaks in 1PP are more asymmetric than those of 2PP. The peak-to-background intensity ratios in 2PP spectra remain nearly constant, while for 1PP high sp-band intensity at negative angles is associated with a low background, while at positive angles low peak intensity is associated with a high background. We attribute these anomalies, along with the strongly asymmetric line shapes, to the interference between the surface and bulk photoemission channels, which is well documented for the Ag(111) surface [102,103]. Because the p-component of the excitation light increases at large positive angles, the surface component corresponding to the background emission is enhanced; the fact that the bulk component does not follow the expectation from the Fresnel equation model suggests that the direct bulk transition is suppressed by destructive interference with the surface photoemission.

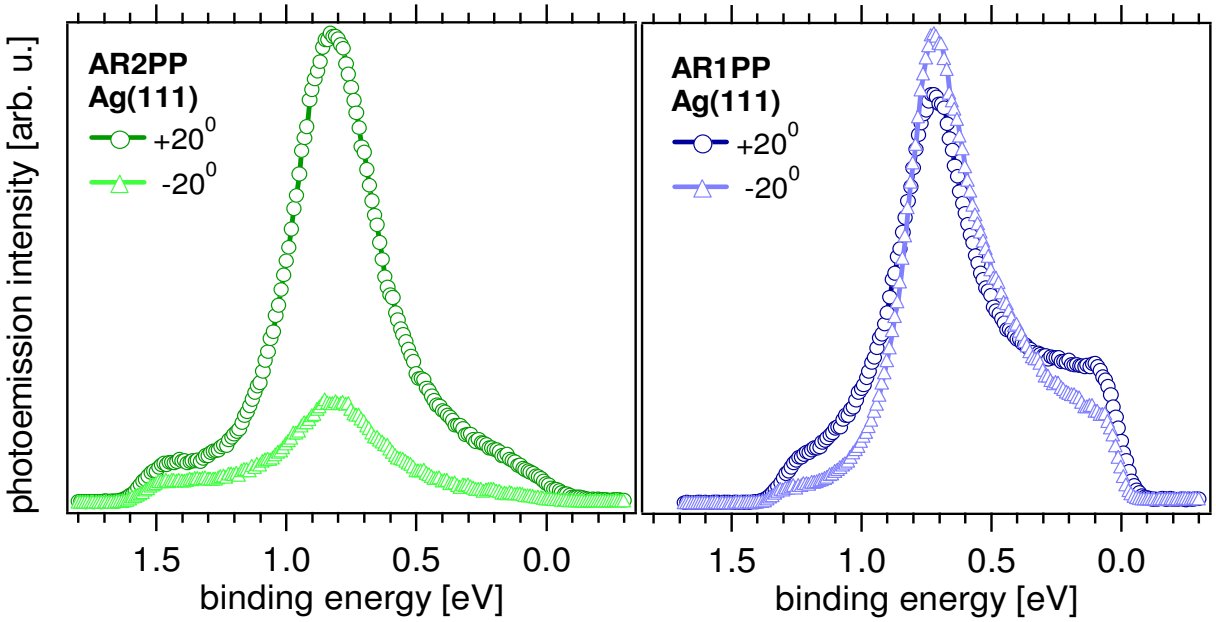

Figure 4.18 AR1PP and AR2PP spectra taken on Ag(111) surface at large angles from the surface normal (+20° and -20°) are juxtaposed to contrast the anomalous behavior of the 1PP data, which is attributed to the interference between the surface and bulk photoemission.

Therefore, we conclude that our model for the angle-dependent intensities accounts accurately for the bulk photoemission as long as the surface component is weak. In the case of AR1PP spectra of Ag(111), a strong surface contribution interferes with the bulk contribution in an angle-dependent manner, precluding analysis with our model based on Fresnel equations. Despite the approximations made, we have shown that it is possible to understand and model the electronic structure and nonlinear two-photon excitation processes at metal surfaces by means of AR2PP experiments [147].

Chapter-5

The Electronic Structure of Chemisorbed Alkali Atoms on Noble Metal Surfaces

As already discussed in Chapter-1, atoms and molecules can interact with surfaces through physical or chemical forces. Alkali atoms are strongly chemisorbed; at low coverage, they donate their valence s-orbital electron to the substrate, and exist in essentially ionic state. There are no spectroscopic features of this ionic bond in the valence state spectra of alkali atom modified metal surfaces. In this chapter, we explore systematically the unoccupied electronic structure of Li through Cs on Cu(111) and Ag(111) surfaces by photoinduced charge transfer excitation mediated 2PP spectra.

When an atom with discrete energy levels is brought into close contact with a metal substrate, which is characterized by a large electron density (~10^{23} per cm^3) [16], the unperturbed ground state energy levels of the atom interact with the continuum of metallic states [162]. Electrons in the metal are polarized by the external charges. Consequently, the energies of the atomic states shift in response to the induced potential, and broaden into a resonance due to the possibility of tunneling into and out of the continuum of electronic states of the substrate [38]. When electrons

tunnel out of singly occupied s-orbitals of atoms such as alkali atoms and are delocalized within the conduction band of the substrate, they leave a positively charged ion on the surface.

Fig. 5.1 illustrates the polarization of electrons in the metal by the external positive and negative charges of an alkali atom. The screening of the external charges induces fictitious image charges of opposite sign and equally distant, but on the opposing side of a fictitious image plane. The distance between the center of the adsorbate atom and the image plane along the z-axis at equilibrium is defined as the 'adsorption height' (R_{ads}). The attractive interaction between the ionic alkali atom core and the substrate is responsible for the strong chemisorption (~2 eV binding energy) of alkali atoms. The repulsive interaction between the *n*s valence electron of alkali atom and the negative image charge of the ionic alkali atom core destabilizes the valence state above E_F, whereby it becomes an unoccupied resonance.

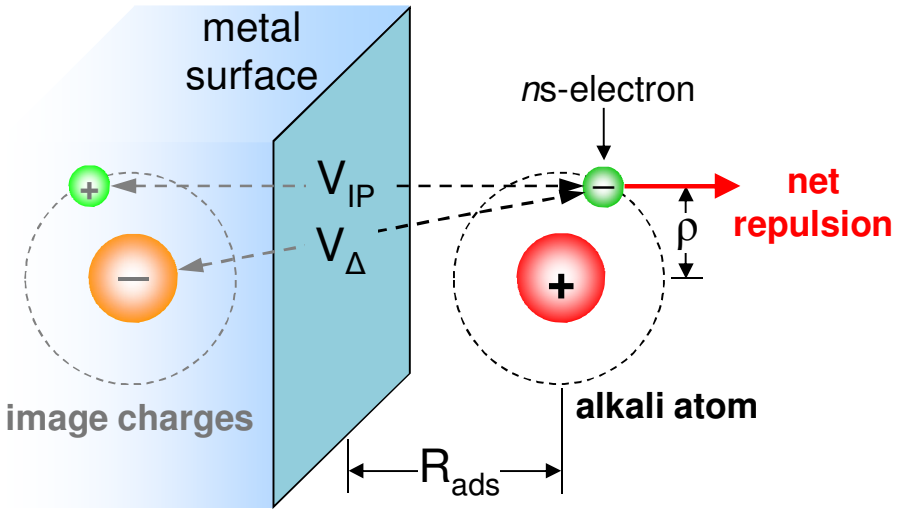

Figure 5.1 Alkali atom adsorption on noble metal surface at chemisorption distance (R_{ads}) leads to formation of the image charges and their interactions with one another. V_{IP} stands for the attractive image potential and V_Δ denotes the repulsive image-charge potential [163].

Noble metals are characterized by electronic structures consisting of sp-band electrons at E_F with slowly varying DOS and fully occupied d-bands several eV below E_F [33]. The sp-bands have structureless, slowly varying DOS distribution in the energy range of our experiments. Alkali atoms have simple electronic structures with one valence electron and low ionization potential. Therefore, alkali atoms form a very simple chemisorption system on noble metal surfaces where any change in the occupied and unoccupied electronic structure of the noble metal due to alkali atom adsorption becomes easy to discern.

Historically, there have been several chemisorption models to explain the alkali metal chemisorption [164]. We mainly consider (1) the Langmuir-Gurney model, and (2) the Muscat-Newns model, which are schematically displayed in Fig. 5.2. According to the Langmuir-Gurney model, when the *n*s valence electron of an alkali atom approaches a metal surface, it is repelled by the positive core-induced image charge within the metal, as shown in Fig. 5.1 [21,38,12]. Beyond a certain distance where the *n*s orbital crosses above E_F, electron tunneling into the unoccupied states of the metal becomes energetically feasible. At the equilibrium chemisorption distance R_{ads}, the *n*s orbital shifts a few eV upward owing to the Coulomb repulsion; the resonance bandwidth in the Langmuir-Gurney model is several eV because of facile tunneling into the conduction band of the substrate. While there is very low alkali atom coverage on the metal, the adsorbate atoms are nearly completely ionized, because only a small portion of the total *n*s state is occupied, as graphically depicted in Fig. 5.2(a). This model qualitatively agrees with the measured work function change curves as a function of alkali atom coverage; it has been generally accepted that the Langmuir-Gurney model describes the basic components of the alkali

atom chemisorption [20]. Later Gadzuk cast the Langmuir-Gurney model for alkali atom chemisorption within the Anderson impurity model [165].

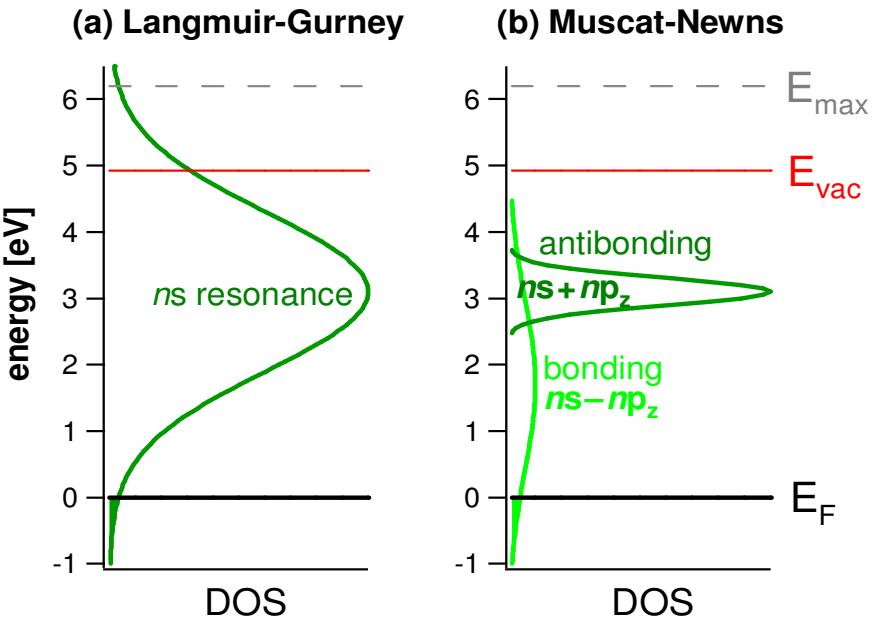

Figure 5.2 Two leading chemisorption models illustrating alkali atom adsorption on noble metals (here on Cu(111) surface) [164]: **(a)** Langmuir-Gurney model and, **(b)** Muscat-Newns model.

The Muscat-Newns model in Fig. 5.2(b) extended the Langmuir-Gurney and Anderson impurity models by considering the intra-atomic hybridization of the *n*s and *n*p$_z$ orbitals of alkali atoms in the proximity of a metal surface. The Muscat-Newns model predicts a pair of new bonding ($n\mathrm{s}-n\mathrm{p}_z$) and antibonding ($n\mathrm{s}+n\mathrm{p}_z$) orbitals, where the electron density is localized between the alkali atom and substrate or it is projected into the vacuum, respectively [58]. The formation (hybridization) of antibonding and bonding states is illustrated in Fig. 5.3. The bonding state has never been observed in photoemission spectra; it was speculated that the large bandwidth and small transition moment prevent detection of its *n*s DOS [39].

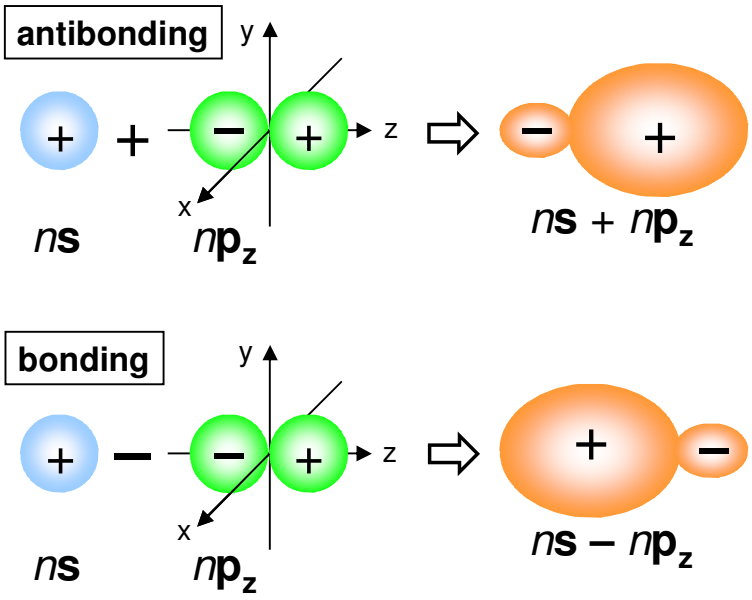

Figure 5.3 Hybridization of antibonding ($n\mathrm{s}+n\mathrm{p}_z$) and bonding ($n\mathrm{s}-n\mathrm{p}_z$) states, where *n*s and $n\mathrm{p}_z$ orbitals of the adsorbate atom interact [166,167].

In section 5.1, a systematic experimental study on the electronic nature of alkali chemisorbed noble metal surfaces is presented in conjunction with theoretical electronic structure calculations carried out by Zhao et al. [163]. Section 5.2 presents the experimental discovery and assignment of new higher lying alkali-induced states, which are antisymmetric with respect to the surface normal plane [168]. Section 5.3 concludes this chapter emphasizing the main points learned.

5.1 The Electronic Potential of Chemisorption Interfaces

Chemisorption of atoms or molecules on solid surfaces modifies the interfacial properties affecting processes such as charge transfer, catalysis, and energy level alignment in molecular electronics. One of the underlying problems in surface physics is to accurately describe the

electronic structure of the interface based on the intrinsic properties of the interacting materials [163]. The emerging field of molecule-based electronics requires the knowledge of how the properties of free adsorbates and bare surfaces determine the interfacial potential on the atomic scale [169,170,171,172].

5.1.1 Motivation

Though theoretical models based on first-principles can accurately predict the geometric structures of adsorbates on metals, routine methods for predicting the electronic structures of such interfaces are still not available [20, 28,52,54,55,173,174,175,176]. Creating a simple model, which can predict the electronic properties of a chemisorption interface from those of the unperturbed surface and free adsorbates and their fundamental interactions, is necessary for advancing the applications of molecule-based electronic devices [169].

Although chemisorption of alkali atoms on noble metal surfaces is one of the earliest and most prototypical systems, describing the chemisorption state presents both experimental as well as theoretical challenges. Despite sizeable charge transfer of the valence *n*s electron from the alkali atom to the substrate, the occupied DOS of the chemisorbed system is spectroscopically silent [39]. Because it is difficult to probe the occupied electronic structure, the extent to which the chemisorption bond can be considered as ionic or covalent has been controversial [35,177,178]. Spectroscopic methods, such as inverse photoemission and 2PP spectroscopy, are capable of probing the unoccupied DOS, which is the key to understanding the nature of alkali/noble metal chemisorption systems [47]. Particularly, the 2PP experiments have provided invaluable

information on how the interfacial electronic structure depends on the nature of adsorbate, alkali atom coverage, and the properties of the substrate [49,50,51,55,56,164,179].

A systematic study on the unoccupied electronic structure of alkali atom adsorbed noble metal surfaces as a function of the alkali atom period, coverage and the kind of the noble metal substrate has been hitherto lacking [163]. Such an investigation could reveal the nature of the chemical and physical interactions between alkali atoms and noble metal substrates. A comprehensive experimental 2PP study of alkali atom adsorption on noble metal surfaces is presented here, and a simple model based on the ideas first discussed by Langmuir [13] is implemented systematically for the first time by Zhao et al. [163] to rationalize the observed material and coverage trends. Our model accurately describes the electronic structure of the alkali atom/noble metal chemisorption interface; thus, it can be further generalized to other chemisorption systems where the valence charge is confined in electronic orbitals of the atomic or molecular adsorbate.

5.1.2 Fundamental Experimental Aspects

Bare Cu(111) and Ag(111) surfaces were cleaned by successive cycles of Ar^+-ion sputtering and high-temperature annealing under UHV conditions. Continuous effusive beams from commercial getter sources were used to deposit alkali atoms (Li, Na, K, Rb and Cs) onto clean surfaces. The orientation of the alkali atom source (Fig. 2.12) and the direction of ensuing beam was aligned very carefully to ensure uniform alkali atom coverage throughout the sample and thereby avoid surface electric field gradients from the local work function variations. All 2PP measurements

with alkali/Cu(111) were performed at 130 K temperature in the UHV chamber, and those with alkali/Ag(111) were performed at 90 K.

5.1.3 One-Photon Photoemission Experiments

Sequential 1PP alkali atom deposition measurements were performed on Cu(111) surface in order to explore, the Shockley surface state shift with respect to the work function change. Characterizing the occupied state spectrum by 1PP is necessary to understand the joint DOS in 2PP spectra. 1PP data acquisition commences with recording the spectrum of the clean surface followed by sequential spectra during the alkali atom deposition. With increasing the alkali coverage, the work function (Φ) decreases. This can be seen by the progressively decreasing low energy cut-off in the 1PP spectra. The spectra are as presented in Fig. 5.4, and the surface state (SS) shifts with respect to the work function shift are given in Fig. 5.5(a).

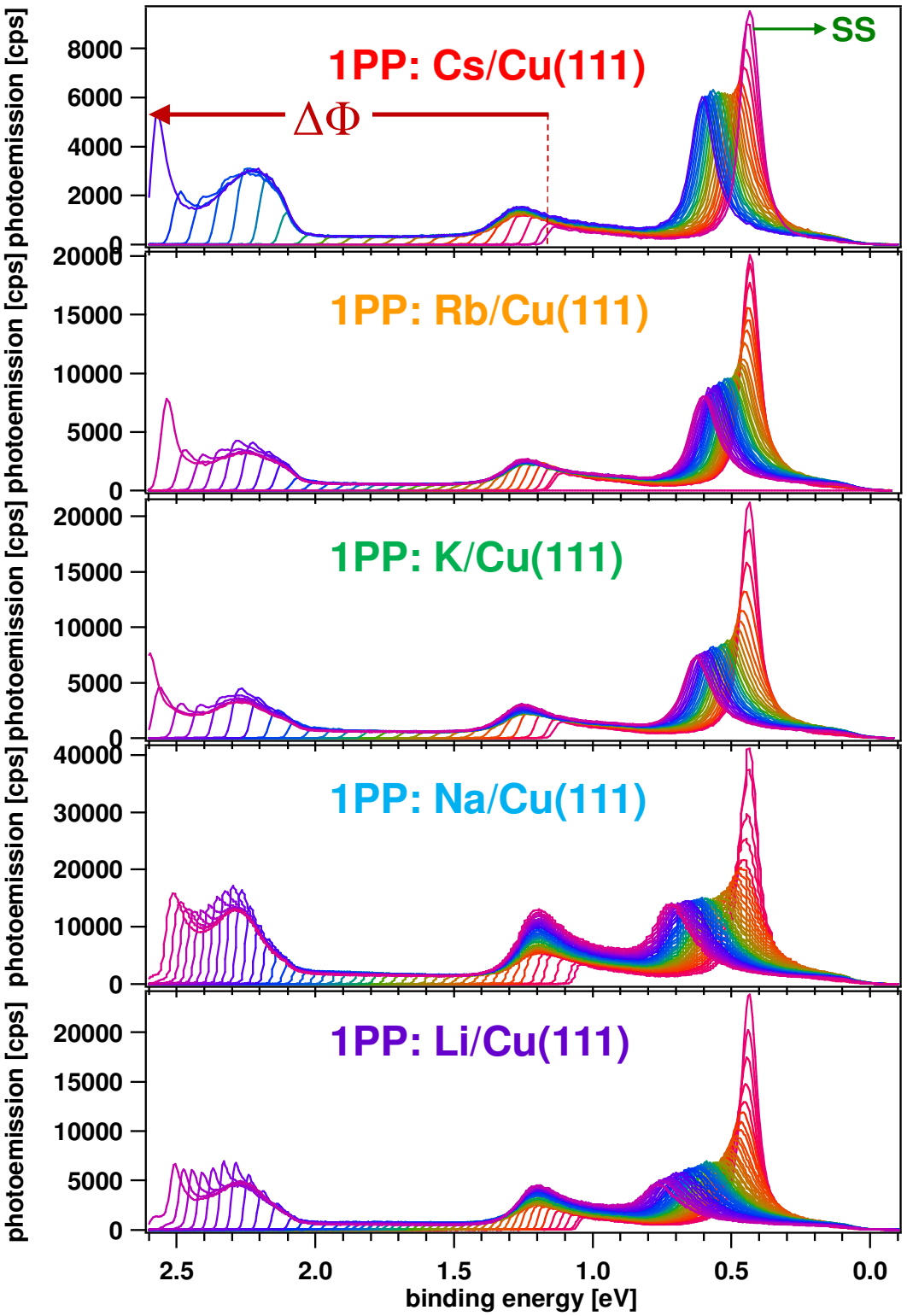

Figure 5.4 Sequential 1PP measurements for Cs through Li on Cu(111). Both the work function (Φ) and the Shockley surface state (SS) shift toward higher binding energy.

From Fig. 5.5(a) we can see that the shift of the surface state depends on the type of the alkali atom. Because we do not have an independent measure of the coverage, we can estimate the relative coverage by assuming that the shift occurs through transfer of a single electron from the alkali atom to the surface state thereby increasing its occupation, and therefore, lowering its binding energy. If the surface state shift can be related to the alkali atom coverage, we can convert the abscissa in Fig. 5.5(a) to the relative adsorbate coverage (σ) in Fig. 5.5(b) by

$$\Delta\Phi = 2\pi\mu\sigma, \qquad [5.1]$$

where the dipole moment is defined in terms of adsorption height as $\mu = 2R_{ads}$. Fig. 5.5(b) shows that the surface state shift depends on the dipole strength of the alkali atom and all alkali atoms produce nearly the same adsorbate coverage at the same surface state shift.

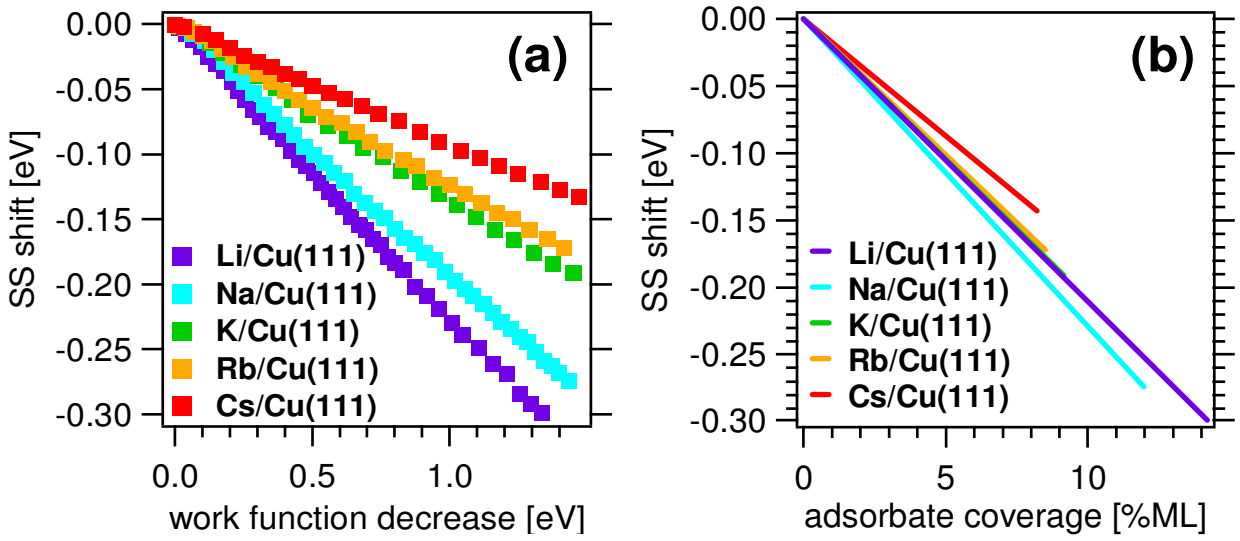

Figure 5.5 The downshift of the Shockley surface state (SS) as a function of **(a)** the work function decrease (ΔΦ) on alkali adsorbed Cu(111) surface and **(b)** the adsorbate coverage. The transformation from (a) to (b) is obtained by equation [5.1].

5.1.4 Two-Photon Photoemission Spectra of the Alkali Atom/Noble Metal Chemisorption Systems

2PP spectra of alkali atom covered surfaces were acquired in a similar fashion as 1PP spectra in Fig. 5.4. The 2PP spectra of alkali/Cu(111) and alkali/Ag(111) systems are presented in Figs. 5.6(a) and 5.7(a), respectively. The deposition was terminated when very intense 1PP signal appeared for $\Phi < 3.4$ eV. Space-charge effects caused by 1PP led to distortions in the 2PP spectra, restricting the maximum alkali coverage to less than about $10 \pm 1\%$ of a ML [49,163,180].

As alkali atoms are progressively deposited on Cu(111) and Ag(111) surfaces, their sequential 2PP spectra exhibit gradual chemisorption-induced changes such as work function reduction already seen in 1PP spectra and emergence of distinct resonance features [52,55]. The 2PP spectra demonstrate how the electronic structure of the alkali atom (Li through Cs) on Cu(111) and (Li, Na, K and Cs) on Ag(111) interfaces depends on the fundamental properties of the adsorbates, such as their sizes, ionization potentials, and how it evolves as a function of the adsorbate coverage.

The possible photoexcitation pathways for 2PP involving the charge-transfer excitation from the initial states of the substrate (bulk and surface), to the intermediate unoccupied *n*s resonance of alkali atoms are indicated for the $k_{\parallel}$-direction in Figs. 5.6(b) and 5.7(b). This unoccupied state is termed as 'antibonding resonance' ('AR' or '$m = 0$' resonance; green lines) due to its wave function symmetry and repulsive interaction with the substrate ('m' is the surface projection of the angular momentum '*l*' on the surface normal, i.e., the z-axis). Since the unoccupied orbital is

localized on alkali atom at low coverages used in our experiment, the optical transition does not have to conserve parallel momentum. Thus, the excitation process integrates over all momentum states (parallel and perpendicular) for which energy is conserved, and that have wave function overlap between the initial and intermediate states in the 2PP process [163]. For instance, the excitation can take place as shown in Figs. 5.6(a) and 5.7(a) from the partially occupied Shockley surface state (SS; red lines), which is located within the L-projected band gaps of Cu(111) and Ag(111) surfaces, provided that the maximum energy separation between the $m = 0$ and the surface state levels is at least as large as the photon energy of 3.1 eV. The excitation to $m = 0$ can also occur from the lower sp-band of noble metals for all initial states where energy is conserved. In order to complete the 2PP process, another photon must be absorbed to promote electron from the $m = 0$ state to above E_{vac} (orange lines, in Figs. 5.6(b) and 5.7(b)). The final states in the two-photon photoexcitation process can either be the upper sp-band of the noble metal, from which the photoelectron can escape into the vacuum, or free electron inverse LEED states, which exist for all energies and wave vectors above E_{vac} [84]. By recording a 2PP spectrum, one obtains information on the joint density of initial and intermediate states that mediate the 2PP process [163].

The most distinct spectroscopic feature of a pristine Cu(111) surface is the Shockley surface state located about 0.42 eV below E_F [3,181]. It is observed via nonresonant two-photon excitation, as described for Ag(111) in Chapter-4. At finite alkali atom coverage, we observe additional features associated with the coverage-dependent interfacial electronic structure. As alkali atoms are chemisorbed on Cu(111) surface, a new peak (labeled as '$m = 0$'; green line in Fig. 5.6(a)) emerges for all alkali atoms Li through Cs. Surprisingly, for Cu(111) this feature has nearly the

same energy of about 2.95 eV above E_F independent of the period of alkali atom. The 2PP intensity increases with the alkali atom coverage because the surface concentration increases, and where the surface state and $m = 0$ peaks overlap in 2PP spectra, due to the tuning of the $m = 0 \leftarrow SS$ transition at $k_{\parallel} = 0$ into resonance with the excitation laser pulse. The 2PP intensity reaches a maximum, when the surface state and $m = 0$ features overlap corresponding to resonant excitation with 3.1 eV photons. The resonance occurs at $m = 0$ energy of about 2.5 eV. For $m = 0$ energies above 2.5 eV, the resonant excitation occurs at $k_{\parallel} \neq 0$. When the $m = 0 \leftarrow SS$ transition at the Γ-point falls below the photon energy for all $k_{\parallel}$, the photoexcitation from the surface state can no longer contribute resonantly, and the photoemission intensity of $m = 0$ starts to decrease. The $m = 0$ state can still function as an intermediate state in 2PP, because it can be populated by photoinduced charge transfer excitation from the lower sp-band of Cu(111). The 2PP signal from the d-bands of Cu(111) can also be seen at the initial state energy of about -2.25 eV in Fig. 5.6(a); however, the d-bands are located too far below E_F to serve as initial states for the excitation of $m = 0$ in a 2PP process with 3.1 eV photons [182].

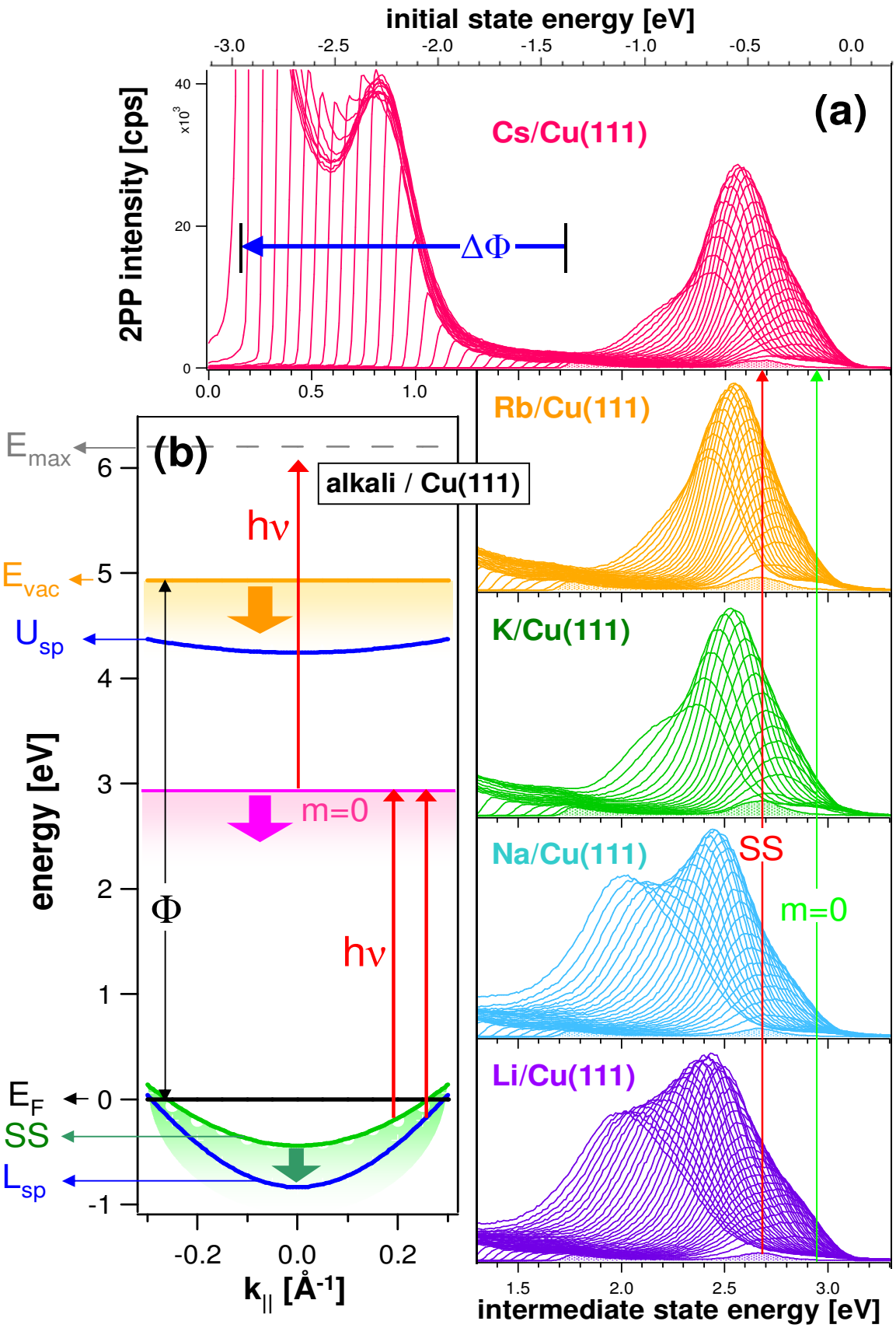
initial state energy [eV]
-3.0
-2.5
-2.0
-1.5
-1.0
-0.5
0.0
2PP intensity [cps]
x10^3
40
20
0
0.0
0.5
1.0
(a)
Cs/Cu(111)
ΔΦ
Rb/Cu(111)
K/Cu(111)
Na/Cu(111)
SS
m=0
Li/Cu(111)
1.5
2.0
2.5
3.0
intermediate state energy [eV]
(b)
alkali / Cu(111)
E_max
E_vac
U_sp
hν
m=0
Φ
hν
E_F
SS
L_sp
energy [eV]
6
5
4
3
2
1
0
-1
-0.2
0.0
0.2
k_|| [Å^-1]

Figure 5.6 The electronic structure of alkali atom modified Cu(111) surface: **(a)** The 2PP spectra of alkali atoms (Li through Cs) on Cu(111) surface during continuous alkali atom deposition plotted versus the initial (top horizontal axis) and intermediate (bottom horizontal axis) state energy [163]. **(b)** The 2PP excitation scheme for alkali atom modified Cu(111) surface for electron momentum parallel to the surface ($\mathbf{k}_{\parallel}$).

Because the $m = 0$ resonance is independent of the alkali atom period for Cu(111) surface, we decided to investigate the electronic chemisorption properties of alkali/Ag(111) surface, in order to understand whether this is a general or specific phenomenon. The 2PP spectra of alkali atom modified Ag(111) surface in Fig. 5.7(a) exhibit some differences as well as some similarities with alkali/Cu(111) surface. The surface state of the bare Ag(111) is located at -0.063 eV, as already discussed in Chapter 4.1 [3]. According to the spectra in Fig. 5.7(a), as alkali atom deposition commences, the $m = 0$ peak first appears at about 2.8 eV and steadily increases intensity as it shifts to lower energy. Unlike the Cu(111) case, the resonant $m = 0 \leftarrow \mathrm{SS}$ excitation energy always remains below the photon energy of 3.1 eV; therefore, the surface state cannot participate as the initial state for the resonant excitation of $m = 0$. Rather, at all coverages the only possible initial state is the lower sp-band. Because the top of the d-bands of Ag(111) is at about -4 eV below E_F [183], they cannot be observed with 3.1 eV photon excitation.

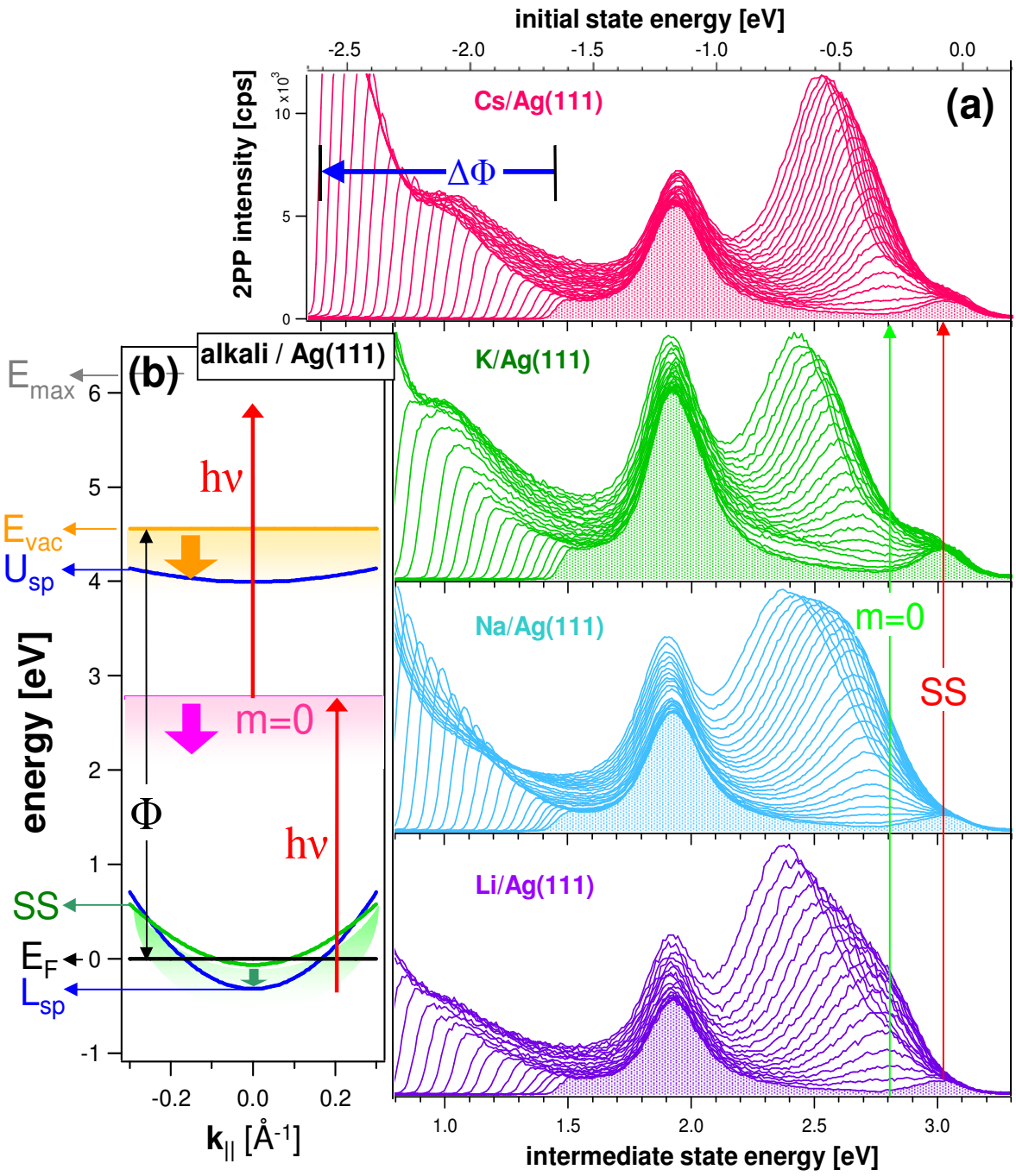

Figure 5.7 The electronic structure of alkali atom modified Ag(111) surface: **(a)** 2PP spectra of alkali atom (Li, Na, K and Cs) modified Ag(111) surface during continuous deposition plotted versus the initial (top horizontal axis) and intermediate (bottom horizontal axis) state energy. The SS is located much closer to E_F than in the Cu(111) case, precluding it as an initial state for the

excitation of the $m = 0$ resonance. **(b)** The surface projected band structure of Ag(111) showing possible photoexcitation pathways: the first step may occur for any $k_{\parallel}$ values as long as energy is conserved, while the second step is observed for $k_{\parallel} = 0$.

The 2PP spectra presented in Fig. 5.6(a) for the chemisorption of different members of the alkali atom group display remarkable similarity: In the zero coverage limit, not only does the $m = 0$ peak emerge at essentially the same energy level for Li through Cs, but with increasing coverage, it is also stabilized with the nearly identical $-(\Delta\Phi)^{3/2}$ dependence, as shown in Fig. 5.9(a) [184]. Because the surface state and $m = 0$ peaks overlap under near-resonant conditions, it is difficult to deconvolve their lineshapes to determine their peak positions precisely. Such deconvolution would require a realistic model for the photoexcitation of the $m = 0$ resonance from both the surface state and the bulk sp-band initial states at different $k_{\parallel}$ values. Hence, the position of $m = 0$ was only determined either far from or at the peak of the resonance with the surface state where deconvolution was not necessary.

By contrast, determination of $m = 0$ peak positions for alkali/Ag(111) is more straightforward. As can be seen in Fig. 5.7(a), the $m = 0$ peaks emerge at about 0.23 eV higher binding energy relative to the Shockley surface state and evolve progressively toward the higher binding energy. In the alkali/Ag(111) case, one notices that the shift of the $m = 0$ peak position with coverage of Li, and to a lesser extent Na, diverge from the trends for larger alkali atoms (Fig. 5.9(a)). Other experiments clearly revealed that the $m = 0$ peak gradually moved to higher energy and declined in intensity after the deposition was terminated, suggesting the disappearance of Li and Na from the surface. We ascribe this behavior to the binary alloy formation, where small alkali atoms

diffuse from the surface into the Ag(111) substrate, which is known to occur for other metals [20,19]. Nevertheless, the 2PP spectra of the larger alkali atoms on Ag(111) and alkali atoms on Cu(111) were quite stable. Measurements of the $m=0$ binding energy on Ag(111) surface verify that its independence of the alkali atom period is not purely coincidental. As seen in Fig. 5.8(a), however, the common asymptotic binding energy (i.e., at zero coverage limit) of the $m=0$ resonances relative to E_{vac} is about 0.15 eV smaller for alkali/Ag(111) chemisorption than for the alkali/Cu(111) one.

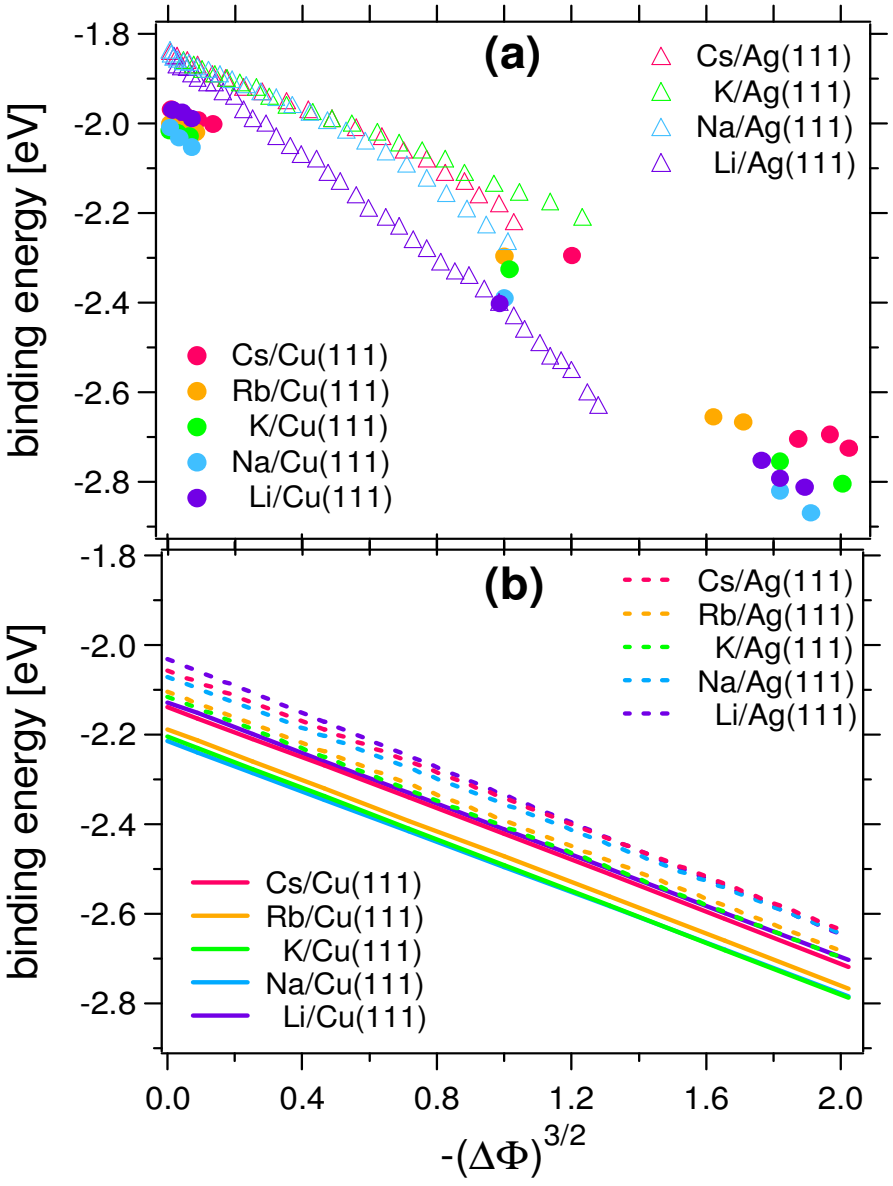

Figure 5.8 The $m = 0$ resonance binding energy (with respect to E_{vac}) variation as a function of the work function decrease [163]: **(a)** The experimentally observed $m = 0$ energies of various alkali atom/noble metal combinations versus $-(\Delta\Phi)^{3/2}$. For Cu(111), the $m = 0$ energies were obtained only at or far from the $m = 0 \leftarrow SS$ resonance. The deviation of the $m = 0$ shift for Li/Ag(111), and to a smaller extent Na/Ag(111), from the common $-(\Delta\Phi)^{3/2}$ form suggests the diffusion of small alkalis into the Ag(111) substrate [19,20]. **(b)** The calculated stabilization of the $m = 0$ binding energy for alkali adsorbed Cu(111) and Ag(111) surfaces by the surface dipole field (by Zhao [163]).

Despite the fact that the ionization potential of alkali atoms decreases consistently with the increasing size (i.e., increasing period number), their periodic differences as adsorbates on noble metals show up in the $m = 0$ linewidth, rather than in their $m = 0$ binding energy [163]. Small alkali atoms (e.g. Li and Na) adsorb closer the substrate metal, where the faster rate of elastic and inelastic electron transfer into the unoccupied states of the substrate conduction band gives rise to a broader $m = 0$ linewidth [55,173,174]. Nonetheless, the width of the $m = 0$ states are narrow (less than 200 meV), since the projected band gaps between the lower and upper sp-bands of Cu(111) and Ag(111) surfaces (shown in Figs. 5.6(b) and 5.7(b), respectively) limit the phase space for the decay through the elastic and inelastic electron decay channels [52,54,55,173,174]. Our results, in general, indicate that the Langmuir-Gurney model suffices to explain the fundamental adsorbate-substrate interactions and the ensuing changes in energy, but it cannot account for the experimentally obtained narrow $m = 0$ state linewidths.

5.1.5 The Model for the Alkali Atom/Noble Metal Chemisorption

The period independent energy of the *n*s resonance of alkali atoms and its characteristic stabilization with the surface alkali atom density for the Cu(111) and Ag(111) surfaces suggest that the universal behavior could be explained with a simple physical model. Therefore, we (Zhao [163]) compute the *n*s resonance energy for Li through Cs based on semi-empirical potentials for the alkali atoms (pseudopotentials [185]) and the noble metal substrates (Chulkov potentials [186]), which successfully simulate the electronic structures of the individual unperturbed systems, and their main mode of interaction via the Coulomb fields of the related charges.

The potentials of all participating uncoupled adsorbate ions and the host substrate surface, Cu(111), are sketched in Fig. 5.9. Furthermore, the resultant effective potential of the chemisorption systems paired at an appropriate chemisorption distance R_{ads} for Li/Cu(111) and Cs/Cu(111) are also presented therein. The uncoupled potentials align at their common reference level, i.e., E_{vac} [169]. The work function of Cu(111) ($\Phi = 4.91$ eV [64]) and the atomic ionization potentials (given in Table 5.1) are such that the *n*s valence states of alkali atoms straddle E_F of the substrate.

			adsorption distance: R_{ads} (a_0)	
	ionization potential		**Substrate**	
alkali atom	kJ/mol	eV	**Cu(111)**	**Ag(111)**
Li	520.2	5.392	1.882	1.829
Na	495.8	5.139	2.580	2.551
K	418.8	4.341	3.403	3.394
Rb	403	4.177	3.647	3.671
Cs	375.7	3.895	3.934	3.996

Table 5.1 The first two columns next to the alkali atoms show their ionization potentials [187]. Equilibrium adsorption distance (R_{ads}) of alkali atoms on 7×7 structures of Cu(111) and Ag(111) substrates (calculated by Zhao [163]) are displayed in the next two columns.

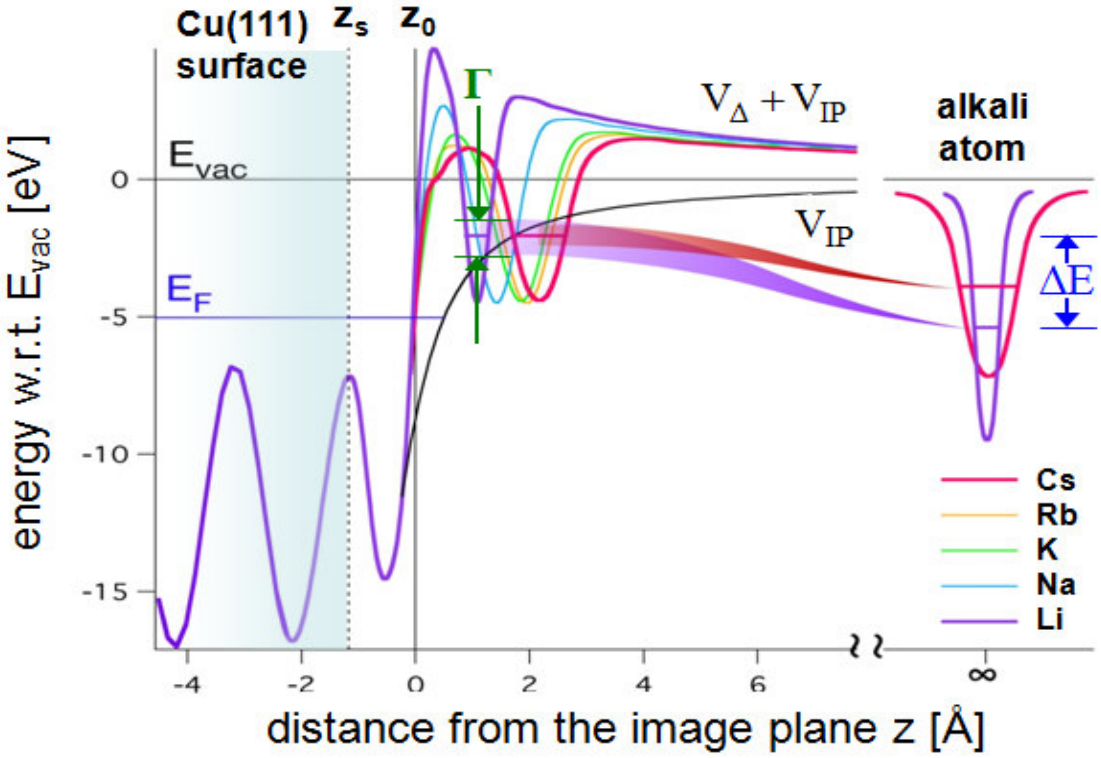

Figure 5.9 The effective one-electron potentials for alkali atoms Li through Cs atoms in front of Cu(111). The horizontal axis is referenced to the image plane (z_0). The image potential for bare surface V_{IP} (black line) and free alkali atom pseudopotentials are aligned to a common E_{vac}. At R_{ads}, the total effective potentials for Li/Cu(111) (purple) and Cs/Cu(111) (pink) are developed from the Chulkov potentials for Cu(111), which includes V_{IP} [186], the Li and Cs pseudopotentials [185], and the image-charge potential V_Δ. Horizontal lines for Li and Cs denote the *n*s energy levels of free atoms and at R_{ads}; the curved lines connecting the free and chemisorbed atom levels

signify the destabilization and broadening (Γ) of the *n*s states into surface resonances, as alkali atoms are brought to the surface.

The chemisorption process alters the electronic structures of the free adsorbate (atoms or molecules) via chemical and image-charge interactions, as well as interadsorbate interactions at higher coverages. The image-charge interaction, which is dominant for alkali atoms interacting with metal surfaces [21,38,188,189,190], arises from the many-body screening of an external charge by the conduction band electrons in metal. The screening response to an external charge can be described through the Coulomb field of its fictitious 'image' charge, which has the opposite sign and is located at the position of the mirror image with respect to the image plane. According to the Chulkov potential, which is employed to simulate the surface structure and the projected band gap of Cu(111) and Ag(111) surfaces, the image-planes are at 2.07 and 2.20 a_0 above the topmost surface layer, respectively [186]. As it is depicted in Fig. 5.1, when an *n*s valence electron of an alkali atom is brought to the adsorption distance with respect to the metal surface, it experiences an attractive Coulomb potential due to its own image given by

$$V_{IP} = -\frac{1}{4z}, \qquad [5.2]$$

and a repulsive potential due to the negatively charged image of the alkali atom ionic core

$$V_{\Delta} = \left((R_{ads} + z)^2 + |\vec{\rho}|^2 \right)^{-1/2}, \qquad [5.3]$$

where 'z' denotes the distance in the direction normal to the surface and $|\vec{\rho}|$ stands for the electron distance parallel to the surface from the adsorbate's center.

According to chemisorption model proposed by Gurney, transporting a free alkali atom to the adsorption distance R_{ads} elevates the energy of its *n*s valence electron through the Coulomb interaction with the conduction electrons of the substrate rendering it an unoccupied resonance in the electronic DOS [21]. Because the experimental linewidths of the *n*s resonances are sharp (less than 0.2 eV) and their energies relative to E_F are high (about 3 eV), according to this model, at low coverage chemisorbed alkali atoms should be fully ionized. As it is illustrated in Fig. 5.9, the image-charge interaction raises the *n*s valence electron energy with respect to the free atom energy by

$$\Delta E = \overline{V}_{IP} + \overline{V}_{\Delta} \approx +1/4R_{ads}\,, \qquad [5.4]$$

where the approximate averaged potentials $\overline{V}_{\Delta} \approx +1/2R_{ads}$ and $\overline{V}_{IP} \approx -1/4R_{ads}$ assuming the *n*s orbital to be centered on ionic core ($z = R_{ads}$, $|\vec{\rho}| = 0$). Figs. 5.6, 5.7, and 5.8 demonstrate that the quasistationary states corresponding to the *n*s valence electron localized on the alkali adsorbate is independent of ionization potential (I) and chemisorption distance (R_{ads}). The resonance energy, however, depends weakly on the species of the noble metal substrate; specifically the binding energies with respect to E_{vac} are on average 1.84 eV and 1.99 eV for alkali/Ag(111) and alkali/Cu(111) systems, respectively. We note that semi-empirical potentials similar to those presented in Fig. 5.9 have been used for a long time to address the scattering of alkali atoms or ions by metallic surfaces [190]. In that case, however, the potential and consequently the *n*s electron binding energy will evolve during the scattering trajectory according to the z-dependence of the Coulomb interaction outlined earlier.

In order to rationalize the period-independent binding energy of $m = 0$ states of alkali/noble metal chemisorption systems, we computed the energies of the alkali-localized quasistationary

states for a range of heights on Cu(111) and Ag(111) surfaces [163]. The time-dependent Schrödinger equation was solved [188,191] for an electron evolving under the influence of the effective potential constructed by adding the core-image repulsion V_Δ to the semi-empirical potentials of the free alkali atoms and the substrate (depicted in Fig. 5.10) [185,186]. To account for the change in the surface potential through the increase of the alkali atom coverages, which stabilizes the $m = 0$ state, the contribution from the surface dipole was also included in the effective potential by the term

$$\Delta E_\mu = -2(\pi\sigma)^{3/2}\mu R_{ads}. \qquad [5.5]$$

This potential can also be expressed in terms of $\Delta\Phi$ by [163]

$$\Delta E_\mu = -(\Delta\Phi)^{3/2}(2\mu)^{-1/2} R_{ads}. \qquad [5.6]$$

In order to compare with the experimental findings, the computed $m = 0$ state energies given in Fig. 5.10(a), which are obtained by solving the Schrödinger equation for the effective one electron potential, have to be taken at the correct adsorption heights R_{ads}. Because the empirical values of R_{ads} are available for a few chemisorption pairs, typically at 1 ML coverage [20], we computed the optimized structures including R_{ads} in the low energy coverage limit (see Table 5.1) by plane wave pseudopotential DFT computations for Li through Cs on Cu(111) and Ag(111) substrates [163,192].

To compare with the experimental measurements in Fig. 5.8(a), the calculated coverage dependent $m = 0$ binding energies for Li through Cs on Cu(111) and Ag(111) surfaces are presented in Fig. 5.8(b). Despite the significant differences between the *n*s electron binding energies of the free alkali metal atoms, in good agreement with the experimental trends, our

theoretical model predicts the common $m = 0$ binding energies of -2.17 and -2.05 eV for the chemisorbed Li through Cs, respectively, on Cu(111) and Ag(111) surfaces.

Based on the successful simulation of the electronic structure of chemisorbed alkali atoms with effective potentials, one can understand the period-independent nature of the $m = 0$ binding energies by simple arguments. Recalling that the *n*s valence electron localized around the alkali ion feels the repulsion ΔE owing to the image-charge interaction, its common binding energy (E_B) can be approximated by

$$E_B = \Delta E - I = \left(\frac{1}{4R_{ads}} \right) - I. \qquad [5.7]$$

This common binding energy evidently requires the period-dependent ionization potential (I) to be compensated by the net Coulomb repulsion (ΔE), which is inversely proportional to the adsorption distance, R_{ads}. Therefore, it suggests that there is an anticorrelation between I and R_{ads}, which can be clearly seen in Fig. 5.10(b) where 'I' is plotted against the calculated values of 'R_{ads}' for Li through Cs on Cu(111) and Ag(111) surfaces. This anticorrelation is a consequence of screening of the Coulomb potential of the alkali atom nucleus by its core electrons. Both the Coulomb potential and the Pauli exclusion determine how the ionic alkali core interacts with its *n*s valence electron and the conduction electrons of the substrate. The binding energy '–I' of free alkali atom *n*s valence electron is related to its chemisorption distance 'R_{ads}' via the same Coulomb interaction and Pauli exclusion.

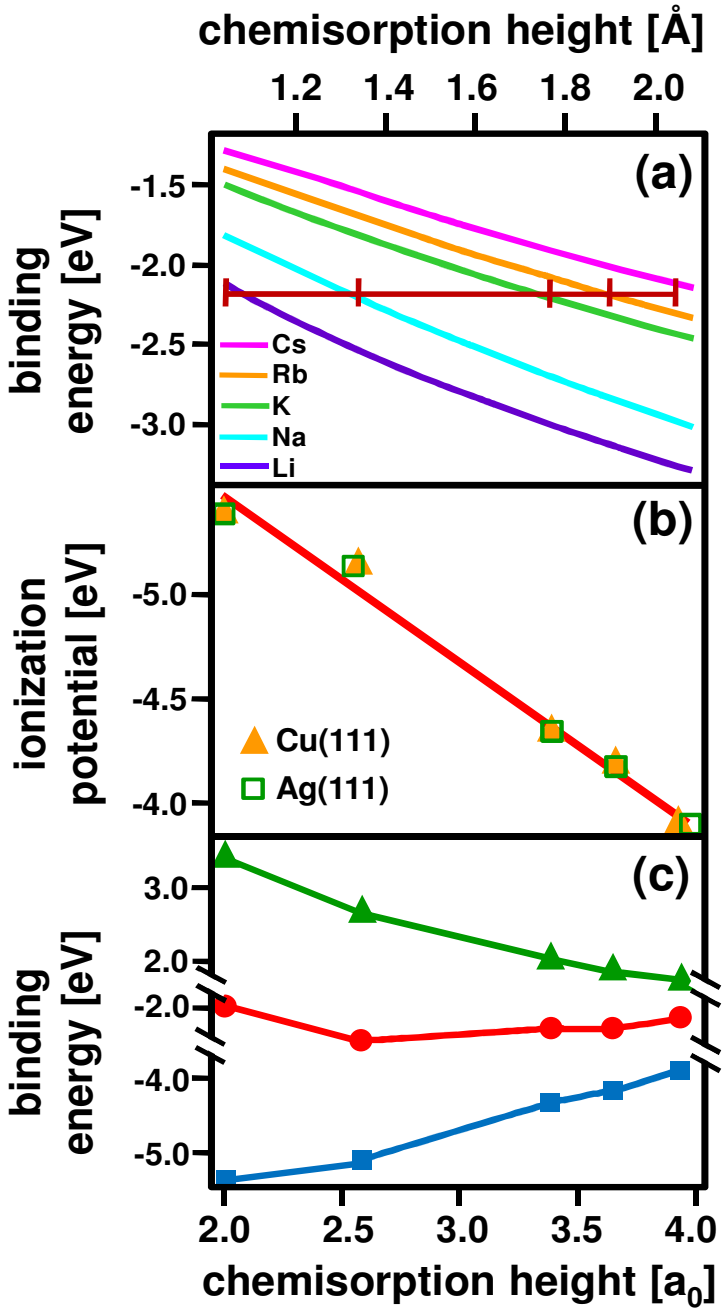

Figure 5.10 Computed results for the alkali/noble metal chemisorption [163]: **(a)** The energies of $m = 0$ states versus the chemisorption height (R_{ads} is given in terms of both atomic units a_0 (lower axis) and Å (upper axis)) for Li through Cs on Cu(111). The horizontal line at -2.17 eV is the computed average alkali atom $m = 0$ binding energy taken at the R_{ads} from DFT calculations (marked by the intersecting vertical lines). **(b)** The anticorrelation between R_{ads} for Li through Cs

(left to right) and the free atom ionization potentials 'I' for Cu(111) and Ag(111). **(c)** The electron binding energy of the free alkali ions (-I; blue squares) and the total level shift ΔE ($= \overline{V}_{IP} + \overline{V}_{\Delta} \approx +1/4R_{ads}$; green triangles) together define the $m = 0$ binding energy E_B ($= \Delta E - I$; red dots) for Li through Cs on Cu(111).

The computed values of the repulsive (ΔE) and attractive (–I) interactions and the resulting binding energy ($E_B = \Delta E - I$) of the *n*s valence electrons at R_{ads} on Cu(111) surface are depicted in Fig. 5.10(c). The electron binding energy of the free alkali atoms (–I; blue squares) and the image-charge repulsion (ΔE; green triangles) increase in magnitude with the opposite sign with decreasing size of alkali ionic core, and therefore R_{ads}. These periodic trends are mostly balanced in their sum E_B (red dots), which is nearly period-independent, and corresponds to an average $m = 0$ binding energy of -2.26 eV in agreement with the more elaborate wave packet propagation calculations (by Zhao [163]).

The experimental results and the successful theoretical models developed for the alkali atom–noble metal interactions in predicting the unoccupied electronic structure of the chemisorption interface corroborates the original proposals of Langmuir and Gurney that the interaction is largely of ionic character [13,21]. This standpoint does not disqualify that covalent interactions may play a minor yet increasingly significant role for smaller alkali atoms and for transition metal surfaces [34,174].

Our model, which was implemented by Zhao [163], accounts for only the Coulomb interaction and the Pauli exclusion experienced by the outermost (*n*s valence) electron of the free and

chemisorbed alkali atoms. It excludes the covalent interactions where bonding electrons occupy orbitals shared between the adsorbate and the substrate. It agrees well with our experimental findings, and explains the period-independent electronic structure of the alkali atom/noble metal chemisorptions interface. Therefore, with the free atom or molecule electron binding energy and the adsorption distance R_{ads} only, one can predict the energy of the quasistationary state at the adsorbate–metal interface with a well-defined charge configuration in both the highest occupied and the lowest unoccupied molecular orbitals (HOMO and LUMO, respectively).

The results presented here substantiate the fundamental role of Coulombic image charge interaction in determining the position of the HOMO and the LUMO of a wide range of molecules chemisorbed on metal surfaces. Though the role of the interfacial dipole potential is generally included in the discussion of orbital energy shifts upon chemisorption, the important V_{IP} contribution is often omitted [163]. The HOMO, and the ionization level in general, of adsorbates is raised by $\Delta E = 1/4R_{ads}$ owing to the interaction with the image charge. This effect compensates the change in the atomic ionization potential (I) for alkali atoms nearly exactly and gives rise to a period-independent binding energy of $m = 0$. Also, the LUMO, or affinity level, is stabilized by the electronic image potential by $-1/4R_{ads}$. This results in an energy difference between HOMO and LUMO equal to $1/2R_{ads}$. Our model for the electronic structure of alkali atom chemisorption is capable of reproducing these shifts as long as the electronic states are localized on the adsorbates; its extension and applications to a wide range of molecule/metal interfaces with definite electronic properties appear to be possible [163].

5.2 Discovery of the $m = 1$ Alkali-Induced Resonance by Angle-Resolved Two-Photon Photoemission

5.2.1 Introduction

In the previous section, we described the experimental and theoretical analysis of the lowest $m = 0$ resonance of alkali atoms on noble metals that was already predicted to exist by Gurney. Although alkali atoms have rich electronic spectra in the gas phase, so far nothing has been known experimentally or theoretically about higher lying electronic states above the $m = 0$ resonance, even though the existence of such resonances has been predicted by calculations of Nordlander and Tully at large atom-surface distances [38]. The first study of the higher lying electronic states at the chemisorption distance was the prediction of an $m = \pm 1$ (or π) resonance 0.5 eV above the m = 0 resonance for Cs/Cu(100) using the same theoretical methods as introduced in the previous section [193]. Such higher lying states could provide additional information on the alkali atom–noble metal interaction that could have broad implications to other adsorbates.

In this section, we describe the experimental discovery of this π-resonance by AR2PP. This new state is observed at $0.3 - 0.7$ eV above the $m = 0$ states, confirming the theoretical predictions [51,193]. Comparison between the experiment and theory shows that these newly found states are formed by the admixture of alkali atom *n*p and (*n*-1)d valence orbitals of the π-symmetry, i.e., they are antisymmetric with respect to the surface normal [163].

5.2.2 Angle-Resolved Two-Photon Photoemission Measurements

We investigated the $m = \pm 1$ symmetry states for Cs and K on Cu(111) and Cs, K, and Na on Ag(111). The experiments were carried out as in the previous section, except that we also measured the angle-resolved spectra using the same procedure as described in Chapter-4.2 for the bare Ag(111) surface.

Figs. 5.11 and 5.12 present the AR2PP spectra for Cu(111) and Ag(111) surfaces. The images on the left side (5.11(a), 5.11(c), 5.12(a), 5.12(c), and 5.12(e)) are the 2PP spectra presented as contour plots of 2PP intensity as a function of the emission angle and the intermediate state energy. The waterfall images on the right side (5.11(b), 5.11(d), 5.12(b), 5.12(d), and 5.12(f)) are the same angle-dependent 2PP spectra that have been displayed on a parallel momentum ($k_{\parallel}$) scale using the conversion given by equation [3.1]. Thus, the waterfall images show the 2PP intensity as a function of the parallel momentum and intermediate state energy. Although the original data are the same, the $\sin\theta$ dependence in equation [3.1] causes the conversion from angle to momentum to be nonlinear.

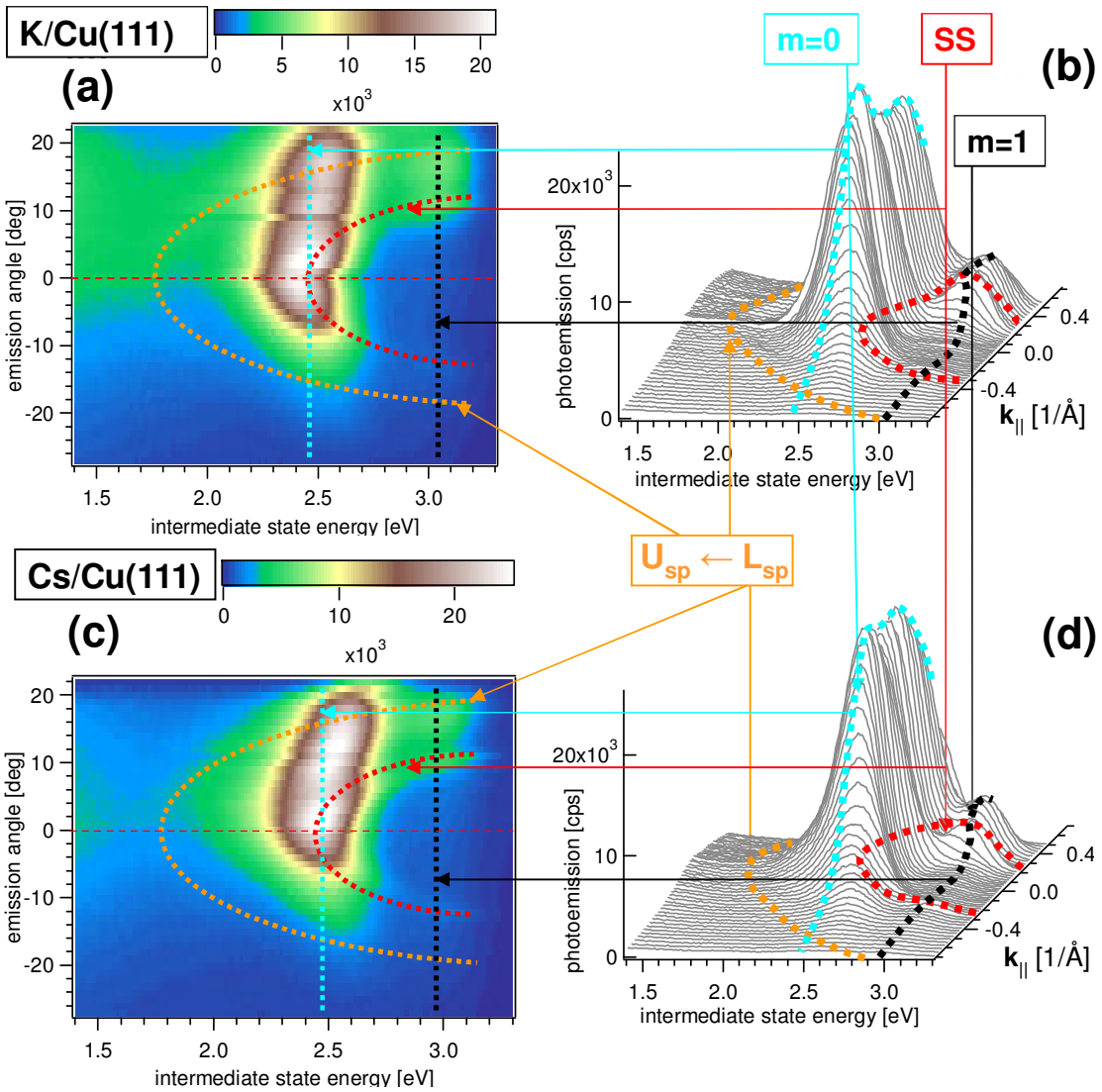

Figure 5.11 The AR2PP spectra of K/Cu(111) surface presented as contour plot **(a)** of 2PP intensity as a function of the emission angle and intermediate state energy. 3.1 eV corresponds to excitation from the Fermi edge. In **(b)** the same data are plotted as a waterfall image of 2PP intensity against the parallel momentum and intermediate state energy. The AR2PP spectra of Cs/Cu(111) surface are also presented as a contour plot **(c)** and the waterfall image **(d)**. The spectroscopic features corresponding to the resonant interband ($U_{sp} \leftarrow L_{sp}$) excitation (orange dashed lines), the Shockley surface state (SS; red dashed lines), the alkali localized $m = 0$ (σ; blue dashed lines) state and the $m = \pm 1$ (π; black dashed lines) intermediate states are indicated.

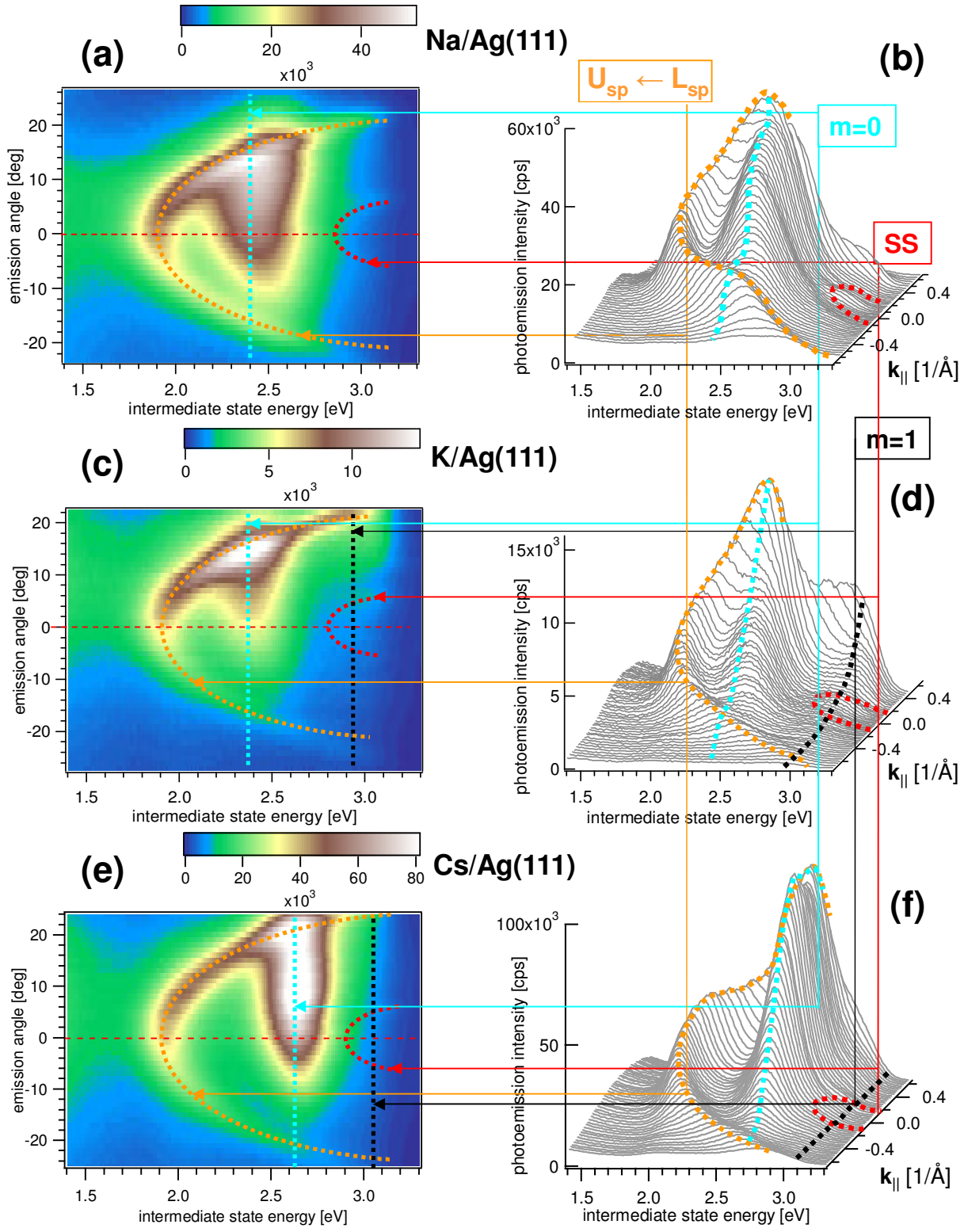

Figure 5.12 **(a)** The AR2PP spectra of Na/Ag(111) surface presented as contour plot of 2PP intensity as a function of the emission angle and intermediate state energy. **(b)** The same data are

plotted as a waterfall image of 2PP intensity against the parallel momentum and intermediate state energy. The contour plots **(c)** and **(e)** and the waterfall images **(d)** and **(f)** of AR2PP spectra of K/Ag(111) and Cs/Ag(111), respectively, are also presented. The spectroscopic features corresponding to the resonant interband ($U_{sp} \leftarrow L_{sp}$) excitation, the Shockley surface state (SS), the alkali localized $m = 0$ (σ) state and the $m = \pm 1$ (π) intermediate states are indicated as in Fig. 5.11. The π-resonance is not observed for Na/Ag(111) surface.

Figure 5.13 shows the energy level structure for K adsorbed Cu(111) and Ag(111) surfaces, the $k_{||}$-dispersion of the of the substrate bands, and 2PP excitation pathways that explain some of the features in AR2PP spectra in Figs. 5.11 and 5.12. Intensity of the 2PP spectra at finite alkali coverage have contributions from photoexcitation from the Shockley surface state and lower sp-band of the substrate. The 2PP signal can be resonant with the adsorbate resonances, or occur through virtual intermediate states, as discussed in Chapter 4.1. For reasons that are unknown, the lower sp-band features in Cu(111) are much less prominent than for Ag(111). The alkali atom resonances, which do not disperse with $k_{||}$, can act as intermediate states in 2PP process as long as energy conservation is satisfied.

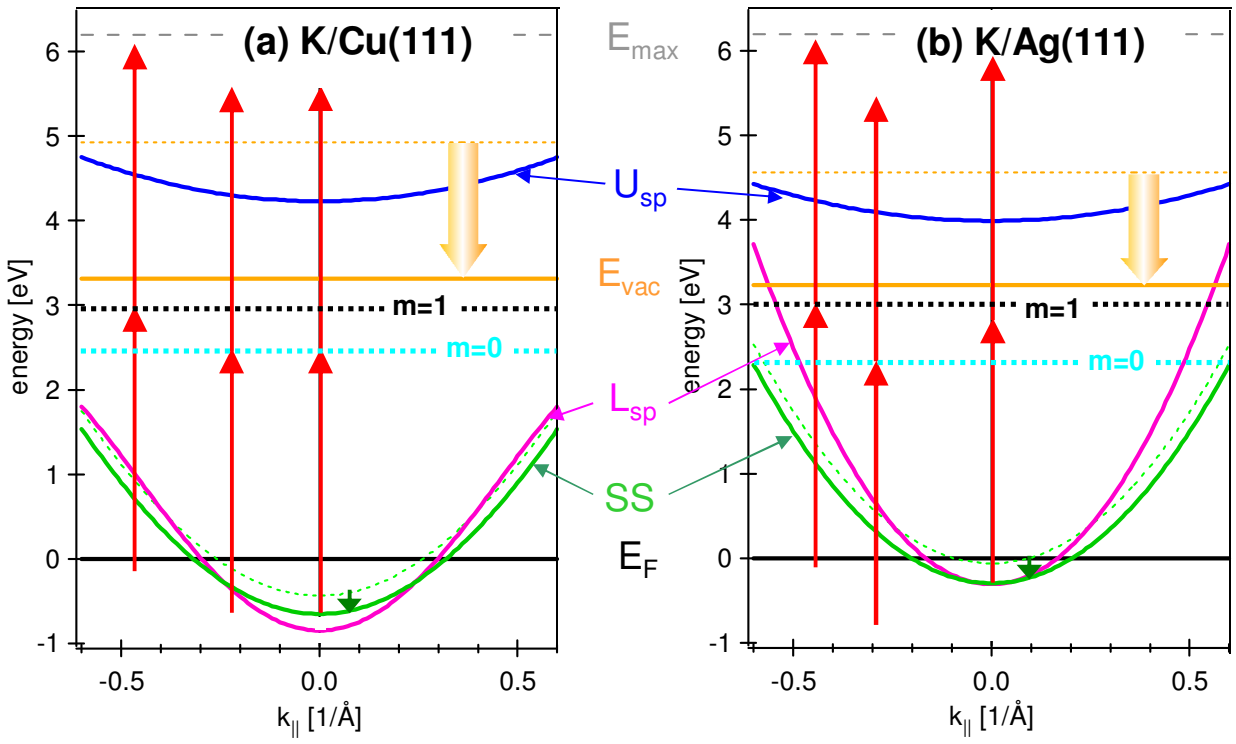

Figure 5.13 Two-photon photoexcitation pathways (red arrows) for **(a)** K/Cu(111), **(b)** K/Ag(111) surfaces and the corresponding energy diagrams of the states with respect to parallel momentum ($\mathbf{k}_{\parallel}$). The clean surface (dashed) and shifted (solid) E_{vac} (orange) and SS (green) energies are indicated. The $m = 0$ and $m = \pm 1$ resonance energies correspond to the observed values in Figs. 5.11 and 5.12.

For all of the chemisorption pairs studied here, except for the Na/Ag(111) surface, in addition to the $m = 0$ resonance, alkali atom adsorption induces another feature at higher energy, which has minimum intensity for normal emission and peaks for emission angles of approximately $\pm 17° \pm 2°$. Based on the calculations of Borisov et al. [51,193] using the same model potentials as in section 5.1, as well as the symmetry implied by AR2PP spectra, we assign these new resonances for K and Cs adsorbed on Cu(111) and Ag(111) surfaces to states with $m = \pm 1$, or π-symmetry

[168]. These new states appear about $0.3-0.7$ eV above the $m=0$ resonance. These newly discovered resonances have to correspond to $|m|>0$ symmetry, i.e., states described by wave functions with a nodal plane in the surface normal direction.

Whereas the $m=0$ resonance, which corresponds to the *n*s and *n*p_z hybridized orbitals, is symmetric with respect to the normal emission angle, the $m=\pm1$ resonance, which corresponds to the hybridization of *n*p_x and *n*p_y with the (*n*-1)d orbitals, is the lowest energy antisymmetric state. Specifically, the *n*p_x and *n*p_y orbitals, which lie in the plane parallel to the surface, give rise to two degenerate π-resonances [168]. As Figs. 5.11(a) and 5.11(c) demonstrate, the AR2PP intensity of the $m=\pm1$ resonance on alkali adsorbed Cu(111) surface manifests a minimum for the emission normal to the surface and distinct maxima at emission angles of $\pm17°\pm2°$. Similar angle-dependent behavior is observed for K and Cs on Ag(111) (Figs. 5.12(c) and 5.12(e)); however, the angular photoemission maxima are obscured by spectral overlap with the more intense $U_{sp}\leftarrow L_{sp}$ two-photon transition. At the angle where the dispersive and nondispersive states overlap, the $m=\pm1$ resonance serves as a resonant intermediate state in the 2PP process; and therefore, its angle-dependent intensity reflects the resonance condition in addition to the wave function symmetry. For both substrates, the photoemission intensity with respect to the surface normal is not symmetric, because rotating the sample alters the Fresnel factors, as discussed in Chapter-4.2 [147]. As a representative example of all of the surfaces discussed here, we give the calculated photoemission angular distribution for the $m=\pm1$ resonance of Cs/Cu(111) case for $m=\pm1$ (Fig. 5.14) based on the wave functions from our calculations. The calculated angular distribution has a minimum for normal emission and a peak at 21° from the surface normal, in agreement with the experimental data [168].

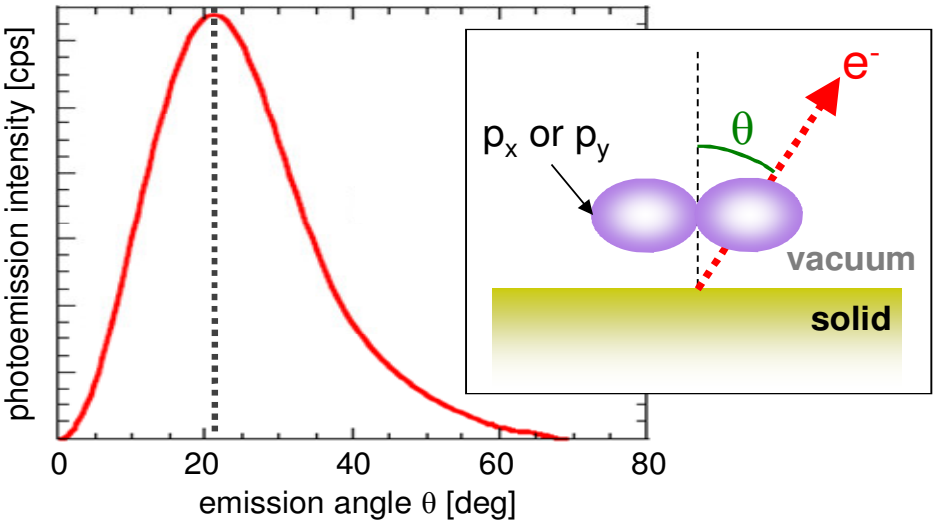

Figure 5.14 Calculated angular distribution of photoelectrons from the quasistationary $m = \pm 1$ resonance on Cs/Cu(111) by Borisov. The calculated photoemission angular distribution from from the np$_x$ and np$_y$ orbitals of Cs atom parallel to Cu(111) surface exhibits a maximum at $\theta = 21^\circ$ from the surface normal [168].

All of the alkali-localized resonances undergo energy downshift toward E_F at finite alkali coverage as discussed for the $m = 0$ resonance in section 5.1 [45,49,51,163]. Within the range of alkali atom coverage permitted by the work function decrease in our experiments, which is more or less 1.5 eV, the stabilization by the surface dipole fields of K and Cs allows observation of both the $m = 0$ and $m = \pm 1$ resonances. Unlike the K and Cs cases, the Na/Ag(111) surface does not reveal any feature of $m = \pm 1$ symmetry, most likely because its energy is more than 0.7 eV above the $m = 0$ state, and thus, it cannot be excited in our experiments. The reason why the $m = \pm 1$ resonance may be at a higher energy for Na, than for K and Cs, is because for Na the $(n-1)$d orbitals are not available to hybridize with the 3p$_x$ and 3p$_y$ orbitals.

Calculations by Borisov et al. [168] predict the location of the $m = \pm 1$ state to be about $0.8 - 1.1$ eV above the $m = 0$ state. Thus, the predicted energy splitting is larger than the experimentally observed values of $0.3 - 0.7$ eV. This can be partially ascribed to the finite adsorbate coverage used in our experiments. The $m = 0$ and $m = \pm 1$ symmetry states undergo different energy shifts due to the potential of the adsorbate dipole layer. In addition to the simple 'electrostatic potential', one also has to take into account the interaction between π-orbitals situated at neighboring adsorbates, which can be larger for $n\mathrm{p}_x$ and $n\mathrm{p}_y$ orbitals than for the ns and $n\mathrm{p}_z$ orbitals [168].

In summary, for alkali atoms on Cu(111) and Ag(111) surfaces we report the discovery of a theoretically predicted π-symmetry ($m = \pm 1$) resonance, in addition to the well-known σ-symmetry ($m = 0$) resonance. These results should be of general nature for metal substrates having a projected energy band gap and adsorbate atoms, which chemisorb mainly in an ionic state. Our experimental observation of an antisymmetric state with respect to the surface normal, which responds to the external electromagnetic fields and resonant states of the substrate with different symmetry selection rules than the well-known $m = 0$ state, opens up new possibilities to study how electronic symmetry influences the adsorbate electronic structure and interactions with the substrate [168]. The discovery of the $m = \pm 1$ states also provides primary information on the influence of atomic orbital symmetry on the angle-dependent photoelectron distribution from a surface that was predicted more than 30 years ago by Gadzuk [194], and exploited in studies of the structure and dynamics of gas phase molecules [195]. Although photoemission spectroscopy has been used for band mapping in solids and wave function imaging in the gas phase [196,197], the

imaging of the wave function angular distributions of chemisorption systems remains a largely uncharted territory. Our work may stimulate fruitful studies in this field.

5.3 Conclusion to Alkali Atom Chemisorption on Noble Metals

Stimulated by theoretical calculations of Borisov et al., we have carried out 2PP and AR2PP experiments on the electronic structure of alkali atoms on noble metal surfaces [163,168]. The model for the interaction of alkali atoms with noble metals successfully describes the unoccupied electronic structure of the chemisorption interface, which was originally proposed by Langmuir and Gurney [13,21]. Our systematic and comprehensive measurements reveal interesting periodic insensitivity of the interfacial electronic structure that allows us to develop a simple and nearly quantitative model for the alignment of the adsorbate-induced resonances. The discovery of a higher lying π-symmetry state on the same chemisorption systems at nearly the expected energy as observed in our experiments substantiates the theoretical model [51,193]. Our experimental investigations coupled with theory enabled us to acquire significant insight into one of the simplest chemisorption interfaces that could be extended to developing a general understanding of the band alignment at metal-molecule interfaces.

Chapter-6

Surface Femtochemistry: Observation of Frustrated Alkali Atom Desorption

Observation of transient intermediate states of a surface chemical reaction is one of the most fundamental problems in surface science [55,198]. The femtochemistry for gas phase chemical reactions have been pioneered by Zewail and coworkers [199]. With femtosecond laser based pump–probe spectroscopic methods, it is now possible to follow the outcome of light-induced chemical reactions in the gas and solution phase on the time scale of the nuclear vibrational motion.

Observing the process of photoinduced chemical reactions on solid surfaces is also of considerable fundamental and technological interest; electronic excitation of surface adsorbates gives rise to considerably different reaction products and product energy distributions than results from conventional thermal activation [56]. A particularly powerful way to follow photoexcitation-induced nuclear dynamics on solid surfaces is by TR2PP [54,55,56]. In surface femtochemistry, ultrafast laser pulses excite adsorbates to dissociative potential energy surfaces and follow the nuclear motion through the evolution of the surface electronic structure. This can

be accomplished with two ultrafast optical pulses to start the desorption process, and after a variable time delay, interrogate the transition state through changes in 2PP spectra during the course of a chemical reaction [51,200]. In addition to the electronic response to the nuclear motion, TR2PP also probes the decay of the excited state population through the elastic resonant charge transfer (RCT) from the adsorbate to the conduction band continuum of the substrate, as well as the inelastic electron-electron scattering with electrons in the Fermi sea [201,202]. The excited state wave packet motion can also change the 2PP process, as we will argue in the case of Cs/Ag(111). So far, surface femtochemistry techniques have been applied to the frustrated desorption of Cs from Cu(111) surface [54,55,56, 203] and electron solvation in protic solvents on metal [204] and semiconductor [205] surfaces.

6.1 Why Ultrafast Techniques?

The outcome of a surface photochemical reaction can be studied either by postmortem methods that detect the desorbed reaction products in the gas phase, or directly on surface during the course of chemical transformation. Because the ultrafast electronic relaxation of adsorbates quenches the dominant dynamical processes before the reaction products can desorb, it is difficult and questionable to extrapolate from the exceedingly small quantum yields and energy distributions of the gas phase products back to the dynamics that led to the observed outcome. The development of femtosecond lasers with pulse durations shorter than the typical period of molecular vibration has made it possible to observe chemical reactions directly on surface in terms of coherent nuclear wave packet motion and even to devise optical fields that can change

their course of evolution, provided that the electronic relaxation does not quench the nuclear motion [56,203,206].

The lifetimes of electronic excitations and their decay pathways on solid surfaces are poorly known. A pessimistic picture emerges from estimates of sub to few femtosecond time scale [207,208] excited state lifetimes based on the analysis of spectroscopic linewidths of the unoccupied states. The main relaxation pathway is RCT from the adsorbate-localized states to the propagating states of the substrate conduction band continuum. Direct TR2PP measurements, however, often show that either or both the ultrafast dephasing and inhomogeneous broadening dominate the linewidths, while the actual excited state lifetimes are considerably longer [180].

Photodesorption is one of the most fundamental surface photochemical processes. Alkali atoms on noble metal surfaces are particularly well-suited for such studies because of their strongly bound ionic ground states, and dissociative neutral exited states. Their simple electronic structures and relatively long excited state lifetimes ($10-50$ fs) have attracted several experimental and theoretical investigations of the photodesorption dynamics [54, 209]. The Cs/Cu(111) chemisorption system has been of particular interest, because the relatively long (~50 fs) lifetime of its $m = 0$ resonance facilitates the observation of its nuclear wave packet motion despite the large mass of Cs atoms [54]. The photoinduced charge transfer excitation prepares the excited state consisting of a neutral Cs atom at the equilibrium position of the ionic ground state, triggering repulsive forces that initiate the dissociative wave packet motion. Interferometric time-resolved two-photon photoemission (ITR2PP) measurements reveal the nuclear wave packet motion during the initial phase of the photodesorption process, which is

eventually terminated by the nonadiabatic transition to the ground state potential through RCT of 6s electron back to the substrate [56]. This frustrated photodesorption of alkali atoms has been the subject of several theoretical publications, which aim to describe the excitation, deexcitation, and wave packet propagation dynamics [210, 211, 212, 213]. Questions remain as to whether similar photodesorption dynamics could be observed for other alkali/noble metal systems. Theoretical calculations for alkali atoms on Cu(111) and Ag(111) surfaces predict the Cs/Cu(111) system to be unique in decoupling the $m = 0$ resonance from the various elastic and inelastic decay channels [28,173,214]. Previous measurements for both surfaces seem to concur [55,214]; in this Chapter, however, we show this pessimistic conclusion to be unfounded.

Photoexcitation in a surface photochemical reaction could proceed, as shown in Fig. 6.1, either directly by the optical excitation of an unoccupied state of adsorbate from the occupied states of the adsorbate or the substrate, or indirectly by the scattering of photogenerated hot electrons from the substrate to the adsorbate [55]. Most literature on surface photochemistry invokes the indirect, hot electron mechanism [215,216,217,218], whereas 2PP spectroscopic studies nearly always find the direct charge transfer excitation from the substrate to be dominant [55,105]. The resonance behavior, for example, for the $m = 0 \leftarrow SS$ excitation for Li through Cs on Cu(111) in Fig. 5.6(a), shows that the direct mechanism dominates for alkali atoms on noble metals.

The electronic quenching of an excited state, which is largely responsible for the low efficiency of surface photochemical reactions, can occur either through RCT or electron-electron scattering. Although it is difficult to distinguish experimentally, theoretical calculations predict that for alkali atoms either electronic quenching mechanism can dominate depending on the properties of

the adsorbate and the substrate [28,173]. The unusually long lifetime of the $m = 0$ resonance of Cs on Cu(111) has been attributed to suppression of RCT by the projected band gap of Cu(111) [28,173]. Because of the band gap, tunneling occurs in an off-normal direction into the resonant conduction band states with $k_{\parallel} \neq 0$. Compared with the normal direction, this involves a larger tunneling barrier, which suppresses RCT so that the inelastic decay channel can dominate for Cs/Cu(111). For smaller alkali atoms that adsorb closer to substrates, e.g., Li and Na, the tunneling barrier is thinner, and therefore, RCT dominates over the inelastic decay channel.

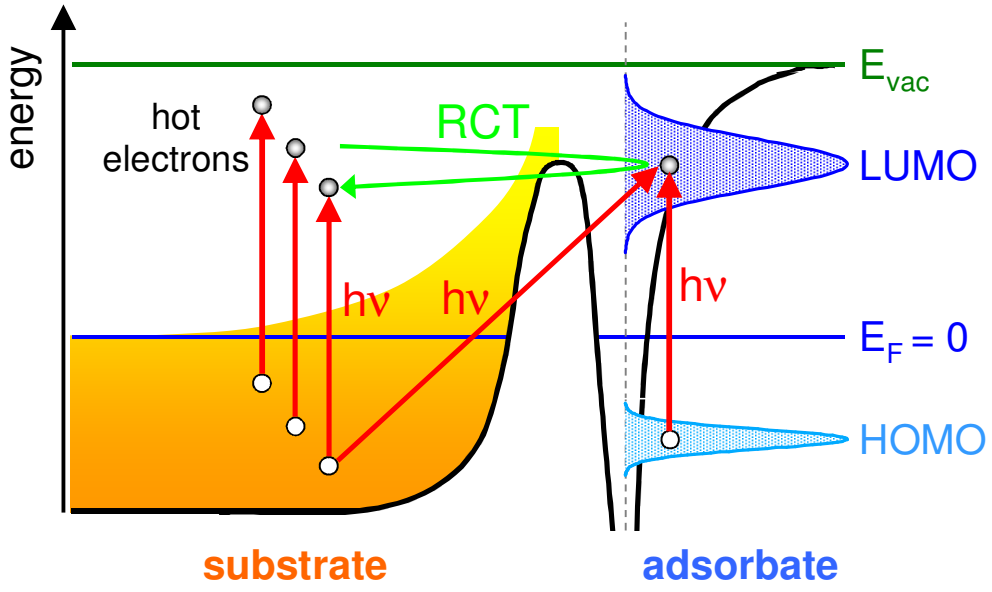

Figure 6.1 Electronic photoexcitation pathways of an adsorbate on a metal surface [55,56]. Surface photochemical reactions are triggered by transient excitation of adsorbate localized resonances: this can happen either indirectly by the scattering of photoexcited hot electrons from the bulk into the unoccupied resonance, or directly by the optical excitation from the occupied states of the substrate or adsorbate. Deexcitation occurs by the elastic RCT or inelastic electron-electron scattering.

6.2 Experiments

We have performed I2PC measurements for alkali atoms (Li, Na, K, and Cs) on Ag(111) and Cu(111) surfaces. As predicted by theory [28], the electronic relaxation of $m = 0$ resonances of Li and Na was too fast to observe the nuclear wave packet motion. Therefore, we focused on K and Cs on Ag(111), for which we performed I2PC measurements as a function of electron energy and emission angle. The angle-resolved measurements were in part motivated by interest in the dynamics of the newly discovered $m = \pm 1$ resonance that is described in Chapter-5.2. For that reason, we also performed angle-resolved I2PC measurements for K and Cs on Cu(111). Also, for Cs on multilayer Ag(111) films, Aeschlimann and coworkers reported angle-dependent intermediate state lifetimes, which they attributed to a contribution to the signal from the bulk intermediate states [53]. Because bulk states do not exist at the energy and $\mathbf{k}_{\parallel}$ of their measurements, the origin of $k_{\parallel}$-dependent lifetimes must be reexamined.

Most of the experimental procedures for the angle-resolved I2PC measurements were similar to those used in Chapter-4.2 and 5.2. In order to ensure that sufficient alkali atom coverage had been achieved to observe the $m = \pm 1$ resonance, K and Cs were deposited from their getter sources with the sample rotated by about 20° from the analyzer axis, while continuously recording 2PP spectra. I2PC scans were recorded at fixed energy increments of 0.1 eV over the energy range extending from the $U_{sp} \leftarrow L_{sp}$ transition ($E_{int} \sim 1.8$ eV) to the Fermi edge. With simultaneous acquisition for 7 different energies, this energy region could be covered with two data acquisition cycles for each angle. Each acquisition cycle corresponded to averaging of $600-800$ pump-probe scans to obtain better statistics. The measurements in each acquisition

overlapped at one energy to check for the consistency between the runs; therefore, data were obtained for 13 distinct observation energies. Moreover, to study the angular dependence of time-resolved measurements, I2PC scans were recorded at various photoemission angles from 0^0 through 22^0 in 2-degree increments. The angle was varied by rotating the sample manipulator manually between the measurements.

6.3 Photoinduced Desorption

Surface femtochemistry occurs by excitation of adsorbates to excited states with potential energy surfaces that drive nuclear motion from reactants into products. Fig. 6.2 shows the potential surfaces that represent the critical features for the photodesorption of Cs from Ag(111). Before excitation, a chemisorbed Cs^+ ion exists in the deeply bound well (~2 eV) in its electronic ground state at the equilibrium distance (R_{ads}). Upon charge transfer excitation of an electron to the $m = 0$ resonance, the ground state probability distribution (green Gaussian curve) is projected onto the neutral $Cs - Ag$ surface. Because of the repulsive interaction between the 6s electron and the image charge of the Cs^+ core, upon the vertical excitation onto the neutral excited state, the Cs atom experiences a strong repulsive force causing the $Cs - Ag$ bond to rupture [51,54,55,56]. Therefore, the wave packet (blue Gaussian curve) motion takes place according to the 'repulsive' Menzel-Gomer-Redhead scheme [219,220]. In this scheme, dissociation will occur either on the excited state surface, or if it is electronically quenched, on the ground state surface. In the latter case, the desorption can only occur, if the kinetic energy acquired by propagating on the excited state surface is sufficient to overcome the potential barrier to products on the ground state surface.

Because the $m=0$ resonance energy decreases as the $Cs-Ag$ bond is elongated, as implied by Fig. 5.9, the photoinduced motion of Cs cause the $m=0$ resonance to appear at a lower energy in 2PP spectra when probed by a delayed probe pulse [184]. This relationship between the $m=0$ resonance energy and the bond length can be understood from Fig. 5.10(a). The asymptotic energy of the Cs^+ desorption product is indicated by the blue horizontal line; the origin of the energy axis corresponds to free Cs atom in vacuum at rest.

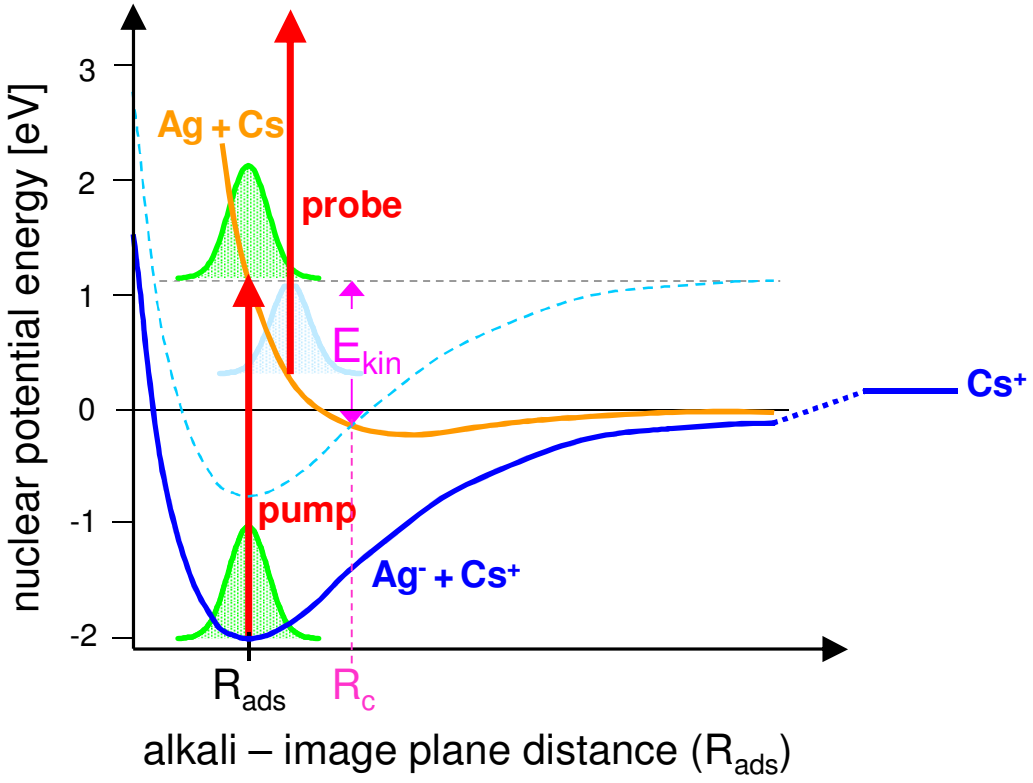

Figure 6.2 The potential energy surfaces for photoinduced desorption of Cs from Ag(111) surface [54,55,56]. The origin of the energy scale corresponds to Cs atom at rest in the vacuum; the blue horizontal line indicates the asymptotic energy of free Cs^+ at rest. The pump pulse projects the ground state wave packet (green Gaussian) onto the excited state, turning on the repulsive forces between Cs and the substrate. The evolving wave packet (blue Gaussian) can be deduced

by changes in the $m = 0$ resonance energy in the photoemission signal induced by the delayed probe pulse. Bond elongation ceases before it reaches the critical distance (R_c) and consequently, desorption is precluded.

An atomic scale illustration of the charge transfer processes occurring in Fig. 6.2 is summarized schematically in Fig. 6.3. Prior to excitation, Cs^+ is chemisorbed in a three-fold hollow site of Ag(111) surface [55] in a fully ionized state (Fig.6.3(a)). Photoexcitation resonantly transfers an electron into the empty 6s orbital of Cs^+ creating a neutral Cs atom at the position of the ion; the change in the electronic occupation turns on the repulsive forces between the adsorbate and substrate (Fig. 6.3(b)). Assuming that the surface atoms remain fixed, the adsorbate atom is pushed away from its equilibrium position into the vacuum. The ensuing dissociative motion reduces the Coulomb repulsion leading to a reduction in the energy of the $m = 0$ resonance (Fig. 6.3(c)). The $Cs - Ag$ bond elongation possibly leads to the atomic desorption. The desorption process is terminated by reverse charge transfer to the substrate, if the adsorbate does not acquire sufficient kinetic energy to break the bond and escape from the surface. Because in the case of Cs/Cu(111) system, the electronic quenching effectively competes with the desorption, we have dubbed the femtochemical process the 'frustrated' desorption.

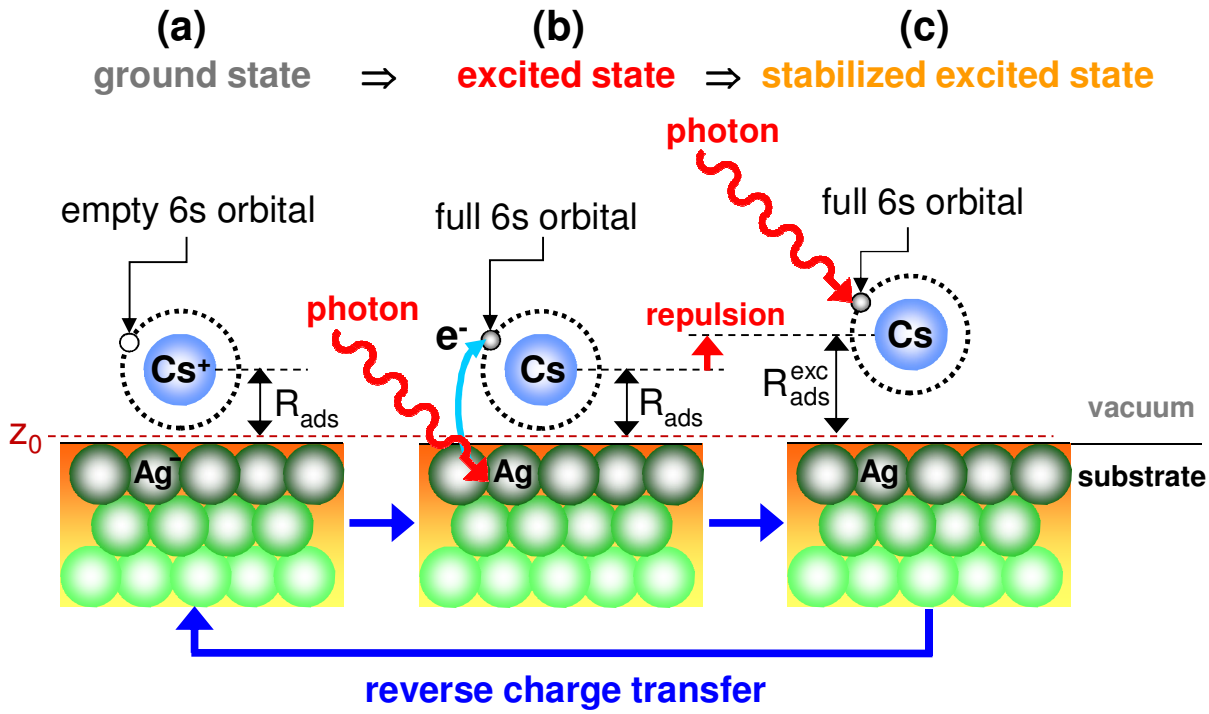

Figure 6.3 Charge transfer processes in photodesorption [209]: **(a)** At the start, alkali atom (Cs) is chemisorbed on a noble metal substrate (Ag(111)) in an ionic state. **(b)** Optical excitation transfers an electron resonantly from the substrate into the empty 6s orbital of Cs^+; the neutralization turns on the repulsive forces. **(c)** The adsorbate atom is displaced away from the surface. Desorption of Cs will occur unless reverse charge transfer terminates the excited state propagation; Cs^+ can still desorb, if the kinetic energy acquired on the excited state can overcome the energy barrier to the dissociation.

In order to explain the spectroscopic changes occurring during Cs atom desorption, the surface projected band structure of Cs/Ag(111) surface as a function of $k_{\parallel}$ is shown in Fig. 6.4. The projected band gap at $k_{\parallel} = 0$ extends from the lower (L_{sp}) and upper (U_{sp}) sp-bands that are located at -0.30 and 3.86 eV, respectively [62]; the Shockley surface state (SS) is located at -0.063 eV [3]. At minimum Cs coverage, the $m = 0$ resonance appears at about 2.7 eV [163]. The direct

photoexcitation of $m=0$ resonance occurs by photoinduced charge transfer from the lower sp-band; because the $m=0$ resonance is localized on Cs atoms, excitation is possible from any momentum state that conserves energy. Following the excitation, the decrease in energy of the $m=0$ resonance with time can be detected after a delay (τ) by completing the 2PP process with the delayed probe pulse. Monitoring the dynamics at different $k_{\parallel}$ should probe the same $m=0$ resonance, which is localized on Cs atom. The evolution of the $m=0$ resonance wave function can change the $k_{\parallel}$ spectrum that defines the localized state.

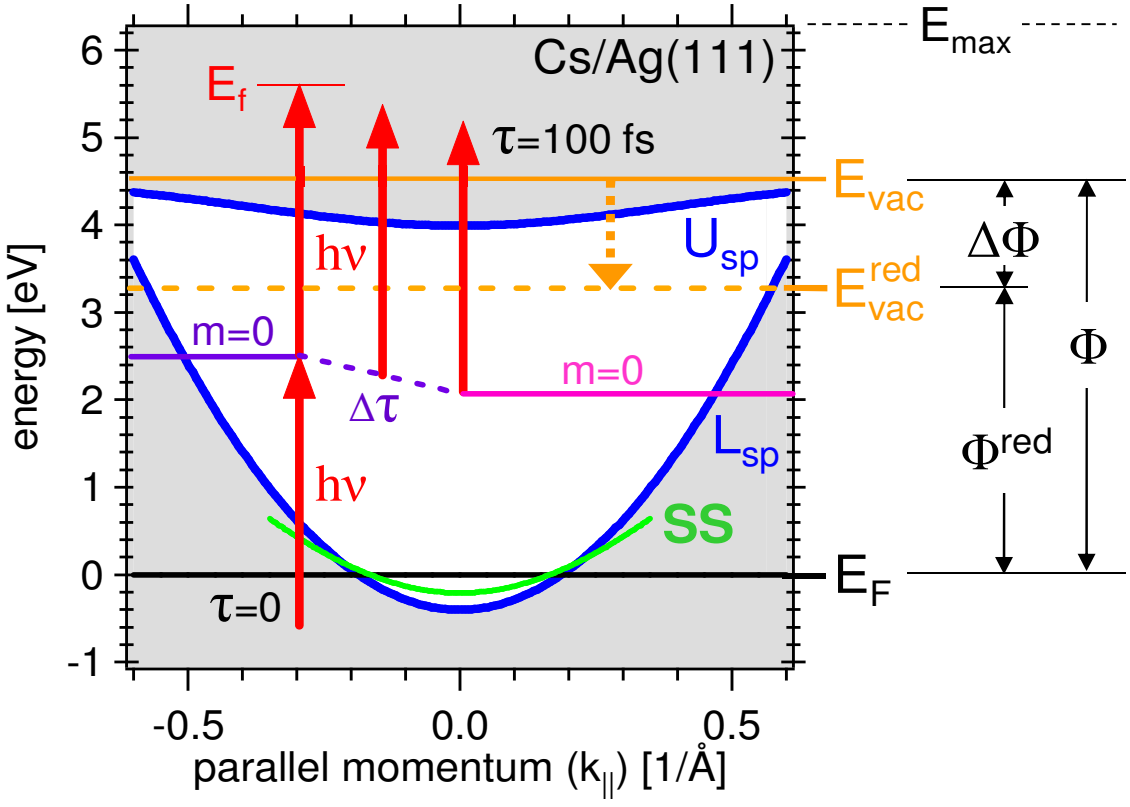

Figure 6.4 The surface projected band structure of Cs/Ag(111) along the parallel component of momentum ($k_{\parallel}$). Energy of the $m=0$ resonance changes with the pump-probe delay due to the dissociative wave packet motion. (τ: pump-probe delay time)

6.4 Interferometric Two-Pulse Correlation Measurements

As discussed in Chapter-2.1, I2PC scans measure the phase and energy dynamics of the coupled states in a 2PP process. In conventional photoemission spectroscopy, the linewidth is often interpreted as a measure of the hole lifetime [221]. In fact, the homogeneous linewidth is a measure of the electron-hole pair dephasing time. Under some circumstances the contribution of electron can be neglected so that the linewidth gives a good measure of the hole dephasing [222]. Likewise, linewidths in 2PP spectra provide information on the electron-hole pair dephasing.

The experimental $m = 0$ resonance linewidths for alkali atoms on Ag(111) surface in 2PP spectra of Fig. 5.7, which are ≥ 0.3 eV, are broader than for Cu(111) surface [54,180]. The larger linewidths may include both homogeneous and inhomogeneous contributions. The homogeneous contributions could be larger on account of faster decay of the $m = 0$ resonance. Aeschlimann and coworkers have reported a lifetime of > 7 fs and later 11 ± 2 fs for Cs on thick (> 5 ML) films of Ag on Cu substrates. The films consisted of thick Ag(111) islands interspersed with thin ($1 - 2$ ML) Ag film [53,214]. These lifetimes agreed with the theoretical calculations by Echenique's group. For a single crystal Ag(111) substrate, however, Petek et al. reported significantly longer lifetime of 30 fs [55]. If one takes the single crystal results to be more representative, then the $m = 0$ resonance lifetime contributes negligibly to the broadening of the experimental linewidth.

Additional contribution to the homogeneous linewidth could arise from the initial state scattering. Because the 2PP process excites an electron from the lower sp-band of the bulk Ag, rather than

the surface state as in the case of Cu(111), the hole scattering could be more effective for Ag(111). Hole-hole scattering in the bulk is usually more efficient than at surfaces [125]. Moreover, the hole binding energies for alkali atom excitation are larger for Ag(111) than for Cu(111) surface, and therefore the lifetimes are expected to be shorter [125].

Furthermore, the $m = 0$ resonance linewidth on Ag(111) surface could also have significant inhomogeneous contribution. Because light couples a broad range of initial k-states of the lower sp-band of Ag to the Cs atom localized $m = 0$ resonance, the inhomogeneous broadening for the excitation could be larger than in the case of excitation from the surface state of Cu(111). As a consequence of these enhanced homogeneous and inhomogeneous broadening contributions, the effective dephasing times associated with the 2PP excitation through the $m = 0$ resonance estimated from our I2PC measurements are too fast (≤ 6 fs) to resolve.

In the case of K and Cs on Ag(111), the population dynamics associated with the $m = 0$ and $m = \pm 1$ resonances occur on a significantly longer time scale than the dephasing making it possible to follow the coupling of electronic and nuclear motion through measurement of I2PC scans. As already introduced in section 6.3, the photoinduced charge transfer excitation can trigger the 'frustrated' desorption of alkali atoms from noble metal surfaces, if $m = 0$, and possibly $m = \pm 1$ resonance lifetimes are sufficiently long to allow appreciable nuclear wave packet motion [54,55,56,180]. In the following, we will discuss mainly the I2PC measurements of $m = 0$ dynamics for K and Cs on Ag(111) surfaces. I2PC measurements were also performed for K and Cs on Cu(111) as a function of emission angle; these data will be discussed as they pertain to the $m = \pm 1$ resonance.

I2PC measurements for normal emission have been previously reported for Cs on both Cu(111) and Ag(111) surfaces [164,180]. Previous measurements for Cs/Cu(111) at 33 K have revealed that the population decay can be monitored on a time scale of roughly 200 fs [54,55,56]. Although the excited state wave packet motion causes the population kinetics to be nonexponential, a lifetime of ~50 fs was estimated [54,180]. In fair agreement with experiment, theoretical calculations predict a lifetime of ~30 fs with dominant contribution from electron-electron scattering [28]. As mentioned above, the lifetime of ~30 fs reported by Petek et al. for Cs/Ag(111) system at 33 K, is significantly longer than those reported by Aeschlimann's and Echenique's groups [55,214].

Our I2PC measurements on Cs/Ag(111) manifest a profound change in the surface electronic structure following the charge transfer excitation of the $m = 0$ resonance that had not been observed before. Fig. 6.5(a) shows a series of '0ω' (phase averaged) envelopes of I2PC scans for different energies that were measured for normal emission from Cs/Ag(111) surface at room temperature. The same normalized data are plotted in Fig. 6.5(b) as a contour map of 2PP intensity with respect to the intermediate state energy and pump–probe time delay. The I2PC scans consist of a Gaussian autocorrelation function of the laser pulse near zero delay, which is slightly broadened by finite dephasing of the coupled states, as already discussed. Here, we focus on the longer time scale population dynamics that is responsible for the dramatic changes in Fig. 6.5.

The population dynamics can be classified into regions above and below the $m = 0$ resonance at 2.43 eV. At and above the $m = 0$ resonance peak, the population decay of the intermediate state

follows exponential kinetics. At the $m = 0$ resonance maximum the population decays with a time constant of 33 ± 3 fs, and it is in good agreement with the published single crystal Ag(111) surface data [55], but not with the thick Ag(111) film data or theory [214]. At the energies below the $m = 0$ resonance, however, the intermediate state population dynamics follow increasingly nonexponential kinetics, which are most pronounced in the $1.9 - 2.1$ eV range.

As in the case of Cs/Cu(111) [54], we interpret the nonexponential population dynamics in terms of the excited state wave packet propagation. According to Fig. 6.2, the photoexcitation creates a neutral Cs atom on a repulsive potential surface. The wave packet propagation leads to the lowering of the $m = 0$ resonance energy as a function of the pump-probe delay. A simplistic, but incomplete, interpretation of the nonexponential behavior is that the wave packet propagation causes the rapid energy stabilization of the excited state population as a function of the delay, and therefore, increasing bond length. According to the contour plot in Fig. 6.5(b), the apparent $m = 0$ state population maximum shifts from ~2.43 eV by ~0.4 eV within a pump–probe delay of 120 fs. For comparison, within the same time window the experiments on Cs/Cu(111) report excited state stabilization of only 0.2 eV [54]. Because there is a strong dependence of I2PC scans on the observation angle, next we present the angle-dependent results.

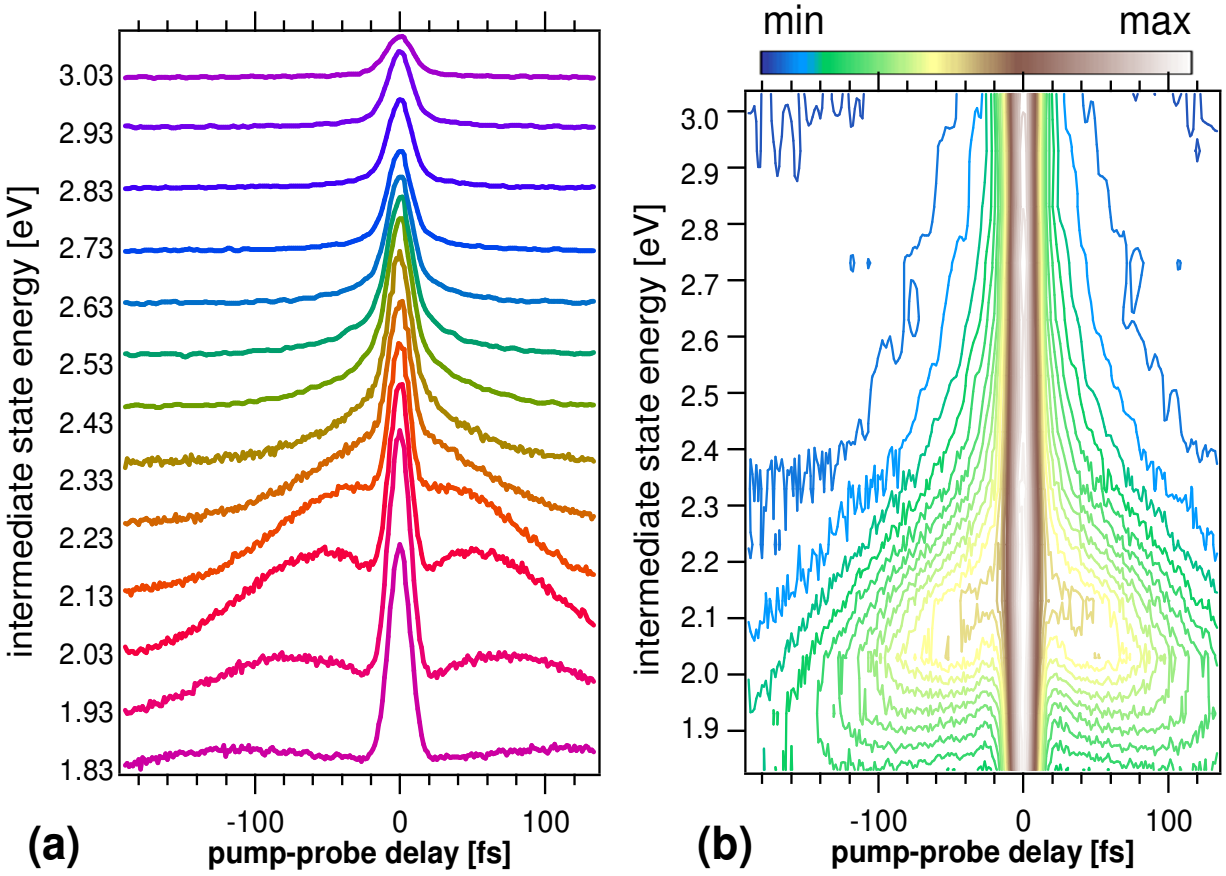

Figure 6.5 **(a)** The measured I2PC '0ω' (phase-averaged) envelopes for different intermediate state energies. The envelope amplitudes reflect the actual signal strength at each measurement energy. **(b)** The 2PP intensity contour plot as a function of the intermediate state energy and pump-probe delay that has been generated from the I2PC envelopes in (a). The envelopes are normalized at zero delay.

6.5 Angle-Dependent Interferometric Two-Pulse Correlation Measurements

We measured off-normal I2PC scans to probe the dynamics following the $m = \pm 1$ resonance excitation. Such measurements were performed for K/Ag(111) and Cs/Ag(111). Fig. 6.6 shows the 0ω envelopes taken for Cs/Ag(111) between 0° and 22° emission angles in 2-degree intervals.

The scans that coincide with the $m = 0$ and $m = \pm 1$ resonances, and the $U_{sp} \leftarrow L_{sp}$ two-photon transition are indicated by blue, green and red lines, respectively. We first discuss the unexpected $k_{\parallel}$-dependence of the $m = 0$ resonance dynamics.

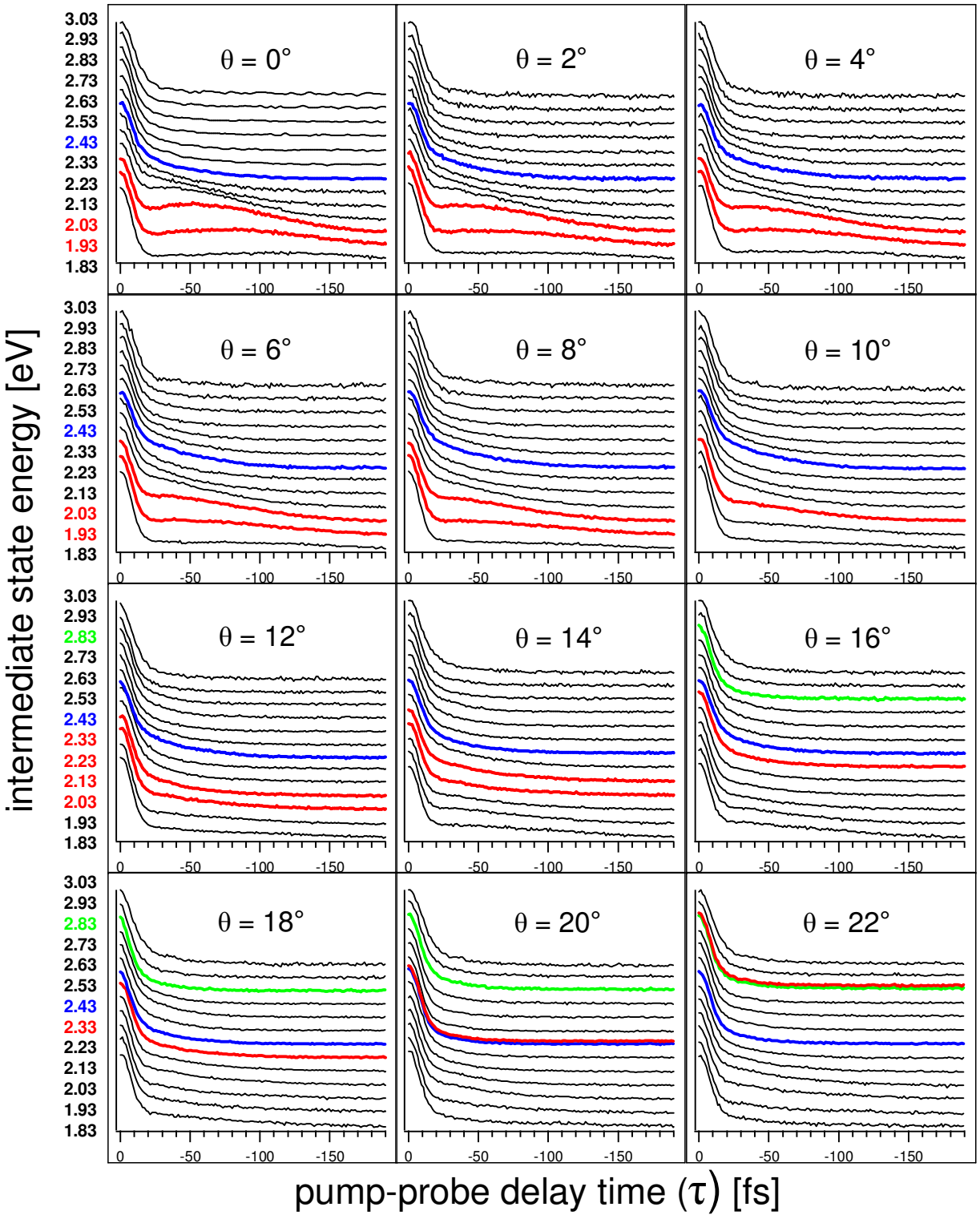

Figure 6.6 I2PC measurements on Cs/Ag(111) as a function of intermediate state energy at photoemission angles from 0° to 22°. The measurements corresponding to $U_{sp} \leftarrow L_{sp}$ transition

(red), $m = 0$ (blue), and $m = \pm 1$ (green) resonances are indicated by the colored lines. Note that at $\theta = 20°$ the $m = 0$ resonance (blue line) acts as an intermediate state in $U_{sp} \leftarrow L_{sp}$ two-photon transition. The $m = \pm 1$ resonance is discernible only at large emission angles.

If the I2PC scans were to measure only the population dynamics, and the $m = 0$ resonance were nondispersive with momentum, then we would not expect to see $k_{\|}$-dependence of I2PC scans. In fact, the $k_{\|}$-dependence is dramatic. The angle-dependent I2PC envelopes in Fig. 6.6 show clear differences particularly in terms of the nonexponential dynamics below the $m = 0$ resonance. The nonexponential behavior is strongest near normal emission, and it becomes unnoticeable to inspection for $\theta > 10°$.

In order to quantify these angle-dependent differences, we developed a simple kinetic model that can reproduce the nonexponential population dynamics. At and above the $m = 0$ resonance, the population decay could be modeled as a simple exponential decay convoluted by the coherent response given mainly by the autocorrelation of the Gaussian laser pulse. Below the $m = 0$ resonance, in addition to the exponential decay, we included an exponential rise to represent the rising part of the excited state population signal. We fit the data taken within the $1.83 - 2.53$ eV energy window, since the $U_{sp} \leftarrow L_{sp}$ transition and the $m = 0$ resonance can be observed within this interval. The I2PC scans are fitted to

$$f_{decay}(t) = A \cdot \exp(-t/\tau_1) \cdot (1 - \exp(-t/\tau_2)) + G \cdot \exp\left(-\frac{1}{2}\left(\frac{t}{w}\right)^2\right) + B, \qquad [6.1]$$

where 'A' is the coefficient of the exponentially decaying and rising components with characteristic times of 'τ_1' and 'τ_2', respectively. 'G' is the coefficient of the Gaussian function

that describes the autocorrelation of the Gaussian laser pulse with a FWHM of 'w', and the 'B' is background corresponding to uncorrelated 2PP signal from the pump and probe pulses acting separately; all parameters were allowed to vary in the fitting procedure except at the $m = 0$ resonance, where the population dynamics could be modeled as a simple exponential decay.

In Fig. 6.7, we present a representative fit of the experimental I2PC data obtained at emission angle $\theta = 0°$ and intermediate energy 1.93 eV to the functional form in equation [6.1]. Fig. 6.7 gives the comparison between experiment (black dots) and the fit (red line) to show the typical success of the model in reproducing the data, and decomposition of the fit into separate contributions to equation [6.1]. The population is seen to decay with $\tau_1 = 68.1$ fs, rise with $\tau_1 = 462$ fs, and have an amplitude $A = 1.66$.

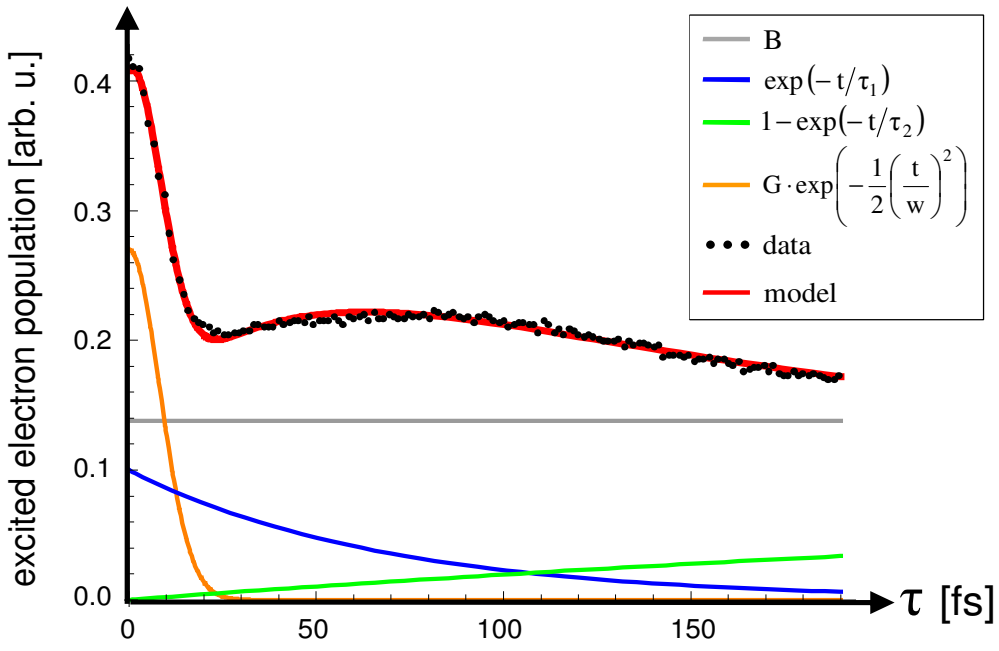

Figure 6.7 Fitting of I2PC data ($\theta = 0°$ emission angle and 1.93 eV intermediate state energy) of Cs/Ag(111) to our kinetic model expressed in equation [6.1]. The fitted curve is decomposed into the individual components according the legend.

In Figs. 6.8 and 6.9, we plot the obtained parameters of angle-resolved I2PC scans as a function of the intermediate state energy and observation angle. The parameters reflect the systematic changes that can be observed in the experimental scans of Fig. 6.6. In Fig. 6.8, we see that the amplitude parameter A is sharply peaked at the maximum value of $A = 2.12$ that is obtained for 2.03 eV energy and 0° emission angle. To calibrate the amplitude scale, according to our normalization procedure, we expect an amplitude of $A = 1/3$ for resonant excitation. The significantly larger amplitude at lower energies and angles is not accumulated through the energy relaxation of the excited state population. The amplitude grows in with a delayed rise far beyond the population that was generated through the direct excitation.

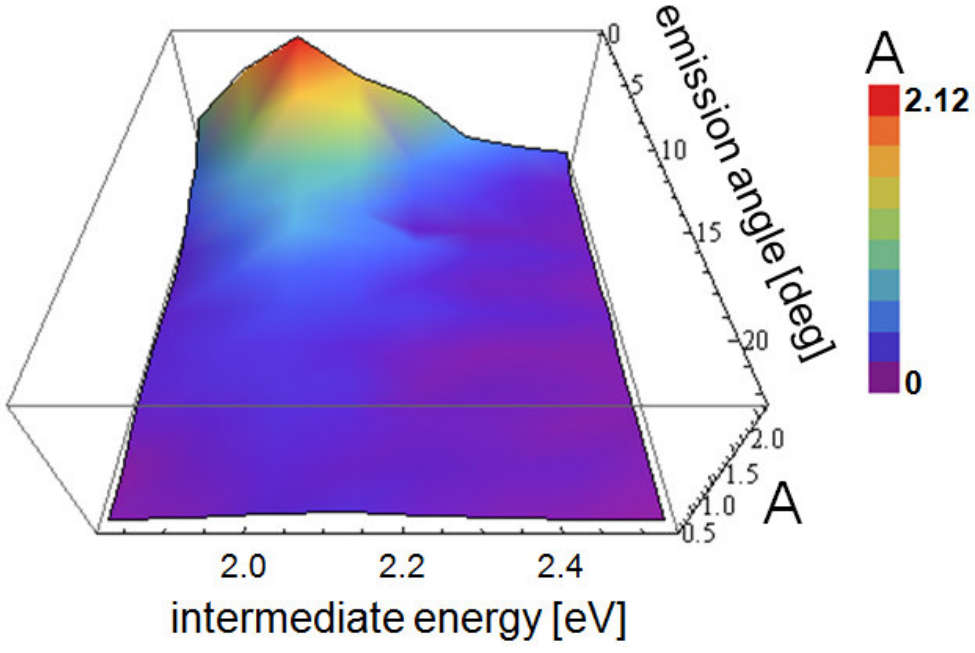

Figure 6.8 The amplitude of 'A' of equation [6.1] as a function of the intermediate state energy and emission angle. The amplitude peaks in the $1.9-2.1$ eV interval and 0°, where the nonexponential behavior is the most pronounced.

In Figs. 6.9(a) and 6.9(b), we show the extracted time constants τ_1 and τ_2 as a function of intermediate state energy and angle. The decay time τ_1 generally increases from ~30 fs at the $m=0$ resonance resonant excitation energy of 2.43 eV and 0° emission angle. The fluctuations in the τ_1 parameter with energy and angle seem to be real rather than a consequence of deviations from the model in equation [6.1]. In the case of τ_2, the rise time is seen to increase monotonically to the maximum value of 900 fs at the lowest energy and 0° emission angle.

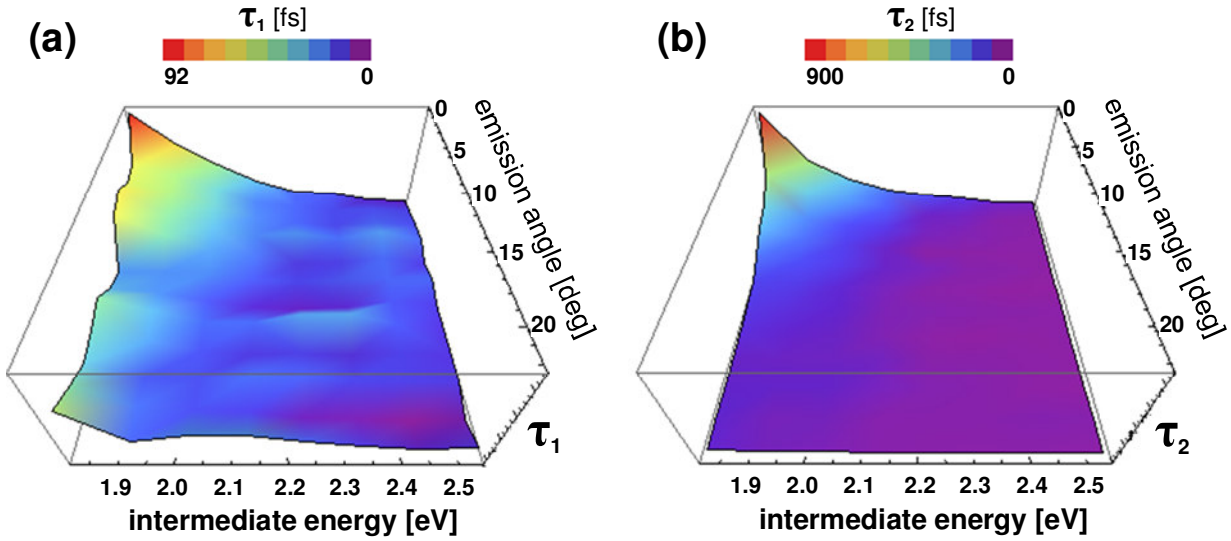

Figure 6.9 The decay time τ_1 **(a)** and the rise time τ_2 **(b)** of equation [6.1] as a function of the intermediate state energy and emission angle. In general, the time constants increase for low energy and small angles. The nonmonotonic changes in τ_1 are statistically significant.

The observed dynamics of Cs/Ag(111) are unprecedented and in many respects puzzling. Here, we provide a heuristic interpretation; the full quantum mechanical modeling required to test the model is far beyond what has been attempted in previous theoretical models of photodesorption dynamics, and therefore, will not be attempted here. The main puzzle is the accumulation of large amplitude at low energies and angles. If we assume that Cs is excited directly, then the maximum amplitude should occur at the $m = 0$ resonance energy. The total amplitude generated should be 1/3 at each angle of observation (note again that the I2PC envelopes at different angles and energies are normalized at $\tau = 0$ fs). For the amplitude to rise to 2.12 at its maximum at 2.03 eV and 0° angle, the excited state has to be either generated by another process, or transition moments for the final excitation step have to depend on the energy and angle of observation.

The intermediate state could be generated by a parallel process such as the hot electron scattering. This, however, can be immediately excluded because the observed lifetimes for the exponential rise far exceed the hot electron lifetimes at 2.5 eV above E_F [125]. The population of $m = 0$ resonance from the higher lying $m = \pm 1$ resonance can also be excluded, because the latter is less efficiently excited than the former. The other alternative of energy- and angle-dependent transition moments is more plausible, but it is more difficult to prove. We will return to discussing it after we consider the time constants in Fig. 6.9.

The decay time τ_1 increases from 30 to 92 fs in the energy range of observation. We attribute it in part to the $m = 0$ resonance decay through RCT and electron-electron scattering. The decay time becomes longer below the resonance, because, $Cs - Ag$ bond length increases through the excited state wave packet propagation. It is natural that the excited state lifetime increases as the

coupling of Cs atom to the surface decreases. What is difficult to explain is why the observed τ_1 parameter should depend on the angle, because the same Cs atom localized state should be observed at all angles of observation. Thus, if τ_1 only represents the $m = 0$ resonance lifetime, then it should be independent of the observation angle. It cannot be explained only by angle- and energy-dependent transition moments invoked earlier. We suspect that the transition moments decrease for larger angles as the $Cs - Ag$ bond length increases. The fluctuations in τ_1 with angle and energy could reflect both the variation in the excited state decay as well as the variation in the transition moments for the intermediate state detection.

The rise time τ_2 is probably most closely associated with the wave packet propagation. It requires time for the $Cs - Ag$ bond to stretch so that the $m = 0$ resonance appears at a lower energy. We can estimate the wave packet motion from the dependence of the 6s resonance energy of Cs atom as a function of distance from the Ag(111) surface, such as we have calculated in Fig. 5.10(a) for Cs/Cu(111). Based on the nearly linear relationship between the $m = 0$ resonance energy 'E_σ' and the bond length 'R', we estimate the force exerted on Cs atoms to be $F = \frac{dE_\sigma(R)}{dR} = 8.7 \times 10^{-8}$ N. From Fig. 6.5(b) we see that the amplitude maximum decreases by ~0.39 eV in 100 fs. Therefore, we ask what is the bond length required to decrease $m = 0$ resonance energy by 0.39 eV, and how long it takes for the $Cs - Ag$ bond to stretch by the required amount. Based on this model, the required bond elongation of 0.72 Å is achieved in 190 fs through acceleration with the constant force. We compare the derived propagation time with the τ_2 rise time of 294 fs at 2.03 eV. Although the observed rise time is longer, we note that we have assumed that all the available momentum is imparted to Cs atom and the surface acts as a massive, rigid wall. This is

a better approximation for Ag(111) surface than for Cu(111) surface, because the atomic mass of the former (107.9 amu) is a better match to Cs atoms (132.9 amu) than the latter (63.5 amu) [223]. We also note that a comparison between classical and quantum mechanical wave packet propagation for Cs on Cu(111) found the classical model to underestimate the propagation time by a factor of ~2 [212]. Thus, we conclude that the τ_2 rise time represents mainly the wave packet propagation.

To conclude the analysis of I2PC scans for Cs/Ag(111) surface, we observe strongly nonexponential excited state dynamics, which we interpret through the excited state wave packet motion. As the wave packet propagates, the excited state decays on the time scale given by τ_1, which progressively gets longer as $Cs-Ag$ bond length increases. At energies below the $m=0$ resonance at $\tau=0$ fs, the wave packet appears with a rise time τ_2. Even though the rise time extends to 900 fs at the lowest observed energies, we can detect parts of the wave packet arriving on ~100 fs time scale. The propagated wave packet rises to its maximum intensity on 100 fs time scale because of the rapid electronic relaxation on time scale given by τ_1. If the transition moments were constant, the intensity of the propagated wave packet would make it difficult to observe such long time scale dynamics. In the case of Cs/Ag(111), however, the changing transition moments seem to selectively amplify the signal so that we can follow the dynamics on nearly 1 ps temporal and 1 Å length scale. To construct this heuristic scenario, however, we had to claim that the transition moments for the final step in photoemission depend on the observation energy and angle. Although we cannot provide a proof, it is easy to rationalize that this should happen because the $m=0$ resonance wave functions will evolve as Cs atom desorbs from the surface. In addition to the change in the Cs atom wave function, the change in the final

state energy that is connected by optical transition to the propagating wave packet will also change during the course of desorption. We leave the modeling of these dynamics as a challenge to the next generation of students.

In addition to Cs/Ag(111), we also carried out angle-resolved I2PC measurements for K/Ag(111) in the range of 0° to 20° in 4-degree intervals. The energy- and angle-dependent changes for K/Ag(111) are much less dramatic than for Cs/Ag(111). The measured population decay time at the $m = 0$ resonance (~2.5 eV) is 18 ± 3 fs where the average and the variance represent the scatter between measurements for different angles. The population decay remains exponential below the $m = 0$ resonance and the lifetimes increase to 56 ± 5 fs while the amplitude of the population decay component decreases. There are no angle-dependent trends as in Cs/Ag(111).

We attribute these differences with respect to Cs/Ag(111) to the lighter mass (39.1 amu) and faster RCT decay of neutral K atoms on Ag(111). Being more than three times lighter than Cs, as well as having shorter R_{ads}, K experiences stronger repulsion and is more effectively accelerated from the surface than Cs. Therefore, below the $m = 0$ resonance, K atoms appear to be somewhat stabilized. Because the I2PC measurements do not show strong evidence for the nonexponential dynamics within the ~200 fs window of our measurements, we conclude that the extracted exponential decay times are determined mainly by the wave packet decay through the elastic RCT process.

Furthermore, our angle-resolved I2PC measurements also probe the $m = \pm 1$ resonance lifetimes. Because $m = \pm 1$ resonance appears within the wings of the more intense $m = 0$ resonance, it is

difficult to attribute the measured decay time constant solely to the $m = \pm 1$ resonance lifetime. The measured I2PC scans at $m = \pm 1$ resonance maxima show single exponential kinetics, therefore, it is not possible to attribute a distinct lifetime to each of the overlapping bands. The effective $m = \pm 1$ resonance lifetimes (in fs) for K and Cs chemisorbed on Ag(111) and Cu(111) surfaces are experimentally determined and compared with the theoretically predicted values in Table 6.1.

chemisorption interface	**theory [fs]**	**experiment [fs]**
K/Ag(111)	22	19±2
Cs/Ag(111)	10	23±1
K/Cu(111)	27	25±1
Cs/Cu(111)	8	26±2

Table 6.1 Comparison of theoretically predicted and experimentally measured lifetimes of $m = \pm 1$ resonances for K and Cs on Ag(111) and Cu(111) surfaces [168].

These lifetimes are in excellent agreement with Borisov's wave packet propagation calculations for K on Ag(111) and Cu(111), however, the theoretical values for Cs on the same surfaces are significantly lower [168]. In the case of Cs on Ag(111) and Cu(111), Borisov predicts a large RCT contribution to the decay rate resulting in 8 and 10 fs decay time constants. Such a rapid decay is not supported by the experimental measurements.

The $m = \pm 1$ resonance lifetimes are, in general, considerably faster than the $m = 0$ lifetimes. The coupling of alkali atom resonances to the propagating states of substrates depends on the extent of their hybridization. The $s - p_z$ hybridization in the case of $m = 0$ resonance is more effective in decoupling the excited state from the decay by RCT and electron-electron scattering than the dominant $p - d$ hybridization in the case of the $m = \pm 1$ resonance. Our I2PC

measurements support this general trend, though the theoretical $m = \pm 1$ lifetimes for Cs on Ag(111) and Cu(111) appear to be anomalous.

6.6 Conclusion to Femtochemistry of Frustrated Alkali Atom Desorption

Femtochemistry of surface processes allows us to examine the mechanisms of fundamental chemical reactions by means of pump-probe spectroscopy techniques such as ITR2PP. Ultrafast lasers are employed to probe surfaces, since they act as an 'ultrafast camera' of femtosecond resolution to study the motion of atoms and/or molecules, the evolution of transient intermediate states of chemical reactions as well as dynamics of electronic charge transfer on solid surfaces [201,202].

In our experiments with Cs and K on Ag(111) and Cu(111) surfaces, the photoinduced charge transfer excitation creates neutralized alkali atoms, when they are at the equilibrium chemisorption bond distance. The subsequent Coulombic repulsion triggers the nuclear wave packet motion into the vacuum, giving rise to a population decay signal (especially for Cs) below the $m = 0$ resonance. From the nonexponential kinetics of Cs/Ag(111) system we can gain substantial information on the wave packet motion, but our knowledge of how to model such dynamics is still rudimentary. In the best case of Cs on Ag(111), we can follow the wave packet motion over several hundred femtosecond time scale as it decays through RCT and electron-electron scattering with a lifetime approaching 100 fs.

The difference of the Ag(111) surface which exhibits more pronounced nonexponential decay kinetics compared to the Cu(111) surface may have a mechanical contribution. Ag atoms, being more massive than Cu atoms, can convert the repulsive force into outward motion of alkali atoms more effectively. Because potential energy can be converted into dissociative motion with less dissipation, nonexponential dynamics of Ag(111) surface can be justified by more pronounced adsorbate–substrate bond elongation, leading to longer lifetimes for the propagated wave packet. The detailed analysis of the dynamics for Cs/Ag(111) system remains elusive. The distinct accumulation of signal amplitude at low energies and small angles, and angle-dependent kinetics suggest that, in addition to wave packet propagation, the I2PC scans are strongly influenced by the evolving transition moment in the photoemission step. These novel effects may reflect the $m = 0$ resonance wave function evolution during the photodesorption process.

The lifetime of alkali-induced $m = 0$ resonance depends on the electronic properties of adsorbate and substrate species such as the atomic polarizability and location of the $m = 0$ resonance within the projected band gaps of the metal substrate. Our measurements on alkali/noble metal interfaces bolster the fact that excited state lifetimes can be more accurately measured by time-domain measurement techniques and corroborate the results obtained in the past [54,55,56]. Further systematic investigations on other chemisorption interfaces are necessary to acquire a thorough comprehension of the phenomena and physical principles involved in the electronic excitation, relaxation, desorption and atomic manipulation of metal surfaces; and possibly observe novel femtochemical phenomena.

Chapter-7

General Conclusions and Future Outlook

The goal of the scientific work presented in this dissertation is to study the electronic structure and dynamical properties of alkali atoms (Li through Cs) chemisorbed on low index noble metal surfaces (Cu(111) and Ag(111)) by time-resolved two-photon photoemission. The simple electronic configuration of alkali atoms with a single valence electron and the conduction band structure of noble metals consisting of sp-bands in the vicinity of E_F make the alkali adsorbed noble metals one of the simplest chemisorption systems. Any minute change at the alkali/noble metal interface due to chemisorption becomes very easy to discern spectroscopically and enables us to gain more insight into the electronic structure and dynamical aspects of a chemisorption interface based on the intrinsic properties of the interacting materials. Understanding chemisorption in terms of its constituent components is useful for explaining with simple principles such complex interfacial phenomena as the charge transport, catalysis, and molecular electronics. It may eventually give us the understanding necessary to develop novel molecule-based electronic devices based on general principles.

To probe and analyze the alkali adsorbed noble metal surfaces, we employ photoemission, which measures the energy and momentum of photoemitted electrons from a surface in response to a flux of energetic photons. For the electron excitation energy used in our experiments, photoemission is an extremely surface-sensitive probe owing to the limited depth of escaping photoelectrons; therefore, photoemission spectra carry information exclusively on the very top few atomic layers. Its vast applications in surface science, materials science and engineering make it an indispensable surface analysis technique.

In 2PP, a pump pulse excites an electron in a solid below E_F to a transiently populated and initially unoccupied state between E_F and E_{vac}, subsequently a probe pulse excites the electron further to a state above E_{vac}, and leads to its ejection from the surface to be detected by a suitable electron energy analyzer. Therefore, 2PP brings the capability of resolving the unoccupied states of a metal between E_F and E_{vac} in addition to the occupied states below E_F. Its resolution and precision surpass the complementary benefits of conventional photoemission and inverse photoemission methods. Integrating temporal resolution to 2PP in the form of TR2PP enables us to resolve in the femtosecond regime the dynamics of transiently occupied electronic states of solid surfaces.

To understand what is measured by 2PP, we simulated the 2PP spectrum of bare Ag(111) surface in response to excitation with 3.1 eV photons. By adopting the procedure of Miller et al. [102,103] for modeling the 1PP spectrum of Ag(111), we could successfully reproduce the 2PP spectrum by employing OBE to describe the two-photon absorption involving nonresonant two-photon absorption between the initial and final states. To obtain quantitative agreement, we had to

account for the background signal that is contributed by the quasielastic electron-phonon and inelastic electron-electron scattering [84]. By comparing the intensity of the sp-band peak in AR1PP and AR2PP, we could conclude that Fresnel equations describe the angle-dependent peak intensities, unless the interference between the surface and bulk photoemission contributions is **k**-dependent [147]. Our model was successful in acquiring information on the electronic structure of metal surfaces, although our photon energy limited us to a small range of available **k**-space. We have assessed the limitations of AR2PP with 3.1 eV photons for band-mapping bulk transitions in solids, and the potential for sensitive determination of the inner potential of a solid provided that the band structure is well-known from other measurements. Our investigations pave the way for quantitative simulation AR2PP spectra of other solids.

Having devised a quantitative model for 2PP on a clean Ag(111) surface, we performed a comprehensive set of experiments on alkali chemisorbed Cu(111) and Ag(111) surfaces. The goal of these experiments was to systematically explore the electronic structure of a simple chemisorption interface. We found that, in the vanishing alkali atom coverage limit, the binding energy of the *n*s electron derived $m = 0$ resonances have a binding energy with respect to E_{vac} of 1.84 and 1.99 eV , respectively, for Ag(111) and Cu(111) surfaces. At finite coverage, the $m = 0$ resonance energy stabilizes proportionally to the alkali atom-induced surface dipole moment and the alkali atom coverage. We implemented a model for the alkali atom chemisorption based on the dominant Coulomb interaction between the *n*s electron and the negative image charge of the alkali ion core, which could explain the period-independent binding energy as a consequence of a delicate balance between the conversely varying ionization potential of alkali atoms in the gas phase and their adsorption distance to the surface. We expect the same interactions to define the

effective electronic potentials for a wide range of molecule/metal interfaces in the case that the electronic states of adsorbates are well-localized on the adsorbate. Thus, our model is useful for estimating the alignment of molecular orbitals of chemisorbed molecules, particularly in applications relating to molecular electronics [163], from the properties of the unperturbed substrate and free adsorbates, when their primary mode of interaction is the Coulomb force.

Furthermore, based on the theoretical predictions of Borisov, we searched in the off-normal emission angles for a higher lying $m = \pm 1$ alkali atom resonance; we found such resonances for K and Cs on Cu(111) and Ag(111), thereby confirming the theoretical predictions [168]. Because of their $m = \pm 1$ symmetry, these higher lying alkali-induced resonances have the maximum emission angle of $\pm 17° \pm 2°$ with respect to the surface normal.

Having developed a quantitative model for the alkali atom chemisorption, we turned our focus on the reverse process of alkali atom desorption. By photoinduced charge transfer excitation of the $m = 0$ resonance, we can study the half-collision of a neutral alkali atom at the equilibrium position of the chemisorbed ion. The same Coulomb force that defines the $m = 0$ resonance energy, turns on the dissociative wave packet motion asymptotically leading to alkali atom desorption. We could study the femtochemistry of frustrated alkali atom desorption by means ITR2PP as had been done previously for Cs/Cu(111) [54,55,56]. Our measurements on Cs/Ag(111) (and to a lesser extent on K/Ag(111)) also manifest a pronounced nonexponential decay of the excited state population following the excitation of $m = 0$ resonance. The I2PC signals could be modeled with energy-dependent exponential rise and decay kinetics reflecting the stabilization of $m = 0$ resonance as the atom–surface distance increases. The more extensive wave packet

propagation on Ag(111) surface could have a mechanical origin considering that the larger atomic mass of Ag favors more efficient momentum transfer to Cs, as compared with Cu. The ability to probe Cs photodesorption from Ag(111) surface may also be strongly affected by the transition moments in the 2PP process. This will require future development of a quantitative model for the 2PP process through the $m = 0$ resonance of alkali atoms. If the nature of the nonexponential decay and bond elongation depend strongly on the respective atomic masses of substrate and adsorbate atoms, one expects the Au(111) surface to manifest an even more pronounced effect. A systematic experimental study on Au(111) needs to be performed to explore such phenomena.

In conclusion, one can claim that photoemission spectroscopy, in the form of 2PP and related methods in particular, will remain one of the most powerful surface probing and analysis techniques to study the electronic structure and dynamics of solid surfaces. In addition to revealing energetic, momentum and/or temporal properties of solids, it can also be coupled with some surface imaging techniques, for example LEED, PEEM, and STM, to acquire a broader and more thorough comprehension of condensed matter systems. Especially, the advancement in the ultrafast laser technology and methodology will enhance the quality and refine the resolution of experimental measurements and enable us to observe novel physical and chemical phenomena that currently are not technologically feasible.

Appendix-A

Alkali Atom Dispensers

The alkali metal dispensing unit (Fig. 2.12) is used to generate a diffusive alkali atom beam to be deposited uniformly on the noble metal samples. The alkali atom flux depends on the current applied to each alkali metal getter source. The manufacturer of the alkali metal dispensers, SAES Getters SpA, recommends the following initial and final currents for new and nearly depleted sources [224].

alkali atom	start of evaporation current (A)	close to depletion current (A)
Cs	4.7	6.5 - 7.0
Rb	5.3	5.5 - 6.0
K	5.3	5.5 - 6.0
Na	6.0	8.0 - 8.5
Li	7.3	9.0 - 9.5

Table A.1 The initial and final currents for new and nearly depleted sources that need to be applied to specific the alkali metal getter sources.

The orientation of the dispensing unit needs to be carefully adjusted in such a way that the flux of alkali atoms incident on the sample must directly target the sample surface and result in a uniform coverage to ensure a uniform work function change throughout. Our experiments show

that the following spherical coordinates for the alkali atom dispensing unit are good starting points to adjust its orientation precisely before starting any real data acquisition:

(a) Left dispenser: radius ~ 4.0 mm; φ ~ 2.7 units clockwise; and θ ~ 1.0 unit downward.

(b) Middle dispenser: radius ~ 3.2 mm; φ ~ 1.0 unit clockwise; and θ ~ 0.8 unit downward.

(c) Right dispenser: radius ~ 4.8 mm; φ ~ 1.9 units counterclockwise; and θ ~ 1.3 units upward.

Bibliography

1. F. Reinert and S. Hüfner, New Journal of Physics, **7**, 97 (2005).
2. E. D. Hansen, PhD Dissertation, University of Illinois at Urbana-Champaign, 1998.
3. S. Hüfner, Photoelectron Spectroscopy, 3rd edition, Springer Verlag, 2003.
4. Y. Wang, W. Wang, K.-N. Fan, and J. Deng, Surface Science, **490**, 125 (2001).
5. M. J. Mehl and D. A. Papaconstantopoulos, Physical Review B, **54**, 4519 (1996).
6. U. Mizutani, Introduction to the Electron Theory of Metals, Cambridge University Press, 2001.
7. R. Courths, H. Wern, U. Hau, B. Cord, V. Bachelier, and S. Hüfner, Journal of Physics F: Metal Physics, **14**, 1559 (1984).
8. R. Courths and S. Hüfner, Physics Reports, **112**, 53 (1984).
9. H. Eckardt, L. Fritsche, and J. Noffke, Journal of Physics F: Metal Physics, **14**, 97 (1984).
10. T. Miller and T.-C. Chiang, Journal of Physics: Condensed Matter, **13**, 11115 (2001).
11. http://facstaff.gpc.edu/~pgore/PhysicalScience/Periodic-table.html
12. I. Langmuir, Journal of American Chemical Society, **54**, 2798 (1932).
13. I. Langmuir, Physical Review, **43**, 224 (1933).
14. J. B. Taylor and I. Langmuir, Physical Review, **44**, 423 (1933).
15. H. Lüth, Solid Surfaces, Interfaces and Thin Films, 4th edition, Springer Verlag, 2001.
16. M. Scheffler and C. Stampfl, Handbook of Surface Science, vol: 2 (edited by K. Horn and M. Scheffler), Elsevier, 2000.
17. http://w3.rz-berlin.mpg.de/~jentoft/lehre/ranke_adsorption_181105.pdf
18. K. Oura, V. G. Lifshits, A. A. Saranin, A. V. Zotov, and M. Katayama, Surface Science, An Introduction, Springer Verlag, 2003.
19. H. P. Bonzel, A. M. Bradshaw, and G. Ertl (editors), Physics and Chemistry of Alkali Metal Adsorption, Elsevier, 1989.
20. R. D. Diehl and R. McGrath, Journal of Physics: Condensed Matter, **9**, 951 (1997).
21. R. W. Gurney, Physical Review, **47**, 479 (1935).
22. N. D. Lang, Physical Review B, **4**, 4234 (1971).
23. N. D. Lang and A. R. Williams, Physical Review Letters, **37**, 212 (1976).
24. N. D. Lang and A. R. Williams, Physical Review B, **18**, 616 (1978).
25. J. E. Inglesfield, Reports on Progress in Physics, **45**, 223 (1982).
26. A. Zangwill, Physics at Surfaces, Cambridge University Press, 1988.
27. N. D. Lang and W. Kohn, Physical Review B, **1**, 4555 (1070).
28. A. G. Borisov, J. P. Gauyacq, E. V. Chulkov, V. M. Silkin, and P. M. Echenique, Physical Review B, **65**, 235434 (2002).
29. J. P. Muscat and D. M. Newns, Progress in Surface Science, **9**, 1 (1978).
30. J. P. Muscat and D. M. Newns, Solid State Communications, **11**, 737 (1972).

31. J. P. Muscat and D. M. Newns, Journal of Physics C, **7**, 2630 (1974).
32. J. P. Muscat and D. M. Newns, Surface Science, **74**, 355 (1978).
33. J. P. Muscat and D. M. Newns, Surface Science, **84**, 262 (1979).
34. H. Ishida, Physical Review B, **38**, 8006 (1988).
35. H. Ishida, Physical Review B, **39**, 5492 (1989).
36. H. Ishida, Physical Review B, **42**, 10899 (1990).
37. H. Ishida and A. Liebsch, Physical Review B, **45**, 6171 (1992).
38. P. Nordlander and J. C. Tully, Physical Review B, **42**, 5564 (1990).
39. B. Woratschek, W. Sesselmann, J. Küppers, G. Ertl, and H. Haberland, Physical Review Letters, **55**, 1231 (1985).
40. H. Wedler, M. A. Mendez, P. Bayer, U. Löffler, K. Heinz, V. Fritzsche, and J. B. Pendry, Surface Science, **293**, 47 (1993)
41. W. C. Fan and A. Ignatiev, Journal of Vacuum Science and Technology A, **6**, 735 (1988).
42. D. Fisher, Z.-Y. Li, and R. D. Diehl, Surface Science, **259**, 85 (1991).
43. G. A. Benesh and D. A King, Chemical Physics Letters, **191**, 315 (1992).
44. D. Heskett, K.-H. Frank, K. Horn, E. E. Koch, H.-J. Freund, A. Baddorf, K.-D. Tsuei, and E. W. Plummer, Physical Review B, **37**, 10387 (1988).
45. D. Heskett, K.-H. Frank, E. E. Koch, and H.-J. Freund, Physical Review B, **36**, 1276 (1987).
46. K.-H. Frank, H.-J. Sager, and D. Heskett, Physical Review B, **40**, 2767 (1989).
47. D. A. Arena, F. G. Curti, and R. A. Bartynski, Physical Review B, **56**, 15404 (1997).
48. K. Giesen, F. Hage, F. J. Himpsel, H. J. Riess, and W. Steinmann, Physical Review Letters, **55**, 300 (1985).
49. N. Fischer, S. Schuppler, T. Fauster, and W. Steinmann, Surface Science, **314**, 89 (1994).
50. N. Fischer, S. Schuppler, R. Fischer, T. Fauster, and W. Steinmann, Physical Review B, **47**, 4705 (1993).
51. J. P. Gauyacq, A. G. Borisov, and M. Bauer, Progress in Surface Science, **82**, 244 (2007).
52. M. Bauer, S. Pawlik, and M. Aeschlimann, Physical Review B, **55**, 10040 (1997).
53. M. Bauer, S. Pawlik, and M. Aeschlimann, Physical Review B, **60**, 5016 (1999).
54. H. Petek, M. J. Weida, H. Nagano, and S. Ogawa, Science, **288**, 1402 (2000).
55. H. Petek, H. Nagano, M. J. Weida, and S. Ogawa, Journal of Physical Chemistry B, **105**, 6767 (2001).
56. H. Petek and S. Ogawa, Annual Reviews of Physical Chemistry, **53**, 507 (2002).
57. N. D. Lang and W. Kohn, Physical Review B, **3**, 1215 (1971).
58. T. Aruga and Y. Murata, Progress in Surface Science, **31**, 61 (1989).
59. K. Wandelt, Applied Surface Science, **111**, 1 (1997).
60. http://www.iupac.org/goldbook/ET07025.pdf
61. A. Kiejna and K. F. Wojciechowski, Metal Surface Electron Physics, Elsevier, 1996.
62. A. Riemann, PhD Dissertation, Free University of Berlin, Germany, 2002.
63. T. Fauster and W. Steinmann, 'Two-photon photoemission spectroscopy of image states', Electromagnetic Waves: Recent Developments in Research, vol: 2 (Photonic Probes of Surfaces), Elsevier, 1995.
64. H. Kawago, Progress in Surface Science, **83**, 1 (2008).
65. H. Hertz, Annalen der Physik, **31**, 983 (1887).
66. H. P. Bonzel and C. Kleint, Progress in Surface Science, **49**, 107 (1995).
67. A. Einstein, Annalen der Physik, **17**, 132 (1905).

68. P. Y. Yu and M. Cardona, Fundamentals of Semiconductors, 3rd edition, Springer Verlag, 2005.
69. H. Ueba and B. Gumhalter, Progress in Surface Science, **82**, 193 (2007).
70. R. H. Williams, G. P. Srivastava, and I. T. McGovern, Reports on Progress in Physics, **43**, 87 (1980).
71. H. Petek and S. Ogawa, Progress in Surface Science, **56**, 239 (1997).
72. K. Siegbahn, Philosophical Transactions of Royal Society of London A, **268**, 22 (1970).
73. M. Cardona and L. Ley, Photoemission in Solids –I, Springer Verlag, 1978.
74. S. Hüfner, S. Schmidt, and F. Reinert, Nuclear Instruments and Methods in Physics Research A, **547**, 8 (2005).
75. B. Feuerbacher, B. Fitton, and R. F. Willis, Photoemission and the Electronic Properties of Surfaces, Wiley, 1978.
76. H. Ueba and T. Mii, Applied Physics A, **71**, 537 (2000).
77. P. M. Echenique, R. Berndt, E. V. Chulkov, T. Fauster, A. Goldmann, and U. Höfer, Surface Science Reports, **52**, 219 (2004).
78. B. Li, PhD Dissertation, University of Pittsburgh, 2006.
79. W. Demtröder, Laser Spectroscopy, 3rd edition, Springer Verlag, 2004.
80. C. Rulliére, Femtosecond Laser Pulses, 2nd edition, Springer Verlag, 2005.
81. B. E. A. Saleh and M. C. Teich, Fundamentals of Photonics, Wiley, 1991.
82. A. Yariv, Quantum Electronics, 3rd edition, Wiley, 1989.
83. J.-C. Diels and W. Rudolph, Ultrashort Laser Pulse Phenonema, Academic Press, 1995.
84. N. Pontius, V. Sametoglu, and H. Petek, Physical Review B, **72**, 115105 (2005).
85. H. Ibach, Physics of Surfaces and Interfaces, Springer Verlag, 2006.
86. J. T. Yates, Experimental Innovations in Surface Science, Springer Verlag, 1997.
87. http://www.saesgetters.com/default.aspx?idPage=470
88. Omicron EA-125 Energy Analyzer, User's Manual, 2001.
89. K. Onda, B. Li, and H. Petek, Physical Review B, **70**, 045415 (2004).
90. Ortec, Modular Pulse-Processing Electronics Catalog, 2001.
91. Omicron CPC 125/65M Channeltron Pulse Counter Electronics for EA125 and AR65, User's Manual, 2001.
92. E. Rotenberg, http://www.coe.berkeley.edu/AST/srms/2007/Lec18.pdf
93. Z. Hussain, http://www.coe.berkeley.edu/AST/srms/2007/Lec17.pdf
94. J. W. Gadzuk, Solid State Communincations, **15**, 1011 (1974).
95. S. T. Shipman, S. Garrett-Roe, P. Szymanski, A. Yang, M. L. Strader, and C. B. Harris, Journal of Physical Chemistry B, **110**, 10002 (2006).
96. H. Ueba and B. Gumhalter, Progress in Surface Science, **82**, 193 (2007).
97. N. DelFatti, C. Voisin, M. Achermann, S. Tzortzakis, D. Christofilos, and F. Vallée, Physical Review B, **61**, 16956 (2000).
98. J. M. Pitarke, V. P. Zhukov, R. Keyling, E. V. Chulkov, and P. M. Echenique, European Journal of Chemical Physics and Physical Chemistry, **5**, 1284 (2004).
99. M. J. Weida, S. Ogawa, H. Nagano, and H. Petek, Journal of Optical Society of America B, **17**, 1443 (2000).
100. W. Nessler, S. Ogawa, H. Nagano, H. Petek, J. Shimoyama, Y. Nakayama, and K. Kishio, Journal of Electron Spectroscopy and Related Phenomena, **88-91**, 495 (1998).
101. S. Ogawa, H. Nagano, H. Petek, and A.P. Heberle, Physical Review Letters, **78**, 1339 (1997).

102. T. Miller, W. E. McMahon, and T.-C. Chiang, Physical Review Letters, **77**, 1167 (1996).
103. T. Miller, E. D. Hansen, W. E. McMahon, and T.-C. Chiang, Surface Science, **376**, 32 (1997).
104. B. Gumhalter and H. Petek, Surface Science, **445**, 195 (2000).
105. M. Wolf, A. Hotzel, E. Knoesel, and D. Velic, Physical Review B, **59**, 5926 (1999).
106. S. Pawlik, R. Burgermeister, M. Bauer, and M. Aeschlimann, Surface Science, **402–404**, 556 (1998).
107. C. Timm and K. H. Bennemann, Journal of Physics: Condensed Matter, **16**, 661 (2004).
108. V. M. Shalaev, C. Douketis, T. Haslett, T. Stuckless, and M. Moskovits, Physical Review B, **53**, 11193 (1996).
109. W. Shockley, Physical Review, **56**, 317 (1939).
110. H. Levinson and E. Plummer, Physical Review B, **24**, 628 (1981).
111. N. V. Smith, Physical Review B, **32**, 3549 (1985).
112. G. D. Mahan, Physical Review B, **2**, 4334 (1970).
113. R. E. Crandall and J. F. Delord, Journal of Physics A: Mathematical and Theoretical, **20**, 2279 (1987).
114. D. Steiger, C. Ahlbrandt, and R. Glaser, Journal of Physical Chemistry B, **102**, 4257 (1998).
115. T. Mii and H. Ueba, Journal of Luminescence, **87-89**, 898 (2000).
116. http://physics.nist.gov/cgi-bin/cuu/Value?bohrrada0|search_for=bohr+radius
117. N. V. Smith, C. T. Chen, and M. Weinert, Physical Review B, **40**, 7565 (1989).
118. M. J. Weida, S. Ogawa, H. Nagano, and H. Petek, Journal of Optical Society of America B, **17**, 1443 (2000).
119. V. Bortolani, N. H. March, and M. P. Tosi, Interactions of Atoms and Molecules with Solid Surfaces, Plenum Press, 1990.
120. G. V. Hansson and S. A. Flodström, Physical Review B, **17**, 473 (1978).
121. J. Nelson, S. Kim, W. Gignac, R. S. Williams, J. Tobin, S. Robey, and D. Shirley, Physical Review B, **32**, 3465 (1985).
122. J. J. Quinn, Applied Physics Letters, **2**, 167 (1963).
123. J. J. Quinn, Physical Review, **126**, 1453 (1962).
124. M. Aeschlimann, M. Bauer, and S. Pawlik, Chemical Physics, **205**, 127 (1996).
125. P. M. Echenique, J. M. Pitarke, E. V. Chulkov, and A. Rubio, Chemical Physics, **251**, 1 (2000).
126. V. P. Zhukov, F. Aryasetiawan, E. V. Chulkov, and P. M. Echenique, Physical Review B, **65**, 115116 (2002).
127. Electronic Structure Database of the National Institute for Material Science (NIMS), Tokyo, 2004, (http://mits.nims.go.jp).
128. T. Miller and T.-C. Chiang, Journal of Physics: Condensed Matter, **13**, 11115 (2001).
129. G. Grimvall, The Electron-Phonon Interaction in Metals, North-Holland, 1981.
130. R. Knorren, G. Bouzerar, and K. H. Bennemann, Physical Review B, **63**, 125122 (2001).
131. R. Knorren, G. Bouzerar, and K. H. Bennemann, Journal of Physics: Condensed Matter, **14**, R739 (2002).
132. http://scienceworld.wolfram.com/physics/DebyeTemperature.html
133. S. LaShell, B. A. McGougall, and E. Jensen, Physical Review B, **74**, 033410 (2006).
134. D. A. Shirley, Physical Review B, **5**, 4709 (1972).

135. A. Kubo, K. Onda, H. Petek, Z. Sun, Y. S. Jung, and H. K. Kim, Nano Letters, **5**, 1123 (2005).
136. C. N. Berglund and W. E. Spicer, Physical Review, **136**, A1030 (1964).
137. K. Giesen, F. Hage, F. J. Himpsel, H. J. Reiss, and W. Steinmann, Physical Review B, **35**, 971 (1987).
138. E. Knoesel, A. Hotzel, and M. Wolf, Physical Review B, **57**, 12812 (1998).
139. S. Ogawa, H. Nagano, and H. Petek, Physical Review B, **55**, 10869 (1997).
140. P. S. Wehner, R. S. Williams, S. D. Kevan, D. Denley, and D. A. Shirley, Physical Review B, **19**, 6164 (1979).
141. J. G. Nelson, S. Kim, W. J. Gignac, R. S. Williams, J. G. Tobin, S. W. Robey, and D. A. Shirley, Physical Review B, **32**, 3465 (1985).
142. M. A. Mueller, A. Samsavar, T. Miller, and T.-C. Chiang, Physical Review B, **40**, 5845 (1989).
143. H. Becker, E. Dietz, U. Gerhardt, and H. Angermüller, Physical Review B, **12**, 2084 (1975).
144. D. J. Spanjaard, D. W. Jepsen, and P. M. Marcus, Physical Review B, **15**, 1728 (1977).
145. S. C. Wu, H. Li, J. Sokolov, J. Quinn, Y. S. Li, and F. Jona, Journal of Physics: Condensed Matter, **1**, 7471 (1989).
146. H. Wern, R. Courths, G. Leschik, and S. Hüfner, Zeitschrift für Physik: Condensed Matter, **60**, 293 (1985).
147. A. Winkelmann, V. Sametoglu, J. Zhao, A. Kubo, and H. Petek, Physical Review B, **76**, 195428 (2007).
148. J. Hager, T. Michalke, and R. Matzdorf, Surface Science, **600**, 1129 (2006).
149. M. V. Klein and T. E. Furtak, Optics, Wiley, 1986.
150. J. D. Jackson, Classical Electrodynamics, 3rd edition, Wiley, 1998.
151. F. Pforte, T. Michalke, A. Gerlach, A. Goldmann, and R. Matzdorf, Physical Review B, **63**, 115405 (2001).
152. A. Gerlach, R. Matzdorf, and A. Goldmann, Physical Review B, **58**, 10969 (1998).
153. P. J. Feibelman, Surface Science, **46**, 558 (1974).
154. M. A. B. Whitaker, Journal of Physics C, **11**, L151 (1978).
155. F. Pforte, A. Gerlach, A. Goldmann, R. Matzdorf, J. Braun, and A. Postnikov, Physical Review B, **63**, 165405 (2001).
156. R. Paniago, R. Matzdorf, G. Meister, and A. Goldmann, Surface Science, **336**, 113 (1995).
157. G. Nikolay, F. Reinert, S. Schmidt, D. Ehm, P. Steiner, and S. Hüfner, Physical Review B, **62**, 1631 (2000).
158. H. Wern, R. Courths, G. Leschik, and S. Hüfner, Zeitschrift für Physik: Condensed Matter, **60**, 293 (1985).
159. S. C. Wu, H. Li, J. Sokolov, J. Quinn, Y. S. Li, and F. Jona, Journal of Physics: Condensed Matter, **1**, 7471 (1989).
160. A. Samsavar, T. Miller, and T.-C. Chiang, Journal of Physics: Condensed Matter, **2**, 1141 (1990).
161. D. K. Saldin and J. C. H. Spence, Ultramicroscopy, **55**, 397 (1994).
162. J. W. Gadzuk, Physical Review B, **1**, 2110 (1970).
163. J. Zhao, N. Pontius, A. Winkelmann, V. Sametoglu, A. Kubo, A. G. Borisov, D. Sánchez-Portal, V. M. Silkin, E. V. Chulkov, P. M. Echenique, and H. Petek, Physical Review B, **78**, 085419 (2008).
164. H. Petek, M.J. Weida, H. Nagano, and S. Ogawa, Surface Science, **451**, 22 (2000).

165. J. W. Gadzuk, Surface Science, **43**, 44 (1974).
166. C. J. Ballhausen and H. B. Gray, Molecular Orbital Theory: An Introductory Lecture Note and Reprint Volume, W. A. Benjamin, Inc., 1965.
167. J. D. Roberts, Notes on Molecular Orbital Calculations, The Benjamin/Cummings Publishing Company, 1961.
168. A. G. Borisov, V. Sametoglu, A. Winkelmann, A. Kubo, N. Pontius, J. Zhao, V. M. Silkin, J. P. Gauyacq, E. V. Chulkov, P. M. Echenique, and H. Petek, Physical Review Letters, **101**, 266801 (2008).
169. H. Ishii, K. Sugiyama, E. Ito, and K. Seki, Advanced Materials, **11**, 605 (1999).
170. X. Y. Zhu, Surface Science Reports, **56**, 1 (2004).
171. D. Cahen, A. Kahn, and E. Umbach, Materials Today, **8**, 32 (2005).
172. F. S. Tautz, Progress in Surface Science, **82**, 479 (2007).
173. A. G. Borisov, J. P. Gauyacq, A. K. Kazansky, E. V. Chulkov, V. M. Silkin, and P. M. Echenique, Physical Review Letters, **86**, 488, (2001).
174. K. Niedfeldt, P. Nordlander, and E. A. Carter, Physical Review B, **74**, 115109 (2006).
175. T. Klüner, N. Govind, Y. A. Wang, and E. A. Carter, Physical Review Letters, **86**, 5954 (2001).
176. J. B. Neaton, M. S. Hybertsen, and S. G. Louie, Physical Review Letters, **97**, 216405 (2006).
177. G. K. Wertheim, D. M. Riffe, and P. H. Citrin, Physical Review B, **49**, 4834 (1994).
178. C. Stampfl, J. Neugebauer, and M. Scheffler, Surface Science, **307-309**, 8 (1994).
179. S. Ogawa, H. Nagano, and H. Petek, Physical Review Letters, **82**, 1931 (1999).
180. S. A. Lindgren and L. Walldén, Physical Review B, **45**, 6345 (1992).
181. A. Eiguren, B. Hellsing, F. Reinert, G. Nikolay, E. V. Chulkov, V. M. Silkin, S. Hüfner, and P. M. Echenique, Physical Review Letters, **88**, 066805 (2002).
182. H. Petek, H. Nagano, M. Weida, and S. Ogawa, Chemical Physics, **251**, 71 (2000).
183. T.-C. Chiang, Surface Science Reports, **39**, 181 (2000).
184. A. G. Borisov, A. K. Kazansky, and J. P. Gauyacq, Surface Science, **430**, 165 (1999).
185. J. N. Bardsley, Case Studies in Atomic Physics, **4**, 299 (1974).
186. E. V. Chulkov, V. M. Silkin and P. M. Echenique, Surface Science, **437**, 330 (1999).
187. http://en.wikipedia.org/wiki/Periodic_table
188. J. W. Gadzuk, Surface Science, **6**, 133 (1967).
189. A. G. Borisov, A. K. Kazansky, and J. P. Gauyacq, Physical Review B, **59**, 10935 (1999).
190. H. Winter, Physics Reports, **367**, 387 (2002).
191. E. V. Chulkov, A. G. Borisov, J. P. Gauyacq, D. Sanchez-Portal, V. M. Silkin, V. P. Zhukov, and P. M. Echenique, Chemical Reviews, **106**, 4160 (2006).
192. J. P. Perdew, K. Burke, and M. Ernzerhof, Physical Review Letters, **77**, 3865 (1996).
193. A. G. Borisov, A. K. Kazansky, and J. P. Gauyacq, Physical Review B, **65**, 205414 (2002).
194. J. W. Gadzuk, Physical Review B, **10**, 5030 (1974).
195. T. Seideman, Annual Review of Physical Chemistry, **53**, 41 (2002).
196. E. W. Plummer and W. Eberhardt, Advances in Chemical Physics, **49**, 533 (1982).
197. J. Cooper and R. N. Zare, Journal of Chemical Physics, **48**, 942 (1968).
198. A. H. Zewail, Journal of Physical Chemistry A, **104**, 5660 (2000).
199. http://www.zewail.caltech.edu/
200. F. C. De Schryver, S. De Feyter, and G. Schweitzer, Femtochemistry: With the Nobel Lecture of A. Zewail, Wiley-VCH, 2001.

201. C. Manescu, PhD Dissertation, University of Florida, 2004.
202. Y. Tanimura, K. Yamashita, and P. A. Anfinrud, Proceedings of the National Academy of Sciences, **96**, 8823 (1999).
203. H. Petek, H. Nagano, M. J. Weida, and S. Ogawa, Journal of Physical Chemistry A, **104**, 10234 (2000).
204. J. Stähler, U. Bovensiepen, M. Meyer, and M. Wolf, Chemical Society Reviews, **37**, 2180 (2008).
205. J. Zhao, B. Li, K. Onda, M. Feng, and H. Petek, Chemical Reviews, **106**, 4402 (2006).
206. J. C. Polanyi and A. H. Zewail, Accounts of Chemical Research, **28**, 119 (1995).
207. L. Bartels, G. Meyer, K.-H. Rieder, D. Velic, E. Knoesel, A. Hotzel, M. Wolf, and G. Ertl, Physical Review Letters, **80**, 2004 (1998).
208. A. Föhlisch, P. Feulner, F. Hennies, A. Fink, D. Menzel, D. Sánchez-Portal, P. M. Echenique, and W. Wurth, Nature, **436**, 373 (2005).
209. B. Hellsing, D. V. Chakarov and L. Österlund, V. P. Zhdanov, and B. Kasemo, Journal of Chemical Physics, **106**, 982 (1997).
210. J. P. Gauyacq and A. K. Kazansky, Physical Review B, **72**, 045418 (2005).
211. J. P. Gauyacq, Surface Science, **602**, 3477 (2008).
212. D. Kröner, T. Klamroth, M. Nest, and P. Saalfrank, Applied Physics A, **88**, 535 (2007).
213. P. Saalfrank, Chemical Review, **106**, 4116 (2006).
214. M. Wiesenmmayer, M. Bauer, S. Mathias, M. Wessendorf, E. V. Chulkov, V. M. Silkin, A. G. Borisov, J. P. Gauyacq, P. M. Echenique, and M. Aeschlimann, Physical Review B, **78**, 245410 (2008).
215. X.-L. Zhou, X.-Y. Zhu, and J. M. White, Surface Science Reports, **13**, 73 (1991).
216. F. Weik, A. de Meijere, and E. Hasselbrink, Journal of Chemical Physics, **99**, 682 (1993).
217. W. Ho, Journal of Physical Chemistry, **100**, 13050 (1996).
218. R. R. Cavanagh, D. S. King, J. C. Stephenson, and T. F. Heinz, Journal of Physical Chemistry, **97**, 786 (1993).
219. D. Menzel and R. Gomer, Journal of Chemical Physics, **41**, 3311 (1964).
220. P. A. Redhead, Canadian Journal of Physics, **42**, 886 (1964).
221. A. Gerlach, K. Berge, A. Goldmann, I. Campillo, A. Rubio, J. M. Pitarke, and P. M. Echenique, Physical Review B, **64**, 085423 (2001).
222. R. Matzdorf, Surface Science Reports, **30**, 153 (1998).
223. http://www.webelements.com/
224. SAES Getters SpA, Alkali Metal Dispensers (AMD) Manual.